University of Nottingham
UK | CHINA | MALAYSIA

Impact of second phase content over rheological behaviour of rock salt under cyclic loading conditions applied to Underground Gas Storage

Carla Martín Clavé

Student Number: 4289912

Dr. Veerle Vandeginste (University of Nottingham)
Dr. Audrey Ougier-Simonin (British Geological Survey)
Dr. Alec M Marshall (University of Nottingham)

A Thesis Submitted to the University of Nottingham
in partial fulfillment of the requirements for the degree of
Doctor of Engineering (EngD).

April 2021

To my beloved and supportive family, especially my dad and brother

Abstract

The use of caverns in rock salt for Underground Gas Storage (UGS) and Compressed Air Energy Storage (CAES) have been identified as a strategic option to meet seasonal energy demand fluctuations in the electricity grid. More recently, the Department for Business, Energy and Industrial Strategy (BEIS) presented for the UK Clean Growth strategy a plan to also integrate rock salt caverns as storage solution for co-located carbon capture, utilisation and storage (CCUS) and hydrogen production. The creation of caverns in halite formations and the operational activities of gas injection and withdrawal occurring under lithostatic pressure are known to lead to local deviatoric stresses, resulting in rock salt creep deformation. Additionally, periodic injection-production activities in response to seasonal temperature changes and associated gas consumption imply regular fluctuation of both mechanical and thermal stresses in salt caverns.

Rock salt is mainly composed of halite and has low i) creep strength, ii) porosity, iii) permeability, and iv) density, making it a very good seal rock to store gas. It also typically contains secondary mineral phases (e.g. anhydrite, polyhalite, carnallite, kieserite), as well as fluids trapped in inclusions in the halite crystals, at halite grain boundaries, or in pores. This presence of other minerals besides halite, or other rock layers between the rock salt formations at a range of scales, can have significant effects on the micro and macro-mechanical properties due to their different rheological behaviours, notably weakening the rock salt under high stress conditions.

This project investigates the impact of the secondary mineral phase content on the rock salt mechanical behaviour under cyclic loading conditions. A series of cyclic mechanical loading experiments, at two different ranges of cyclic mechanical load, have been performed on different rock salt samples with different types and amounts of second phase minerals content. In the first set of tests, different confining pressures of 12, 25 and 45 MPa and different temperatures, of 22-25, 55 and 75^{o}C, have been applied whilst the axial stress was cycled between 4.5 and 7.5 MPa, at 0.5 kN/s loading rate, during 48h (7200 cycles). In the second set of experiments, the axial stress was cycled between 6 and 20 MPa, at 0.5 kN/s loading rate, during 48h (7200 cycles) and confining pressures of 25 and 45MPa and temperatures of 22-25, 55 and 75^{o}C. Thin sections of each sample's microstructures, before and after mechanical deformation, were analysed by transmitted light microscopy and Scanning Electron Microscopy (SEM) to identify the micro-mechanisms and early damage induced by the cyclic loading conditions.

The results demonstrate that high second phase content such as anhydrite layering operates as a strength weakening agent by displaying larger brittle deformation features in comparison to samples with a lower content in anhydrite, polyhalite or clay as second phase content. This rheological behavior is further exacerbated by the cycling mechanical conditions and recorded by a marked step on Young's modulus and Poisson's ratio value evolution. The microstructure analysis reveals how halite grains accommodate most of the deformation induced by the cyclic mechanical loading conditions through brittle deformation with micro-fracturing network development. Other structures

from different deformation mechanisms are also discussed. Two types of new porosity are observed: i) pores around isolated crystals of second phase minerals as a result of grain rotation under cyclic mechanical deformation, and ii) micro-cracks in areas with high concentration of secondary minerals (such as anhydrite, polyhalite, carnallite or kieserite). This porosity change has strong implications for both the mechanical behaviour of the material and its potential permeability.

Acknowledgements

Throughout the writing of this dissertation I have received a great deal of support and assistance.

I would first like to thank my main supervisors, Audrey Ougier-Simonin and Veerle Vandeginste, whose expertise was invaluable in supporting my research and development of my thesis. Their insightful comments and suggestions have helped me not only to complete my research work but also to shape myself as a researcher, helping me to sharper my thinking and bringing my work to a higher level.

Secondly, I want to thank my two amazing colleagues, Grace Belshaw and Josh Baptist, who have helped me and supported me every time I have needed it.

I also want to thank the British Geological Survey (BGS) and all the people working at the Rock Mechanics and Physics Laboratory at BGS, for supporting me in my experimental work and investing their time supervising me during my experimental tests.

Finally, and not less important, I want also to show my gratitude to the Winsford and Boulby Mine for providing me with rock salt samples to conduct the mechanical tests for my research.

List of Publications

1. Martin-Clave, C., Ougier-Simonin, A., Vandeginste, V. (2021). Impact of Second Phase Content on Rock Salt Rheological Behavior Under Cyclic Mechanical Conditions. Rock Mechanics and Rock Engineering, 1-23.

2. Martin-Clave, C., Ougier-Simonin, A., Vandeginste, V. (2020, December). Impact of impurities and structural analysis of salt rock for underground gas storage. In 82nd EAGE Annual Conference Exhibition (Vol. 2020, No. 1, pp. 1-5). European Association of Geoscientists Engineers. https://doi.org/10.3997/2214-4609.202011862

Contents

List of Tables

List of Figures

Chapter 1

Introduction

This PhD thesis addresses the rheological behaviour of rock salt under cyclic mechanical conditions applied to Underground Gas Storage (UGS) activities, particularly, the impact of second phase content present in rock salt. The study of how mechanical properties of rock salt can be affected by rock sample composition under different cyclic mechanical conditions at different temperature and confining pressures. The first chapter of this thesis offers a description of the methodologies used to deliver the research work. The research is conducted by a pre-deformation description of rock samples, using X-Ray diffraction analysis and transmitted light microscopy, and a post-deformation structural analysis under cyclic mechanical conditions. Chapter two gives an extensive review of the two main geological sites from where the rock salt samples have been collected, Winsford Mine (Triassic) and Boulby Mine (Permian). A review on the main properties of rock salt and deformation mechanisms are also given as well as an introduction to Underground Gas Storage in salt caverns. The different pressure and temperature conditions at which rock salt is subjected in UGS activities are analysed in this chapter too.

A mineralogical and structural description of rock salt samples before deformation is offered in Chapter 3. Samples are analysed before mechanical tests to arrange different testing groups based on the second phase content. A

microstructural description is also performed in order to identify the main deformation mechanisms during the cyclic mechanical loading tests. Mechanical data under cyclic conditions at different temperature and confining pressure is discussed in Chapters 4, 5 and 6. A review on the compositional implications on mechanical properties is also discussed. Chapter 7 summarises and the final remarks from all analyses performed in the previous Chapters.

1.1 Motivations

Underground geological storage of gas is an effective solution to accommodate fluctuations in energy peak demands by storing of CH_4, H_2 and used for Compressed Air Energy Storage (CAES). For this reason, in the last years there has been a growing interest around UGS in salt caverns.

Rock salt (Halite) has been assessed as a very effective seal for trapping hydrocarbons on petroleum systems at geological time scales. However, human activities of gas injection and withdrawal cause stress in the rock salt layers which can differ from the experienced in natural systems. The gas injection-withdrawal cycles in salt caverns results in a fluctuation of pressures and temperatures resulting in differential stress and affecting the rheological behaviour of the rock mass. Rock salt deformation under has been investigated different temperature and pressure conditions. However, a better understanding of how cyclic variations of pressure and temperatures applied for UGS and CAES is needed.

Rock salt, which is mainly composed of halite (NaCl), can present other associated evaporites such as anhydrite, polyhalite, gypsum, kieserite, carnallite... This second phase mineralogy in rock salt can lead to a completely different rheological behaviour under deformation also influenced by a change of pressure and temperature inside salt caverns. Therefore, not only a better un-

derstanding on how second phase content can affect the mechanical properties of rock salt, but also the impact of mechanical and temperature fluctuations linked to UGS activities in salt caverns. Investigation of the different mechanical behaviour from rock salt with a diverse mineralogical composition will help to understand better the deformation mechanisms implied and how to improve the stability of salt caverns under different ranges of pressure and temperatures. Safety and assessment of the long-term integrity in solution mining can be enhanced with a better understanding of the different mechanical properties of rock salt depending on the second phase content.

1.2 Aims and scope

The main aim of this PhD project is to study the impact of impurities on the environmental risks and hazards of methane-hydrogen storage and CAES in salt caverns. Salt layers are not uniform in their composition and structure. Salt rock predominantly consists of halite but can also contain inclusions or large units of anhydrite, gypsum, clay and other minerals or mudrock. The presence of these impurities affects the rock salt characteristics and potential risks (Bérest et al., 2005, 2006). Moreover, different salt structures, such as bedded undeformed layers versus salt diapirs, can have an impact on the stability of salt caverns. With this, the EngD Research Project on Impact of Impurities and salt structures on environmental risks of Methane- Hydrogen Storage in Salt Caverns aims to identify the main deformation mechanisms linked to different types of impurity content and how it affects environmental risks and hazards of methane-hydrogen storage in salt caverns. The methodology included in the research involved:

- Chemical and mineralogical analysis of salt rock samples from Salt Mines from the UK to identify main impurities.

- Micro-structural and mineralogical description of rock salt samples before deformation under cyclic loading conditions.

- Cyclic mechanical loading tests to study the implications of impurity content and how the impurity content affects the mechanical properties of salt rock under different confining pressure and temperature.

- Post- deformation micro-structural analysis to identify the main deformation mechanisms involved in the deformation of samples at different confining pressure and temperature conditions. Analyse the effect of impurity content over deformation mechanisms from salt rock.

Salt caverns are located at depths between 500 m and 2000 m, and for this reason the confining pressures used for many authors are between 7 MPa and 45 MPa (Kruck et al., 2013; Ma et al., 2013; Djizanne, 2014). From the research plan presented in September 2018, three different scenarios based on the depth at which Salt Caverns can be found have been and are still being tested. The testing conditions of confining pressure (Pc) and temperature tested correspond to 200- 500 m depth, 500- 800 m depth and 800- 1200 m depth.

1.3 Technical challenges

Salt caverns used for Underground Gas Storage are subjected to pressure and temperature fluctuations linked to injection-withdrawal periods. However, a complete injection-withdrawal cycle can vary depending on the type of activity storage and stored gas. While CAES presents daily injection-withdrawal cycles Natural Gas storage is seasonal, to meet the seasonal peak demand in the electricity grid in to winter and colder months. However, due to the amount of samples to test and the time limitations, the cyclic mechanical loading test were not able to reproduce seasonal injection-withdrawal cycles. For this reason, the planned mechanical tests had a duration of 48h where the rock salt

samples were tested under a worst scenario with several cycles but always keeping the stress state within the compaction domain. Samples were never tested under dilatation stress conditions in order to avoid the sample failure under dilatancy. The reason of avoiding sample failure was to understand the impact of secondary mineral phases rock salt under critical cyclic stress applicable to UGS and study the implications on rock porosity creation.

Initially, synthetic rock salt samples were considered to be tested and compared to the rock mechanics data from natural rock salt. The aim of using synthetic samples was to have a better control on the second phase content and texture of the tested samples. The creation of synthetic samples with different content in halite and anhydrite, and different distribution of secondary mineral phase, would add valuable information about how second phase content, and its distribution within the rock salt sample, affects the rheological behaviour of rock salt under cyclic mechanical conditions. However, considerable technical challenges arose during the synthetic salt samples confection related to the grain size and crystallisation process of synthetic samples. When compared to the natural rock salt being tested in the lab, the synthetic salt samples presented smaller grain size and higher inergranular porosity. In order to induce a recrystallisation process to reproduce similar rock texture to natural samples, the synthetic specimens had to be subjected to an annealing process in a high-pressure vessel with high temperature. Unfortunately, the pressure vessel used at the British Geological Survey had an important leak which resulted in a loss of pressure and failure of the annealing experiment. Methods and issues were discussed with professionals from the solution mining industry at the SMRI Annual Conference in Belfast in October 2018 who showed their scepticism about using synthetic rock salt as a representative alternative to natural samples. For this reason and due to the technical problems and complexity of synthetic rock salt samples creation, I decided to focus the project on data from natural rock salt testing only.

In the last months of the project, the interruption of lab work due to Covid-19 outbreak resulted in delays to finish part of the sample analysis after deformation. Unfortunately, due to restrictions to access the facilities at the University of Notthingham, a complementary structural analysis with EBSD could not be completed. The micro-structural description of thin sections after deformation had to be carried out with thin sections by using the transmitted light microscope.

1.4 Contributions

This section compiles a list with the work presented in conferences and seminars. The work presented here is the result of the research work conducted during the PhD within the framework of the Carbon Capture and Storage and Cleaner Fossil Energy CDT at the University of Nottingham (UK).

1.4.1 Poster presentations

Underground Gas Storage in Salt Caverns. Advances in Production Geoscience as an enabler for maximising economic recovery and ensuring a future for the UKCS. Geological Society Events, Petroleum Group, 2018 Year of Resources. 06- 07 June 2018. Aberdeen, UK. https://www.geolsoc.org.uk/expired/PG-Production-Geoscience

Carla Martin- Clave, Audrey Ougier- Simonin, Alec M. Marshall and Veerle Vandeginste. Impact of Impurities in Salt Rock for Underground Gas Storage in Salt Caverns. Geophysical Research Abstracts Vol. 21, EGU2019-16684-2, 2019 EGU General Assembly 2019. https://meetingorganizer.copernicus.org/EGU2019/EGU2019-16684-2.pdf

1.4.2 Oral presentations

Structural analysis and effect of impurity content in Salt Rock deformation under Cyclic Thermo-Mechanical Loading Conditions. 13th EURO- Conference on Rock Physics and Geomechanics – The Gueguen Conference. 2- 6 September 2019 Potsdam, Germany. https://events.gfz-potsdam.de/euro-2019/

Impact of impurities on the rheological behaviour of Salt Rock for Underground Gas Storage in Salt Caverns. Clean Energy Science Lecture. The Fuel and Energy Research Forum. 7th October 2019, London. https://cathyhillevents.co.uk/ferf/Clean%20energy%20sci%20lecture/Clean%20energy%20sci%20lecture.html

1.4.3 Session chairing

Conference session chairing at Session 7: Compaction and damage of porous rock II at 13th EURO- Conference on Rock Physics and Geomechanics – The Gueguen Conference. 2- 6 September 2019 Potsdam, Germany https://events.gfz-potsdam.de/euro-2019/program/

Chapter 2

Rock salt intrinsic properties for underground gas storage: a review

2.1 Introduction

Rock salt is a sedimentary rock which consists of sodium chloride (NaCl). It forms where large volumes of brine or saline water evaporites under arid-climate conditions. Variations in topography, water depth and salinity can lead to different sequences of evaporites overlying and overlapping. Other type of sedimentary or of detrital particles can be found interlayering or scattered as result of sedimentary additions from outside the basin. All this factors in addition to post depositional processes such as diagenesis will result in an evaporite formation with physical and chemical properties according to its composition and texture.

In this chapter the different depositional environments for evaporite sediments are described to provide an insight of initial deposition conditions and how those conditions can imply changes in composition and secondary mineralogy associated to rock salt formations. Different rock composition can have direct

implications over the rock texture and physical properties. This chapter aims to offer a first view about the initial processes involved in the first stages of rock deposition to understand the origin of compositional variance and different facies associated to evaporites, also known as second phase content. This introductory information about deposition of evaporites will help the reader to understand the origin in the chemical and textural composition of Triassic and Permian rock salt formations in the UK.

After a brief introduction about the deposition of evaporites and associated mineralogy, the reader will find a description about basic measurements of rock mechanics parameters and rheological behaviour of rock salt. Different second phase content can imply changes in the rheological behaviour of rock salt which will be further discussed with the work presented in this thesis.

2.2 Precipitation and formation of rock salt

Rock salt is an evaporite and results from saline brine evaporation generally occurring in isolated water by a barrier or sill, known as "primary deposits". Those lagoons are typically found in arid and warm climates, with water temperature from between 15° and 35°C (Gevantman and Lorenz, 1981; Jeremic, 1994). However, evaporites can be deposited as a result of sea basin's closure like the Messinian salinity crisis of the Mediterranean Sea (Tekin et al., 2010). Rock salt is mainly composed of halite (NaCl) frequently associated with other minerals such as dolomite, calcite, gypsum, anhydrite and potash minerals (Gevantman and Lorenz, 1981). It is thus a polycrystalline material formed mainly by grains of halite (NaCl) with a grain size range between less than 1 mm to several dm and a density of about 2.16 kg/m^3 (Hunsche and Hampel, 1999). Halite is colourless and rock salt natural coloration is due to the inclusion of other minerals as interstitial matter - impurities - and struc-

tural defects in the crystal lattice (Sonnenfeld, 1995).

The appearance of other evaporites associated to halite occurs as result of the chemical differentiation of the saline water by precipitation, their relative solubility and depositional order. Due to different solubility between different salt minerals, deposition occurs in facies where the most soluble salts are deposited at the end of the depositional process (Jeremic, 1994). Different sequences of evaporites overlying and overlapping can occur as result of variations in topography, water depth and salinity due to the subsidence and sedimentary fillings of the basin. Therefore, rock salt can also contain silt, sands or coarse, granular sediments as secondary mineralogy as result of detrital particles added to the basin during depositional processes (Gevantman and Lorenz, 1981).

In this thesis, all the tested samples were collected from bedded rock salt formations. However, rock salt formations can occur as bedded rock salt or rock salt diapirs. Salt structures are unlikely to develop spontaneously from a tabular layer of evaporites due to buoyancy alone (Jackson and Vendeville, 1994; Harding and Huuse, 2015). Salt diapirism or salt movement is attributed to regional extensional deformation. According to Vendeville and Jackson (1993) the different phases of diapirism can be described as i) reactive, as a response to extension of the brittle overburden, ii) active, when the reactive diapir has gained sufficient vertical extent and the overburden has been thinned by extension (Schultz-Ela et al., 1993; Jackson et al., 1994), and iii) passive, when the diapir has intruded and pushed aside the overburden to the point of salt emergence at the sedimentation surface (Hudec and Jackson, 2007).

2.2.1 Depositional environments

The most accepted depositional model for bedded rock salt was first described by Ochsenius (1877) as the bar-basin theory. Ochsenius (1877) proposed a depositional model where sea circulation is restricted by a natural barrier such as a sand bar, ridge or reef resulting in salt water evaporation. An alternation between periodic influxes of fresh sea water (by inlets or channels cutting across the barrier) and evaporation, and a limitation of the outflow, leads to an evaporite minerals precipitation into basin-wide beds. The precipitation of the chemical sediment take place in closed environments where evaporation the rate is higher than the water input supplied by rain, rivers and oceans. Periodic or continuous inflow of marine water can occur through channels across the topographical barrier that isolates the basin or seepage inflow (Figure 2.1) (Ochsenius, 1877; Gevantman and Lorenz, 1981; Jeremic, 1994; Melvin, 1991).

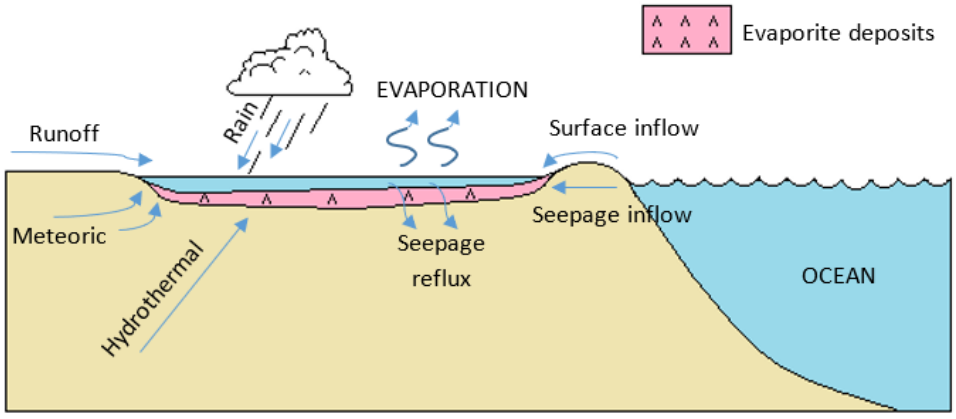

Figure 2.1: *Model of evaporite formation (After Melvin (1991)). The schematic picture shows an example of closed marine basin. The picture show the different elements such as brine and water inflow and evaporation which results in precipitation of evaporites on the bottom of the closed marine basin.*

Evaporites can be deposited in different environments from marginal-marine salinas or sabkhas to saline lakes and non-marine lacustrine depositional environments (Melvin, 1991). Rock salt is mainly deposited in marginal marine salinas take place above the sea level as a result of supratidal coastal sabkhas,

distal margins of fan deltas and ephemeral stream deltas, and interdune depressions (Figure 2.2). Marginal marine salinas are subaqueous and subaerial depositional environments likely located in a coastal plain. In areas with a high relief, alluvial fans can be developed whereas in areas with a low relief, ephemeral streams or wadis commonly empty into a salina (Melvin, 1991).

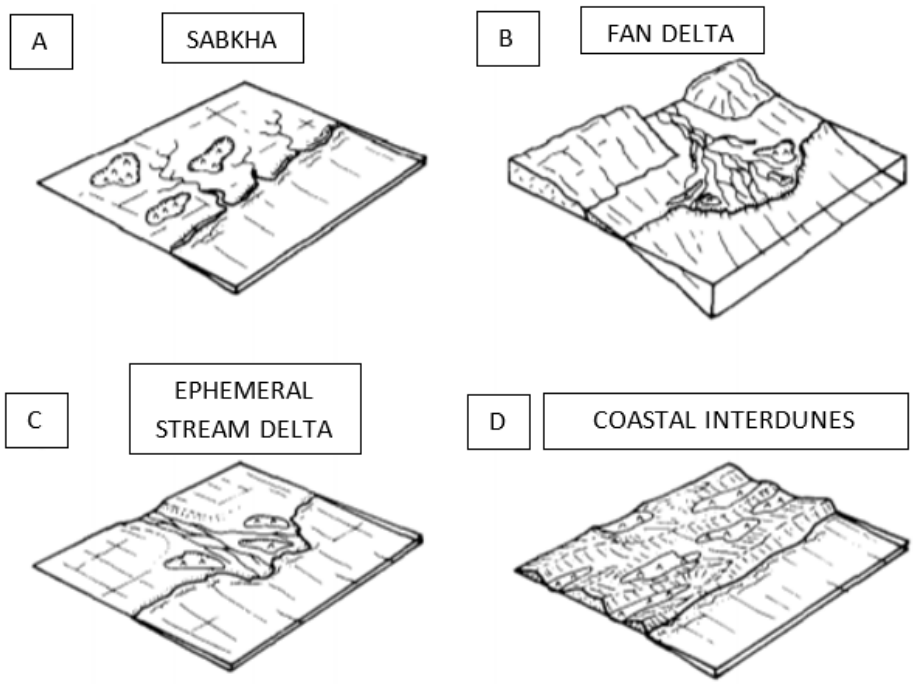

Figure 2.2: *Schematic picture showing the different marginal marine depositional environment where rock salt can be deposited: A) Sabkha, B) fan delta, C) ephemeral stream delta and D) coastal inter-dunes (Melvin, 1991).*

Temperature contrast of air and water, wind speed, humidity of the atmosphere and water surface turbulence control evaporation. A part of evaporation, loss of brine can occur by seeping through the basin sediments. In that case a good balance between flow rate escaping from the basin and inflow is basic to maintain the depositional environment. If the rate of flow leaving the basin exceed the inflow, the system terminates (Melvin, 1991).

2.2.2 Second phase content in rock salt

The Ring Theory (Figure 2.3) explains the chemical differentiation between evaporite sediments based on their relative solubility and depositional order (Jeremic, 1994).

Since Precambrian time, several evaporite deposits have been formed and buried all over the globe. Due to the different solubility of the elements present in the sea water, the sedimentary formations present different chemical compositions. Rock salt results from saline brine evaporation generally occurring in isolated water by a barrier or sill, known as "primary deposits". Some evaporite deposits, known as "secondary-cycle", are formed by a re-deposition of dissolved primary deposits. Moreover, evaporite sediments can also suffer post-depositional mechanical alteration as folding and faulting structures and chemical alteration by water solution from water percolation in the evaporite rock formation. Other parameters like environmental depositional conditions, post-depositional changes may affect the chemical composition of rock. During depositional processes other rock components can be deposited and incorporated in the rock such as clays or other detrital sediments (Jeremic, 1994).
All these modifications and disruptions are sources of second phase content. This complexified microstructure therefore is likely to have an significant impact on the geomechanical properties of the resulting rock (Liang et al., 2007; Wang et al., 2013).

Four different saline facies can be distinguished based on the chemical composition of the microstructure: i) calcium sulphate facies, ii) sodium salt facies, iii) chloride facies, and iv) potassium facies (Jeremic, 1994).

Calcium sulphate facies are represented basically by two main facies: gypsum ($CaSO_4 \cdot 2H_2O$), which precipitates first at a temperature below 34°C, and

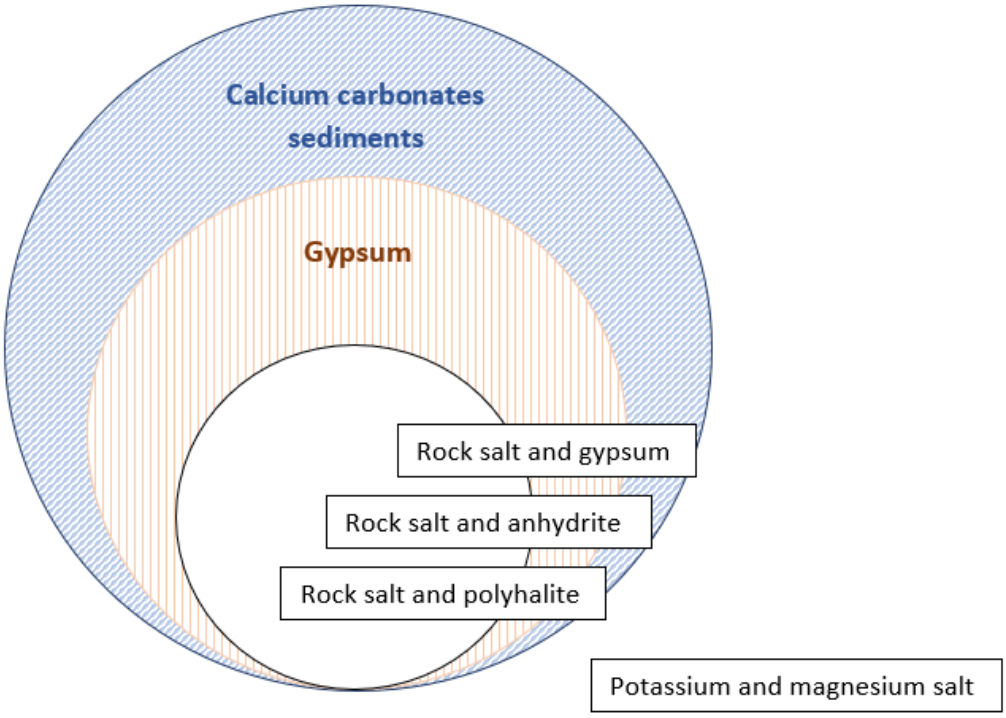

Figure 2.3: *Scheme of the Ring Theory chemical differentiation during evaporite sedimentation from a saline brine (Image adapted from Jeremic (1994)). Chemical differentaiation of mineral solution takes place on the basis of their relative solubilities. Therefore, according to this theory, gypsum is deposited in the outer ring (of the basin) and halite is deposited in the inner ring (of the basin).*

anhydrite ($CaSO_4$), formed at a temperatures above 34°C. In post-depositional diagenetic processes, calcium sulphate facies can be also formed as second stage precipitation product from chemical alteration.

Sodium salt facies are linked to restricted basin environments as lakes without water outlets and with a water input, with dissolved-solids and dissolved-chloride, into the lake rich in sodium (Jeremic, 1994; Ging et al., 1996). Sodium-rich salts are formed from brines rich in sodium chloride, sodium carbonate, sodium bicarbonate and sodium sulphate. The mineralogy associated to this salt facies are shortite ($Na_2CO_3{\cdot}2CaCO_3$), northupite ($Na_2CO_3{\cdot}MgCO_3{\cdot}NaCl$), pirssonite ($Na_2CO_3{\cdot}CaCO_3{\cdot}2H_2O$) and bradleyite ($Na_3PO_4{\cdot}MgCO_3$).

Chloride salt facies are represented mainly by halite ($NaCl$) and the associated mineralogy in chloride facies are ardite (Na_2SO_4), glanberite ($Na_2Ca(SO_4)_2$) and bloedite ($Na_2Mg(SO_4)_2{\cdot}4H_2O$).

Potassium salt facies indicates a completed evaporite sedimentation cycle which culminated with the precipitation of the brine solution until the dryness. Potassium facies are deposited after the chloride facies and are conformed by magnesium and potassium chloride and sulphates. The associated mineralogy to this facies is the presence of carnallite ($KCl{\cdot}MgCl{\cdot}6H_2O$), kainite ($MgSO_4{\cdot}KCl{\cdot}3H_2O$), langbeinite ($K_2SO_4{\cdot}2MgSO_4$), polyhalite ($K_2SO_4{\cdot}2CaSO_4{\cdot}2H_2O$), sylvite ($KCl$) and often kierserite ($MgSO_4{\cdot}H_2O$).

2.3 Rock salt formations in the UK

The salt formations in the UK are of Triassic (252-201 Mya) and Permian age (299-251 Mya). During Permo-Triassic times, the UK was placed in an arid hinterland of the supercontinent Pangea, created by the collision of Laurasia and Gondwana (Plant et al., 1999). The salt rock was deposited under a

continental climate with very restricted rainfall climate and in alternation with a sequence of continental sediments such as aeolian, fluvial and playa-lake materials. Marine transgressions entered into land from the north-west in Late Permian and Mid and Late Triassic and from the south and west at the end of Triassic times. Triassic salt in the UK can be found mainly in bedded strata in the Cheshire Basin and, to a lesser extent, in Northern Ireland, Lanchashire, the Isle of Man and Walney, Staffordshire, Worcestershire and Somerset. Permian salt fields extend in the northeast of England (Yorkshire) and Northern Ireland (Beutel and Black, 2005). The rock salt samples tested are from Boulby Mine (Permian Zechstein) and Winsford Mine (Triassic Mercia Group)(Figure 2.4).

2.3.1 Permian rock salt from Boulby Mine

Permian (299-251 Mya) salt deposits in the UK belong to the Zechstein Group sequence, which is found eastwards from the northeast of England in Yorkshire (Figure 2.4) to Germany and Poland. The Permian deposits from the Zechstein group crop out onshore only in the UK and are exploited in Boulby Mine. The Permian Zechstein sequence, from Cleveland Basin, is composed mainly of thick units of anhydrite, halite and potash. The Permian salt deposits in Yorkshire are divided in four cycles, which have been named Zechstein I to IV from the base upwards and originated as a cyclic drying out of a landlock sea in the Permian age (Beutel and Black, 2005). Each cycle starts with a carbonate rock unit passing to anhydrite, polyhalite and into halite. Other mineralogies associated with these Permian Zechstein rock salt deposits are kieserite, carnallite and sylvinite. The thickest rock salt sequence in Yorkshire belongs to the second Zechstein cycle (Zechstein II) corresponding to Fordon Evaporites, with a thickness of 75-90 to 120 m (Figure 2.5). The Zechstein II has been assessed as a potential geological site to host salt caverns (Beutel and Black, 2005). The Zechstein Group is already hosting salt caverns in the region

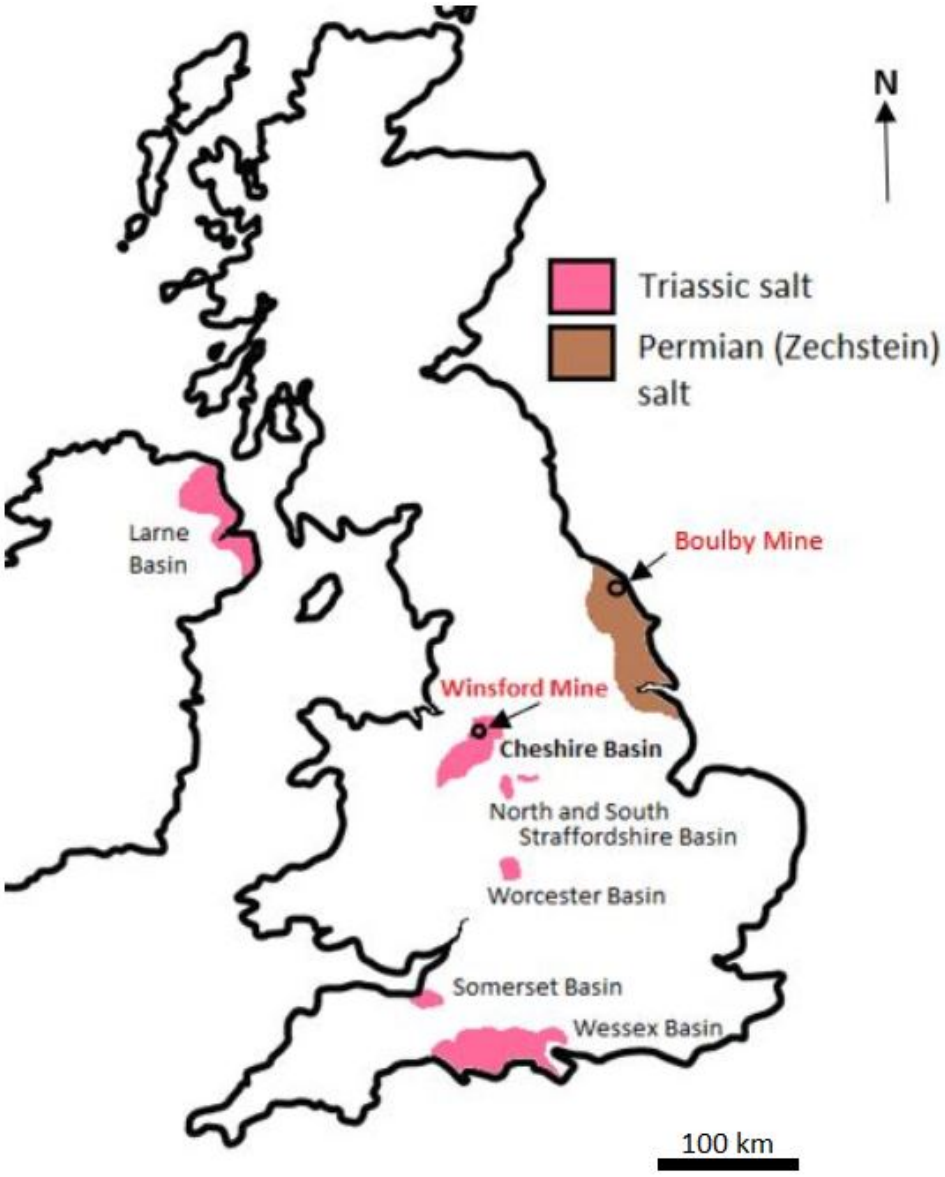

Figure 2.4: *Permian and Triassic rock salt formations and main basins with evaporites in the UK with the location of Boulby and Winsford mine.*

of Teesside in brine fields north (Saltholm) and south (Wilton) of the River Tees. According to Beutel and Black (2005) the salt caverns have been used to store light hydrocarbons, propane, propylene, crude oil, gas oil, naphtha, ethylene, nitrogen and hydrogen.

Boulby Mine is located in the Zechstein Permian Basin that extends from eastern England to the Netherlands, North Germany and Poland (Ziegler, 1990; Van Wees et al., 2000; Zhang et al., 2013). The Zechstein salt sequence was deposited under arid climate conditions and as a result of a series of marine transgression and regression episodes during the Upper Permian (Zhang et al., 2013). The formation sequence presents clastic sediments of aeolian sandstones, fluvial fans and shallow-lake deposits from Lower Permian passing through cyclic deposition of salt alternated with anhydrite and mudstone during the repeated transgression-regression episodes during the Upper Permian (Zhang et al., 2013; Strohmenger and Strauss, 1996). Overlying the Upper Permian (Zechstein) formation of carbonates and evaporites, the sequence passes to red-bed fluvial to lacustrine sediments and sabkha deposits from the Lower Triassic and shallow marine carbonates from Middle Triassic (Zhang et al., 2013; Kossow and Krawczyk, 2002). The deposition during the Mesozoic was controlled by the regression and transgression of the Tethys Ocean (Ziegler, 1990; Zhang et al., 2013).

2.3.2 Triassic rock salt from Winsford Mine

Triassic (252-201 Mya) rock salt in the UK was deposited under semi-arid environmental conditions within mainly a fault- controlled endorheic basin linked to the major depositional centres of the North and Irish Sea (Cooper, 2002) resulting in a brown-red and some slightly green-grey coloured sequences of evaporitic and sedimentary deposits (Cooper, 2002; Howard et al., 2008). Winsford Mine is located within the Cheshire Basin which is one of the largest British

onshore post- Variscan rift basins. The basin is filled with the formations assigned to Appleby, Cumbrian Coast, Sherwood Sandstone, Mercia Mudstone, Penarth and Lias Groups (Plant et al., 1999). The Mercia Mudstone Group consists of reddish-brown mudstones and siltstones alternating beds of halite (Evans and Holloway, 2009). Within the Triassic Mercia Mudstone Group, the main rock salt resources are displayed in two salt- bearing formations, the lower Northwick Halite Formation with a maximum thickness of 280 meters of pure halite beds alternating with mudstone and siltstone levels and an upper Wilkesley Halite Formation in alternation with mudstone (Cooper, 2002).

Figure 2.5: *Permian rock salt sequence in Boulby Mine (Modified image from Talbot et al. (1982)). On the left there is an vertical stratigraphic column in Boulby area. On the right, there is a sligthly more detailed schematic picture of different Zechstein evaporites and depths in Boulby Mine.*

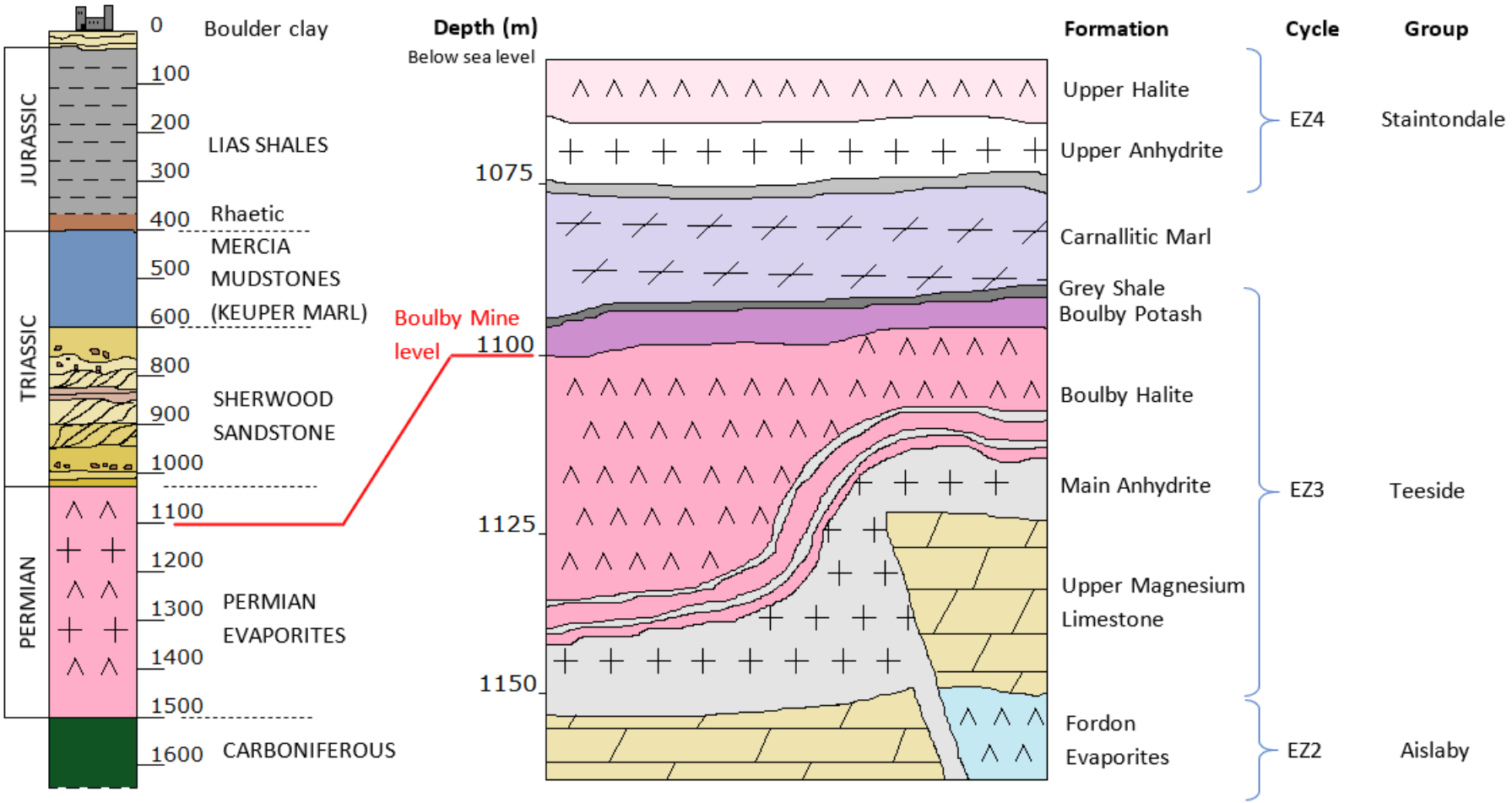

Figure 2.6: *Triassic rock salt sequence in Winsford Mine (Modified image from Swift et al. (2001); Howard et al. (2008)). On the left, there is a sonic and gamma-ray log (with the corresponding geological formations) from the KNUTSFORD SJ77NW/4 borehole in Cheshire Basin and Winsford area from Howard et al. (2008). On the right, there is a vertical section from the Bostock No. 5 Panel in Winsford Mine showing the different rock salt levels, Layer B and Layer F. The schematic picture is from Swift et al. (2001).*

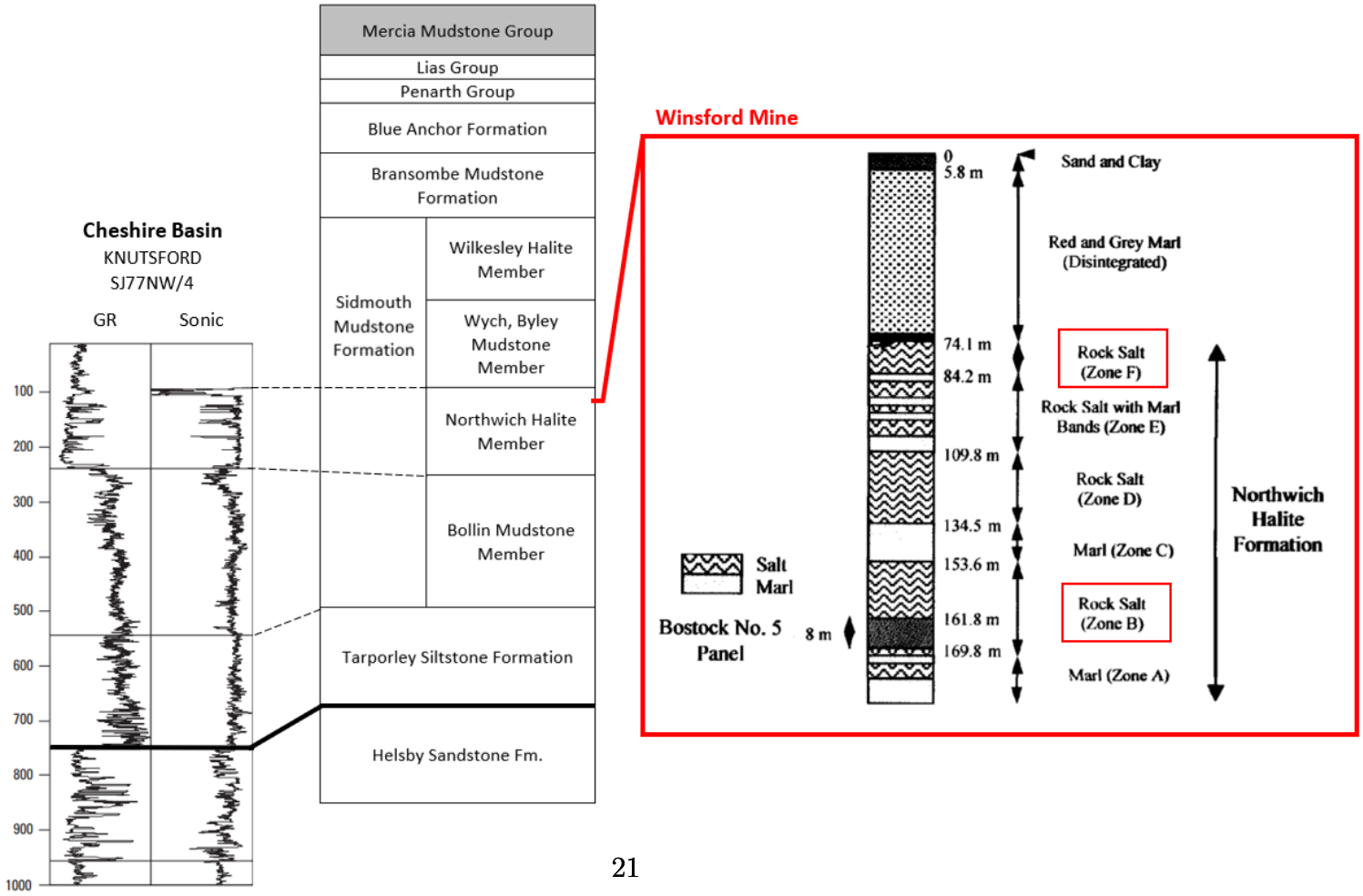

Winsford Mine is stratigraphically located at the base of the Northwich Halite Formation, which contains 92% NaCl, and the extraction is made by room and pillar mining (Norton et al., 2005). Within the salt mine, two different economically workable levels of rock salt have been differentiated on the halite purity, namely Zone B and Zone F. Zone B and Zone F are located between 130 and 200 m depth, respectively (Figure 2.6). Layer B has a higher concentration of halite, where the purest material is at the basal part of the salt bed. Layer F has a higher content of second phase mineralogy, mainly anhydrite and clay, and a lower concentration in halite. The geological formation, of approximately 150 meters in thickness, was deposited during the Triassic under arid climatic conditions with terrigenous reddish-brown sediments containing red clay and other silicates. The mine extension and structure are limited by two main faults crossing the geological formation on the east and the west, and the mining activity in the site is limited to the zone in between the fault lines. During mining extension works in layer B, horizontal and vertical boreholes were drilled in order to delimit the location of the working horizon within the salt bed and the limits dictated by the structural settings of the site. The site engineers kindly provided core samples from the boreholes for testing in the laboratory. Additional rock salt samples were collected on site from layers B and F.

2.4 Elastic parameters and rock mechanics fundamentals

The behaviour of a material under pressure is first described by the theory of elasticity, or Hooke's law. It studies displacements, strains, and stresses in a solid subjected to external forces. In 1678, Robert Hooke (1635-1703) established how a displacement x is directly proportional to the force F applied to extend or compress the material. It can be expressed as:

$$F = kx \tag{2.1}$$

In other words, the elongation is proportional to the stiffness of the deformed material (Pelissier et al., 2007). Hooke had thus established the relation between the components defining the state of deformation or strain ε and the components of the state of stress σ for an elastic strain of low amplitude (Figure 2.7). In the case of a uniaxial deformation, Hooke's law is expressed as:

$$\sigma = E\varepsilon \tag{2.2}$$

where E is Young's modulus, an intrinsic characteristic of the material further detailed in a next paragraph, expressed in GPa. In this form, stretching or compression is only characterized in one dimension. However the total strain law has no reason to be linear except in the particular case where a small strain is considered (Pelissier et al., 2007). According to Haupt (1991), the relation between creep and relaxation can only be influenced by the elastic constant E. Therefore, relaxation behaviour will be ruled by creep behaviour and Young's modulus.

In material science, the strain rate of a rate dependent material can be divided into an elastic and a viscous part:

$$\dot{\varepsilon}_{ij} = \dot{\varepsilon}^{el}_{ij} + \dot{\varepsilon}^{vis}_{ij} \tag{2.3}$$

where the elastic strain rates are assumed to follow Hooke's law as

$$\dot{\varepsilon}_{ij} = \frac{1}{2G}\dot{s}_{ij} + \frac{1}{9K}\dot{\sigma}_{kk}\dot{\delta}_{ij} \tag{2.4}$$

where G and K are the shear and the bulk modulus and $\dot{s}_{ij}$ are the deviatoric stress rates (Haupt, 1991).

2.4.1 Stress-strain relationship

Stress-strain plots show how much strain results from the (un)loading stress, which is a fundamental mechanical properties of a material (Jaeger et al., 2007). The force applied over a surface is called a stress: it is a unit of pressure per unit area with Pascal (Pa) as SI unit (Fanchi, 2002). The strain is the relation between the amount of deformation in the direction of the applied force and the original length of the sample (Figure 2.7).

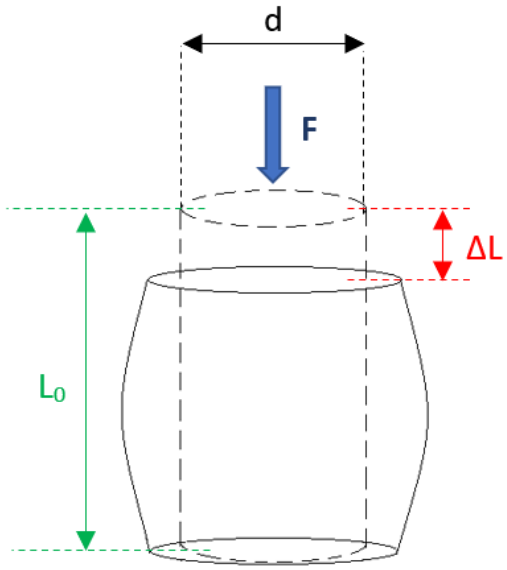

Figure 2.7: *Schematic picture of core deformation and shortening of sample where d= diameter, F= Force, L_0= initial length and ΔL= length variation after applying force F.*

For given a cylindrical core sample with an initial length L_0 and a diameter d, and an area A, subjected to a compressive force F, stress σ and strain ε would be calculated as

$$\sigma = \frac{F}{A} \tag{2.5}$$

$$\varepsilon = \frac{\Delta L}{L_0} \tag{2.6}$$

Stress-strain curve provides information about the elastic and plastic (brittle or ductile) properties of a material under stress. Figure 2.8 shows a schematic

picture of a stress-strain curve. In the initial stages a linear relation between stress and strain can be appreciated. This initial stage of the graph is defined as elastic zone and is limited by the elastic limit. The elasticity determines the ability of a material to recover its original form after removing the force which changed its shape (Jin et al., 2020). This applies to time-independent deformation in materials which disappears on the release of the load making elastic deformation reversible. Once the elastic limit is reached, the slope of the stress–strain curve decreases. The stress-strain curve enters in the plastic zone where the ultimate strength will be reached. The curve start to decrease after arriving to the ultimate strength and the necking domain starts until the sample fails.

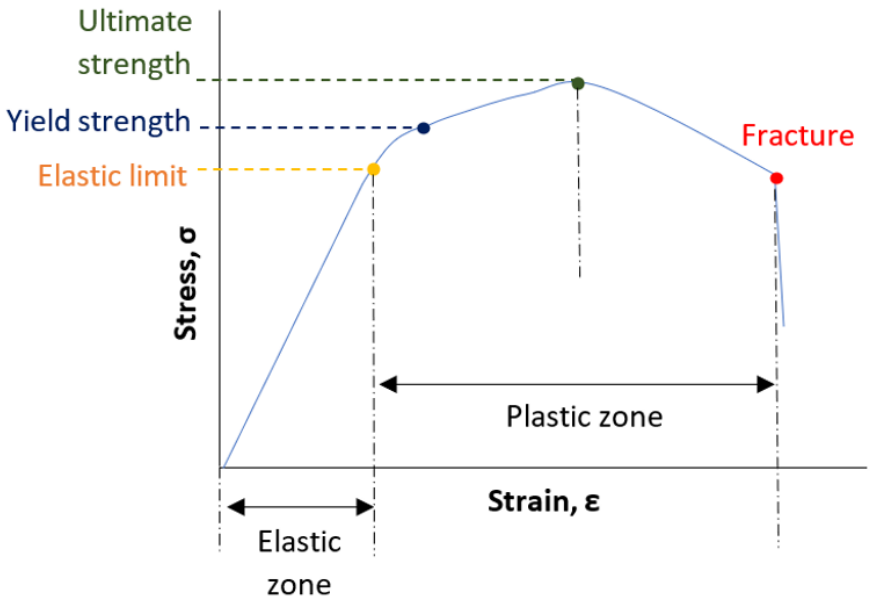

Figure 2.8: *Schematic picture of stress-strain cure under Uniaxial Compression Strength (UCS) Test. The stress-strain curve stays as a straight line in the first stage known as the elastic zone. After it reaches the elastic limit, the slope of the stress-strain curve decreases entering the plastic zone of the deformation curve. The point where the curve slope changes is known as the yield strength. From the yield strength, the curve increases at a lower pace until reaching its maximum at the ultimate strength point. The last stage after reaching the ultimate strength is failure or fracture.*

2.4.2 Young's modulus

Young's modulus E is a measure of stiffness of an elastic material defined as the ratio between axial stress and axial strain under uniaxial conditions. The Young's modulus calculated from strain measurements is referred as static modulus. Young's modulus can be also calculated from sonic logs in boreholes and ultrasonic surveys in laboratory; it is then termed adiabatic Young's modulus (Ma and Holditch, 2016).

$$E = \frac{(\frac{F}{A})}{(\frac{L}{L_0})} = \frac{\sigma}{\varepsilon} \tag{2.7}$$

2.4.3 Poisson's ratio

Poisson's ratio (ν) is the ratio of lateral strain (ε_l) to axial strain (ε_a) in the direction of the stretching force. It therefore depends on the lithology, confining stress, pore pressure, and porosity of the rock. Poisson's ratio from laboratory experimental results show that static Poisson's ratio increases as porosity increases (Zhang, 2019).

$$\nu = -\frac{\varepsilon_l}{\varepsilon_a} \tag{2.8}$$

Note that here tensile deformation is considered positive whereas compressive deformation is considered negative, therefore ν is positive for a compressive deformation state (Jaeger et al., 2007; Zhang, 2019). Dynamic Poisson's ratio can also be calculated from elastic wave velocity measurements.

2.4.4 Bulk modulus

The Bulk modulus K measures the changes in volume with an increase in pressure and how resistant a material is to compression (Fanchi, 2002). It can be calculated either from the Young's modulus and Poisson's ratio (equation 1) or also from the axial stress σ_1 applied and volume change of the sample

(equation 2).

$$K = \frac{E}{3(1-2\nu)} \tag{2.9}$$

$$K = \frac{\sigma}{\frac{\Delta V}{V}} \tag{2.10}$$

2.5 Rheological behaviour of rock salt

Intact rock salt has high ductility, very low permeability, providing great tightness and self-healing properties (Peach, 1991; Carter et al., 1993; Hunsche and Hampel, 1999; Schulze et al., 2001). Rock salt also presents low creep strength and low density (Urai et al., 2008). Therefore, rock salt caprocks are considered a very good seal in petroleum systems and are also used as a host rock for gas and oil storage and targeted for radioactive waste disposal (Schulze et al., 2001).

Rock salt deforms under pure creep where irreversible deformation (plastic) take place without fracture development, but it can also present brittle deformation related to crack formation (Hunsche and Hampel, 1999). Rock salt can deform by two stress-dependent domains as described by Van Sambeek et al. (1993) and Cristescu and Hunsche (1998), with the i) dilatancy domain and ii) compaction domain, separated by the dilatancy-compaction boundary that depends on the loading geometry, or internal microstructure from natural deformation and sedimentary processes (Covey-Crump et al., 2016), and rock salt lithology (Schulze et al., 2001); see Figure 2.9. When the state of stress stays in the dilatancy domain, the deformation of rock salt is driven by micro-crack formation and propagation resulting in an increase of the permeability and creep failure, mechanical weakening and acoustic emissions. In the non-dilatant compaction domain, plastic deformation and compaction of

micro-cracks can lead into a healing process and closure of fractures with a decrease of permeability. Pure creep as result of dislocation movement and elastic deformation is observed in the non-dilatant compaction domain (Hunsche and Hampel, 1999; Schulze et al., 2001).

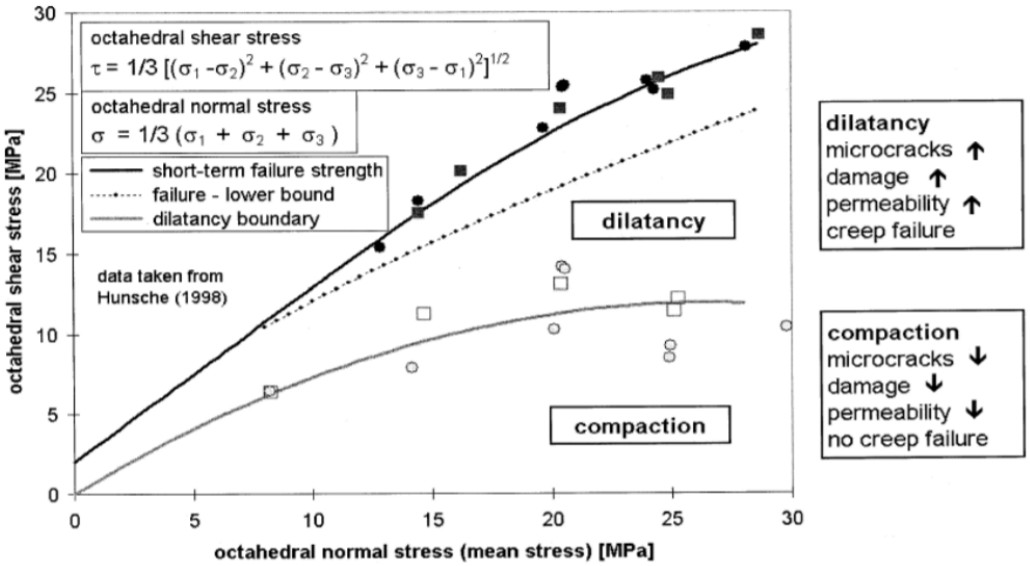

Figure 2.9: *Dilatancy boundary and compression (short- term failure strength) for rock salt (Figure from Schulze et al. (2001) after Hunsche (1998)). The bold line represent the short-term failure strength and the discontinuous line the lower bound of failure. The non-bold continuous line represent the boundary between the domains of dilatancy and compaction.*

2.5.1 Creep deformation of rock salt

Creep is defined as the time-dependent deformation of rock under a small load, that is less than the short term strength of the rock, over long periods of time (Griggs, 1939).

Following Hooke's law of elasticity (equation 2.1) and the equation (2.4) for rate dependant materials, two different creep rates can be distinguished for rock salt deformation under a constant stress, upon the viscous part $\dot{\varepsilon}_{ij}^{vis}$ describing i) transient creep with decreasing creep rate and ii) steady-state with constant creep rate (Figure 2.10). The last stages of creep deformation are represented by the tertiary creep followed by creep rupture (Haupt, 1991).

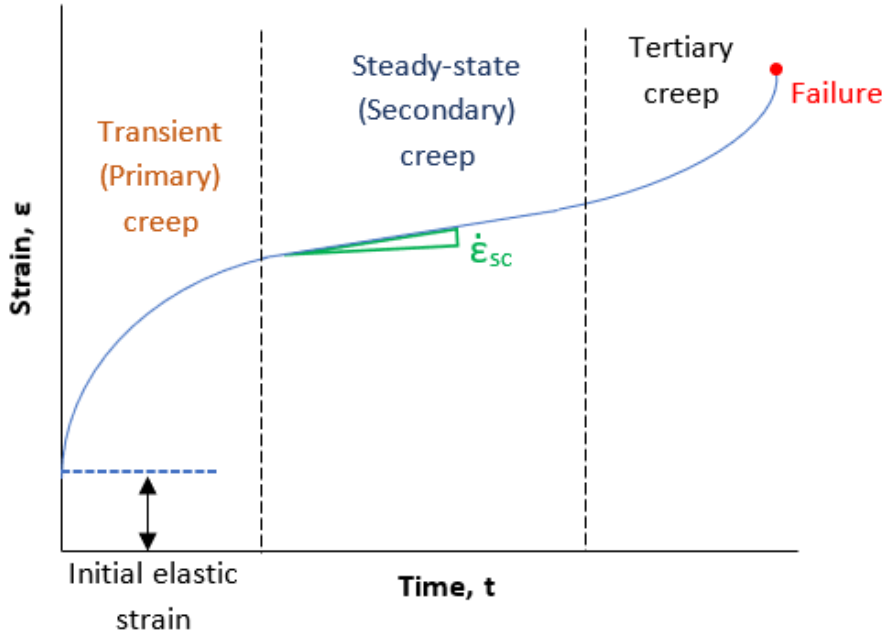

Figure 2.10: *Schematic picture about the different creep stages during a compressive test at a constant stress load where $\dot{\varepsilon}_{sc}$ is the secondary or steady-state creep rate.*

Creep in rock salt can be affected by external factors such as temperature and stress but also to materal parameters such as rock structure, water content and second phase content (Günther et al., 2015).

2.5.1.1 Transient creep

Transient creep is history dependent and steady-state creep rate depends on stress and temperature (Hunsche and Hampel, 1999) and air humidity resulting in a rate increase by a factor of 50 above the dilatancy boundary (Hunsche and Schulze, 1996).

Transient creep take place in the first stages of deformation and shows a decreasing creep rate generally described by time hardening or strain hardening theory or or to a decrease in free or mobile dislocations, which depends on time (Haupt, 1991; Abe, 2008).

2.5.1.2 Steady-state creep

Steady-state creep or secondary creep is characterised by showing constant rate and follows Arrhenius's Law. Secondary stage creep, following Arrhenius's law, is described as

$$\dot{\varepsilon}_{ss} = A\sigma^n e^{-\frac{Q}{RT}} \tag{2.11}$$

where the creep rate $\dot{\varepsilon}_{ss}$ is determined by shear stress σ^n and along with A, as a material dependent parameter, activation energy Q, temperature T and R as the gas constant (R = 8.314 J $mol^{-1}K^{-1}$ (Li and Urai, 2016; Robinson et al., 2021).

2.5.2 Mechanical properties of rock salt

Damage and deformation-induced crack density in rock salt is strongly controlled by confining pressure (Schulze et al., 2001) (Figure 2.11). Rock salt strength and plasticity increases with increasing confining pressure and when the state of stress stays below the dilatancy domain, failure occurs gradually, not spontaneously. A decrease in rock strength and strain hardening can occur as result of accumulating micro-damage during loading beyond the dilatancy boundary. In the non-dilatant compaction domain, plastic deformation and steady state creep are steady under effective stress (Schulze et al., 2001).

Pore pressure increase as result of permeation of fluids may develop and lead to a reduction of the confining effect of lithostatic pressure (effective pressure) resulting in fracturing damage and dilatancy (Schulze et al., 2001).

Rock salt deformation is very sensitive to an increase of temperature. Indeed, the stiffness of rock salt decreases with the increase of temperature (Senseny et al., 1992) at a rate of

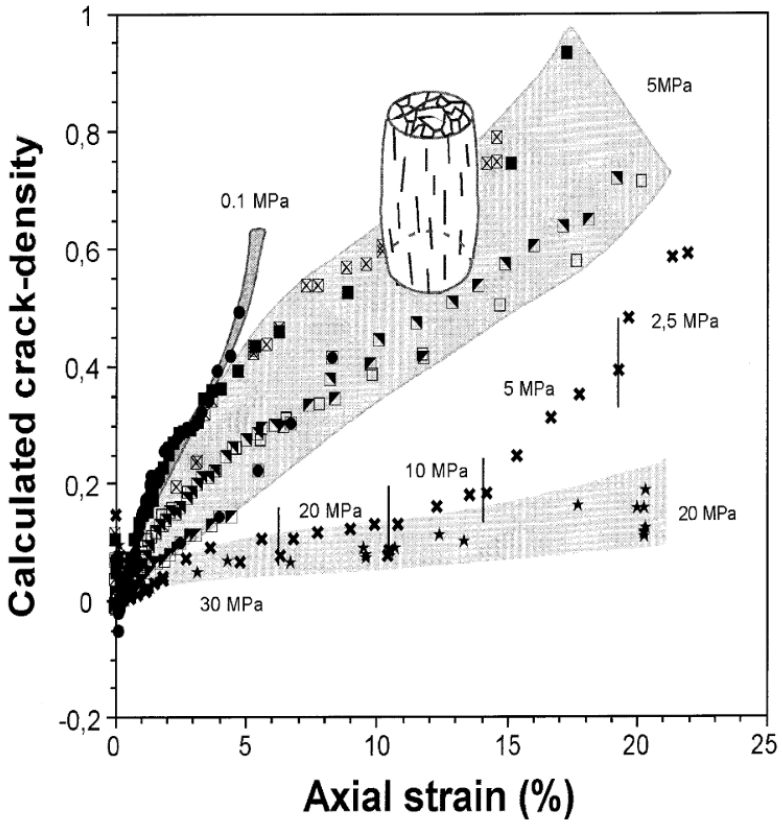

Figure 2.11: *Dependence of the calculated crack density on confining pressure during deformation in compression in rock salt (Schulze et al., 2001).*

$$-0.04 \leqslant \frac{\partial E}{\partial T} \leqslant -0.016 GPa/K \tag{2.12}$$

where E is the Young's modulus and the temperature T is expressed in Kelvin (K).

2.5.3 Deformation mechanisms

Deformation mechanisms are the processes leading to internal microstructural changes of the rock under the action of external conditions, such as stress and temperature (Zhang et al., 2021). According to Pfeifer (2009), in material science, plastic deformation is the permanent distortion that occurs when a material is subjected to tensile, compressive, bending, or torsion stresses that exceed its yield strength and cause it to elongate, compress, buckle, bend, or twist. Plastic deformation in rock salt deformed at low temperature (room temperature) and low differential stress, is mainly driven by microcracking

and and brittle rheological behaviour (Popp et al., 2001; Peach et al., 2001). However, experimental data from Carter et al. (1993) and Schenk and Urai (2004) show that wet rock salt can show deformation by dislocation creep with "fluid-assisted" dynamic recrystallisation processes at low temperatures, and variations in temperature can lead to thermoelastic strains within the crystal latice (Bérest et al., 2005).

According to material science, the total one-dimensional strain in any solid material is given by:

$$\varepsilon = \varepsilon_e + \varepsilon_p + \varepsilon_t + \varepsilon_s + \varepsilon_a \tag{2.13}$$

Where ε_e is elastic strain, ε_p is plastic strain, ε_t is transient or primary creep strain, ε_s is steady-state or secondary creep strain and ε_a is the accelerating or tertiary creep strain (Carter et al., 1993).

Plastic deformation in rock salt is controlled by two main deformation mechanisms: dislocation creep, which is the result of dislocations moving through the material, and pressure-solution (solution-precipitation) creep, which is a stress-driven mass transfer process (Spiers et al., 1990; Urai et al., 2008; Sato, 2013). Ductile deformation in rock salt, mainly, is promoted by dislocation movement. Dislocations are defects described also as disturbances in the internal arrangement of the crystal lattice. The movement of dislocations, under a certain pressure and temperature, leads to a time-dependent ductile deformation called "creep". The total strain rate ($\dot{\varepsilon}$) is the sum of the strain rate controlled by dislocation creep ($\dot{\varepsilon}_{DC}$) and the strain rate controlled by pressure-solution ($\dot{\varepsilon}_{PS}$) (Spiers and Carter, 1998; Urai et al., 2008).

$$\dot{\varepsilon} = \dot{\varepsilon}_{DC} + \dot{\varepsilon}_{PS} \tag{2.14}$$

Munson (1979) designed a deformation mechanism map identifying five mechanisms controlling deformation in rock salt for constitutive models with imposed stress or temperature. The five deformation mechanisms are i) defect-less flow at extremely high stresses; ii) dislocation glide controlling quasi-static stress-strain tests; iii) dislocation climb and iv) diffusion creep controlling creep in two variations, Nabarro-Herring creep by volume diffusion material transport and Coble creep by grain boundary material transport; and finally v) a region controlled by undefined mechanism (Figure 2.12).

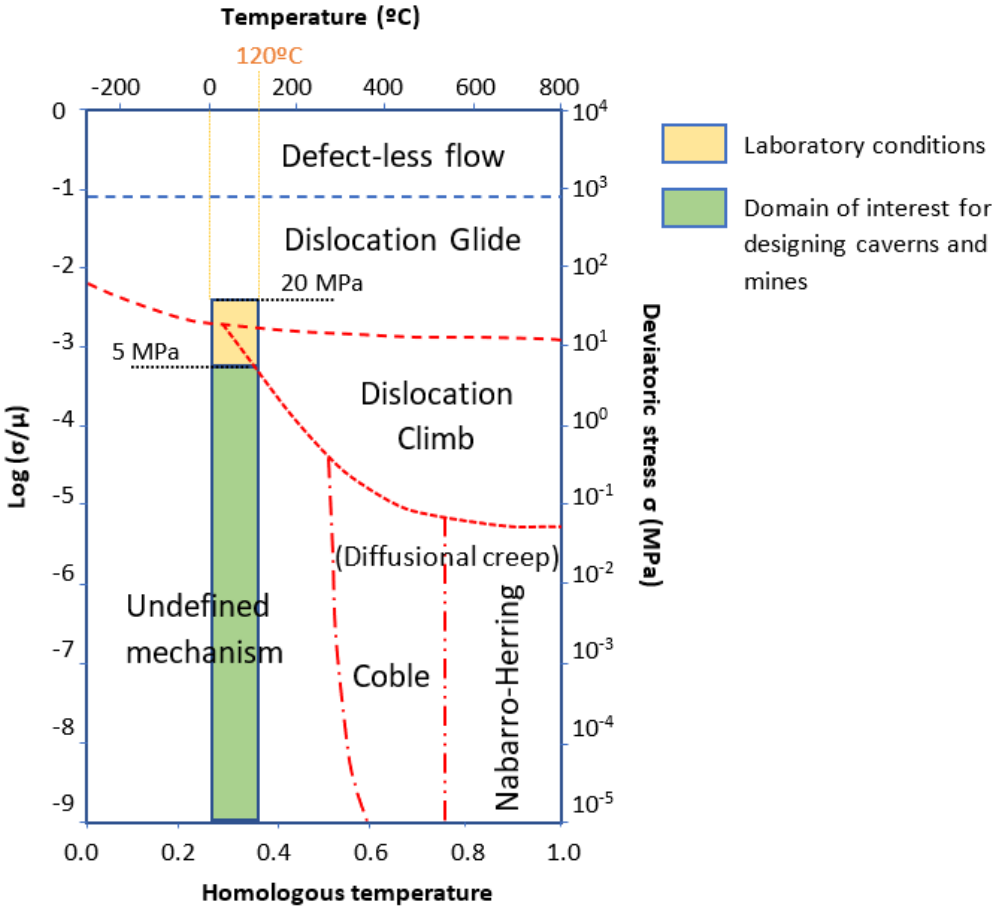

Figure 2.12: *Deformation mechanism map. μ is the elastic shear modulus. (Figure adapted from Bérest et al. (2019) after Munson (1979)). The yellow square represents the temperature and stress conditions in the laboratory and the green area defines the deviatoric stress and range of temperatures of research interest for salt caverns.*

The upper shaded rectangle in beige colour represents the domain for im-

posed stress and temperature in laboratory conditions. The larger green rectangle represents the domain of interest for salt cavern construction. Micromechanisms controlling creep in low-stress domain are still not fully understood where pure empirical data is used to extrapolate rheological behaviour in this domain (Bérest et al., 2019).

2.5.3.1 Dislocation creep

In laboratory conditions, dislocation creep is promoted by free dislocations. Dislocations are migration or diffusion of crystal defects within the crystal lattice under stress (Urai et al., 2008; Li and Urai, 2016). Dislocation creep has been extensively studied in laboratory experiments (Senseny et al., 1992; Cristescu, 1993; Franssen, 1994; Peach and Spiers, 1996; Hunsche, 1998) and results in strain of the crystalline lattice and change of shape without brittle deformation. When rock salt is subjected to a stress, shear stresses inside the crystal lattice drive the movement along crystallographic planes (glide plane), also called glide mechanism. The two different types of dislocations are a) edge dislocations and b) screw dislocations (Senseny et al., 1992; Carter et al., 1993; Spiers and Carter, 1998) (Figure 2.13). Edge dislocations are the limit of an extra layer of atoms moving perpendicular to the dislocation plane within the crystal lattice. Edge dislocation movement is parallel to the applied stress. Screw dislocations form a jump from one lattice point moving in parallel direction to the dislocation plane. Screw dislocation movement is perpendicular to the applied stress.

Dislocations move along the crystal lattice until the movement is stopped by an obstacle (Hunsche, 1998). According to Hunsche (1998) most common obstacles in the lattice structure are other dislocations, impurities or grain boundaries. As a result of this interference in the dislocation propagation an increase of the amount of dislocations occurs. The accumulation of dislocations increases the dislocation density within the crystal lattice. This increase in the

dislocation density can be related to "strain hardening" on the stress-strain plot resulting in a resistance against deformation and a decrease in the velocity of dislocation movements and creep deformation rate. The creep deformation rate decrease is identified as the limit of "transient" creep.

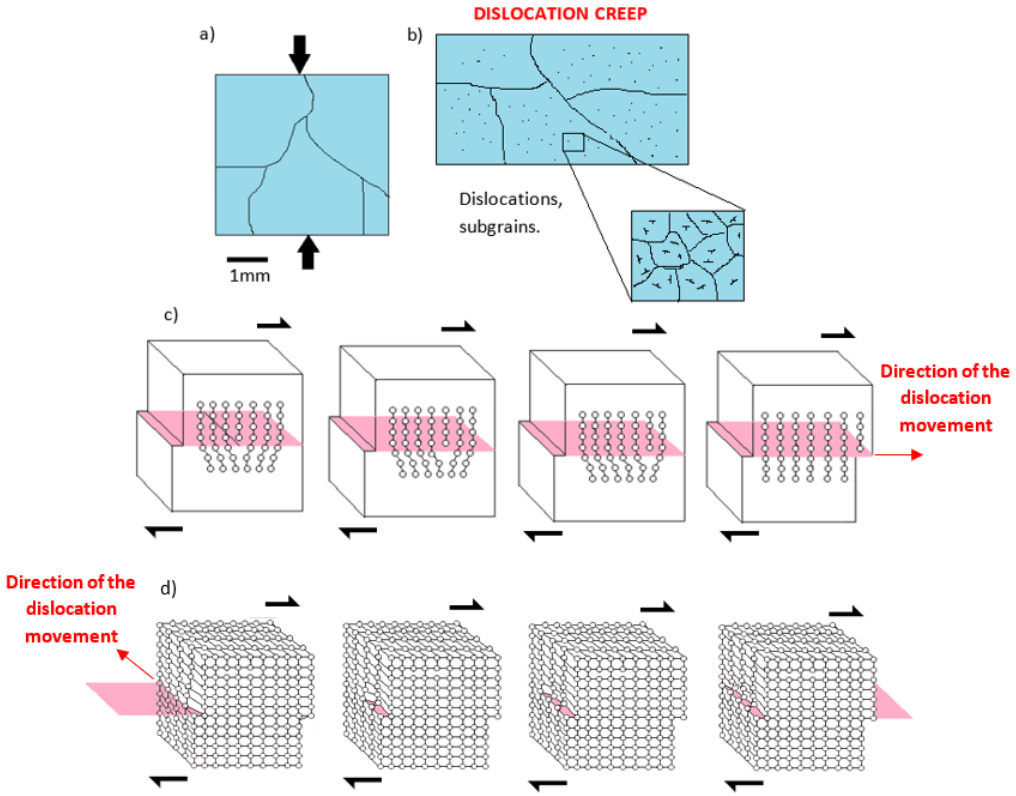

Figure 2.13: *Schematic picture of dislocation creep where a) an intact rock deforms by dislocation creep (b) resulting in dislocation and subgrain formation (After Li and Urai (2016)). Picture c) shows a sequence of how crystal defects move along the crystal lattice through an edge dislocation and picture d) a screw dislocation.*

The increase of dislocation density increases the stored strain energy leading to dislocation climb where the dislocation jumps to a different glide plane allowing dislocation creep to continue. Structurally, the result of the dislocation movement along the crystal lattice is the formation of subgrains, promoted by "cross slip" and "climb" processes, and slip bands (Senseny et al., 1992).

The equation for the steady-state strain rate controlled by dislocation creep (2.3), where differential stress (σ_1-σ_3) and strain rate ($\dot{\varepsilon}_{DC}$) are related based

on the flow stress σ using a non-Newtonian law creep equation (Li and Urai, 2016):

$$\dot{\varepsilon}_{DC} = A(\Delta\sigma)^n = A_0 exp(-\frac{Q}{RT})(\sigma_1 - \sigma_3)^n \tag{2.15}$$

where strain rate is $\dot{\varepsilon}_{DC}$; differential stress $(\sigma_{Diff}) = \sigma_1 - \sigma_3$, viscosity of rock salt is $A_0 exp(-\frac{Q}{RT})$ where A/A_0 is a material dependent parameter, Q is the specific activation energy, R is the gas constant and T is temperature (Li and Urai, 2016). Carter et al. (1993) established that for rock salt the power law creep equation for dislocation creep was:

$$\dot{\varepsilon}_{DC} = 8.1 \times 10^{-5} exp(-\frac{51600}{RT})(\sigma_1 - \sigma_3)^{3.4} \tag{2.16}$$

Strain hardening in rock salt leads to recovering and re-crystallisation processes. Research form Carter and Heard (1970) and Guillope and Poirier (1979) results in the differentiation of two re-crystallisation domains: migration domain and rotation domain (Figure 2.14). Rotation re- crystallisation takes place for all stresses under critical temperature and stresses below a critical value and higher temperatures than critical temperatures. This re-crystallisation process does not have any impact on the creep curve as there is a continuous rotation of sub-grains during the constant creep state. The migration re-crystallisation domain is limited by larger stresses than critical stresses and higher temperatures than critical temperature conditions but migration re-crystallisation does not take place for strains as high as 80%.

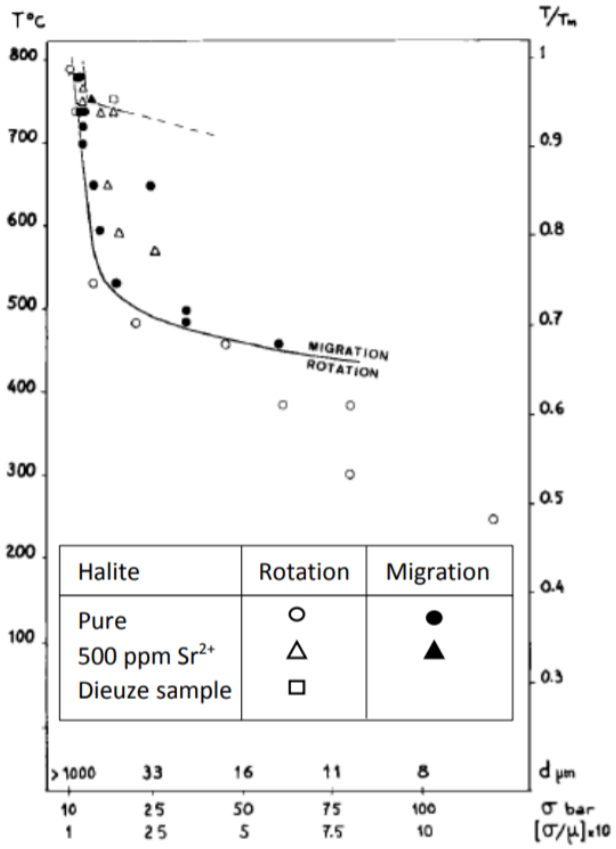

Figure 2.14: *Critical curve in the temperature- stress (σ, T) plane between the rotation crystallization domain and migration crystallization by Carter and Heard (1970).*

Processes of dynamic re-crystallisation, which take place during deformation, such as grain boundary migration (GBM) and subgrain rotation can help to reduce the stored strain energy within the crystal lattice and can result in a re-arrangement or removal of dislocations. Grain boundary migration reduces the stored strain energy by transferring atoms to the lower-energy neighbour's crystal lattice. The subgrain rotation consists of rotation of the low angle sub-grains boundary resulting in a higher angle.

2.5.3.2 Pressure-solution creep

Deformation of rocks by dissolution-transport-precipitation mechanisms (pressure-solution) has been reported in the literature since many years (Heald, 1955; Li and Urai, 2016). Pressure-solution creep is a deformation mechanism that

implies diffusive mass transfer, or diffusion creep, through the grain-boundary and dissolution at grain-contact margins (Figure 2.15). Diffusive mass transfer takes place when there is a transfer of material from high compression stress zone to a low compression stress zone (Spiers and Schutjens, 1990; Li and Urai, 2016). Pressure-solution is the responsible mechanisms involved in the mechano-chemical time dependent compaction of sediments during diagenesis and also controls porosity variations in fault gouges (Renard et al., 2001).

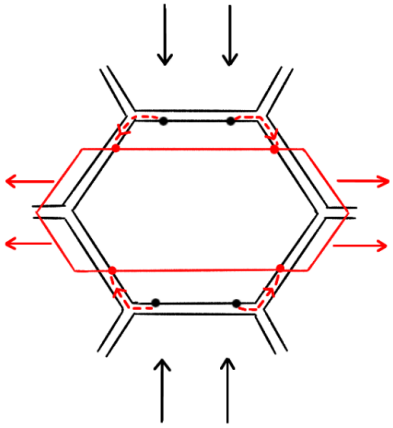

Figure 2.15: *Mass transfer in diffusional creep during pressure-solution (After Spiers and Schutjens (1990)). Black arrows show the direction of the principal stress applied whereas red arrows meant to show the elongation direction of halite crystals. Discontinuous red arrows show the mass transfer from high pressure areas to lower pressure areas around the crystal boundary.*

Spiers and Schutjens (1990) reported pressure-solution creep as a dominant deformation mechanism in wet fine-grained rock salt samples. The power law creep equation for pressure solution is defined as:

$$\dot{\varepsilon}_{PS} = B(\Delta\sigma) = B_0 exp(-\frac{Q}{RT})(\frac{\sigma_1 - \sigma_3}{TM^m}) \tag{2.17}$$

where Q is the specific activation energy for pressure-solution creep.

Spiers and Schutjens (1990) defined the pressure-solution power law creep equation for rock salt as:

$$\dot{\varepsilon}_{PS} = 4.7 \times 10^{-4} exp(-\frac{24530}{RT})(\frac{\sigma_1 - \sigma_3}{TM^3}) \tag{2.18}$$

Where M is grain size diameter in mm, T is temperature in °C and σ_1 and σ_3 are in MPa.

Grain boundary sliding can occur in conjunction with diffusive mass transfer when the grains slide along the common boundary.

Based on experimental evidence, the pressure-solution mechanism governs deformation of rock salt in the low-stress domain. During pressure-solution, deviatoric stress and strain rate would keep a linear relationship (Bérest et al., 2019).

2.6 Impact of second phase content in rock salt

The strength of rock salt under deformation can differ depending on the chemistry of the sample. According to Heard and Ryerson (1986) the addition of small amounts of cations (Ca^{2+},Mg^{2+},K^{1+}) have an important impact over constitutive properties and strength rock salt samples linked to solid solution hardening, which is the attainment of an increase in matrix strength through addition of different soluble elements. This distortion of atomic lattice caused by the misfit of atomic radius inhibits dislocation movement (Liu et al., 2022).

Results from both natural and synthetic rock salt samples from Heard and Ryerson (1986) showed a sample strength and cation content relationship where samples with K^{1+} and Mg^{2+} had higher strength in comparison to pure halite and samples with Ca^{2+} presented lower strength in comparison to pure halite. Solid solution hardening occurs as a result of elastic strain within the crystal lattice as result of substitution of cations with radii different from Na^{1+}. Therefore, solid solution hardening was attributed to the difference between the

impurity cation radius and Na^{1+} cation rather than the formation of divalent cation-cation vacancy pairs. Sample strengthening occurs from the movement of dislocations across the crystal lattice and its interactions with the strain field caused by cation substitution with a radii different to Na^{1+}.

Inter-laying second mineralogy, such as mudstone or anhydrite, in a bedded rock salt formation can induce brittle behaviour of rock salt during deformation (Liang et al., 2007; Wang et al., 2011). According to Liang et al. (2007), rock salt samples with interlayered anhydrite are weaker than pure anhydrite under similar deformation conditions.

Pure rock salt presents higher viscoplastic behaviour than the anhydrite specimens under unconfined conditions (Liang et al., 2007). The failure mode for samples with lithology mixtures is complicated and complex as one or the other component of the rock may dominate the mechanical behaviour. Anhydrite has brittle-elastic behaviour and mudstone has brittle behaviour whereas rock salt presents a ductile-plastic response under the same deformation conditions. Therefore, different physical properties lead to different rheological behaviour under stress making failure a complex combination of tensile fracture mode, shear displacement and general visco- plastic dilatant distortion (Liang et al., 2007; Wang et al., 2016). As impurity, mudstone seems to show a greater weakening effect on rock failure than anhydrite (Liang et al., 2007).

Different deformation micro-mechanisms seem to operate in rock salt with variations in chemical composition and second phase content. This preference for certain deformation mechanisms might be linked to the variations in the rheological behaviour from different mineral phases. According to the research conducted by Závada et al. (2015) on the Lower Hormuz formation (Iran), intergranular solid inclusion-rich rock salt deformed by solution-precipitation and grain boundary sliding (GBS) dominated creep with supplemental trans-

granular cracking and subordinate grain boundary migration (GBM) accommodated dislocation creep. Therefore, the studies concluded that rock salt with higher second phase content presents higher rates of solution-precipitation creep as deformation mechanism due to accelarated diffusion rates at halite-solid phase interfaces (Renard et al., 2001; Závada et al., 2015). According to Renard et al. (2001), geological observations indicate that clay or mica particles could greatly enhance mechano-chemical compaction due to holding a contact at a micron scale which would enhance a higher diffusional transport rates. Hickman and Evans (1995) also observed that the presence of montmorillonite clays at the interface between two halite lenses increases the rate of shortening.

An increase of brittle deformation in rock salt could be linked with a higher content of secondary phase mineralogy. Schulze et al. (2001) links the evolution of damage to the loading geometry in the rock salt formation but other parameters such as second phase content causing specific crack geometry and inter-connectivity should be also further studied. Crack patterns and permeability increase develop anisotropically being controlled by the loading geometry of the rock sample (Schulze et al., 2001).

Rock salt formations contain halite that might have fluid inclusions within the crystals and other hydrous second phase content such as polyhalite, gypsum and clay (Weck et al., 2014). Therefore, the thermal behaviour of rock salt might vary based on the water-bearing phase content. Polyhalite is an important hydrous ($K_2SO_4{\cdot}2CaSO_4{\cdot}2H_2O$) second phase mineral that coexists with halite (Xu et al., 2017).

2.7 Underground Gas Storage in Salt Caverns

Underground gas storage (UGS) in salt caverns helps to meet seasonal fluctuations in gas supply and demand by reducing peak load and increasing the supply security from the grid (Xing et al., 2015). Salt caverns have already been used for many years to store natural gas but nowadays UGS in salt caverns is also known as a promising technique for Hydrogen storage and Compressed Air Energy Storage (CAES).

Salt caverns are artificial cavities created by solution mining in geological formations of rock salt (Bérest, 2011). The creation of artificial underground cavities disturbs the natural stress state of the rock salt formation and induces deviatoric (shear) stresses in the rock salt near the cavern (Mellegard and Düsterloh, 2012). Therefore, if there is not an abrupt pressure change inside the salt cavern, the deviatoric stresses have the highest magnitude near the cavern walls, and especially at abrupt changes in geometry, but decreases with distance into the geological formation.

2.7.1 Temperature and pressure fluctuation in salt caverns for UGS

Salt caverns are located at depths between 200 m and 2000 m, and for this reason the confining pressures used for many authors are between 7 MPa and 45 MPa (Bérest, 2011; Kruck et al., 2013; Ma et al., 2013; Djizanne, 2014). Temperature and pressure variations can play an important role when ensuring protection and safety operations in UGS. Rheological responses to deformation can change with increase of temperature or confining pressure (Schulze et al., 2001; Klafki et al., 2003; Khaledi et al., 2016a; Bérest et al., 2019).

Operational pressure reported in the literature can vary based on the storing purpose of the salt cavern. Table 2.1 compiles the different pressure ranges

Table 2.1: Summarized information from literature about operational pressure range depending on the type of gas storing purpose in salt caverns (Kruck et a., 2013; Djizanne et al., 2014; Landinger et al., 2014, Fan et al., 2016, Jiang et al., 2016, Khaledi et al., 2016).

Reference	Site type	Operation pressures
	CAES	4.7 - 7.2MPa
Khaledi et al., 2016	CAES	2.2 - 4.7MPa
	CAES	5 - 8MPa
Landinger et al., 2013;	CAES (Huntorf, Germany)	4.3 - 7MPa
He et al., 2017	CAES (Mcintosh, Alabama, USA)	4.5 - 7.6MPa
Fan et al., 2016	UGS	0 - 34.8MPa
Fan et al., 2017	UGS	1.5 - 34.8MPa
Jiang et al., 2016	UGS	0 - 34.8MPa
Djizanne et al., 2014	Hydrogen storage (Teeside, UK)	7 - 21MPa
Kruk et al., 2013	Hydrogen storage (Clemens, USA)	7 - 13.5MPa
Kruk et al., 2013	Hydrogen storage (Moss Bluff, USA)	5.5 - 15.2MPa

reported in the literature review linked to the type of storing activity and stored gas (Kruck et al., 2013; Landinger et al., 2013; Fan et al., 2016; Jiang et al., 2016; Khaledi et al., 2016b; Fan et al., 2017; He et al., 2017). Use of salt caverns for natural gas storage has seasonal injection and withdrawal cycles whereas salt caverns used for CAES and hydrogen storage operate with daily cyclic periods (Khaledi et al., 2016b) where, according to Crotogino et al. (2001), the charge and discharge time of the cavern for CAES operations are 8 and 2 h, respectively.

Operation activity of gas injection and withdrawal can induce temperature changes inside the salt cavern (Klafki et al., 2003; Berest et al., 2007; Brouard et al., 2012; Khaledi et al., 2016a). Most common ranges of temperature fluctuation reported in the literature review are from around 20°/25°C-40°/55°C (Brouard et al., 2012) (Brouard et al., 2012; He et al., 2017) and high temperature operations with temperatures from 40°C up to maximum 100°C, inside

the salt cavern, with a mean temperature of 80°C in the rock salt (Khaledi et al., 2016a) (Figure 2.16).

Bérest et al. (2019) makes an analysis of how temperature fluctuations affects low-stress laboratory creep tests. Temperature fluctuations can alter the transient and steady-state viscoplastic strain rates by generating an additional thermoelastic strain. However, it is important to clarify that, while temperature affects the creep strain rate of the rock salt by increasing the strain rate with the increase of temperature (Fjar et al., 2008), thermoelsatic strains are the result of even small variations of temperature that can be corrected if temperature during the experimental testing is recorded precisely (Bérest et al., 2005). Bérest et al. (2019) states that, by assuming a thermal expansion coefficient of salt approximately of α_{th}= 4 x 10^{-5} °C, if the room temperature by the end of the test is warmer than at the beginning by ΔT = 0.1°C, then the thermal strain will be larger than the accumulated viscoplastic strain ($\Delta\varepsilon_{vp}$).

Rock mass temperature is assumed to increase linearly with depth following the geothermal gradient. According to Bérest (2011), in salt rock, a typical value of the geothermal gradient is 0.016°C/m. However, other authors assume a geothermal gradient of 0.03°C/m (Khaledi et al., 2016a; Serbin et al., 2015). In addition to the geothermal gradient, gas injection and withdrawal activities lead to temperature variations in the salt caverns walls. Klafki et al. (2003), conducted a study of temperature fluctuation inside salt caverns during different operating modes by using long-term downhole fibre optic temperature measurements and CFD-modeling.

Due to differences in temperature between the rock salt formation and the inner boundary of the salt cavern, there is an exchange of thermal energy through the salt rock as a medium of conduction (Khaledi et al., 2016a). When air temperature inside the salt cavern increases, during gas injection, heat is transferred

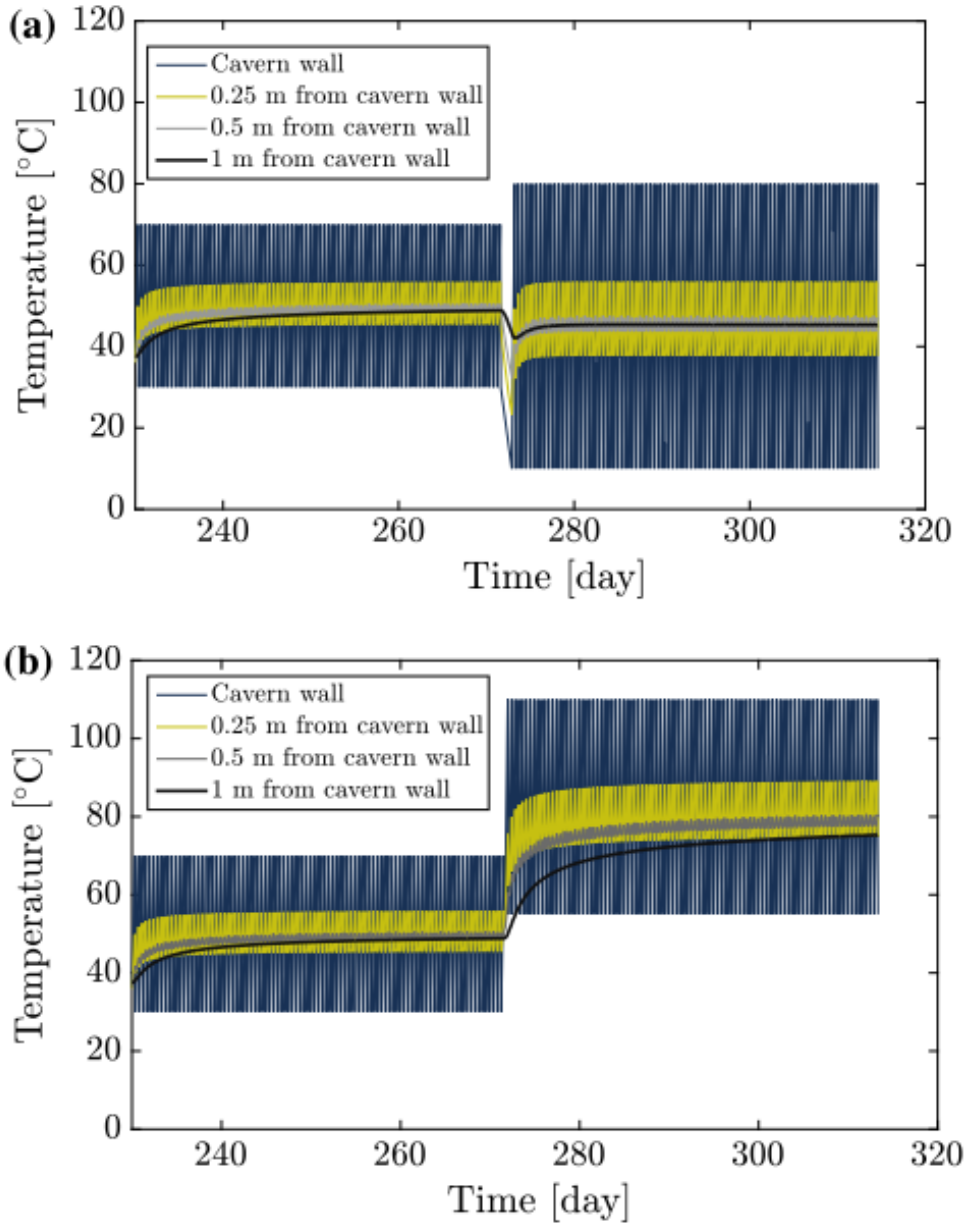

Figure 2.16: *Variation of rock salt temperature at selected distances from the cavern boundary during cyclic loading phase. Graph a) low- pressure operation. Graph b) high-temperature operation (Khaledi et al., 2016a).*

from the air inside the salt cavern to the rock mass increasing the temperature of the surrounding rock.

Temperature fluctuations due to gas injection and withdrawal can lead to thermal tensile stresses resulting in perpendicular fractures to the cavern wall. Although original penetration depth of fractures is small Bérest et al. (2014) suggests that depth of penetration of the fractures must be computed to prove that they cannot be a concern from the point of view of cavern tightness.

2.7.2 Stability and integrity of salt caverns

Rock salt deposits are a very good material to allocate stable and tight salt cavern construction, suitable for storing hydrocarbon products (oil and natural gas) and compressed air and hydrogen gas. However, some operating conditions could cause a disturbance, such as dilatancy and damage in the salt formation. Safety and stability issues can limit cavern size, shape, spacing and targeted gas pressure values (Ozarslan, 2012; Wang et al., 2013; Li et al., 2015).

A dilatancy study can be useful to prevent and heal damage in salt used as storage caverns because it can help to make a qualification of micro- fracking volume (Van Sambeek et al., 1993). Such damage could increase the permeability in the salt rocks, which is something that we want to avoid in order to provide a safe gas storage site (Ozarslan, 2012). Several studies were performed during the 90's to study the impact of creep deformation over rock salt microstructure (Spiers and Schutjens, 1990; Senseny et al., 1992; Carter et al., 1993; Cristescu, 1993; Van Sambeek et al., 1993; Franssen, 1994; Peach and Spiers, 1996; Hunsche, 1998; Spiers and Carter, 1998). Salt caverns must be carefully designed according to site specific salt properties and operational circumstances and requires the analysis of geomechanical safety. However, de-

spite all the research about geomechanical stability inside salt caverns in the 90's, more investigations are needed to understand the effects of temperature and pressure fluctuations due to seasonal gas injection. Moreover, in this study the presence of impurities that rock salt presents naturally was not considered.

In the process of creating the cavern in the salt formation, pressure effects of overburden sediments and cohesion of rock salt can affect the stability of the salt cavern. During the operational activities of salt caverns for gas storage use, the fluctuation of injection and extraction of gas can have implications in the cavern stability (Schulze et al., 2001; Bérest et al., 2005, 2006; Huang and Xiong, 2011; Wang et al., 2013; Xiong et al., 2015), like micro- fracking with an associated permeability increase.

2.7.3 Cyclic loading mechanical tests in the literature review

Several investigations have been conducted to study the mechanical behaviour of rock salt under cyclic mechanical conditions (Khaledi et al., 2016b). Geomechanical tests under cyclic loading conditions can provide valuable data about how the gas injection fluctuations can affect the rocks surrounding the salt cavern. Second phase content, affecting the anisotropy of the rock formation, can have a more brittle response in comparison of halite after a certain number of cycles (Liang et al., 2012). The studies of Liang et al. (2012) demonstrates that other lithotypes that can be presented as interlayers in rock salt formation respond to deformation differently compared to pure salt samples, under cyclic loading conditions. However, further reaserch is needed to analyse rock salt with different second phase content to better understand how different secondary mineralogy affects elastic and physical rock properties before rock failure.

Ma et al. (2013), studied the stress state of salt in gas storage caverns during long term gas injection-ejection activity and the effects of cyclic loading under confining pressure conditions. To carry out the experimental investigation a triaxial cyclic loading test was performed by using salt rocks. To simulate the cyclic loading during the gas injection and withdrawal periods stress parameters where set as: σ_{max} as maximum applied stress, σ_{min} as minimum applied stress, a stress amplitude represented by σ_a= (σ_{max}-σ_{min})/2 and a mean stress σ_m= (σ_{max} + σ_{min})/2. The effects of the confining pressure over the axial strain were analysed and they observed an axial strain rate decrease with an increase of the confining pressure on the time- dependent behaviour, under cyclic loading conditions.

After an increasing number of loading cycles, a decrease of the elastic modulus of salt rocks was observed. However, this elastic modulus degradation seemed to be independent of the stress and confining pressure applied during the cyclic loading tests (Ma et al., 2013). The authors also analysed the relationship between the transient and steady- state strain rates and the maximum and minimum applied stress. With an increase of the maximum applied stress or decrease of minimum applied stress, the transient and steady- state strain rate showed a tendency to increase.

Computational modelling can provides valuable information about rock salt long-term behavior under different pressure and cyclic loading conditions. Cyclic operation phases can be numerically simulated to study volume changes, damage propagation and permeability changes in salt caverns at different time scale (Khaledi et al., 2016b). Therefore, although Wang et al. (2011) and Wang and Xie (2012),studied the mechanical implications of thin mudstone layers in underground salt caverns without applying cyclic mechanical conditions, numerical modeling could be used to study the long-term impact of second phase content at different cyclic loading conditions. Models from Wang et al. (2011)

and Wang and Xie (2012) were developed to predict the shear and dilatancy zones inside the cavern to evaluate the deformation tendency through time, without applying pressure fluctuations.

Wang et al. (2011); Wang and Xie (2012) found a large differential deformation between the mudstone interbeds and the salt rock, as mudstone presents stronger rheological characteristics compared to salt rock. A relation between the internal cavern pressure and deformation velocity was performed to understand how internal pressure of salt caverns can affect cavern closure rates. When the internal pressure increased, the velocity of wall closure inside the cavern decreased, and the differential deformation between mudstone and salt rock was smaller. Related to the injection cycle of gas in salt caverns, Liang et al. (2012) supports that a substantial range of strain rates in gas storage exist, where the higher values are obtained during gas withdrawal, for consumption (and lower during gas injection for storage), also known as "stress fluctuation". The authors confirm that this "stress fluctuation" phenomenon should be investigated further from a microstructural deformation point of view. Bérest (2013) argue that the main force for cavern creep wall closure is due to the difference between geostatic pressure and cavern pressure.

2.8 Summary

Rock salt forms as a result of saline brine evaporation normally related to lagoon isolation by a barrier or sill. However, primary deposits can suffer chemical and mechanical alterations due to diagenetic processes, water intrusion or rock deformation. Rock salt that is mainly formed by halite (NaCl) can present second phase mineralogy such as anhydrite, gypsum, polyhalite, carnallite, etc. It can also contain other detritic sediments linked to the depositional environment such as mudstones, sands or clay.

Therefore, rock salt or evaporite facies can have different chemistry. Different chemistry can result in a different rheological behaviour. Different second phase content can have distinct structural configuration depending on the components properties of each mineral and it can have an influence over the deformation mechanisms of rocks.

The salt formations in the UK are of Triassic (252-201 Mya) and Permian age (299-251 Mya). Triassic salt in the UK can be found mainly in bedded strata in the Cheshire Basin and, to a lesser extent, in Northern Ireland, Lanchashire, the Isle of Man and Walney, Staffordshire, Worcestershire and Somerset. Permian salt fields extend in the northeast of England (Yorkshire) and Northern Ireland.

Rock salt presents optimal rheological properties, very low permability, providing great tightness, and self-healing properties for which it is considered as a potential option for gas and energy storage activities. Rock salt presents a high ductility, and under mechanical deformation it can deform by two stress dependent domains: dilatancy domain, with an increase of micro-cracks and rock permeability, and compaction domain, where plastic deformation and compaction takes place and healing of micro-fractures with a decrease in permeability occurs. When rock salt deforms within the compaction domain, a ductile deformation takes place without cracks and fracture development known as creep deformation. Creep deformation is driven by the movement of defects in the crystal lattice, known as dislocation creep, and by dissolution-transport-precipitation mechanisms, known as pressure-solution creep. However, second phase content in rock salt can affect these deformation mechanisms having an effect on the rheological behaviour of rock salt.

Rock salt subjected to salt caverns construction and UGS activity can be subjected to pressure and temperature fluctuations as well as disturbance of

the natural stress state of the rock due to the cavity construction. Temperature fluctuations in salt caverns can lead to thermal tensile stresses and fracture generation. Although these initial fractures might be small, there is still uncertainty about how those micro-cracks will evolve after several injection-withdrawal cycles.

Chapter 3

Mineralogical and structural characterisation of core samples

3.1 Introduction

Rheological behaviour of rock salt is linked to rock composition and texture. As described in the previous chapter, rock composition is related to original brine from where the rock was deposited and post-depositional chemical and physical changes. Those post-depositional processes can involve variation in temperature and pressure or exposure to other weathering agents. These chemical and textural changes in the rock salt will imply different rheological behaviour within different samples. This chapter aims to provide an initial description of the tested samples. This initial chemical and textural description will provide an starting point of differentiation between samples to understand the different geomechanical responses from samples with different composition and texture, under similar testing conditions.

To provide an insight in the rock composition, a series of chemical analysis were combined with a description of thin sections. The mineralogical analysis was conducted by combining Powder X-Ray Diffraction (PXRD) analysis and polarized light microscopy using thin sections. The petrological description of

samples provided information about the colour and texture of samples before deformation. The texture analysis was performed by using thin sections, for the micro-textural description, and macro-textural description also to assess the integrity of the core sample to be tested, layering description and grainsize analysis. The grainsize counting was performed with digitalised pictures in Matlab for creating histograms of the frequency for different ranges of grain sizes.

3.2 Methodology

3.2.1 Compositional analysis with Powder X-Ray Diffraction (PXRD) analysis

In general, X- Ray Diffraction analysis is a technique for crystallographic characterisation of materials providing information about crystallographic structures, crystal phase and preferred crystal orientations (PCO). Compositional analysis by Powder X- Ray Diffraction (PXRD) in this study was completed on an X'Pert PRO PANalytical MPD X-ray Diffractometer. Bragg-Brentano geometry and CuKα radiation at 40 kV and 40 mA was used with sample holders of 20 mm diameter and samples were scanned over a sampling range of 5 to 70 °2θ with a step size of 0.0066(°2θ) and a scan speed of 0.23 °2θ per second. For phase identification the PDF4 (ICDD, 2020) database was used within the software DIFFRAC.EVA to identify the mineral peak patterns. The PXRD data was combined with mineralogical description of blue dye impregnated, one-side polished thin sections at 200 microns. The thin section analysis was performed using a ZEISS transmitted light polarization microscope (using a magnification 10x and 20x). Samples before deformation from XRD analysis and to create the thin sections were obtained from the cutoffs from core sample preparation (Figure 3.1).

The PXRD technique consists in analysing a monochromatic beam of X-rays scattered at different range of angles after interacting with the atomic structure of a tested material (Bunaciu et al., 2015). The monochromatic induced X- Ray beam, created by filtering a polychromatic X- ray through a monochromator, interacts with the lattice planes of the samples resulting in peak intensities in relation with atom distribution within the lattice in the form of an X- Ray diffraction pattern (Das et al., 2014). Figure 3.2 shows a schematic picture from the XRD machine used at the University of Nottingham and a

Figure 3.1: *Schematic image of core sample preparation for cyclic mechanical loading tests. The red rectangles show the core edges that were removed and used for thin sections and XRD analysis before deformation. The discontinuous lines represents the limit and the final core material for cyclic mechanical testing.*

schematic picture of the machine and the analysis mechanism. Different chemical components can be identified by analysing the emitted peak intensities and the resulting X- Ray diffraction pattern (Bunaciu et al., 2015). The X- Ray diffraction pattern results from recording the X- ray intensity, represented in counts or counts per second, in relation to the detector at 2θ position. The detector moves in a circle around the sample and, to keep the 2θ relation between sample and detector, the sample keeps accordingly in motion (Bunaciu et al., 2015). Figure 3.3 shows a schematic diffraction patterns as example with the X- ray intensity, in counts, plotted as a function of 2θ. In the diffraction pattern intensity peaks related to halite, anhydrite, polihalyte, kieserite and carnallite can be identified.

One of the challenges from using XRD techniques is that different minerals, but with similar chemical composition, can provide also similar diffraction patterns potentially resulting in some mistakes or low accuracy in mineral identification if the mineralogical analysis is only based on XRD patterns (Ouhadi and Yong, 2003). For this reason, the mineralogical analysis was combined with

microscopical analysis by thin sections and transmitted light microscopy to support and confirm the identification of main mineralogy, also making the interpretation of measured XRD patterns easier and more reliable. The XRD technique also provides a semi-quantitative analysis of mineralogical composition, based on reference intensity ratio and spiking methods (Bruker, 2020), allowing to distinguish the different tested samples based on their percentage in second phase content such as anhydrite, polyhalite, carnallite, kieserite or clay.

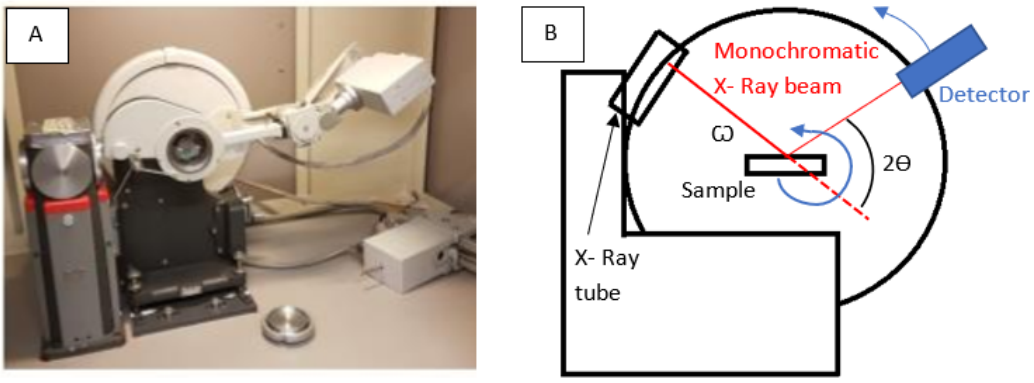

Figure 3.2: *Picture of the X' Pert PRO PANalytical MPD X- ray Diffractometer used for the PXRD analysis at the University of Nottingham (A) and schematic picture explaining how the machine works and the analysis mechanism (B)*

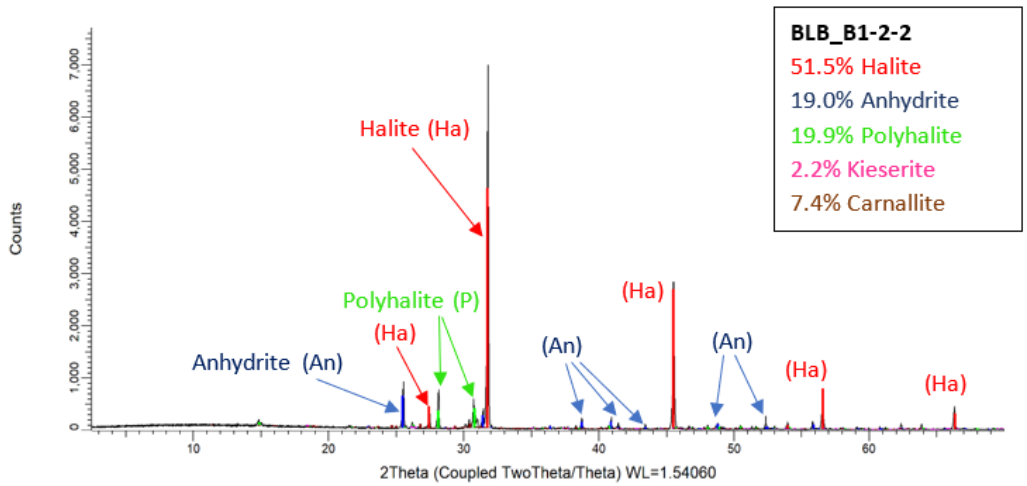

Figure 3.3: *Example of PXRD pattern of a rock sample from Boulby Mine obtained by data analysis with the software DIFFRAC.EVA. The XRD pattern shows halite, Anhydrite and polyhalite as main components of the rock sample. The lower intensity peaks from the background of the pattern matched with kieserite and carnallite, both also spotted in the mineralogical analysis made by using thin sections or cited in the literature review.*

3.2.2 Calculation of standard deviation

During core samples preparation, an initial PXRD analysis was performed for all the rock salt samples. Based on an initial compositional analysis the core samples were assembled in series of rock samples. Core samples with similar compositional characteristics, based on both the petrographic analysis and PXRD data, were grouped in the same series to be tested at different conditions according to the aims and objectives of the project.

To assess heterogeneity of rock samples and achieving representative compositional analysis, three extra sampling from some of the tested specimens were collected to repeat the PXRD analysis. This procedure was used as an assessment of heterogeneity to quantify the error and to improve the mineralogical analysis along the whole sample. The extra powder samples to analyse with PXRD technique was obtained by drilling in the selected areas of the core samples with a Dremel microdrill to induce the lower damage possible. Three samples were collected along the core length i) at the upper part ii) in the middle of the core and iii) the bottom part of the core sample. Due to the unavoidable inferred damage to the core samples by this sampling technique, the extra PXRD analysis was performed always after the cyclic loading tests. Figure 3.4 shows three different samples after drilling the control sampling points to test by using PXRD analysis.

A standard deviation has been calculated to determine the mineralogical heterogeneity of the different series and samples tested. The calculation was done by using the XRD analysis data from each three individual drilled hole per sample (Figure 3.4) and using the standard deviation formula

$$s = \sqrt{\frac{1}{N-1}\sum_{i=1}^{N}(X_i - \bar{X})^2} \tag{3.1}$$

where $\{X_1,X_2,...,X_i\}$ are the data values for each sampling points and $\bar{X}$ in

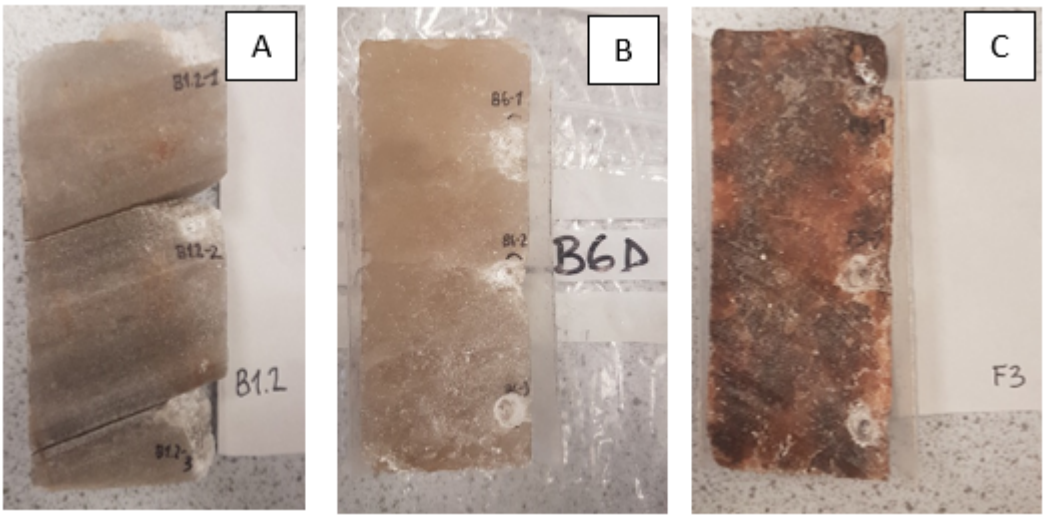

Figure 3.4: *Images of core samples from Boulby Mine (A, B) and Winsford Mine (C) with three control sampling points to provide a better analysis of compositional variation within a core sample.*

the mean value calculated from the sampling points and N is the number of sampling points used (which is 3 per core sample).

3.2.3 Transmitted light microscopy

The compositional analysis, from the PXRD data, was combined with a mineralogical description with thin sections. The thin sections were analysed by both using transmitted light microscopy and Scanning Electron Microscopy (SEM). By combining transmitted light and Scanning Electron Microscopy (SEM) it is aimed to identify the deformation mechanisms incurred during the cyclic mechanical loading test in different types of rock salt with different amounts and types of second phase content. The combination of both techniques provides a wider image from the microstructural analysis from μm to mm scale.

Polarized- light microscopy can be either used with transmitted or reflected light for performing a qualitative analysis from anisotropic materials. A conventional light microscope can be converted into a polarized light microscope

by adding two polarizing filters in the optical system (Buschow et al., 2001). A polarized light microscope includes two polarizing elements, one located in the illumination path before the condenser and the second one placed in the imaging path before the objective lens (Oldenbourg, 1998).

In a transmitted light microscope, the light source is placed below the sample and passes through a polarizing element called "polarizer" before interfering with the sample, used to polarise the light supplied by restricting the plane of vibration of the light in only one plane. After interacting with the sample, the light is filtered again through a second polarizing element called "analyser" which analyses the polarization of the light after passing through a birefringent specimen. After passing through a birefringent sample, the one plane- polarised light splits into two vibrating planes with different orientations known as ordinary and extra- ordinary rays (Figure 3.5). After going through the "analyser", ordinary and extra- ordinary rays are recombined into a same phase ray, restricting the light to one plane (Oldenbourg, 1998; Nikon Instruments, 2020).

Normally, the two polars are in crossed position so that the analyser absorbs most of the light passing through the polarizer (Oldenbourg, 1998). When the microscope works only with one polarizing filter properties like pleochroism or refractive indices can be appreciated but by using cross polars (both polarising elements) extra optical properties like isotropy/anisotropy, extinction angle or birefringence colours can be observed (Frandsen, 2016).

The analysis of natural salt rock samples by using the polarizing microscope allows recognition of the main minerals that form the rock through their optical properties. Transmission light microscope analysis requires thin sections of the rocks that were manufactured in Poland and the British Geological Survey in Keyworth (UK). Each mineral behaves differently under polarized light due to specific structural and crystallographic characteristics. Under polarized

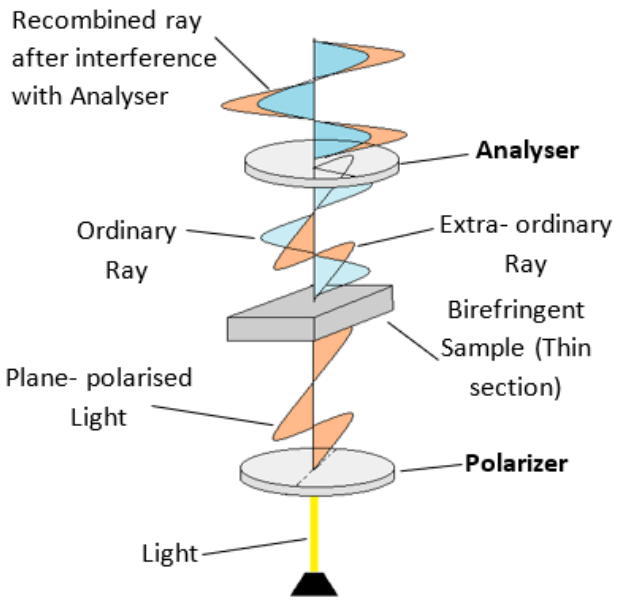

Figure 3.5: *Schematic image of the optical system in a Polarized Light Microscope. The image polarizer converts the light from the light source into a one plane-polarised light before it interacts with the sample (thin section). After interacting with a birefringent sample, it results in an ordinary and extra-ordinary ray in different planes. The analyser recombined ray.*

light different minerals show a variety of colours (pleochroism) and change of colours when the sample is rotated, cleavage, relief, shapes and extinction angles. Due to these varied characteristics, a mineralogical characterisation of the natural rock sample can be conducted. When using crossed polars, minerals show different birefringence colours depending on the crystalline system they have. The birefringence showed under crossed polars can be classified in 1st, 2nd, or 3rd Order Birefringence depending on the intensity of the colours (Kendall, 2009). The mineralogical characterisation of natural salt samples was performed using a Polarizing Microscope with transmission light. The microscope used was a Zeiss Microscope (Figure 3.6).

3.2.4 Preparation of the thin sections

The thin sections where prepared by the British Geological Survey (BGS) in Keywoth, UK. Depending on the stability of the samples, some of them were

Figure 3.6: *Zeiss Microscope used for the mineralogical characterisation of thin section at the nano and micro- scale Research Centre (nmRC) at the University of Nottingham.*

surface impregnated, prior to cutting, with blue dye epoxy resin, after which they were cut into sub sample size, using a dry, diamond saw. All samples were then blue resin impregnated, under vacuum, to ensure thorough penetration of the samples.

The samples were dry cut from the block of resin and a flat surface generated on one side of the sample. This was achieved by using silicon carbide abrasive paper of various grades, 120, 240 and 400. The final surface was then prepared using a suspension of aluminium oxide powder in isopropyl alcohol on a flat glass plate.

Glass slides, 48x28mm, were pre-ground on a Logitech lapping machine to produce slides of a constant thickness. The samples were then bonded to the glass slides using clear epoxy resin. The bonded slides were then allowed to cure in a low temperature oven overnight. The excess material was then cut and ground away to a thickness of about 800 microns, at which point the slides were put back on the Logitech and lapped to final thickness using the aluminium oxide suspension in isopropyl alcohol.

Polishing was carried out using mono-crystalline diamond paste, of grades, 15, 6 ,3 and 1 micron, applied to a polishing cloth. The finished, polished slides were stored in a desiccator to protect the surface from absorbing moisture from the atmosphere. At all times the samples were kept free from water, and Local Exhaust Ventilation was used to control dust and vapours.

3.3 Results

3.3.1 Sample description

The procedure for the description of samples from both Winsford and Boulby Mine was the same. An initial texture and mineralogical description was performed in the lab to select suitable samples for mechanical testing. Some samples from Boulby mine had to be discarded after damage caused during transportation. The reason of the damage during transporation was because those samples were sent by mail from Boulby Mine. An inspection with photographs was performed to all the tested samples to make sure the core specimens used in the cyclic mechanical loading tests were in optimal conditions.

The suitable samples were grouped in different series of samples based on their second phase content and texture. Thin sections and XRD analysis were performed to describe the main features from the different core specimens for each group of samples. However, due to the natural heterogeneity of the samples, some samples resulted in showing a bigger variability in composition from the XRD analysis, in comparison to other samples from their same group. The main mineralogy, texture and heterogeneity from the tested rock salt samples is presented and discussed in this section.

3.3.1.1 Boulby Mine

An initial petrological description was performed on the different rock salt samples in order to make a first assembly of samples in different groups to be tested. Up to three different series of samples came up from the initial petrological description in i) series A, ii) series B, iii) series C.

Series A of samples are non-clastic and vitreous/crystalline white-transparent to light brown coloured rock salt, with some thin layers of anhydrite, with a greasy lustre, only presented in some samples (Figure 3.7). The layers of anhydrite had a thickness oscillating from 3 mm to 1 cm of maximum and presenting a bedding dip of 20° from the horizontal. In general, the core samples corresponding to this Series of samples consist of clear rock salt with slightly elongated grains with sizes from 1-2 mm to 1.5-2 cm maximum approximately (Figure 3.8 and figure 3.9).

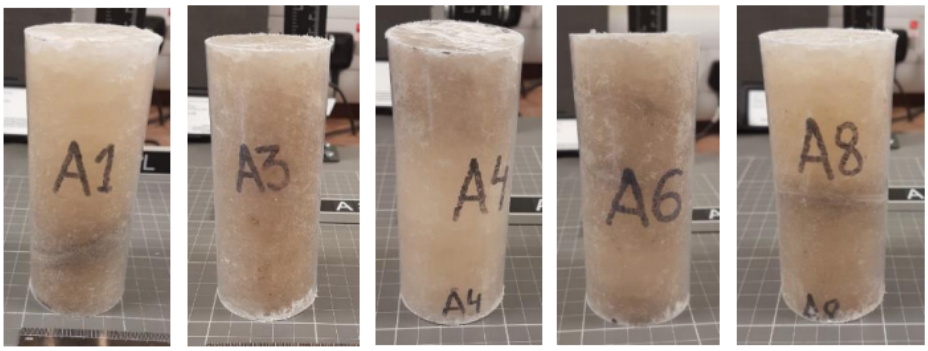

Figure 3.7: *Core samples from Series A.*

The histograms for grainsize have been performed by using the Graphical User Interfaces (GUI) tool from Matlab. This tool provides point-and-click control to process an image and by providing an initial scale bar, an histogram for grainsize can be created in one direction of a surface at once.

In order to have the most representative data from grainsize, the counting of grain boundary has been performed in two directions at once, one in the di-

rection in which grains are shorter and the other in which grains are longer. The texture of the rock samples from series A is formed by 1-2 mm to 1.5-2 cm maximum sub-angular and elongated crystals of halite. Due to the elongated crystals, only grain counting in two, perpendicular to each other, directions were used to create the histograms for the grainsize analysis.

In the mineralogical analysis performed by using thin sections, the main mineralogy observed was mainly, halite and anhydrite, and polyhalite (as expected from the XRD analysis in section 3.3.2). Two different ranges of grain size can be distinguished, (i) colorless or light-yellow halite crystals of 200 μm to 1.5 mm in diameter and which can contain fluid inclusions, and (ii) smaller mainly anhedral and some few prismatic anhydrite crystals with sizes of 10 μm to 200 μm in diameter (Figure 3.10). Both halite and anhydrite are colorless and with no pleochroism in plane polarized light, but under crossed polars halite turns completely black due to the cubic crystal system, and anhydrite displays third order interference colors from green and light blue to light pink. Polyhalite occurs as colorless crystals with a maximum size of 200 μm, and displays low interference colors from grey to white and inclined extinction under crossed polarised light. This mineral also shows twinning typical of polyhalite (Biehl et al., 2014).

The distribution of second phase content is mainly concentrated around the halite crystal boundaries, surrounding the anhedral and equant halite crystals (Figure 3.10 A and B). Occasionally, second phase minerals are also included within some halite grains but appearing in lower quantity. Anhydrite tends to show mainly spherical shapes, although some prismatic crystals can also be observed, whereas polyhalite occurs as prismatic crystals. Kieserite is identified in the thin sections by a vitreous luster, very high birefringence and may have also twinning structures. Prismatic polyhalite can be observed enclosing finer crystals of anhydrite. Polyhalite crystals can be recognised under crossed

polars for the low interference colours and the small microcrystals of anhydrite enclosed in the polyhalite are recognised by the third order interference colors and parallel to inclined extinction (Figure 3.10 C,D and E).

Figure 3.8: *Histograms for grainsize analysis for samples A7 and A5 from Series A, Boulby Mine. The histograms show that the grain size observed in samples from series A ranges from 1 mm to 18 mm maximum with a higher frequency of grains with sizes between 2 to 6 mm.*

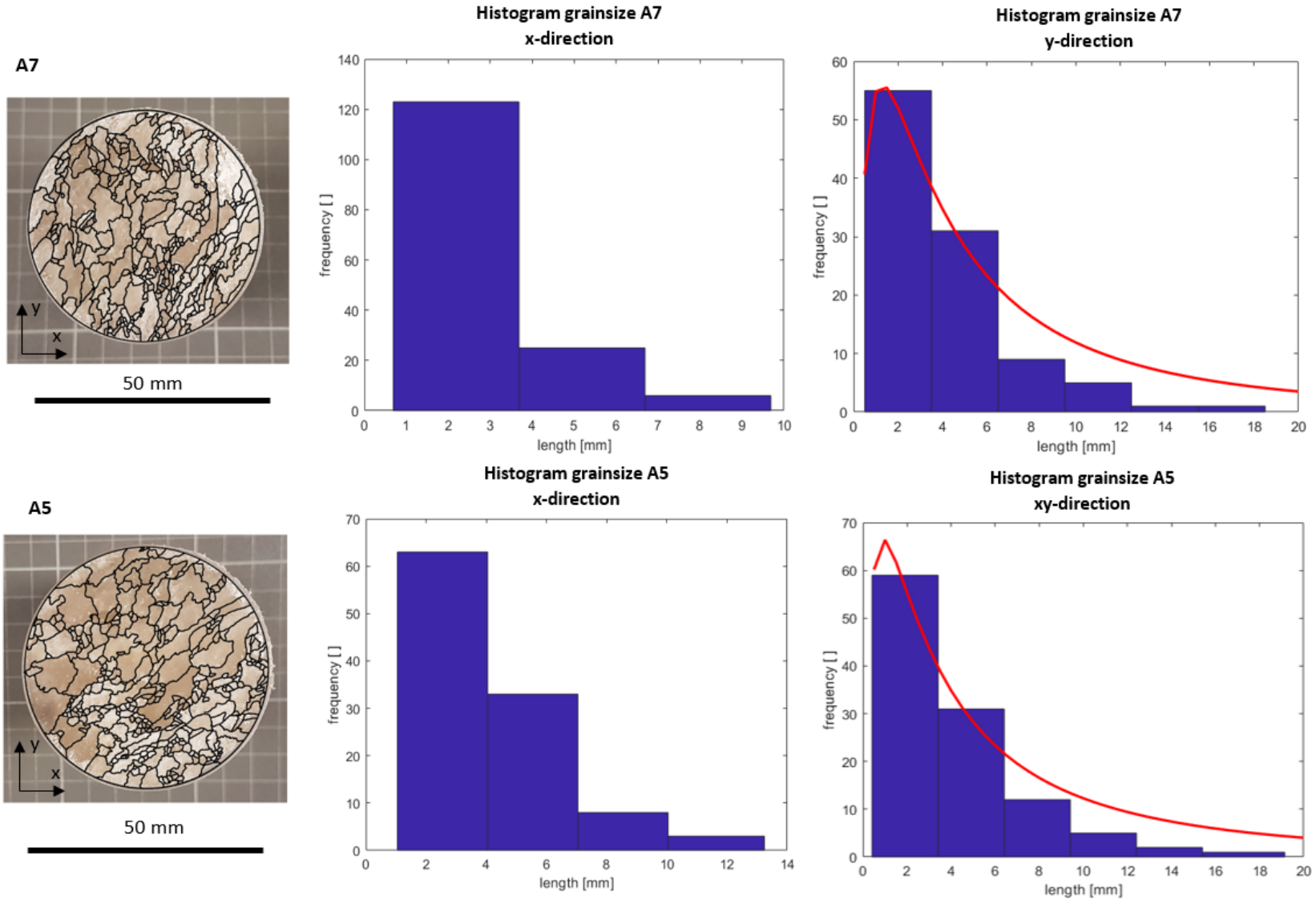

Figure 3.9: *Histograms for grainsize analysis for samples A3 and A4 from Series A, Boulby Mine. The histograms show that the grain size observed in samples from series A ranges from 1 mm to 20 mm maximum with a higher frequency of grains with sizes between 1 to 6 mm.*

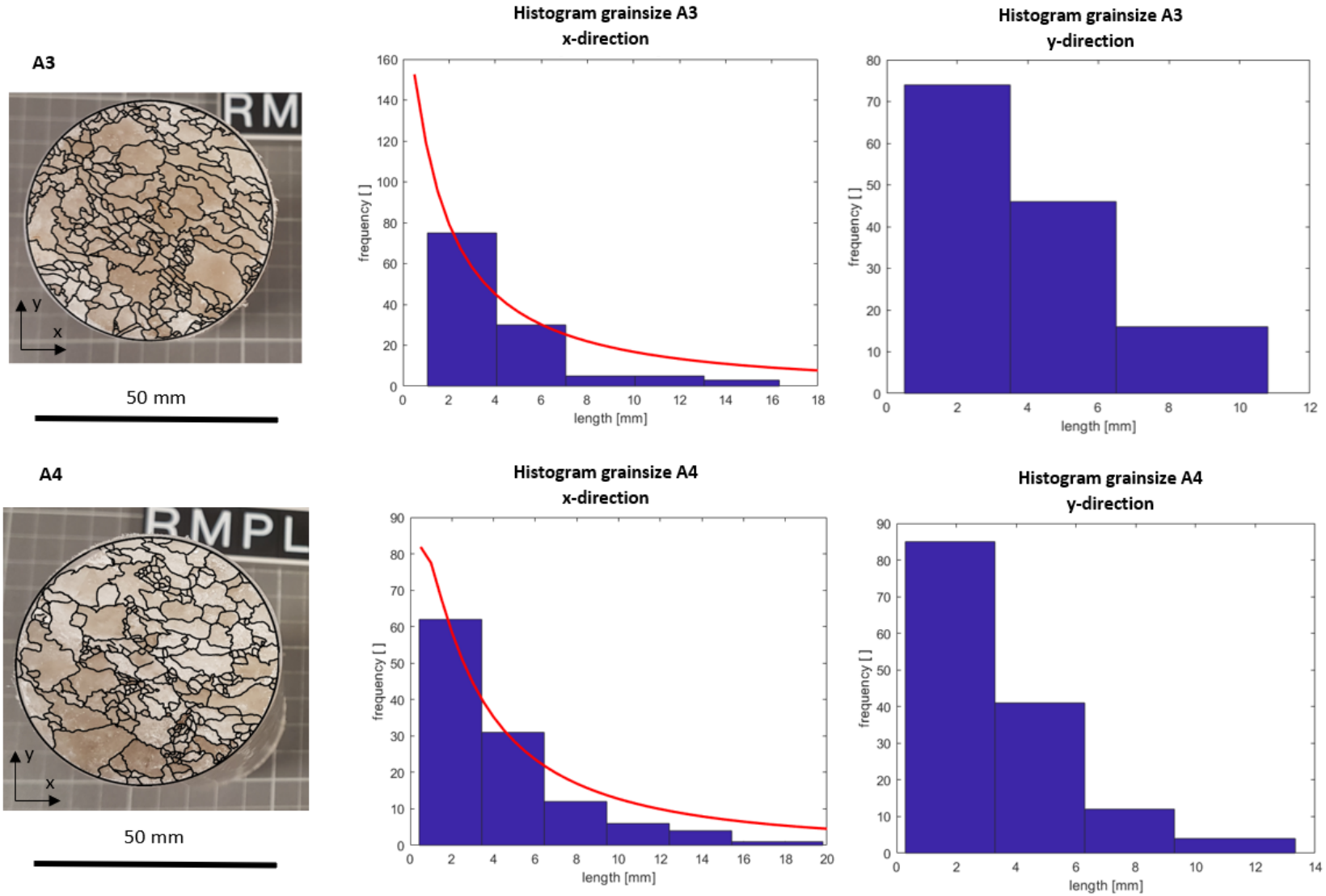

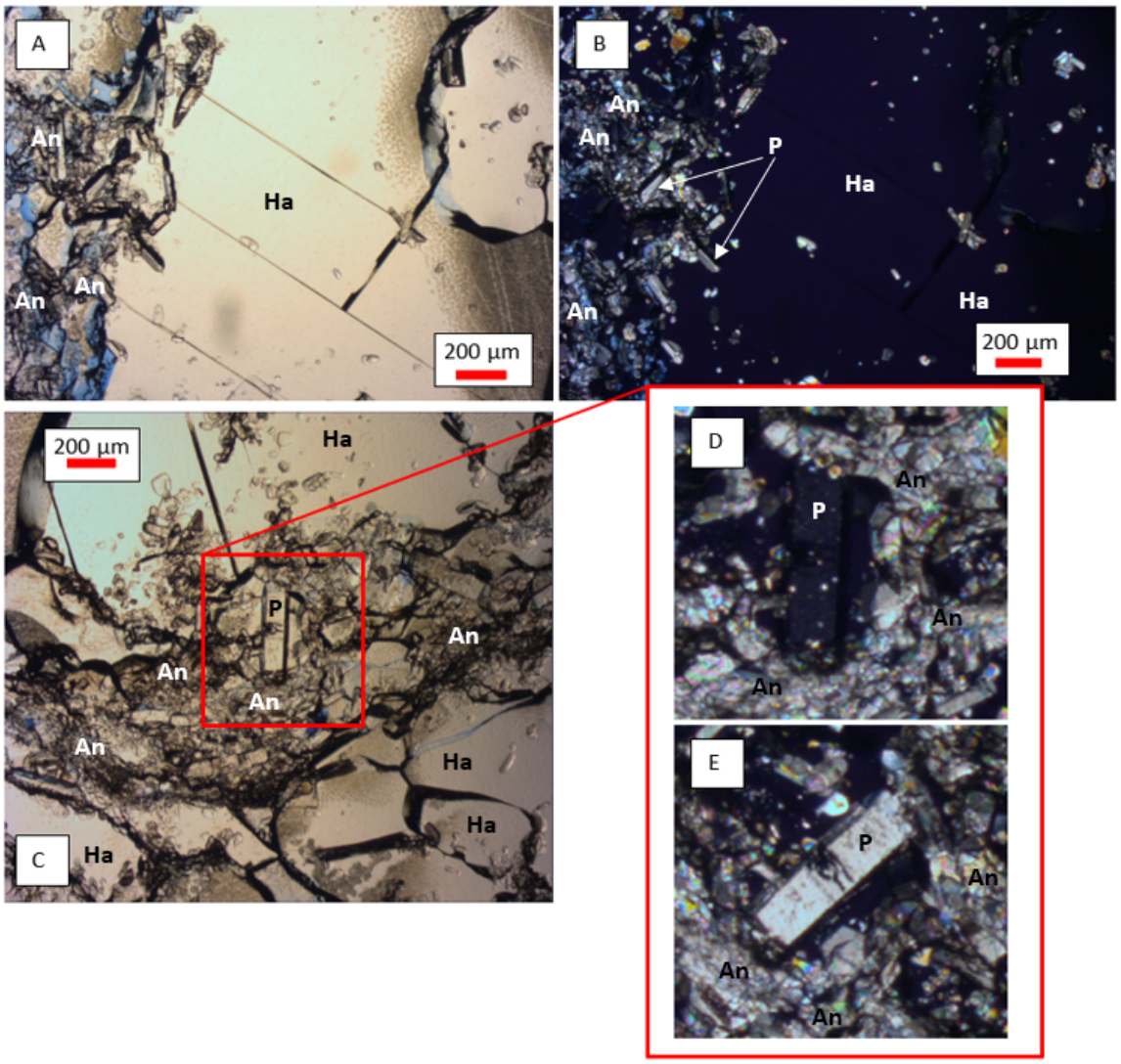

Figure 3.10: *Images A and B are from the thin section from A4 under transmitted light (A) and using crossed polars (B). In these image show 200 µm to 1.5 mm crystals of halite (Ha) surrounded by smaller mainly anhedral and some few prismatic anhydrite (An) crystals, with sizes from 10 µm to 200 µm, and some prismatic polyhalite (P) crystals up to 200 µm. C, D, E: Prismatic polyhalite (P) enclosing finer anhedral crystals of anhydrite from sample A3. Figure C is under transmitted light and D and E are by using crossed polars.*

Series B is the series of rock samples, from Boulby Mine, with the highest content in second phase minerals. This series of rock samples consists of a maximum of only 5 cores of 50 mm diameter and lengths between 110 and 115 mm because most of the core samples broke during transportation. The strong layered structural arrangement promoted the failure of the samples along the layering planes before being tested. The cylindrical core samples show an alternation of layers from 2 mm to 2cm thick of brown and dark grey coloured

anhydrite and polyhalite and very light grey to grey halite (Figure 3.11). The layers show a dip of approximately 20° from the horizontal. The anhydrite-rich layers are fine-grained with a greasy lustre whereas the halite-rich layering is composed by vitreous and elongated crystals of halite with sizes between 1 mm to 1.5 cm maximum (Figure 3.12).

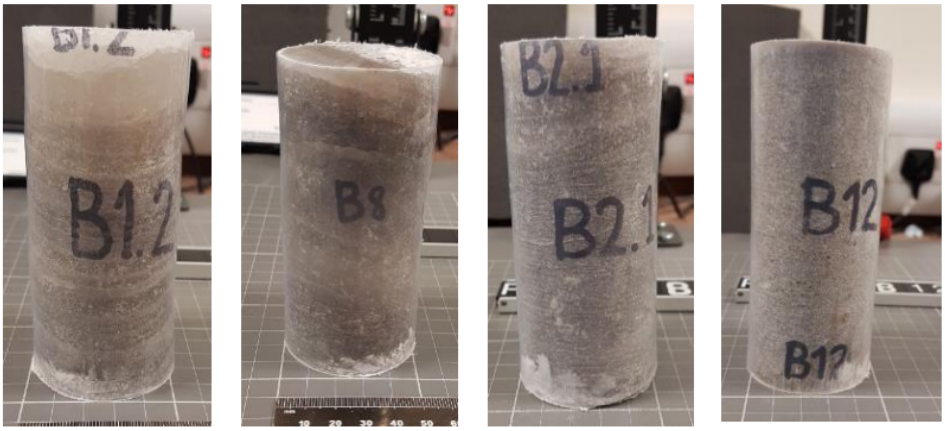

Figure 3.11: *Core samples from Series B, Boulby Mine. Brown and dark grey anhydrite and polyhalite layering can be observed in alternation with brown to light brown layering of halite.*

Crystal size is slightly smaller than in samples from series A and C, with grain sizes between fine micro-crystalline and a few mm up to 1 cm (Figure 3.12 and 3.13). Both the analysis of thin sections and the XRD analysis show an important increase in second phase content such as anhydrite and polyhalite in this series of rock samples B. This increase in polyhalite is observed with an increased content of prismatic shaped crystals in comparison to samples from the other series (Figure 3.14).

Figure 3.12: *Histograms for grainsize analysis for samples B1-2 and B6 from Series B, Boulby Mine. The histograms show that the grain size observed in samples from series A ranges from 0.5 mm to 9-15 mm maximum with a higher frequency of grains with sizes between 1 to 3 mm.*

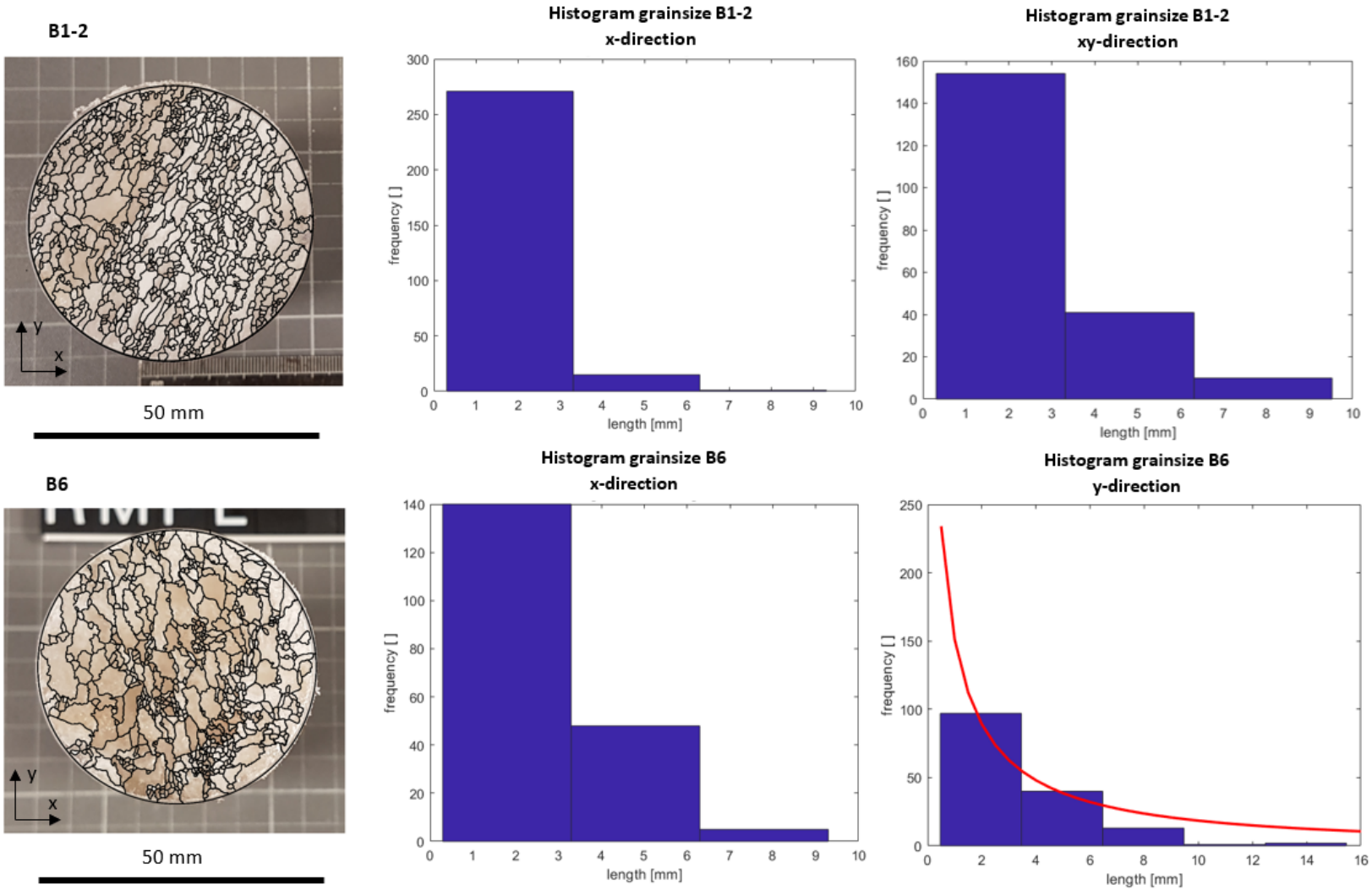

Figure 3.13: *Image from micro-crystalline anhydritic layering in sample B2-1 from Series B, Boulby Mine. Images from microscope in the right show the micro-crystalline matrix of anhydrite under transmitted light (A) and with crossed polars (B).*

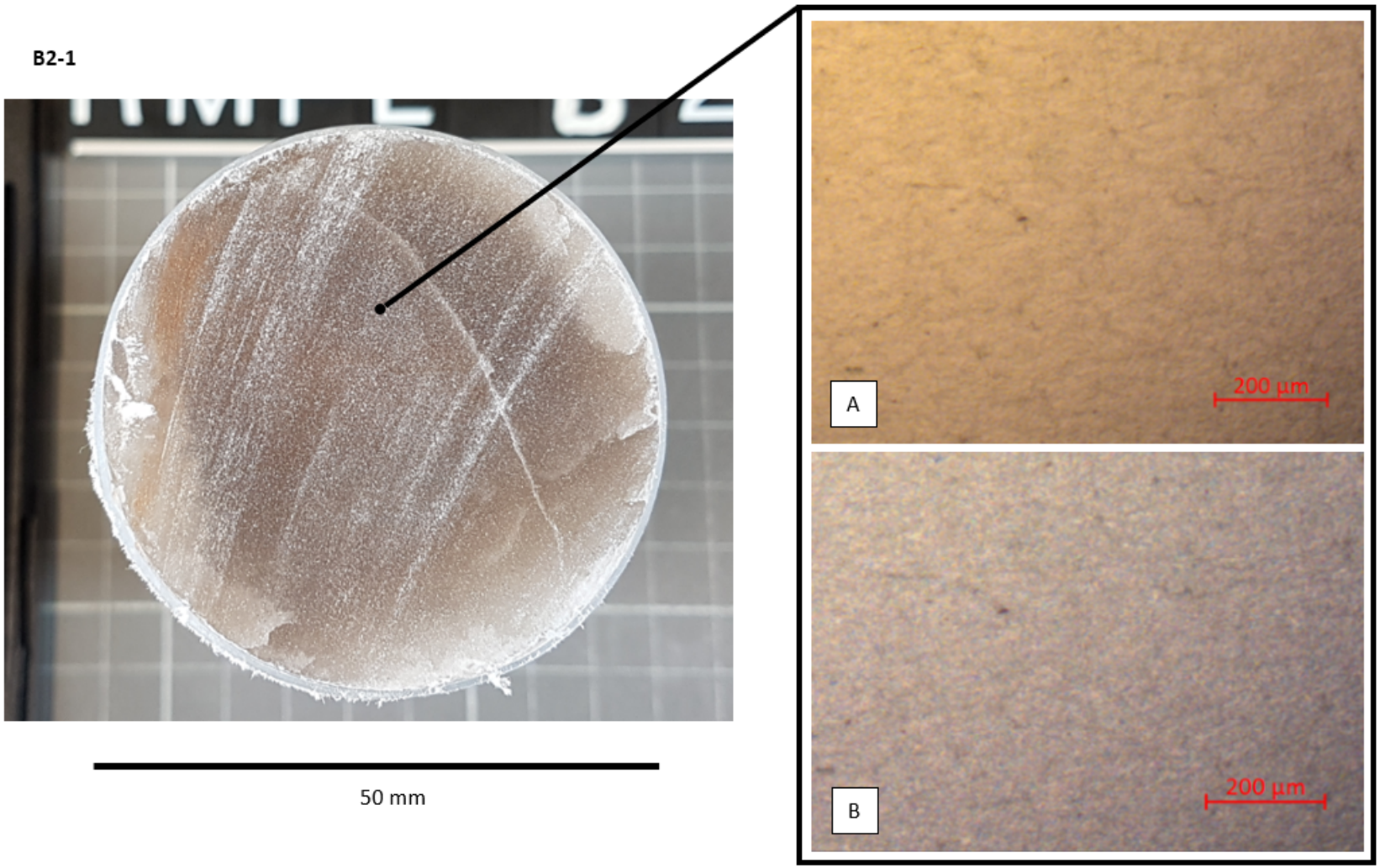

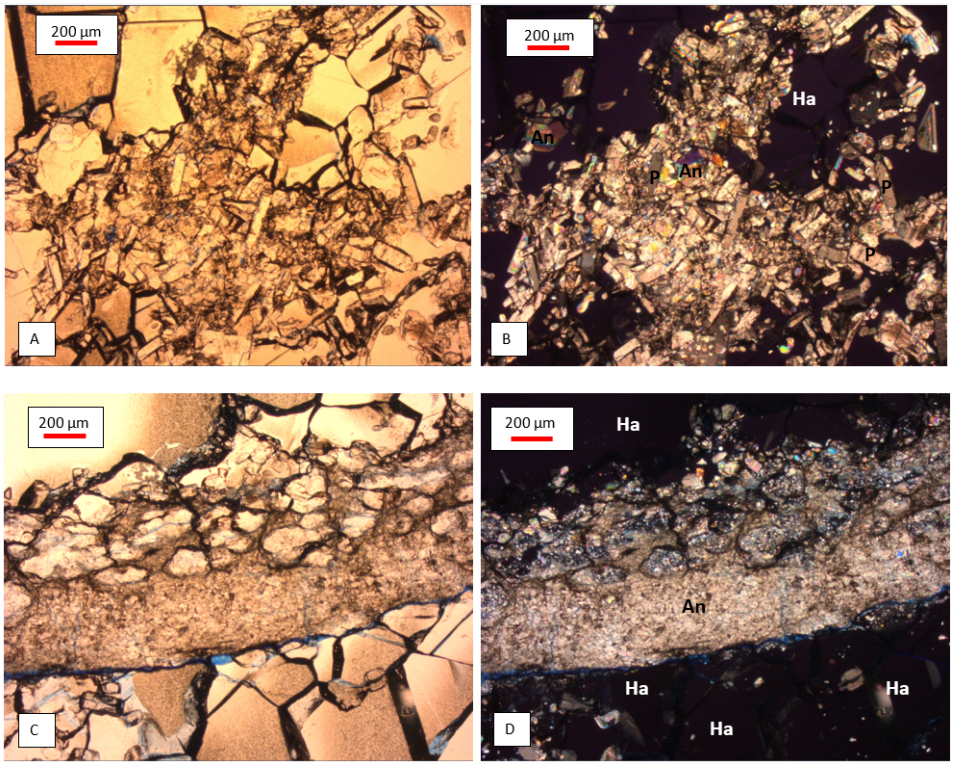

Figure 3.14: *Image A shows a picture from sample B6 through transmitted light and B shows the same frame from the same thin section through crossed polars. The combination of both images allows identifying the main mineralogy of the salt rock sample with halite (Ha), anhydrite (An) and polyhalite (P).*

Under transmitted light microscopy, the anhydritic layering observed from the core sample (Figure 3.11) is seen as layers of a micro-crystalline anhydrite matrix alternating with levels of anhedral halite crystals. The boundary between halite and anhydrite layers can be sharp or gradual. Figure 3.14 E-F show a well defined discordant boundary of a microcrystalline matrix of anhydrite, abruptly cutting the halite crystals on the base. On the top of the layer, a gradual mineralogical transition from anhydrite to halite can be observed. This transition presents a slight increase of anhydrite crystal size from the microcrystalline matrix to anhedral crystals from 10 μm to 50 μm and bigger halite crystals of 200 μm enclosing the smaller anhydrite crystals. In the anhydrite-halite contact zone, there are some fractures.

Series C shows clear white-greyish to light grey salt crystals (Figure 3.15) with sizes from 1mm to maximum 1.4 cm and no layering. All samples presents

a clear nonclastic and crystalline texture with slightly elongated anhedral halite crystals. Two main ranges of halite grain size can be identified. Some small grains from 0.5 to 4 mm and then, a second range of sizes from 4 mm to maximum 1.4cm. Grain size from 0.5 to 4mm is the main range of grain size for samples from series C (Figure 3.17). The thin section analysis shows halite crystals from 0.5mm to 1.4 cm (around 90%) with some anhydrite crystals (up to maximum 10%) with sizes from 10 to 50 μm mainly located between halite grain boundaries and, sporadically, enclosed withing halite grains (Figure 3.16). The PXRD analysis from series C identifies halite as the main mineralogy with the lowest variation in content in comparison to the other series tested. Series C also shows a small content of anhydrite (around 6%) and carnallite (around 4%) and very low content of polyhalite (3%) and kieserite (0.7%) (Table 3.1). The thin sections from series C show a structure formed by relatively bigger, in comparison with the previously discussed samples, halite crystals (from 500 μm to 1.5 cm) with lower second phase content. Similar to the observations in the previous samples, the few second phase minerals are generally located at the halite crystal boundaries, although small (about 10 μm) anhedral anhydrite crystals also occur enclosed in more central parts of the halite crystals.

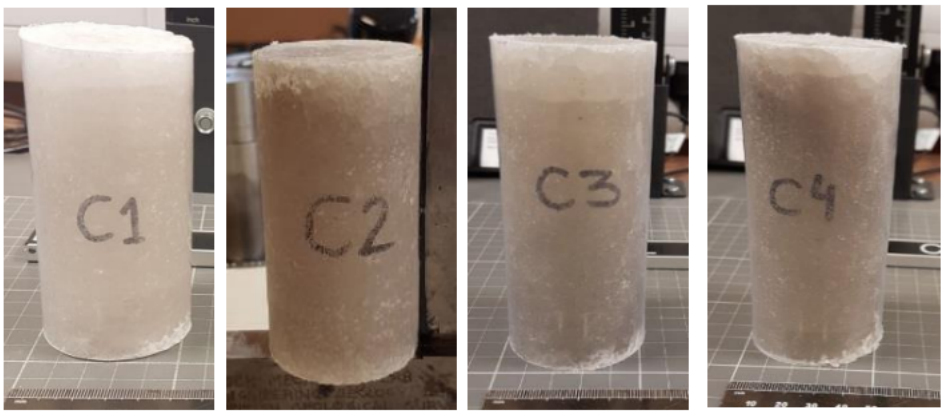

Figure 3.15: *Images of some of the core samples from Series C, Boulby Mine.*

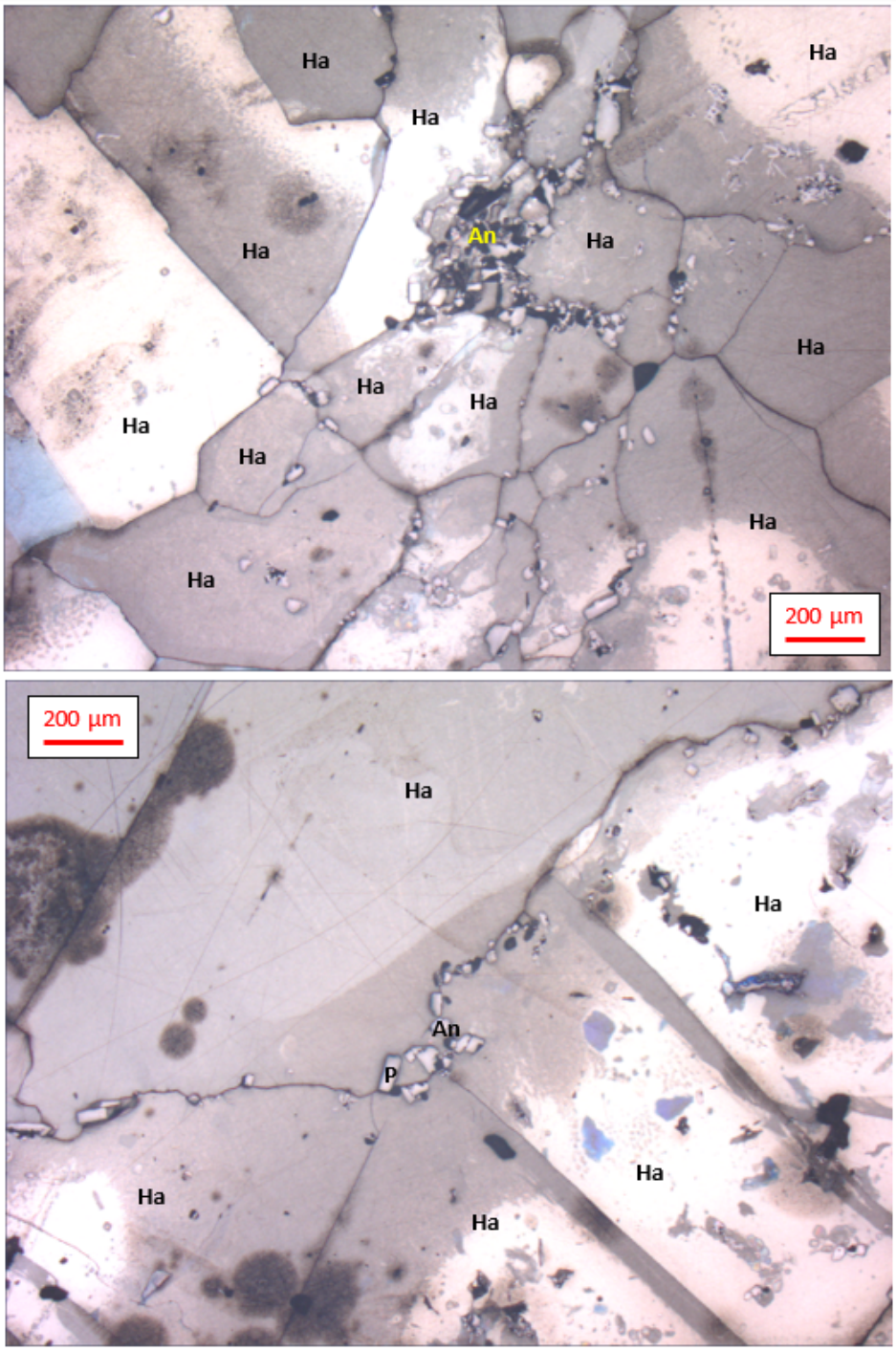

Figure 3.16: *Images from thin section C3 before deformation. A main mineralogical composition of halite (Ha), around 85-90%, can be observed with some second phase content such as anhydrite (An) and polyhalite (P), in a quantity around 10-15%.*

Figure 3.17: *Histograms for grainsize analysis for samples C3 and C4 from Series C, Boulby Mine. The histograms show that the grain size observed in samples from series A ranges from 1 mm to 13 mm maximum with a higher frequency of grains with sizes between 1 to 6 mm.*

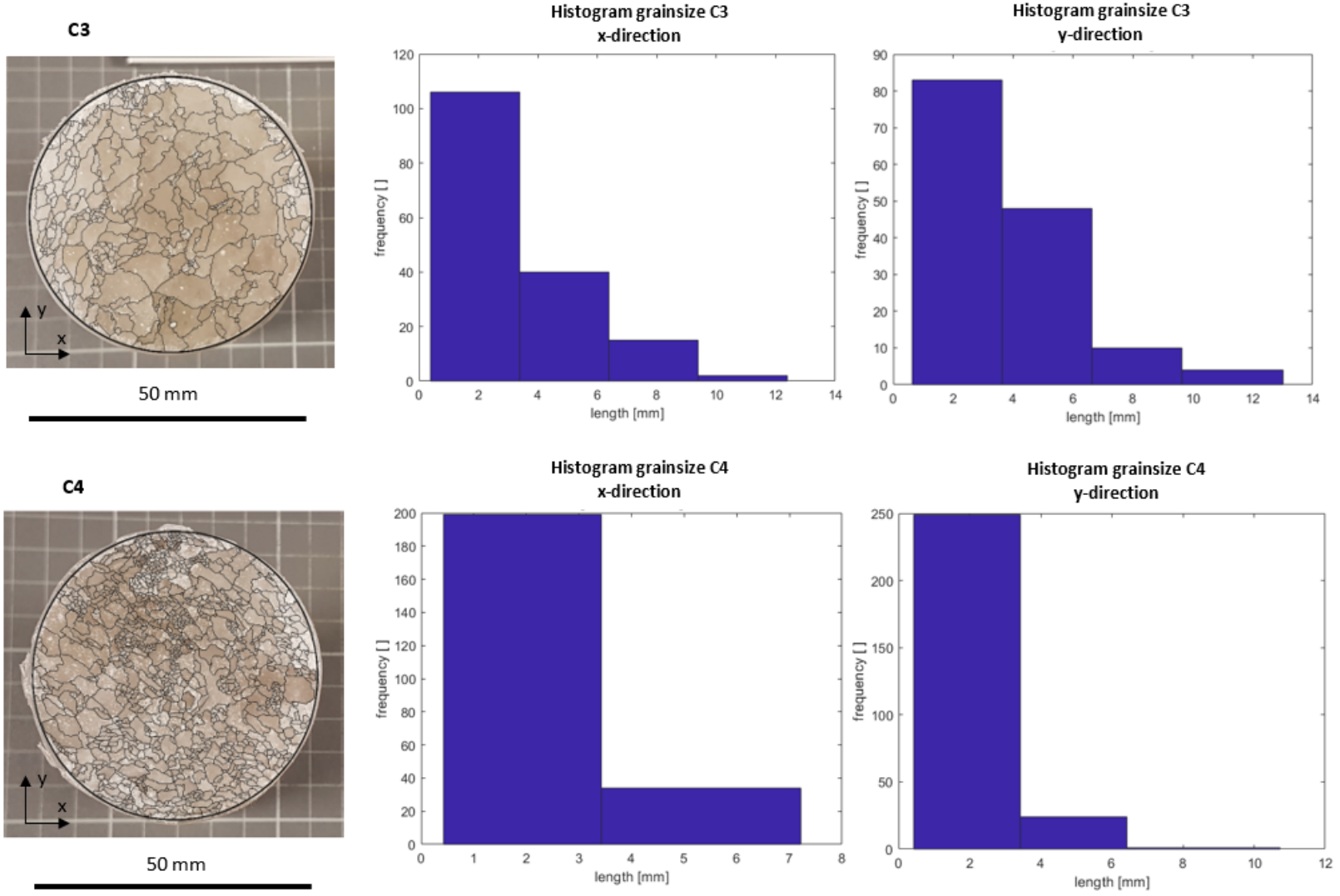

3.3.1.2 Winsford Mine

Samples from Winsford Mine were divided into three different groups: WB, F and LB, based on the origin point from the mine. In Winsford Mine two different rock salt exploitable levels are defined under the names "Layer B" and "Layer F". Samples from Layer B were grouped in the Series of samples WB and samples from Layer F in the Series F. During the visit to Winsford Mine, some samples from a new horizontal well the mine operators were doing were also included in the study. The horizontal well was part of the works to extend the mine operations in Layer B. The aim of this well was to find the major fault that limits Winsford Mine's extension. Due to the proximity to the fault, the samples from the drill core present a breccia texture. These samples were grouped in Series LB.

Series WB from Winsford Mine belongs to samples collected from the economical exploitable level "Layer B". Samples from Series WB presents a non-clastic and crystalline texture with soft-brown to brown-reddish halite grains. Grain size of halite grains is mainly from 1-5 to 6-9mm although some grains can be 1.5 cm maximum (Figure 3.18 and figure 3.19).

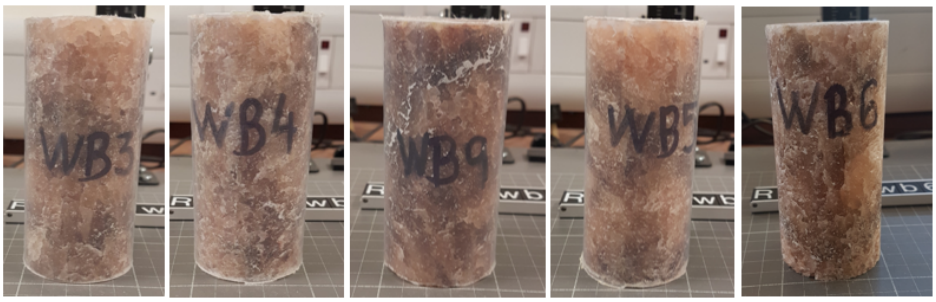

Figure 3.18: *Images of some of the core samples from Series WB, Winsford Mine.*

Figure 3.19: *Histograms for grainsize analysis for samples WB1 and WB7 from Series WB, Winsford Mine. The histograms show that the grain size observed in samples from series A ranges from 1 mm to 15 mm maximum with a higher frequency of grains with sizes between 1 to 6 mm.*

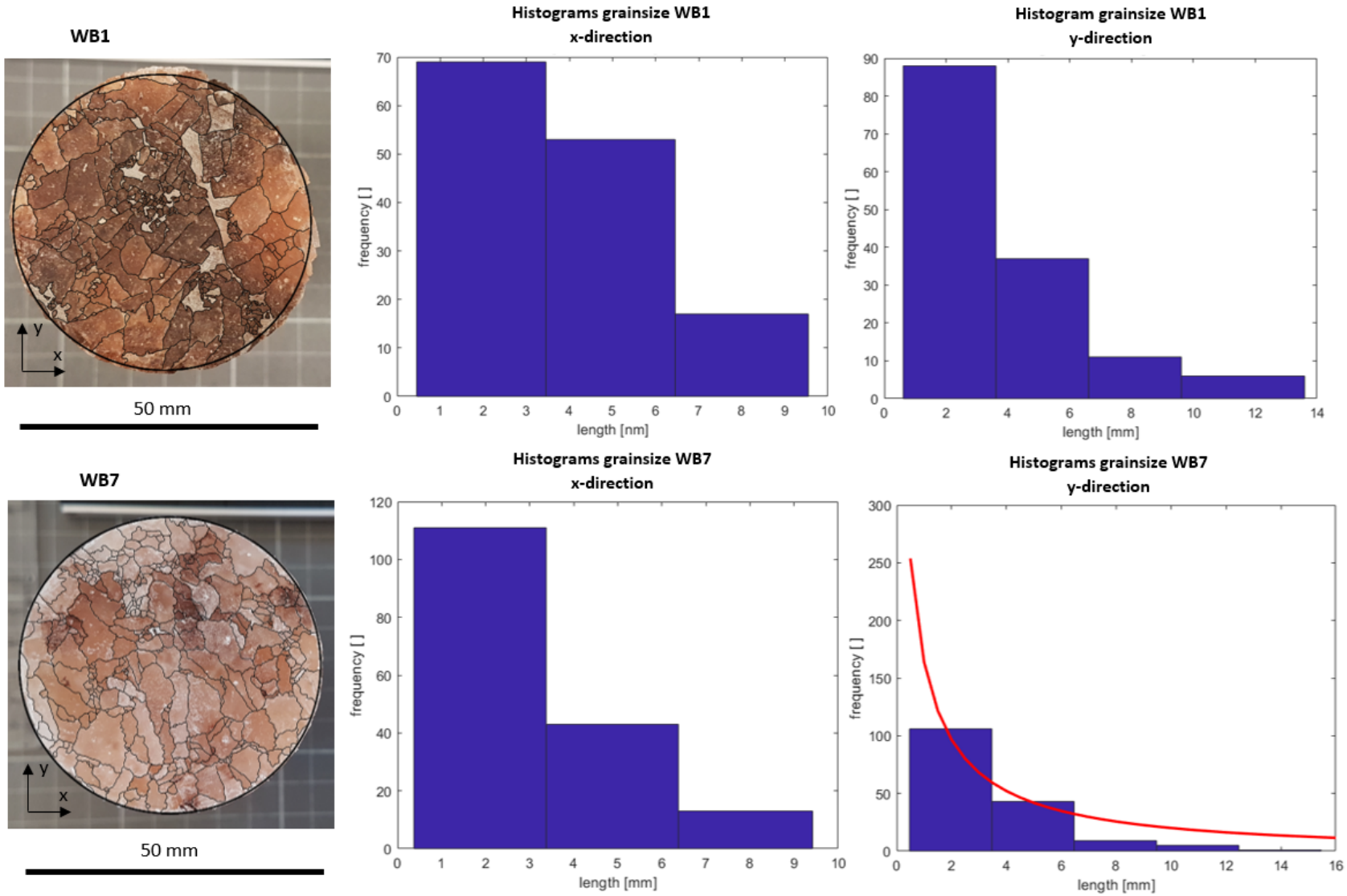

The halite grains presents anhedral shapes although few grains with an elongated habit can also be observed and some crystals also show a perfect cleavage at [010] characteristic of the cubic system. The main impurity observed in this series of samples is reddish clay. The clay is mainly around and along the halite grain boundaries although sometimes clay can be observed interstitially distributed inside halite crystals (Figure 3.20). Therefore, it can be interpreted that halite crystal growth and crystallisation took place within the clay matrix.

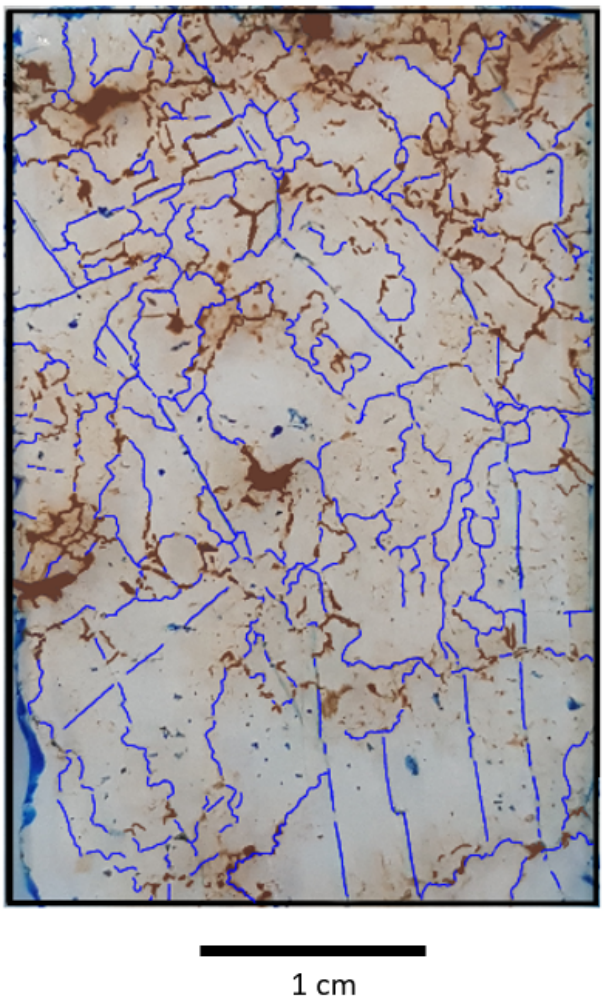

Figure 3.20: *Image from a sample from the series WB before deformation, Boulby Mine. Halite grain boundary is represented in blue while second phase content (clay) appears around the halite grains in brown-reddish colour.*

The optical microscope analysis showed that the main minerals present in the Winsford Salt Rock were halite (80%), anhydrite (around 5%), clay (15%) and

quartz. Halite crystals between 0.5 and 1 cm long with interstitial clay are observed. Clay surrounding the halite crystals interstitially contains microscopic scale quartz grains (from 10 to 80 μm) and aggregates of anhydrite crystals with grain sizes from 10 to 200 μm (Figure 3.18).

Series F presents similar purity in halite as series WB. Series F corresponds to the samples collected from the Layer F from Winsford Mine, which is the second economical exploitable level at Winsford Mine. Samples from series F have very similar features, in terms of mineralogical composition and texture, to samples from series WB althought a slightly grain size increase is noticed. The samples from series F are composed of light-brown to reddish-brown halite grains with sizes from 0.5 mm to 2.5cm (Figure 3.22). Main range of grain size is from 1 to 6mm with an anhedral and also elongated crystal habit. The main second phase content is clay, which is mainly distributed along halite grain boundaries (around halite grains).

The analysis from thin sections shows a matrix of clay surrounding the bigger crystals (0.5-1cm) of halite. This matrix of clay minerals have 50 μm crystals of quartz and anhydrite forming aggregates of crystals of around 10-50 μm to 100 μm. The aggregates of anhydrite show different morphologies: some of them are displayed in circular aggregates with a radial distribution of anhydrite crystals (Figure 3.23). Other aggregates have elongated morphology. It is difficult to recognise a crystal orientation in the elongated aggregates. Fewer grains of quartz can also be recognised within the clay matrix with sizes between 10 to 50 μm maximum. All these grains of quartz and anhydrite aggregates are held in the clay matrix.

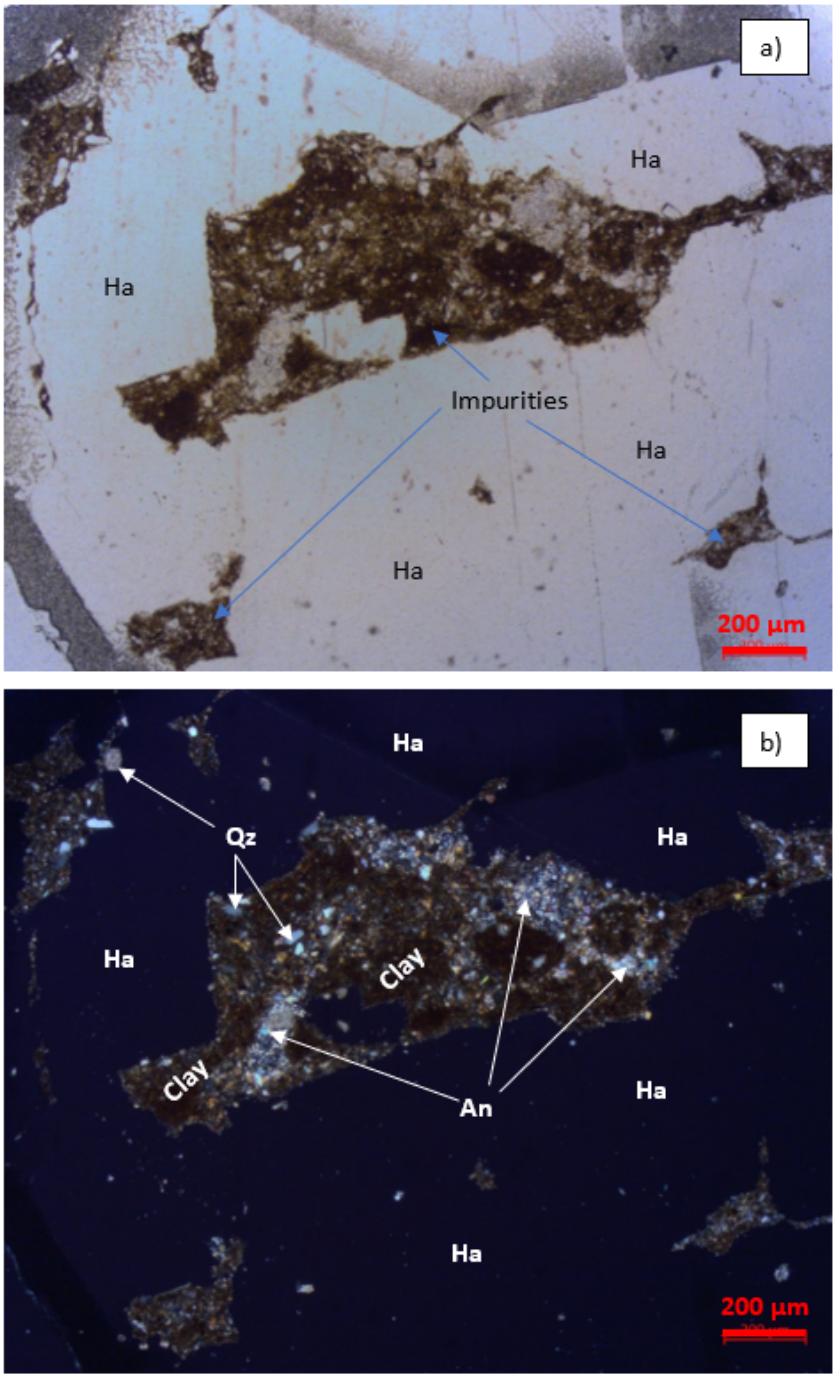

Figure 3.21: *Pictures from the thin section analysis of Winsford Mine salt rock. The figure contains two pictures showing the same bit of sample under polarised light (a) and crossed polars. In picture a) an aggregates of impurities with, clay, anhydrite (An) and some grains of quartz (Qz) interstitially disposed in bigger halite (Ha) crystals (around 0.5 cm) can be observed. Picture b) shows the same sample described above but with crossed polars. Crossed polars allows to differentiate Anhydrite and Quartz grains inside the clay matrix. Halite crystals appear completely extinguished under crossed polars because they crystallise in the cubic crystallographic system. Quartz and anhydrite are easily differentiated under crossed polars thanks to the birefringence. Quartz have a very low birefringence (grey- light grey) while anhydrite presents higher birefringence colours (green- blue).*

Figure 3.22: *Histograms for grainsize analysis for samples F1 and F6 from Series WB, Winsford Mine. The histograms show that the grain size observed in samples from series A ranges from 1 mm to 20 mm maximum with a higher frequency of grains with sizes between 1 to 3 mm.*

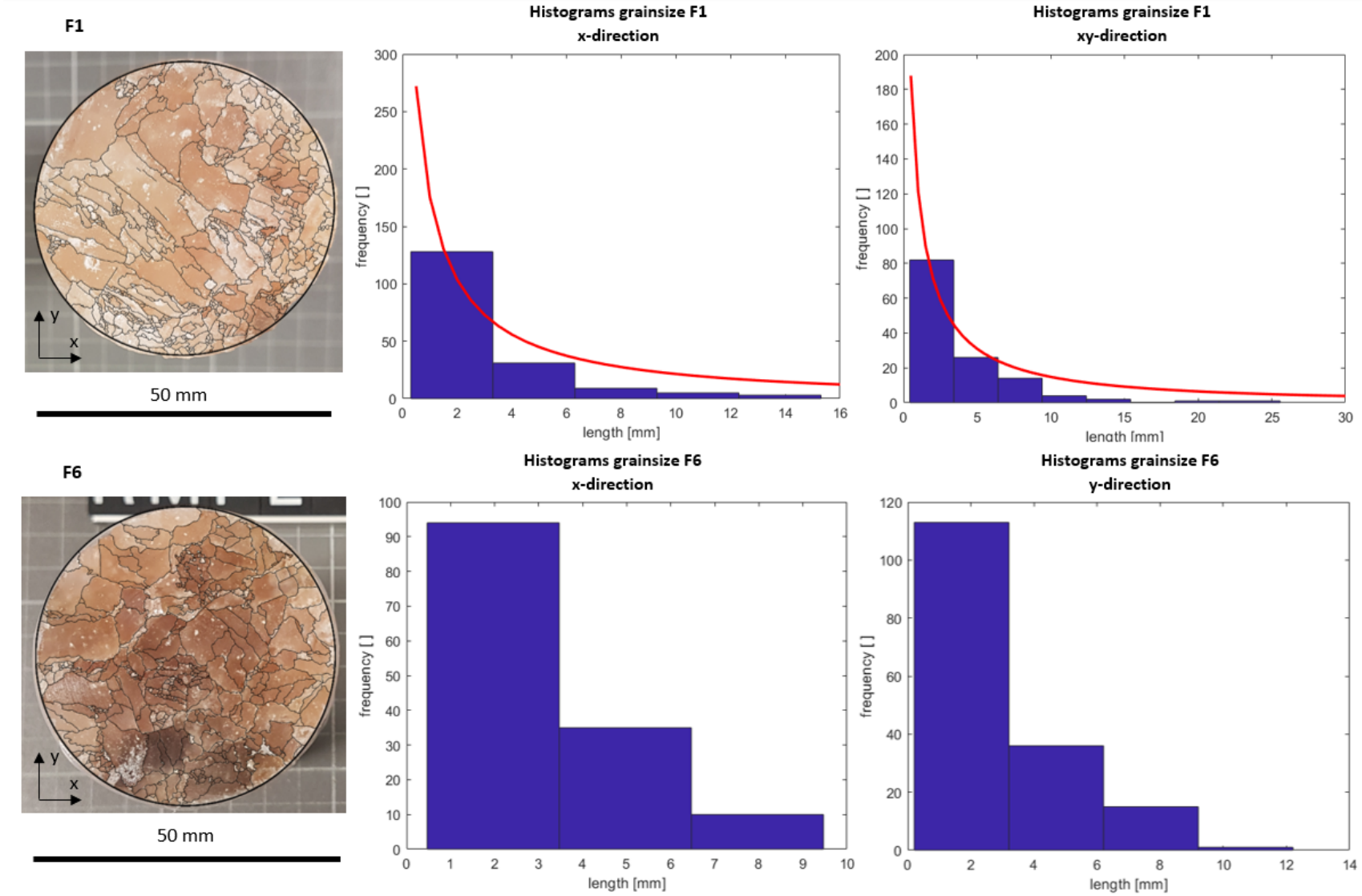

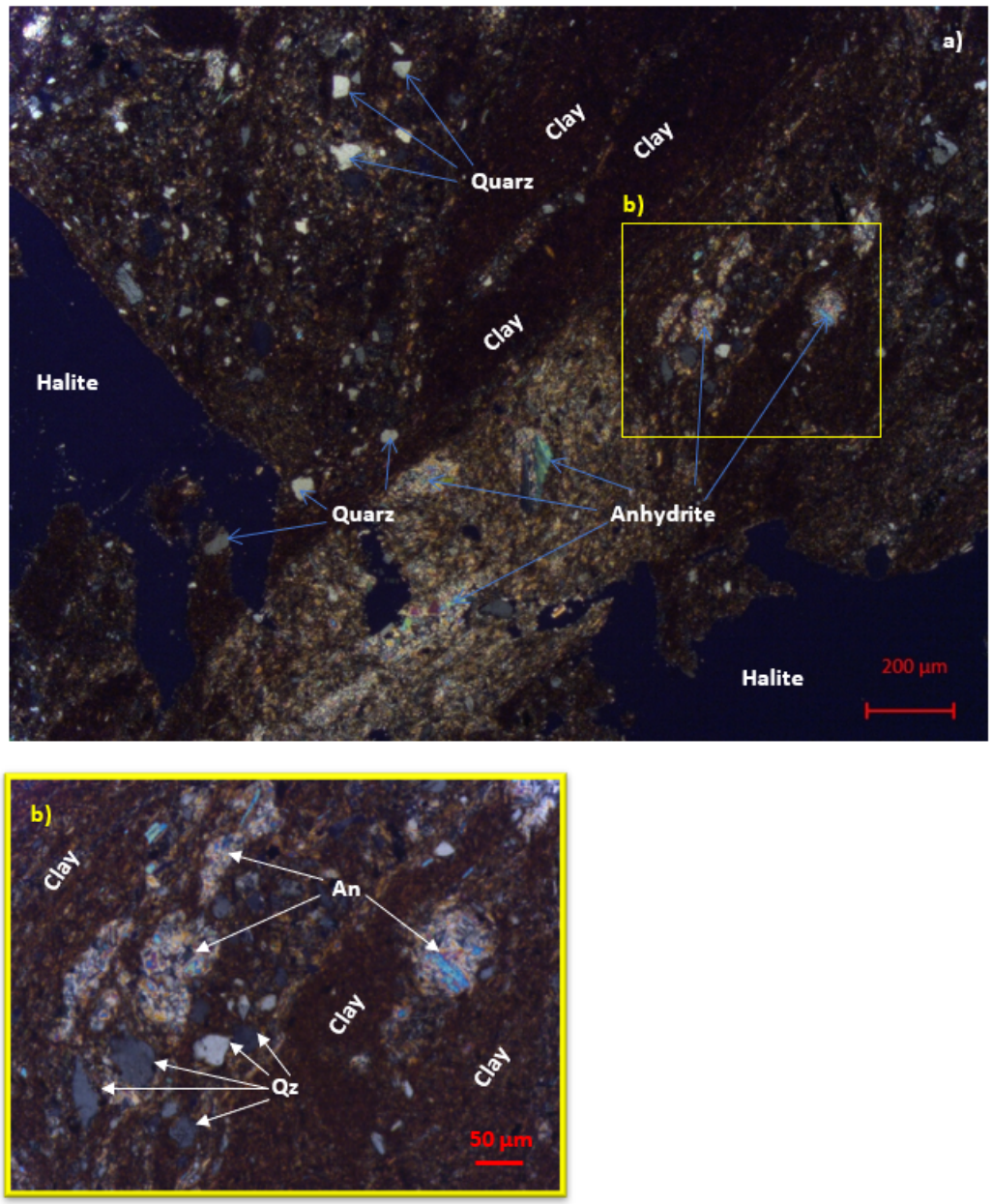

Figure 3.23: *Images from a thin section, Winsford Mine salt rock sample, viewed under polarising microscope. In picture a) under crossed polars in the petrographic microscope, a matrix of clay surrounding the big crystals (0.5-1cm) of halite can be observed. This matrix of clay minerals have 50 µm crystals of quartz and anhydrite conforming aggregates of crystals around 50-100 µm. Picture b) shows a zoomed image from an area in picture a). In this image, the aggregates of anhydrite crystals (An), with crystal sizes between 10- 50 µm are observed. These aggregates show different morphologies: some of them are displayed in circular aggregates with a radial distribution of anhydrite crystals. Other aggregates have elongated morphology. It is difficult to recognise a crystal orientation in the elongated aggregates. Secondly, grains of quartz with sizes between 10 to 50 µm (Qz) can also be seen. All these grains of quartz and anhydrite crystal aggregates are held in a clay matrix.*

Series LB is the last series of samples that were included in the project. Although these samples are coming from the Layer B in Winsford Mine, they

have a completely different texture. The series LB presents a breccia texture due to the proximity to the main fault that structurally limits the extension of Winsford Mine. The core samples were obtained from an horizontal well from the extension works in the level from Layer B in Winsford Mine.

Samples from LB show a smaller cataclastic-breccia grain texture, in comparison to the other series from Winsford Mine, with elongated crystal habit and grain size from 1mm to maximum 1cm. The coloration of halite grains is orange-reddish to dark-brown (Figure 3.24).

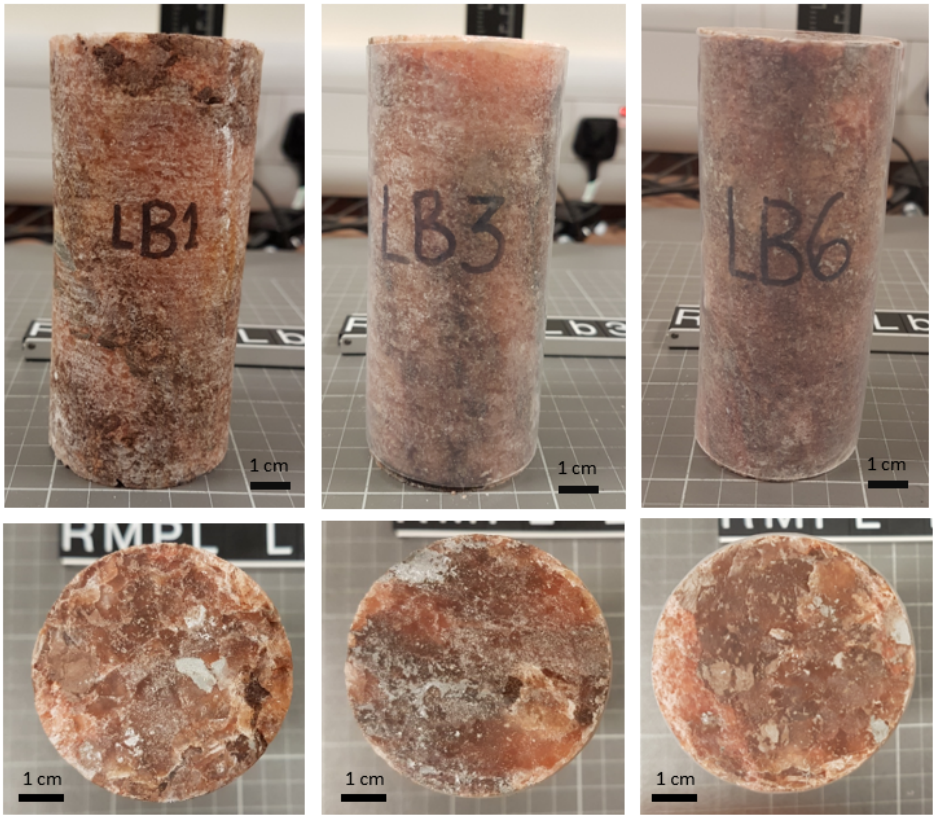

Figure 3.24: *Core samples from a series LB (LB1, LB3, LB6) before cyclic mechanical loading test, Boulby Mine. Core samples show a breccia texture with reddish-brown halite grains, from 1mm to 1cm, supported in a matrix of dark-brown clay.*

The analysis with thin sections shows halite grains of around 800-500 μm to 1cm with a more elongated grain shape in comparison to all other rock salt samples (Figure 3.25). Second phase content is formed by a matrix of clay and micro-crystalline anhydrite aggregates. The second phase content is

mainly located along halite grain boundaries although micro-crystals of anhydrite with shapes of around 10 μm can also be observed in an important quantity enclosed in some halite grains. Signs of plastic deformation and even some previous fractures can be observed tinted by the epoxy blue resin used during the preparation of the thin section. Previous-to-test fractures show two different trends where i) some develop along the halite grain boundary or halite cleavage and ii) other fractures extend through halite grains.

3.3.2 X-Ray Diffraction (XRD) Analysis

The mineralogical results from the PXRD analysis are shown in table 3.1, for samples from Boulby Mine, and in table 3.2, for samples from Winsford Mine. The table shows the average values from the XRD analysis from 4/3 different powder samples that were collected from each sample to calculate the standard deviation in each core sample. The 3 powder samples were collected after cutting the core sample (axially) to make the thin sections, and in some cases, a XRD analysis was also performed previous to the cyclic mechanical test. For this reason the average values where calculated using 4 powder samples instead of only 3 from after the test. However, the table also shows the results for some samples from which no thin section was made, therefore they do not show results in standard deviation because only 1 XRD analysis was performed. However, since I considered these to be valuable data for the compositional analysis, they have also been included.

As explained previously, samples from Boulby Mine were grouped in series A, B and C, based on the petrological description and data from mineralogical analysis, and samples from Winsford Mine were grouped in series WB, LB and F based on the origin rock formation layer from where they were collected in Winsford Mine. Therefore, the mineralogical analysis was performed based both on the mineralogical phase identified in the thin section analysis and also

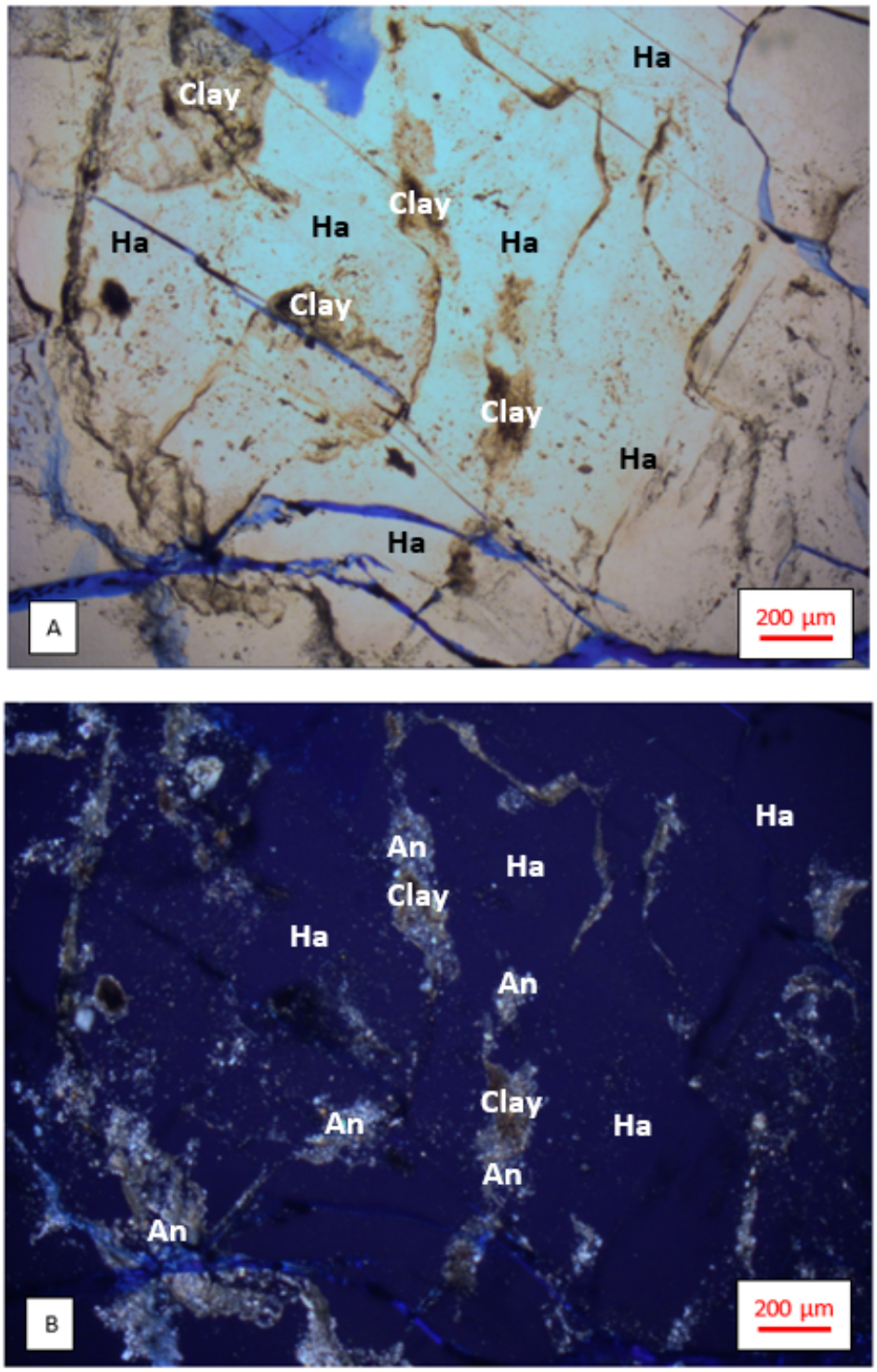

Figure 3.25: *Image from a sample from the series LB before deformation, undre trensmitted light (A) and crossed polars (B), showing strongly elongated grain shape of halite (Ha), with sizes of 800-500 µm, with clay (Clay) and anhydrite (An) as main second phase content around the halite grains in brown-reddish colour. The image also shows previous fractures tinted by the epoxy blue resin used during the preparation of the thin section.*

based on the literature review presented in chapter 2. Due to the insertion of halite and anhydritic-polyhalite rich layering, some samples from Boulby Mine show a higher variation in second phase content.

For samples from Boulby Mine, the main mineralogy analysed from the XRD data were halite, anhydrite, polyhalite, kieserite and carnallite, with anhydrite and polyhalite as the main relevant second phase. Kieserite and carnallite appeared conforming basically the background of the XRD diffraction pattern in very small quantities. All series but series B had a very high content of halite of 75% to 90% on average. However, in samples A8 and A10, from series A, a slight decrease to 51% and 54%, respectively, can be appreciated in table 3.1. The reason of this important decrease in halite content is because, during the multiple sampling collection, one of the powder samples was taken from one of the individual thin layers of anhydrite/polyhalite (with no more than 1cm of thickness) across the sample with a 20° dip as shown also in figure 3.7. Therefore, the standard deviation for those samples is very high for halite, anhydrite and polyhalite with standard deviation values from around 20 to 30%. It is also of relevance that, by checking the XRD data and corresponding standard variation values, the composition of the thin layer from sample A8 was mainly polyhalite whereas the one from A10 was anhydrite.

Samples from series A show an average content of 70% halite, 20% anhydrite and 7% polyhalite, around 3% kieserite and carnallite.

Series B has an average halite content of 45% for all samples and significant variations in the second phase content within the same core sample which is related to a strong anhydrite-halite layering (Figure 3.11). In terms of second phase content, samples from series B prestents up to 30% anhydrite and 15% polyhalite. The percentage by weight has about 30% standard deviation due to the alternating halite and anhydrite thin layers. The PXRD results

for Series B indicate a halite content varying from 10 to 60% within the same sample. Second phase content in Series B samples consist of anhydrite (6 to 30%), polyhalite (3 to 65%), kieserite (1 to 5%) and carnallite (5 to 10%).

Series C show an average of 87-90% of halite, around 7% of anhydrite and less than 3% of polyhalite, kieserite and carnallite on average. Samples from series C are the samples with the lower second phase content from Boulby Mine.

For samples from Winsford Mine, the main mineralogy phases analysed from the XRD data were halite, anhydrite and clay. Quartz was analysed only as part of some peaks in the diffraction pattern background. All samples from Winsford Mine show a high content in halite with average values of 77-90% in halite content. The main second phase content for all series from Winsford Mine are anhydrite and clay with average content of 5-18% and 3-12% respectively. Regarding the standard deviation, all samples show quite stable and low values around 0-7% except for F10, WB4 and WB8 that showed a slightly higher standard deviation (12-25%) in halite and anhydrite.

Table 3.1: Mineralogical characterisation from X-Ray Diffraction analysis for samples from Boulby Mine, sd*= standard deviation

Sample	Halite		Anhydrite		Illite		Quartz		Polyhalite		Kieserite		Carnallite	
	wt%	sd*	wt%	sd	wt%	sd	wt%	sd	wt%	sd	wt%	sd	wt%	sd
A1	80	10.6	14	9	-	-	-	-	2.2	0.8	0.5	0.6	4	2.2
A3	78	6.7	17	8	-	-	-	-	2	0.6	0.5	0.1	3	2
A4	85	6	10	6	-	-	-	-	2	0.4	0.5	0.4	2.5	0.65
A6	81	10	27	17	-	-	-	-	2	0.1	0.25	0.1	3	1
A7	74.5	12	20.5	12	-	-	-	-	2	1	1	0.7	2.47	0.8
A8	51	37	4	3	-	-	-	-	35	32	4	3	5.6	3
A9	74	13	20	14.5	-	-	-	-	2	2	0.5	0.3	3	2
A10	54	24	40	26	-	-	-	-	2	0.2	1	1	4	2.5
B1-2	64	15	10.6	9	-	-	-	-	16	8	2	0.5	8	1
B2-1	34	-	18	-	-	-	-	-	36	-	4	-	8	-
B6	62	18	26	18	-	-	-	-	2.5	1	1	0.2	8	3
B12	20	-	72	-	-	-	-	-	3	-	0.6	-	5.4	-
C1	90	3	6	3.3	-	-	-	-	1.2	0.8	0.4	0.2	2	1
C2	88	2	7	3	-	-	-	-	1.5	0.4	0.4	0.2	3	0.4
C3	87	5	8	4	-	-	-	-	2	1	0.25	0.2	3	1.4

Table 3.2: Mineralogical characterisation from X-Ray Diffraction analysis for samples from Winsford Mine, sd*= standard deviation

Sample	Halite		Anhydrite		Illite		Quartz		Polyhalite		Kieserite		Carnallite	
	wt%	sd*	wt%	sd	wt%	sd	wt%	sd	wt%	sd	wt%	sd	wt%	sd
F	89	3	7	3	4.5	0.6	0.2	0.2	-	-	-	-	-	-
F1	89	4.6	6	3.6	4	1	0.4	0.3	-	-	-	-	-	-
F3	89	6.4	7.3	5	2.7	1	0.6	0.35	-	-	-	-	-	-
F4	88	7	7.3	6.4	4.4	0.2	0.4	0.6	-	-	-	-	-	-
F5	89	2.5	6	2	4.2	0.3	1	1	-	-	-	-	-	-
F8	88	7.5	8.3	6.6	3	0.5	0.5	0.3	-	-	-	-	-	-
F9	91	3.8	4.5	2.6	4	0.5	1	0.7	-	-	-	-	-	-
F10	64	25	10	3.7	4.4	0.7	0.5	0.2	-	-	-	-	-	-
F11	77	-	16	-	6	-	1	-	-	-	-	-	-	-
LB	90	2	5	1	5	1.3	0.1	0.1	-	-	-	-	-	-
LB1	86	3.2	8	4	4.5	0.3	1.3	0.3	-	-	-	-	-	-
LB1	86	3.2	8	4	4.5	0.3	1.3	0.3	-	-	-	-	-	-
LB4	85	8	5	1.5	10.4	9	0.3	0.2	-	-	-	-	-	-
LB5	91	3	5.3	3	4.1	0.6	0.1	0.0	-	-	-	-	-	-
LB6	89	3	6.5	3	4.3	0.1	0.4	0.4	-	-	-	-	-	-
WB	85	6	7.57	3.51	4.6	0.6	2.7	2.5	-	-	-	-	-	-
WB1	88	1.1	5.5	1.6	5	1	1.4	0.7	-	-	-	-	-	-
WB3	87	1.7	9	1.8	3.8	0.4	0.3	0.3	-	-	-	-	-	-
WB4	78	13	18	14	3.87	1	0.3	0.2	-	-	-	-	-	-
WB5	89	2.4	7	2.2	3.7	0.06	0.3	0.3	-	-	-	-	-	-
WB8	79	12.3	16	11.5	3.6	0.4	1.07	1	-	-	-	-	-	-
WB9	81.5	-	6	-	12.8	-	0.1	-	-	-	-	-	-	-
WB16	85.5	6	9	5.2	4.4	0.2	1.3	1	-	-	-	-	-	-
WB18	89.6	2	5.4	1.8	4.2	0.4	0.7	0.4	-	-	-	-	-	-

3.4 Summary and discussions

3.4.1 Second phase content

The main second phase content analysed in all rock salt samples is anhydrite. However, other second mineralogy have been also described based on the origin of the different samples. For samples from Boulby mine, polyhalite and, in lower quantity, kieserite and carnallite have also been identified. For samples from Winsford Mine, other second phase identified is clay, which is observed in the thin sections as a matrix supporting anhydrite and some small crystals of quartz. The anhydrite is observed in sizes from micro-crystalline to grains of 50 μm in samples from Boulby Mine and as spherical aggregates in samples from Winsford Mine. Polyhalite is observed as prismatic crystals that can be observed poikilotopically enclosing finer crystals of anhydrite in samples from Boulby Mine.

From Boulby Mine, series A and C shows the highest halite content, with a halite content of around 75-85% (excluding A8 and A10 which show high standard deviation from halite) and 87-90%, respectively. Series B is the series of samples with a higher second phase content with a content in halite around 30-60%, and content of anhydrite and polyhalite of 10-30% and 15-30% respectively. Series B can also presents up to 10% of kieserite and carnallite.

All Series (F, WB and LB) from Winsford Mine present a halite content of 75-90% and 5-20% of anhydrite and up to 10% of clay.

3.4.2 Thin section analysis before deformation

In general, only samples from Boulby Mine, presenting a strong alternation of layers with halite and anhydrite/polyhalite, have higher values of standard

deviation. Therefore, samples from Winsford Mine, without a clear layering arrengement, present a lower standard deviation in comparison to samples from series B.

All samples present a nonclastic and crystalline texture excepting series LB from Winsford Mine which has a breccia texture. In general, except series LB, all series of rocks presents noneclastic/crystalline texture with halite grains sizes from 0.5mm to maximum 1.5/2cm. In regards to the internal structure of rock salt samples, pressure solution and also diffusion creep can be observed. Some samples also show anhedral and also slightly elongated halite grains which manifests that samples have been naturally exposed to deformation. However, no important fracturing is observed excepting for samples from series LB, from Winsford Mine, and series B, from Boulby Mine. Samples from series B presents some small fractures with no connectivity located only in the layers of anhydrite. However, samples from series LB, which have a breccia texture, presents a more important number of fractures with higher connectivity. These fractures can develop along grain boundary but also across halite grains. It is important to emphasise that these fractures or joints can have direct implication in physical properties of final strain during the cyclic loading tests.

Samples from Series LB are the only samples with a breccia texture. All other series present a polycrystalline rock salt texture.

3.4.3 Limitations

Up to 3 different powder samples were taken in the majority of rock salt samples in order to have a better estimation of each sample heterogeneity. The standard deviation, combined with a description of how the different miner-

alogy is arranged within core samples (around grain boundary, in layers alternating different mineralogy...), helps to have a better picture of the real mineralogical composition of each sample and their heterogeneity. However, regarding a better determination of sample heterogeneity, it was not possible to get different powder sampling along the core specimen (before the deformation test) due to the destructive nature of this technique. Before the thin sections were made, after the cyclic loading tests, the XRD analysis to group the different samples in series were performed from discarded bits (the cut-off parts) from the core sample preparation process. One XRD analysis was performed for core sample and from discarded parts of the core that never were tested. Unfortunately, althought the first XRD analysis to group samples were originally from a part of the core sample, the previous analysis was not representative enough due to the natural heterogeneity of the samples. For this reason, although the previous to mechanical deformation mineralogical description was performed combining different techniques, after being able to get additional samples for XRD analysis I realised some core samples could have been tested in a different group.

Chapter 4

Rheological behaviour of rock salt under cyclic loading: impact of second phase content

4.1 Introduction

After assessing a mineralogy and texture description of each sample, and assembling them into a different group of samples, a series of cyclic mechanical condition tests were performed. The aim of this chapter is to analyse the results of rheological behaviour from different rock samples tested under similar cyclic mechanical conditions applied to Underground Gas Storage. The analysis of the results will provide information to discuss the impact of different second phase content and texture over the physical properties of rock salt.

A total of 51 cylindrical core samples, with a diameter of 51 mm and length between a minimum of 100 mm and a maximum of 120 mm, were tested under cyclic mechanical loading. Two different amplitudes for cyclic mechanical loading conditions have been investigated. A first set of cyclic mechanical tests was performed with cyclic axial pressures between 4.5 and 6.5 MPa, related to cyclic conditions in salt caverns used for CAES. A second set of cyclic me-

chanical tests was performed with cyclic axial pressures between 6-20MPa, in relation to salt caverns subjected to cyclic conditions when storing hydrogen (H_2) and natural gas (CH_4).

The cyclic mechanical loading tests were undertaken on a triaxial servo-controlled stiff frame (MTS 815 rock test system with a maximum axial load up to 4600 kN) using a cyclic loading rate of 0.5kN/s for a maximum of 48h. The samples were tested at different confining pressures and temperatures. It is important to recall that the cyclic mechanical tests performed had a maximum duration of 48h with a big number of cycles within this amount of time. In comparison, salt caverns are subjected to fewer cycles within longer periods of time. However, the main aim was to study the effect of cyclic loading conditions in rock salt with different second phase content under a worst-case scenario of cyclic mechanical conditions.

Mechanical data, such as axial and lateral strain, and elastic parameters such as Young's modulus, Poisson's ratio and bulk modulus are described and compared between samples tested under different conditions of confining pressure and temperature.

The results of mechanical data in this chapter is displayed and described from a compositional perspective. The data is plotted alongside with samples with different second phase content and rock texture to provide an insight of the impact of those chemical and physical changes over rheological behaviour of rock salt.

4.2 Methodology

4.2.1 Defining the thermo-mechanical conditions of testing

Solution-mined salt caverns are subjected to pressure and temperature fluctuation linked to gas injection and withdrawal periods. As the main aim of the project was the analysis of rheological behaviour of salt rock under cyclic thermo-mechanical conditions for Hydrogen (H_2), Natural Gas (CH_4) and CAES, cyclic mechanical loading tests have been designed based on three different scenarios, considering the depth reported in literature at which salt caverns can be found, and operational pressure conditions based on the usage of salt caverns also reported in the literature. Operational pressures in salt caverns vary depending on the operational scheme of the storing activity (if it for CAES, UGS or Underground Hydrogen Storage) and depth of storage site (see Table 2.1). For instance, according to Kruck et al. (2013), for a salt cavern located a 1000m depth, the operational pressure can be between 6.5 MPa and 18 MPa. In another example, the salt caverns for 3 hydrogen storage sites in Teeside, UK, operate between 7 and 21 MPa (Djizanne, 2014).

Salt caverns are generally located at depths between 500 m and 2000 m below the surface (Kruck et al., 2013; Ma et al., 2013; Djizanne, 2014), thus here in this study, the confining pressures (Pc) and temperatures (T) conditions were setup between 12 MPa and 45 MPa, and room temperature and 75°C to correspond to:

- 200-500 m depth, for shallow salt caverns depth scenario,
- 500-800 m depth, for medium depth-based scenario,
- 800- 1200 m depth, for deep depth-based scenario.

The temperatures that tested in the thermo-mechanical loading tests were

25 (room temperature) and 55°C for shallow conditions, 25, 55 and 75°C for average depth conditions, and 55 and 75°C for deep conditions. This representation of temperatures was decided based on the representativity of the average depth operational conditions in salt caverns and the extreme depth scenarios (shallow and deep conditions).

Table 4.1: Confining Pressure (Pc) and temperature (T) conditions for the different testing scenarios for cyclic mechanical loading tests

Case scenario	Pc	T
200-500m depth	12MPa	25°C 55°C
500-800m depth	25MPa	25°C 55°C 75°C
800-1200m depth	45MPa	55°C 75°C

In order to have a better understanding of rock salt deformation behaviour under pressure fluctuations, previous studies have investigated the behaviour of rock salt under cyclic mechanical loading (Liang et al., 2012; Ma et al., 2013; Khaledi et al., 2016a) and cyclic thermo-mechanical loading conditions (Serbin et al., 2015; Blumenthal et al., 2016). According to literature, the confining pressures used in salt rock testing related to UGS activity are ranging from 7 MPa to 25-45 MPa maximum (Ma et al., 2013).

After considering these available data and information, two different cyclic loading conditions were designed. A first set of cyclic mechanical tests was performed with cyclic axial pressures between 4.5 and 7.5 MPa, related to cyclic conditions in salt caverns used for CAES (Table 4.2). A second set of cyclic mechanical tests was performed with cyclic axial pressures between 6-20MPa (Table 4.3), in relation to salt caverns subjected to cyclic conditions when storing hydrogen (H_2) and natural gas (CH_4). In the first set of cyclic loading tests, a total of 17 samples from Boulby Mine and 20 samples from

Winsford Mine were tested. The first set of cyclic thermo-mechanical loading tests were performed with a cyclic axial stress between 4.5 and 7.5 MPa with a loading rate of 0.5 kN/s for a maximum period of 24h, giving a maximum number of 7200 cycles per test (Table 4.2).

The exact testing conditions with respect to the corresponding confining pressures and temperatures calculated at each depth scenario are tabulated in Table 4.1.

Table 4.2: Core samples from Boulby and Winsford Mine tested under cyclic axial stress between 4.5 and 7.5 MPa at a loading rate of 0.5 kN/s for a duration of 24h and a maximum number of 7200 cycles at different temperature (T) and confining pressure (Pc) conditions linked to each salt cavern depth case scenario tested. *Room temperature oscillated between 21-22°C

Pc	12 MPa		25 MPa			45 MPa	
T	21°C*	55°C	21°C*	55°C	75°C	55°C	75°C
A	A4	A14	A3	A7.1	A6	-	A5
B	B1.2	-	B8	B6	B2.1	B12	-
C	C4	-	C3	C5	C2	C6	C1
F	F1	F2	F3	F4	F5	F6	F7
LB	LB1	LB3	LB4	LB5	LB6	LB7	LB2
WB	WB18	WB14	WB16	WB1	WB8	WB9	-

The second set of experiments were performed at a cyclic axial stress of 6-20 MPa, keeping the same loading rate of 0.5 kN/s during a maximum of 48h, giving a total number of 1500 cycles. In the second set of experiments with a cyclic axial stress between 6 and 20 MPa, only the middle depth and deep depth case scenarios were tested (Table 4.3). The reason for misestimating the shallow depth case scenario was that by testing samples at a loading stress range between 6 and 20 MPa at a low confining pressure of 12 MPa, the sample would have been brought to tension state increasing the probability of damage under non- compression and that would have originated a completely new mechanical context to analyse. For this reason, only mechanical analysis under compression state was considered and the shallow depth case scenario was removed from the second set of experiments.

Table 4.3: Core samples from Boulby and Winsford Mine tested under cyclic axial stress between 6 and 20 MPa at a loading rate of 0.5 kN/s for a duration of 24h and a maximum number of 1500 cycles at different temperature (T) and confining pressure (Pc) conditions linked to middle and deep depth case scenario tested.
*Room temperature oscillated between 21-22°C

Pc	25 MPa			45 MPa	
T	21°C*	55°C	75°C	55°C	75°C
A	A10	A1	A9	A8	A15
F	F8	F9	F10	F11	-
WB	WB3	WB4	WB5	WB6	WB7

The core samples used for the cyclic mechanical loading tests were cylindrical cores with a diameter of 51 mm and length between a minimum of 100 mm and a maximum of 120 mm. So, the force used in the cyclic loading test was between 9 and 15 kN that, over a cylindrical surface of 51 mm diameter, gave a cyclic axial stress ($\sigma 1$) between 4.5 and 7.5 MPa. With a loading rate of 0.5 kN/s and a maximum of 48h per test, the cyclic loading tests between 4.5 and 7.5 MPa gave a maximum number of 7200 cycles per test (Figure 4.1). In the second set of experiments with a larger range cyclic axial stress, the force applied over the cylindrical 51 mm diameter surface oscillated between 12 and 41 kN giving a cyclic axial stress between 6 and 20 MPa with a maximum of 1500 cycles in 48 h.

4.2.2 Core sample preparation

Tested samples were Permian and Triassic salt rock originally from Boulby Mine (Permian salt rock) and Winsford Mine (Triassic salt rock), as described in the previous chapter. While Boulby Mine had available cylindrical borehole cores for this study, Winsford Mine could only provide a few borehole cores so rock salt blocks of 0.5m x 0.5m x 0.5m approximately were also collected.

Boreholes cores from Boulby Mine were 50 mm diameter with different lengths between 5 cm and 250 cm. Thus all the core samples not meeting the minimum requirement of length-to-diameter ratio of 2:1 (Jaeger et al., 2007) (to

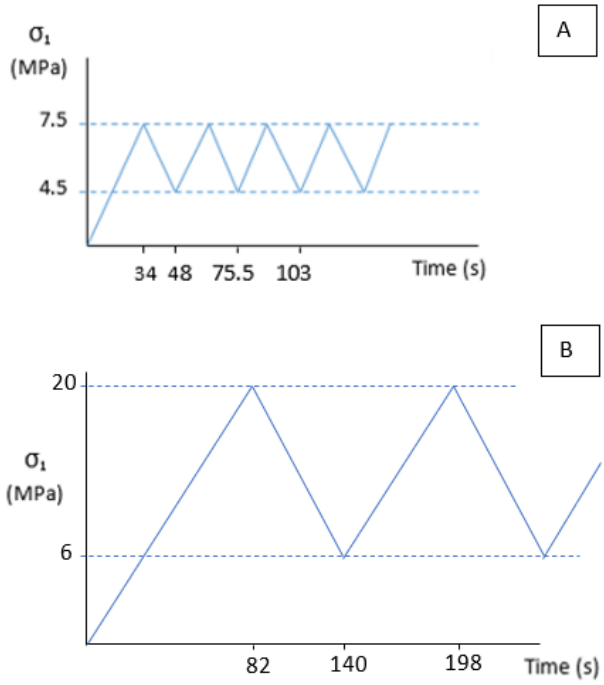

Figure 4.1: *Schematic picture of the cycles in time (s) for the cyclic mechanical tests between 4.5 and 7.5 MPa (A) and between 6 and 20 MPa (B) at a loading rate of 0.5kN/s for a maximum of 48h each test.*

be mechanically tested) were only used for mineralogical analysis. It resulted in a more limited amount of sample material available for testing. Each viable core was cut and trimmed appropriately to produce the samples whilst ensuring the perpendicularity and flatness required for triaxial testing, as per the International Society for Rock Mechanics recommendations (ISRM 1975-2007).

Winsford Mine provided a very limited number of 50 mm diameter core samples, 13 core samples in total, originally from a borehole performed during mining planning operations on the site. The peculiarity of those sample is that the borehole was performed to find one of the main tectonic faults that limits the mine production area. Therefore, the samples provided from this borehole had a tectonic/fault breccia texture giving the opportunity to test different textures of salt rock under cyclic thermo-mechanical conditions. Due to the fragility of the core samples however, only 8 samples were finally prepared for testing. The rest of Winsford Mine samples were produced from

the blocks that had to be cut, lathed, and trimmed to obtained the 50 mm diameter right cylinders required for triaxial tests.

A diamond tipped abrasive wheel (as shown in (Figure 4.2) was used to cut and trim the ends of each sample to the best flatness and perpendicularity practical, given the inherent fragility (large crystals are prone to chip). No lubricant was used to reduce the likelihood of the sample deteriorating if in contact with cooling water. Prior to the cutting, each core was wrapped in a heat-shrinked jacket to further reduce any contact with ambient moisture and inhibit chipping at the edges during the preparation. A re-purposed lathe machine was used for shaping the prismatic cut block into a cylindrical geometry (Figure 4.3A). Finally, each sample was controlled to meet the minimum length-to-diameter ratio of 2:1 as recommended by the International Society for Rock Mechanics (ISRM), and to ensure the flatness and smoothness of the bases required for straight samples (Figure 4.4). A total of 51 right cylindrical samples was produced. The leftovers from cutting the sample edges were used for XRD analysis and thin sections to provide mineralogical analysis and texture description before testing.

4.2.3 Sample assembly and triaxial experiments

Each cylindrical sample was mounted between two hardened steel platens prepared with a layer of heat resistant silicone tape for sealing purpose. The assembly was then encased in two 5 mm heat-shrink Polytetrafluoroethylene (PTFE) membranes to prevent ingress of confining fluid into the sample. Locking wires were used to complete the seal between the PTFE jacket and the platens (Figure 4.5B). The sample was then instrumented with two axial extensometers (MTS 632.90F-12, accurate to $\pm 0.01\%$), positioned diametrically opposite each other over the central 50 mm of the sample, and a circumferential

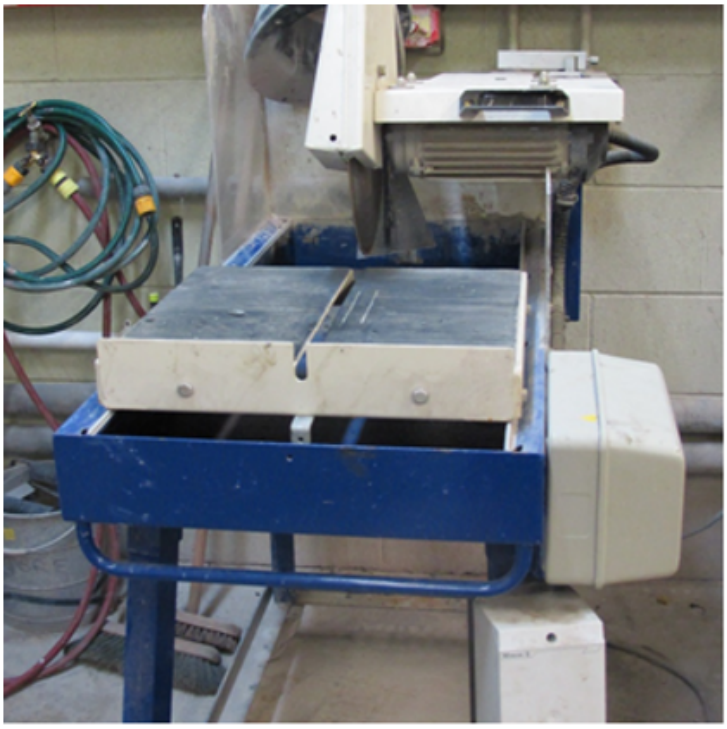

Figure 4.2: *Diamond tipped abrasive wheel machine for cutting core sample under mechanical test requirements. Rock preparation laboratory at the British Geological Survey.*

chain extensometer (MTS 632.92H-03, accurate to ±0.01%) positioned at mid-length. A third platen, not part of the aforementioned sample assembly, was spherically seated to prevent eccentric loading. This spherically seated platen was in turn fixed to a 2.6 MN capacity force transducer (MTS 661.98B.01, accurate to ±0.32% of load) to measure the load applied to the sample.

The cyclic mechanical loading tests were undertaken on a triaxial servo-controlled stiff frame (MTS 815 rock test system with a maximum axial load up to 4600 kN) with a confining pressure vessel rated to 140 MPa, at the Rock Mechanics and Physics Laboratory, British Geological Survey (BGS). A thermocouple was placed as close as possible to the sample to monitor the temperature. The confining pressure vessel was then closed and an initial axial load of $\sigma_1 = 1$ kN was applied to ensure a stable contact and alignment of the platens whilst the vessel was filled with mineral oil confining fluid.

For the tests done at room temperature between 22°-25°C and moisture condi-

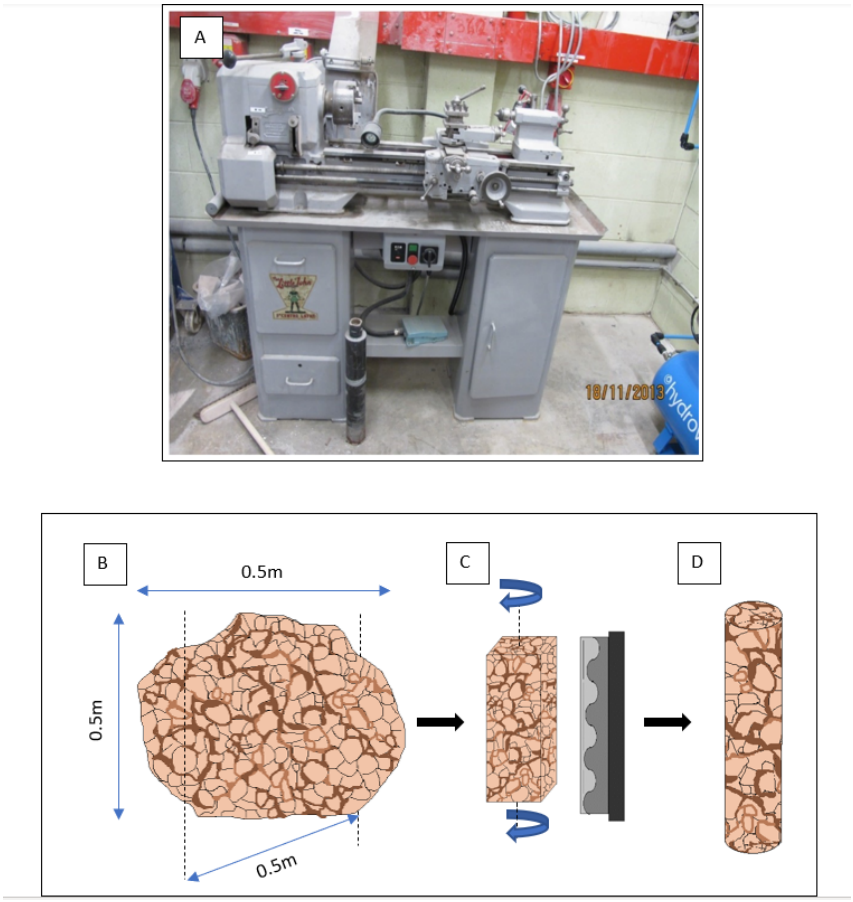

Figure 4.3: *Cutting machine for creating cylindrical core samples from the initial square prismatic shapes from salt rock blocks collected at Winsford Mine (A). Below, a schematic picture shows the process from the salt rock block (B) to the initial square Prisma (C) introduced in the cutting machine for creating the final 50 mm diameter cylindrical core sample to be tested (D).*

Figure 4.4: *Picture of a salt rock core sample being evaluated for cyclic mechanical test. All samples were previous- to- test checked to be as straight as possible in the perpendicular from the horizontal.*

tions, the confining pressure ($P_c = \sigma_2 = \sigma_3$) was then applied hydrostatically at 1 MPa/min to the desired value for each test. Once reached, the sample was subjected to the cyclic loading as indicated in Section 4.2.1 and further detailed hereafter.

For the tests performed at elevated temperature, a small initial P_c of 0.5 MPa was first applied whilst an axial differential pre-load of 1 MPa was maintained. Then, the temperature was increased at a rate of 1°C/min to the targeted value (55° or 75°C here), ensuring the sample was not thermally shocked and a low gradient of temperature across the sample. Note that the confining pressure intensifier had to be reprimed manually during heating as a result of the thermal expansion of the confining oil. Moreover, due to this oil expansion and thermal conductivity, an average of 10 minutes were given to allow all parameters recorded by the extensometers to settle before starting the cyclic mechanical test.

Two different ranges of cyclic mechanical loading were tested. First, 37 samples with different second phase content were tested under a cyclic axial stress between 4.5 and 7.5 MPa, with a loading rate of 0.5kN/s, for a period of 48h that corresponds to a total number of 7200 cycles. Secondly, 14 extra samples were tested under a cyclic axial stress between 6 and 20 MPa, with a loading rate of 0.5kN/s, for a period of 48h that corresponds to a total number of 1500 cycles.

The axial load, axial load actuator displacement, axial stress (σ_1), differential stress ($Q = \sigma_1 - \sigma_3$), confining pressure P_c, confining pressure actuator displacement, axial strain (ε_{ax}), circumferential strain (ε_{circ}) and temperature were monitored throughout the test at sampling frequencies of 5s and 2.5kN.

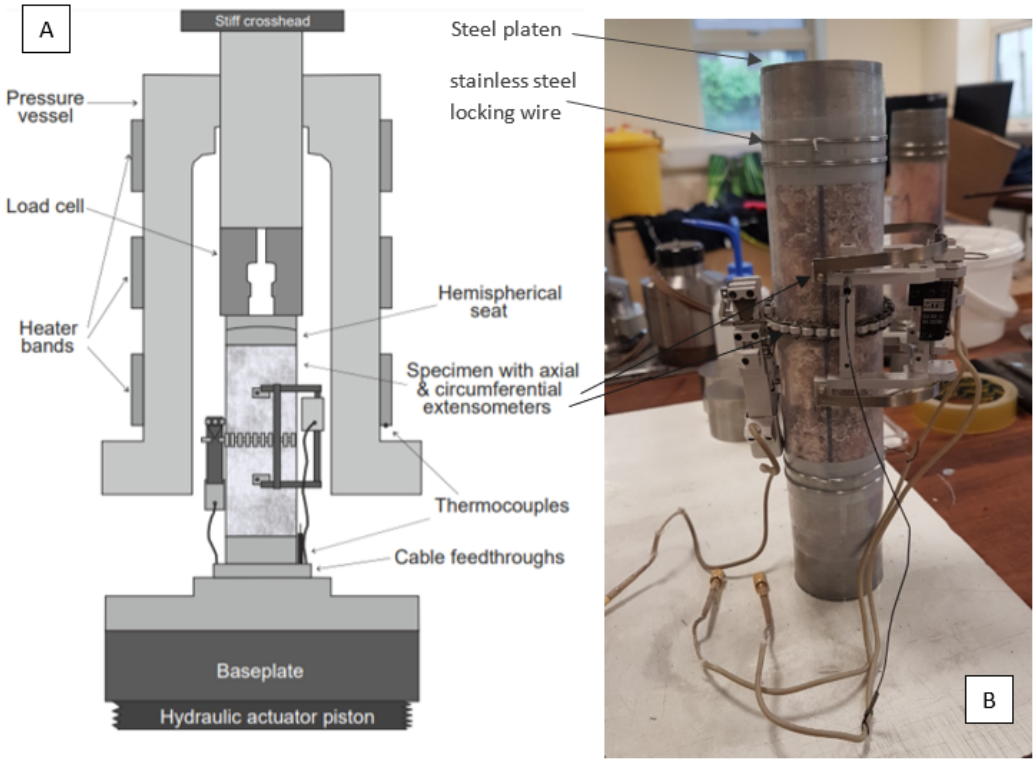

Figure 4.5: *A) Schematic picture of MTS apparatus used for the cyclic mechanical loading tests (Woodman, 2020). B) Image from a salt rock core sample prepared for mechanical testing.*

4.3 Experimental results

4.3.1 Cyclic loading tests between 4.5 and 7.5 MPa

A total of 37 samples from both Boulby and Winsford Mine were tested at an axial cyclic mechanical conditions between 4.5 and 7.5 MPa at a loading rate of 0.5kN/s for 48h (Table 4.2). These cyclic loading conditions were tested at different confining pressures and temperatures corresponding to depth scenarios explained in section 4.2.1 and table 4.1. The tested confining pressures and temperatures were kept constant during the whole cyclic loading mechanical experiment.

4.3.1.1 Tests conducted at 12 MPa confining pressure and temperatures of 25 and 55°C.

A maximum of 10 samples were tested under cyclic loading conditions at 12 MPa of confining pressure: all series of samples were tested at room temperature (21-22°C), however, due to a sample shortness from series B and C (from Boulby Mine) only Series A, F, LB and WB were tested at 55°C (Table 4.4). Figure 4.6 and figure 4.7 show the results of stress-strain for the aforementioned samples. Both figures show the values for the final axial strain (ε_{ax}). Maximum final axial strain, recorded at the last highest axial stress (σ_1) applied of 7.5MPa, and the minimum final axial strain, recorded at the minimum axial stress applied of 4.5MPa within the last loading mechanical cycle of the cyclic mechanical loading test.

Looking first at the results from Boulby Mine samples (with anhydrite and polhyhalite as main second phase content), sample B1-2 is the sample showing the highest final strain with a maximum final ε_{ax} =0.28% and a minimum final ε_{ax} =0.25%. Sample A4 is the sample with the second highest final strain recorded, tested under the same conditions, with a maximum and minimum final ε_{ax} of 0.18% and 0.16%, respectively. Sample C4, from series C, is the sample showing the lowest final strain with values of 0.11% (max. ε_{ax}) and 0.09% (min. ε_{ax}). Due to a lack of samples, only sample A14 from series A was tested at 12MPa and 55°C. Although sample A14 was tested at a higher temperature, 55°C, the final ε_{ax} recorded for A14 was 0.16% (max)-0.14% (min) which is very similar to the final ε_{ax} recorded from sample A4 (0.18%-0.16%) tested at a lower temperature.

Samples from Series LB (LB1 and LB3) from Winsford Mine (with anhydrite and clay as second phase content), show the highest final strain from all core samples (both from Boulby and Winsford Mine) tested at 12MPa (Figure

Table 4.4: Core samples from Boulby and Winsford Mine tested under cyclic axial stress between 4.5 and 7.5 MPa at a loading rate of 0.5 kN/s for a duration of 24h and a maximum number of 7200 cycles at a confining pressure (Pc) of 12MPa and 21-22° and 55°C temperature (T).
*Mean room temperature oscillated between 21-22°C

Temperature (T)	21°C*	55°C
Boulby - Series A	A4	A14
Boulby - Series B	B1.2	-
Boulby - Series C	C4	-
Winsford - Series F	F1	F2
Winsford - Series LB	LB1	LB3
Winsford - Series WB	WB18	WB14

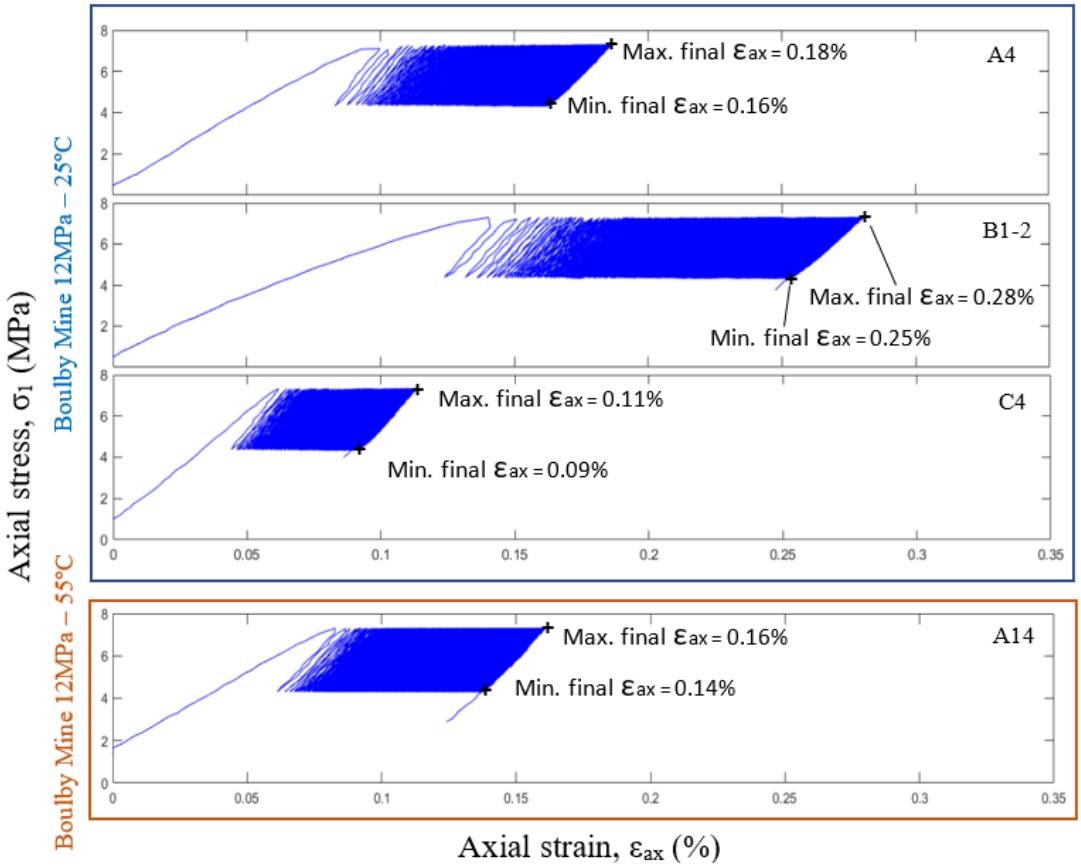

Figure 4.6: *Stress-strain curve for samples tested at 12MPa and 21-22° C and 55° C from Boulby Mine. Cyclic stress between 4.5-6.5 MPa at a loading rate of 0.5kN/s during 48h. The maximum number of cycles is 7200. It can be observed how sample from series B, with a higher content of anhydrite and polyhalite, shows records a larger strain only is the first cycle in comprison to samples from series A and C.*

4.7). LB3, tested at 55°C and 12MPa, has the highest registered maximum ε_{ax} (0.51%) and a minimum ε_{ax} (0.48%). LB1, the equivalent sample to LB3 but tested at room temperature, has the second highest recorded ε_{ax} with 0.42% and 0.40% as maximum and minimum final ε_{ax} respectively.

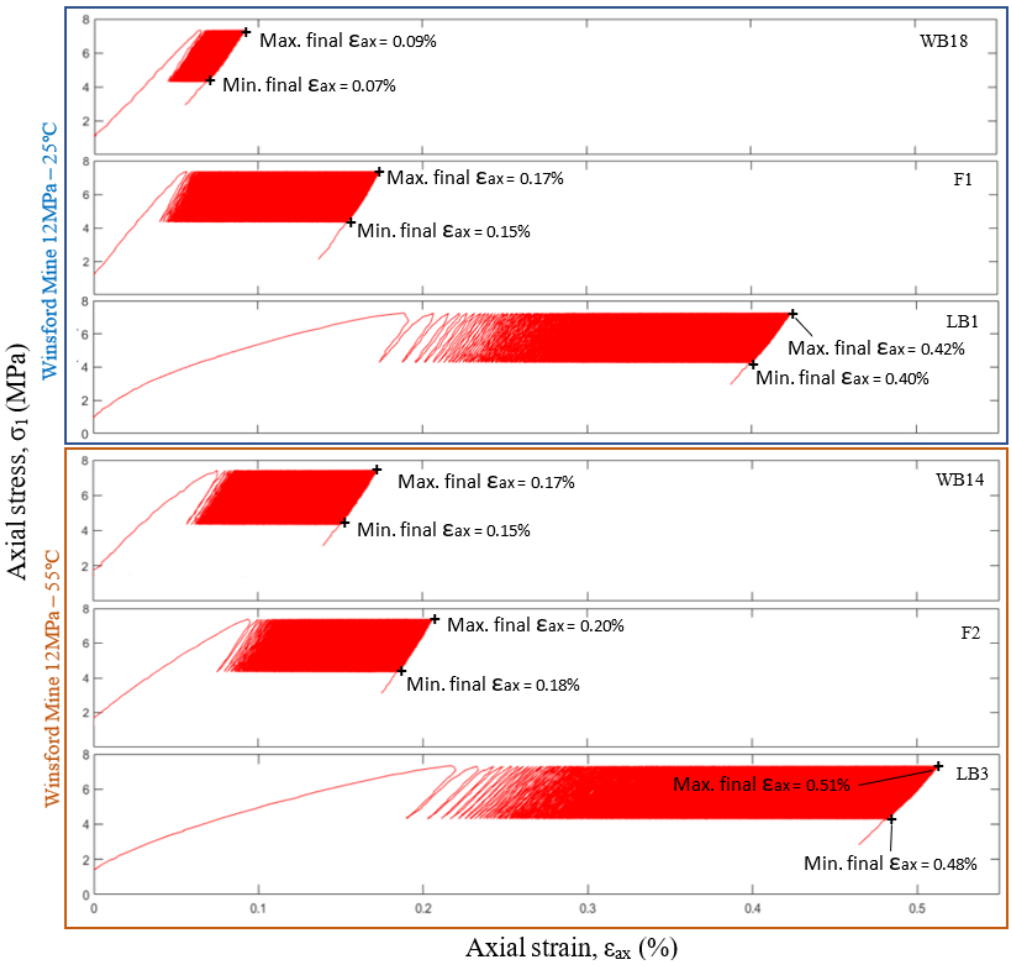

Figure 4.7: *Stress-strain curve for samples tested at 12MPa and 25° C and 55° C from Winsford Mine. Cyclic stress between 4.5-6.5 MPa at a loading rate of 0.5kN/s during 48h. The maximum number of cycles is 7200. It can be observed how samples from series LB, with breccia texture, records a larger strain first only during the first mechanical load and also by the end of the whole cyclic mechanical test.*

A close analysis of the deformation pathway reveals hysteresis in the stress-strain data. Indeed, the stress-strain plot for each cycle forms a loop so that the ε_{ax} during loading is different from the ε_{ax} during unloading at the same applied stress; this hysteresis further varies as the number of cycles increases and the mineralogical difference of the samples is greater (Figures 4.17, 4.10

and 4.11). The fact that every cycle forms a separated hysteresis loop indicates that deformation along the different loading and unloading episodes has both an elastic and inelastic (irreversible) component.

Both samples A4 and B1-2 show a positive increase of ε_{ax} per cycle whereas data from C4 records a positive increase in ε_{ax} until cycle number 1500 (yellow loop) and then it shows a strain recovery (a negative increase in ε_{ax}). Strain hardening can be observed in all samples, with a decrease in distance from one loop to another, being especially notable in both samples A4 and C4 around cycles 1500-2500. Sample B1-2 does not show any negative increase of ε_{ax} during the whole test. Both samples A4 and C4 show also a reduction in the loop shape (a closure of the shape loop is observed) evidencing an increase of elastic recovery during deformation.

Sample A14 (Figure 4.9), tested at 55°C, shows a clear increase of elastic deformation per cycle reflected in a reduction in shape of all hysteresis loops in comparison with samples tested at lower temperature (room temperature). Although a increase of elastic component can be noticed, A14 presents very similar stiffness as A4. Strain hardening can be noticed from cycle 2500 although smoother than the stain hardening observed in samples A4 and C4.

Sample WB18 is the one with the lowest maximum ε_{ax} =0.09% and minimum ε_{ax} =0.07%. Sample F1 (tested at room temperature) presents maximum ε_{ax} =0.17% and minimum ε_{ax} =0.15% and F2 (tested at 55°C) has maximum ε_{ax} =0.20% and minimum ε_{ax} =0.18%. A clear tendency to ε_{ax} increase with an increase of testing temperature can be observed here for all samples. However, although all samples record an increase in ε_{ax} with the increase of temperature, series WB shows the highest increase (with an increase by 200% from strain recorded at 12MPa) evidencing a higher sensitivity to changes in temperature. This drastic increase observed in series WB can be also no-

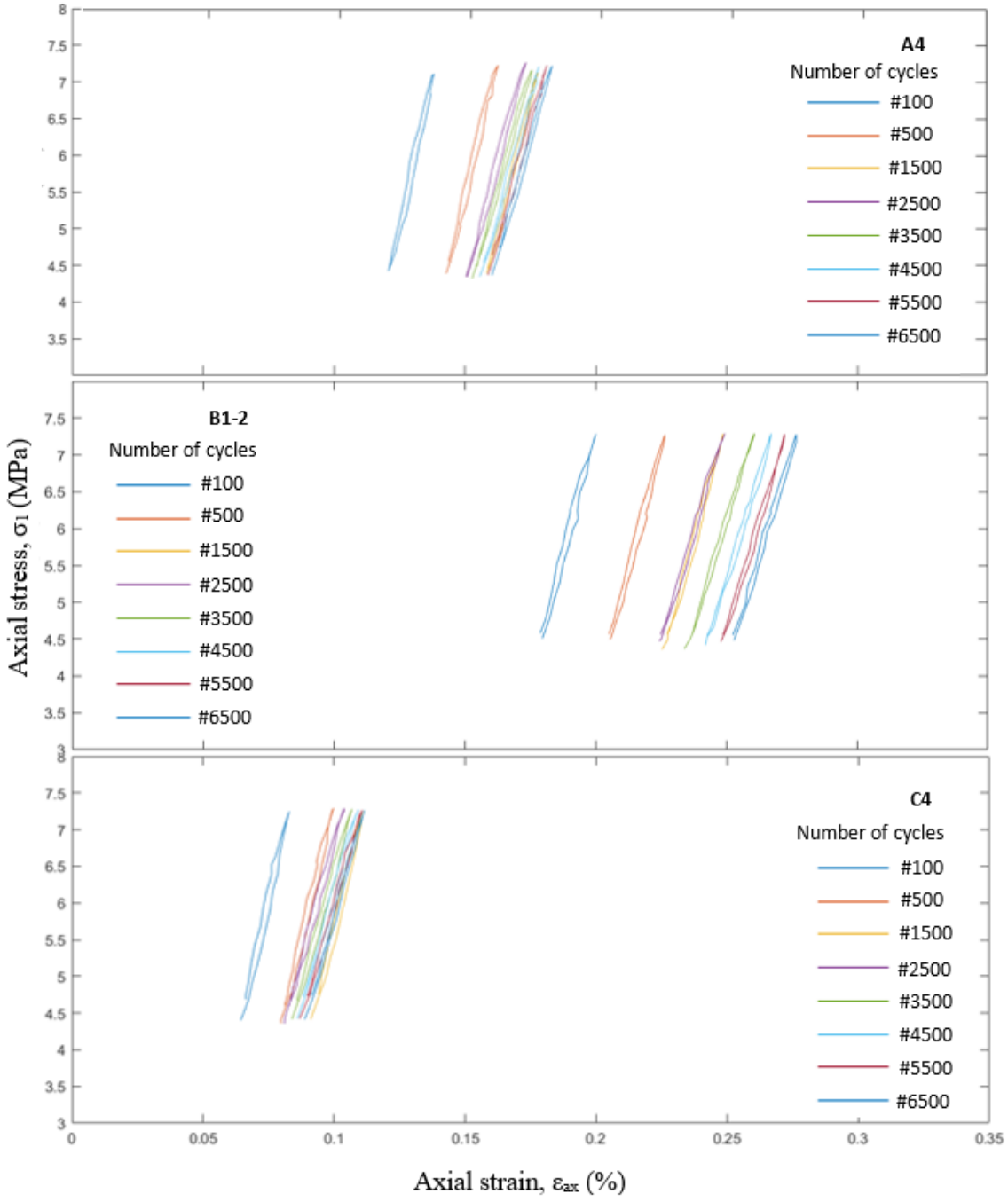

Figure 4.8: *Hysteresis loops of stress-strain for samples from Boulby Mine tested at 12 MPa and room temperature. The hysteresis loops show the stress-strain recorded by individual cyclic mechanical load. In this figure, the hysteresis loops reveal that the larger amount of strain is recorded within the first 500 cycles for samples from series A and C, with a lower second phase content, and within the first 1500 cycles for samples from series B, with a higher content in anhydrite and polyhalite.*

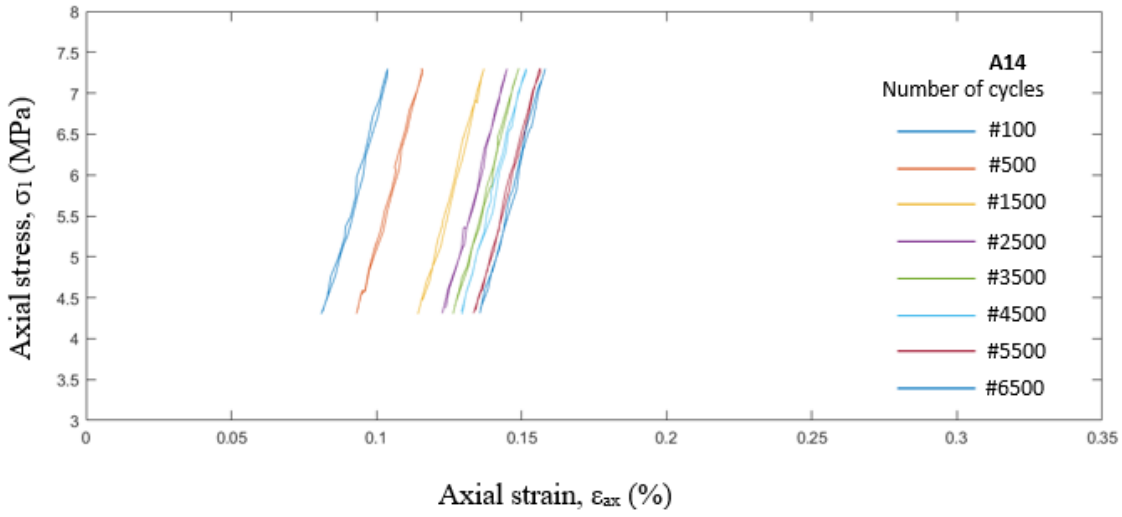

Figure 4.9: *Hysteresis loops of stress-strain for sample A14 from Boulby Mine tested at 12 MPa and 55°C. In this figure, a closure of the loop's shape can be observed related to an increase in the testing temperature.*

ticed in both figures 4.10 and 4.11. The hysteresis loops for different cycles at room temperature (WB18) appear very close almost overlying one another. In contrast, sample WB14 shows more distanced hysteresis loops. While WB18 shows a highly elastic behaviour with hysteresis loops very close to each other, WB14 shows a great inelastic deformation during the first 1500 cycles (where hysteresis loops appear to be very separated between one another) and strain hardening after 1500 cycles.

Both samples F1 (room temperature) and F2 (55°C) show very similar patterns. The general trend for series F is a positive increase of ε_{ax} with strain hardening observed around 1500 cycles for both samples tested at room temperature and 55°C.

As discussed before, samples LB1 and LB3 show the greatest ε_{ax} with a positive increase of ε_{ax} along the whole test. The hysteresis loops reflect a great amount of plastic deformation between cycles until 1500 cycles and a strain hardening process from 1500 cycles onward. Although strain hardening is ob-

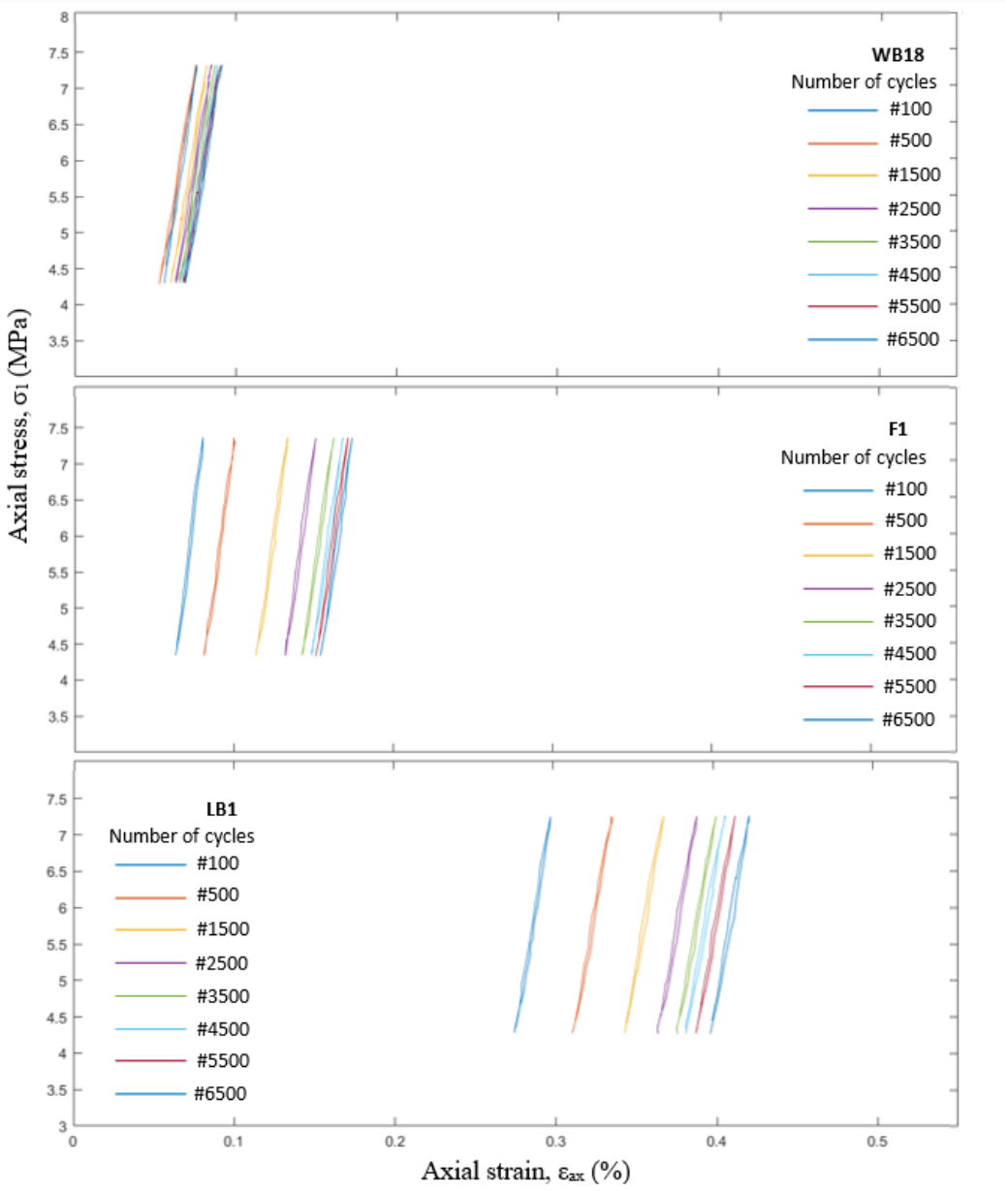

Figure 4.10: *Hysteresis loops of stress-strain for samples from Winsford Mine tested at 12 MPa and room temperature. This figure shows how samples from series LB, with a breccia texture, records larger strain within the first cycles in comparison to samples with a non-clastic polycrystalline texture.*

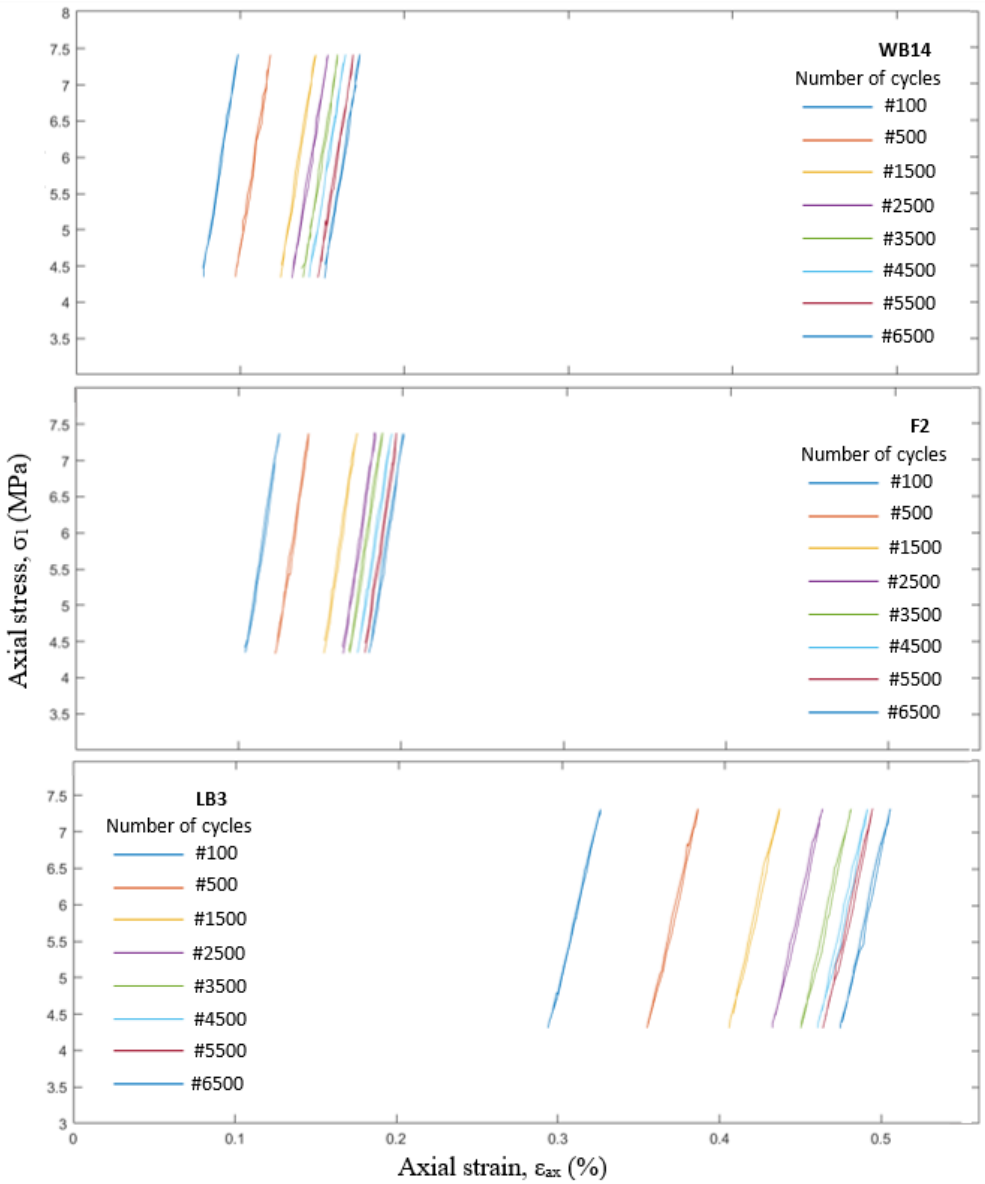

Figure 4.11: *Hysteresis loops of stress-strain for samples from Winsford Mine tested at 12MPa and 55° C. The increase in testing temperature results in an increase of strain for all samples although samples from series LB, with breccia texture, show a larger increase in strain in comparison to samples with a polycristalline texture.*

served for both samples (LB1 and LB3), LB3 (tested at a higher temperature of 55°C) shows an slightly smoother strain hardening in comparison to LB1, where hysteresis loops still show a notable separation.

All samples with clay and anhydrite content show a decrease in stiffness with the increase of temperature. This decrease in stiffness can be observed in a decrease of the stress-strain curve also indicating a larger plastic deformation component. An increase in elastic deformation per cycle for all these samples can also be noticed in comparison to samples with anhydrite and polyhalite. The hysteresis loops from Triassic rock samples containing clay (Winsford Mine) show a very closed shape which make them look almost like simple lines. This closed shapes evidences a deformation per cycle with a highly elastic component.

Lateral strain (ε_{circ}) was also calculated. First, lateral variations of core samples are recorded by using a circumferential chain extensometer. The ε_{circ} is calculated as the difference between original diameter and lateral variations along the whole test. A measure of the samples diameter is recorded every 5 seconds. Very small oscillations in the diameter changes can be appreciated as result of the cyclic loading conditions.

Lateral strain (ε_{circ}) for samples from Boulby Mine tested at 12 MPa and room temperature and 55°C are shown in figure 4.12. A very rapid increase is recorded from all tested samples from 0 to 0.05 % in lateral strain within the first 500 cycles. Samples A4 and C4 tested both at room temperature show almost the same negative logarithmic pattern. In the following 500 cycles the big initial increase gets steady around 0.06 % ε_{circ}. After reaching the first 1000 cycles the increase in lateral strain drastically decreases with an increase of 0.06 % to 0.08% ε_{circ} from the first 1000 cycles until the end of the test. Sample B1-2 has the highest lateral strain from this series of tested samples.

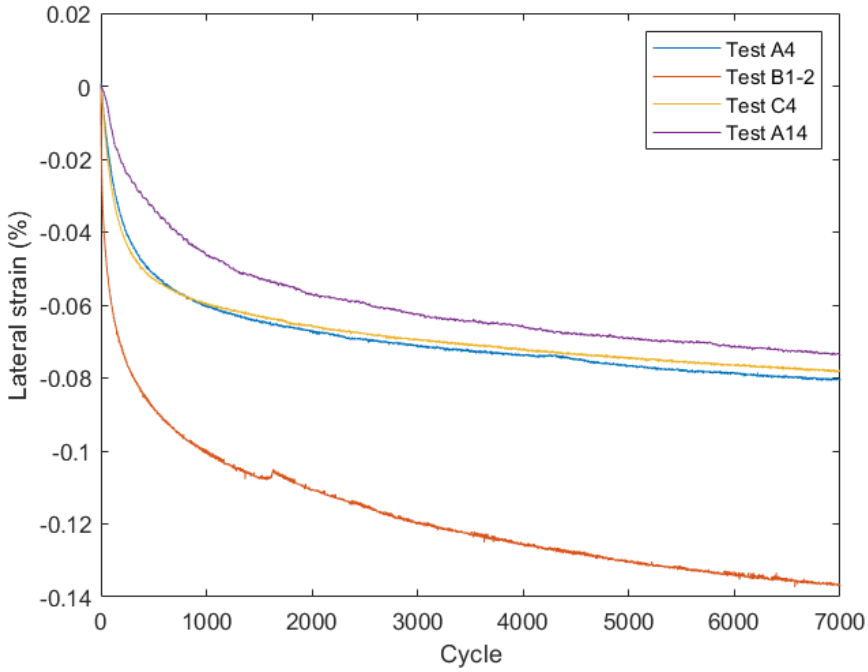

Figure 4.12: *ε_{circ} for samples tested at 12MPa and 21-22°C and 55°C from Boulby Mine. This figure shows that samples with a higher amount in anhydrite and polyhalite (Series B) presents larger lateral strain in comparison to the rest of series from Boulby Mine tested under the same conditions of pressure and temperature.*

Sample B1-2 shows a very prominent increase in ε_{circ} from 0 to 0.09% during the first 500 cycles. After the 500 cycles until the end of the test ε_{circ} increase is slowed down with an almost linear trend going from 0.09 to almost 0.14% ε_{circ}.

Sample A14, tested at 12MPa confining pressure and 55°C, has the lowest ε_{circ} recorded from this series of cyclic mechanical loading experiments. An important increase of ε_{circ} is also recorded in the first 500 cycles from 0 to 0.04% approximately. From 500 cycles to around 2000 cycles the increase in ε_{circ} slows with a increase from 0.04 to 0.05% and from 2000 cycles until the end of the test the ε_{circ} increase stabilises with an increase of 0.01% from 0.05 to 0.06% by the end of the test.

Figure 4.13 show data from ε_{circ} for all samples tested at 12MPa confining pressure and 21°C and 55°C from Winsford Mine. In general, all samples with polyhalite (Boulby Mine) tested at room temperature (21-22°C) showed lower

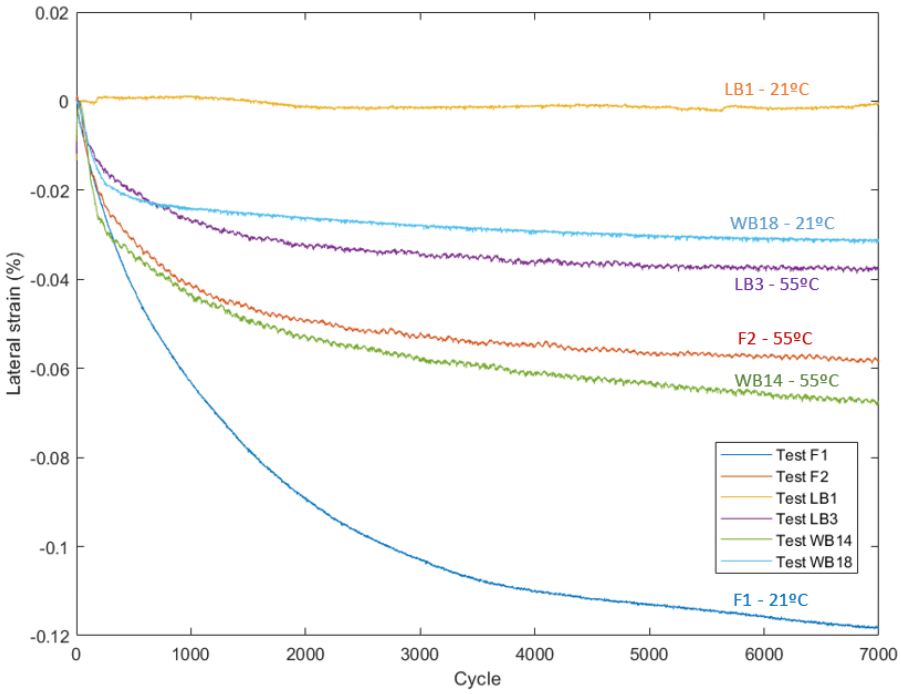

Figure 4.13: *ε_{circ} for samples tested at 12MPa and 21-22° C and 55° C from Winsford Mine. This figure shows that sample from series F (F1) is the sample with the larger lateral strain in comparison with the rest of series of samples from Winsford Mine tested under the same conditions of pressure and temperature. Sample LB1, with breccia texture, is the samples with the lowest lateral strain.*

ε_{circ} in comparison to samples tested at 55°C except sample F1. We can also notice that although samples from series LB were the ones recording the largest ε_{ax}, both LB1 and LB3 show very low lateral extension in comparison to the other samples.

Sample F1, tested at 12MPa and room temperature, showed the largest ε_{circ} from this set of tested samples. F1 shows a dramatic increase (in comparison to all the rest samples) in ε_{circ} from 0 to 0.1% in the first 2000-2500 cycles. From 2500 to 4000 cycles the increase in ε_{circ} is less dramatic with an increase in ε_{circ} to 0.11%. From 4000 cycle until the end of the test, a smooth and linear small increase is recorded from 0.11% to almost 0.12%. Sample LB1 is the samples with the lowest ε_{circ} or nonexistent as ε_{circ} for LB1 stays almost at 0% the whole test. It seems to very slightly increase during the first 1000 cycles, but the trend line keeps almost perfectly flat around the value

of 0% in ε_{circ}. These ε_{circ} values for LB1 contrast with the results observed from ε_{ax} from figure 4.7. Interestingly, both samples from series LB show the largest ε_{ax} with a maximum final ε_{ax} of 0.42% and 0.40% of minimum final ε_{ax}.

Sample WB18 (12MPa confining pressure and room temperature), shows a perfect negative logarithmic trend pattern. It shows an important increase in ε_{circ} within the first 300 cycles from 0 to 0.02%. The initial trend slows down from around the first 300-500 cycles to 1000 cycles and get steady around 0.025%. From 1000 cycles until the end of the test ε_{circ} increases to maximum 0.03%.

Samples LB3 and WB14 tested at 55°C show higher ε_{circ} than their equivalents tested at room temperature. Both samples LB3 and WB14 show a rapid increase during the first 1000 cycles although the increase is higher in sample WB14. WB14 increases from 0 to almost 0.05% in the first 1000 cycles whereas LB3 increases from 0 to 0.03%. After the first 1000 cycles, ε_{circ} for both LB3 and WB14 increases very slowly from 0.025% to almost 0.04% and from 0.05% to almost 0.07% respectively.

Finally, F2 is the only sample from this group of samples, tested at 55°C, showing a lower ε_{circ} than its equivalent (F1) tested at room temperature. However, F2 shows ε_{circ} values between LB3 and WB14 values (also tested at 55°C). F2 shows a rapid and initial ε_{circ} increase from 0 to 0.04% in the first 1000 cycles. from 1000 cycles until the end of the test, ε_{circ} records an increase from 0.04% to almost 0.05%.

4.3.1.2 Elastic parameters for samples tested at 12 MPa confining pressure and temperatures of 25 and 55° C

The slopes of the stress-strain curves along the different cyclic mechanical loads applied provide information about the degradation of the Young's modulus per

cycle after each compression stage which is observed as a decrease of E along the cyclic mechanical test. The Young's the modulus per cycle was derived from the slope of each loading cycle in the stress-strain curve (Equation 4.1). The data processing was conducted using MATLAB and the script used can be find in Appendix B.

$$E = \frac{\sigma_{max} - \sigma_{min}}{\varepsilon_{max} - \varepsilon_{min}} \tag{4.1}$$

Figure 4.14 shows a mean value of Young's modulus per cycle for samples from Boulby Mine tested at 12MPa confining pressure and at room temperature and 55°C (only A14). A general trend observed was that samples tested at room temperature show greater stiffness than samples tested at 55°C. Sample C4 and A4 show a slightly higher stiffness than sample B1-2, with a Young's modulus oscillating between 12.5 and 15.1 GPa for both samples (Table 4.5). Sample B1-2 shows a slightly lower Young's modulus with a value that oscillated between 11.1-13.5 GPa during the cyclic mechanical loading tests. Samples tested at room temperature also show a decrease in Young's modulus after a certain number of cycles. This slight decrease in Young's modulus can be interpreted as an increase in damage due to cyclic loading conditions.

Sample A4 shows a Young's modulus (E) of 15 GPa that decreases constantly along the first 2500 cycles by 8% down to 13.8 GPa. After decreasing to 12.8 GPa, Young's modulus for A4 shows a slightly bigger drop from 13.8 to 12.8 GPa (a drop by a 10%) in only 500 cycles (from 2500 to 3000 cycles). After this dramatic drop, E keeps steady until the end of the test with a Young's modulus around 12.8 GPa. The same trend is observed for samples B1-2 and C4.

B1-2 registers a slightly lower initial Young's modulus with a value of E=13.5

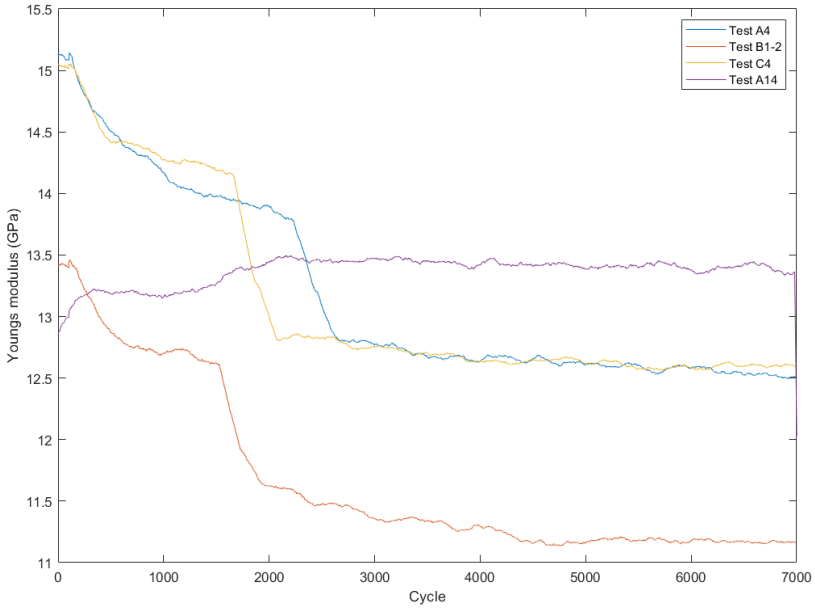

Figure 4.14: *Value of elastic modulus E/cycle for samples tested at 12MPa and 21-22° C and 55° C from Boulby Mine. This figure plots the Young's modulus calculated in each loading cycle versus the number of cycles. A degradation of Young's modulus can be observed for samples tested at lower temperature (room temperature) with a noticeable drop around 2000-3000 cycles. Sample A14, tested at higher temperature, does not show Young's modulus degradation.*

GPa with a constant decrease during the first 1500 cycles by 6% to 12.6 GPa. At around 1500 cycles E from B1-2 shows a higher drop down to 11.5 GPa, a reduction of 9% in only 500 cycles (from 1500 to 2000 cycles). From 2000 cycles to 4500 the decreasing trend tends to get steady registering a drop by 3% in 2500 cycles. From 4500 to the end of the experiment, Young's modulus for B1-2 normalises its trend without important variations. Sample C4 shows very similar values of Young's modulus as A4 and also the same trend along the whole test. Initial E is 15 GPa and there is a constant decrease during the first 2000 cycles down to 14.3 GPa. However, after the first 2000 cycles there is a dramatic drop of E by 10% from 14.3 GPa to 12.8 GPa in almost only 200 cycles. Afterwards, from 2200 cycles and until the end of the test the values of Young's modulus keep steady around 12.8 GPa, similar values as for A4.

Sample A14, tested at 12 MPa confining pressure and 55°C, shows a com-

pletely different trend in comparison to the other samples tested under the same mechanical conditions but at room temperature (21-22°C). In general, A14 shows a quite steady Young's modulus along the whole test with an initial increase from 13GPa to 13.3 GPa in the first 100 cycles. Afterwards, E keeps almost steady until 1800 cycles. From cycle 1800 to cycle 2100 approximately, there is another slightly increase from 13.3 to 13.5 GPa. In the last stage of the test, from approximately cycle number 2100 until the end of the test, Young's modulus keeps steady with a very small jump fluctuations but always around 13.5 GPa.

Samples with a content in anhydrite and clay, tested under the same cyclic mechanical conditions as samples with anhydrite and polyhalite, as main second phase content, and at room temperature, did also show an initial decrease of E although with a different and smaller trend in comparison to samples from Boulby Mine (Figure 4.15). Sample F1 shows the higher Young's modulus: it first decreases from 17.2 GPa to 15.8 GPa in the 200 first cycles then keeps a steady value of 15.8, with very small variations (smaller than - 0.1). Sample WB18 shows a small increase within the first 100 cycles from 14.2 GPa to almost 14.4 GPa. After this small increase, E drops from 14.4 to almost 13.5 GPa within the following 100 cycles. From 200 cycles until the end of the test, E keeps steady around 13.5 GPa. LB1 also shows a very modest initial increase (within the first 50 cycles) but always in the range of 13 GPa. In the first 100 to 200 cycles LB1 records a small drop from 13 GPa to 12.5 GPa approximately. After the first 200 cycles E values for LB1 keep steady in the range of 12.5 GPa.

For samples with clay content tested at a higher temperature of 55°C, a different trend in the development of Young's Modulus is observed. Samples F2 shows just a slightly lower E values in comparison to F1 tested at room temperature. However none of the samples tested at 55°C show the initial drop in

Young's modulus observed in samples tested at room temperature. F2 shows an initial E value of 14.5 GPa approximately with a small but notable initial jump around the first 100 cycles and then a slower increase from the first 100 cycles to approximately 1500 cycles from 14.5 GPa to 15 GPa. Around 1500-2000 cycles, Young's modulus for F2 reaches the highest value of 15 GPa and, from 2000 cycles until the end of the test, it experiences a very small and low decrease but always within the range of 14.5-15 GPa.

Sample WB14 shows a slightly higher Young's modulus in comparison to its equivalent sample (WB18) tested at a lower temperature. Although the difference is very small, sample WB14 is the only sample showing a slightly higher Young's modulus than the equivalent sample from the same series tested at a lower temperature. The normal trend always observed is that samples tested at a higher temperature tend to show slower Young's modulus. WB14 shows an initial an very steady Young's modulus around 14.5GPa for the whole test. Sample LB3 is the sample with the slower Young's modulus with an initial and very steady E values always around 9-9.5 GPa. LB3 has an initial E value of 9 GPa showing a small increase within the first 200 cycles of just 0.5 GPa. Both samples LB1 and LB3 are the samples with the lowest E recorded as expected from the low stiffness observed from stress-strain curves (Figure 4.6 and 4.7).

Poisson's ratio keeps steady for all samples without important fluctuations along the whole test. From rock salt samples containing polyhalite and anhydrite, samples A4 and C4 were the samples with a very higher Poisson's ratio with values. A4 presents ν of 0.5 and C4 ν of 0.64 which is not a normal values for Poisson's ratio. Unfortunately, problems with the measuring gauges have been detected in some experiments and this abnormal value of ν could be related to a technical issue that needs to be check. Sample B1-2 presents a Poisson's ratio of 0.33 and sample A14, tested at a higher temperature of 55°C, shows a Poisson's ratio of 0.13. For samples with clay content (Winsford

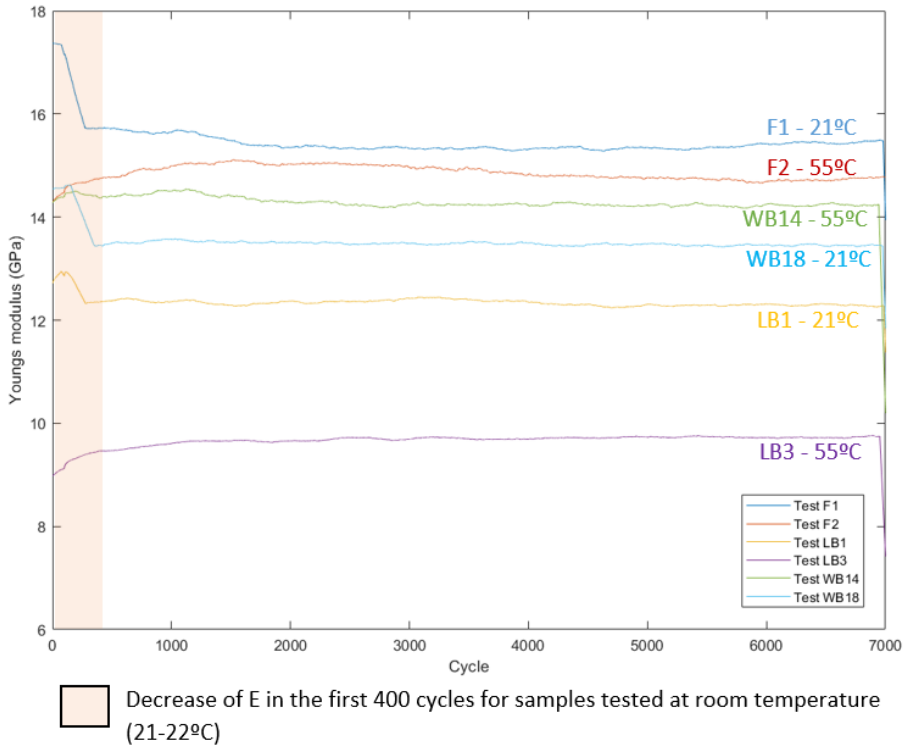

Figure 4.15: *Young's modulus E/cycle for samples tested at 12MPa and 21-22° C and 55° C from Winsford Mine. This figure plots the Young's modulus calculated in each loading cycle versus the number of cycles for samples from Winsford Mine with anhydrite and clay as main second phase content. As in the previous figure 4.14, samples tested at room temperature show a degradation in Young's modulus. However, this degradation take place within the first 500 cycles. Again, samples tested at a higher temperature of 55° C do not show this degradation of the Young's modulus.*

Mine), samples tested at a lower temperature of laboratory environment (21-22°C) are the samples showing a higher Poisson's ratio with values of 0.25 for sample WB18, 0.42 for sample F1 and 0.13 for sample LB1. Samples tested at a higher temperature of 55°C show notably lower Poisson's ratio with values of 0.05 for WB14, 0.03 for F2 and 0.09 for LB3.

Table 4.5 also shows values for bulk modulus (K). Bulk modulus is computed from the Young's modulus and Poisson's ratio. For samples with content in anhydrite and polyhalite and tested at room temperature, B1-2 shows lower K value which fluctuates between 22.8-23.0 GPa. Bulk modulus for A4 fluctuates with values between 23.7-23.96 GPa. C4 shows a bulk modulus fluctuating between 24.0 and 24.3 GPa. Sample A14, tested at 55°C, shows very similar K values as A4 tested at room temperature. Bulk modulus for A14 fluctuates between 23.5-23.6 GPa. The only notable difference between samples tested at 21-22°C and samples tested at 55°C is that the fluctuation of bulk modulus along the whole test is smaller for samples tested at a higher temperature.

Samples with a content in anhydrite and clay, show a smaller variation of bulk modulus always in the range of 23-24 GPa. Sample WB18 has a bulk modulus of 24 GPa with very small variations along the whole test. F1 presents K values of 23.98-24.1 and LB1 is in the range of 24.2 GPa. Samples with clay content tested at 55°C show very similar bulk modulus as samples tested at a lower temperature. WB14 has K values in the range of 23.8-23.9 GPa, F2 in the range of 23.7-23.8 GPa and LB3 in the range of 23.9-24 GPa.

Table 4.5: Minimum and maximum values of the static elastic parameters for all tested samples at 12MPa confining pressures (Pc) and cyclicl mechanical loading conditions between 4.5-7.5MPa.

Sample origin	Sample ID	Pc MPa	T C°	Young's modulus E (GPa)	Bulk modulus K (GPa)	Poisson's ratio ν
Boulby (Permian)	A4	12	21-22*	12.5-15.1	23.7-23.96	0.50
Boulby (Permian)	B1-2	12	21-22	11.1-13.5	22.8-23.0	0.33
Boulby (Permian)	C4	12	21-22	12.6-15.02	24.0-24.3	0.64
Boulby (Permian)	A14	12	55	12.9-13.5	23.5-23.6	0.13
Winsford (Triassic)	WB18	12	21-22	13.5-14.6	24.0	0.25
Winsford (Triassic)	F1	12	21-22	15.3-17.4	23.98-24.1	0.42
Winsford (Triassic)	LB1	12	21-22	12.2-12.9	24.2	0.13
Winsford (Triassic)	WB14	12	55	14.2-14.5	23.8-23.9	0.05
Winsford (Triassic)	F2	12	55	14.4-15.1	23.7-23.8	0.03
Winsford (Triassic)	LB3	12	55	9-9.7	23.9-24	0.09

*Room temperature oscillated between 21-22°C

4.3.1.3 Tests conducted at 25 MPa confining pressure and temperatures of 25, 55 and 75°C

Samples with different content of anhydrite, polyhalite (from Boulby Mine) and clay matrix with anhydrite aggregates (Winsford Mine) were also tested under cyclic mechanical loading conditions (4.5 and 7.5 MPa at a loading rate of 0.5 KN/s) and 25 MPa confining pressure. This second series of experiments corresponds to the case scenario of gas storage at depth ranges of 500-800m (Table 4.1). The temperatures used in the tests at 25 MPa confining pressure were i) room temperature (21-22°C), ii) 55°C, and iii) 75°C (Table 4.6).

Table 4.6: Core samples from Boulby and Winsford Mine tested under cyclic axial stress between 4.5 and 7.5 MPa at a loading rate of 0.5 kN/s for a duration of 48h, i.e. a maximum number of 7200 cycles at a confining pressure (Pc) of 25 MPa. *Mean room temperature oscillated between 21-22°C

Temperature (T)	21°C*	55°C	75°C
Boulby - Series A	A3	A7	-
Boulby - Series B	B8	B6	-
Boulby - Series C	C3	C5	C2
Winsford - Series F	F3	F4	F5
Winsford - Series LB	LB4	LB5	LB6
Winsford - Series WB	WB16	WB1	WB8

The data presented in this section regarding samples tested at 25 MPa confining pressure and room temperature can be find published in the paper "Impact of Second Phase Content on Rock Salt Rheological Behavior Under Cyclic Mechanical Conditions" by Martin-Clave et al. (2021).

The stress-strain data under cyclic mechanical conditions are reported in figure 4.16 for samples from Boulby Mine and figure 4.21 for samples from Winsford Mine. Due to a very limited number of samples for series A and B, only series C from Boulby Mine was tested at 75°C. The temperatures were kept constant

during the whole tests.

Sample A3 has a maximum axial strain ε_{ax} =0.14% at the last 7.5 MPa loading (maximum final ε_{ax}) and ε_{ax} =0.13% at the last 4.5 MPa unloading (minimum final ε_{ax}). Sample C3 ranges from ε_{ax} =0.11% at 7.5 MPa and ε_{ax} =0.09% at 4.5 MPa. In comparison, sample B8 ranges from ε_{ax} =0.17% at the last 7.5 MPa loading and ε_{ax} =0.15% at the last 4.5 MPa unloading. Both samples A3 and C3 also have a similar stiffness whereas sample B8 shows a notably lower stiffness.

Looking at the impact of temperature on the mechanical behaviour, overall one can see that there is an increase in the final amount of ε_{ax} compared to the results obtained at room temperature. Interestingly, at 55°C, all three samples from Series A,B and C exhibit very similar values of ε_{ax} across the tests, reaching a maximum final ε_{ax} =0.22±0.01% and minimum final ε_{ax} =0.19±0.01%. Also at 55°C, all samples show a very similar stiffness, whereas in samples tested at room temperature, B8 is showing a notably lower stiffness than A3 and C3. Samples A7 and B6 show very similar curve slopes whereas C5 is the only sample still showing a slightly higher stiffness, although lower than C3 (tested at room temperature). At 75°C, sample C2 presents the lowest stiffness as shown with the lowest stress-strain curve's slope, yet similar amount of ε_{ax} overall; maximum final ε_{ax} =0.19% and minimum final ε_{ax} =0.16%.

The analysis of the hysteresis loops of the stress-strain data per cycle shows that the increase of ε_{ax} is not constant (Figure 4.17). Indeed, as observed in the data at lower Pc, the stress-strain pathway forms at every cycle a hysteresis loop indicating that deformation along the different loading and unloading episodes has both an elastic and inelastic (irreversible) component. The more opened the loop is, the greater the inelastic component is.

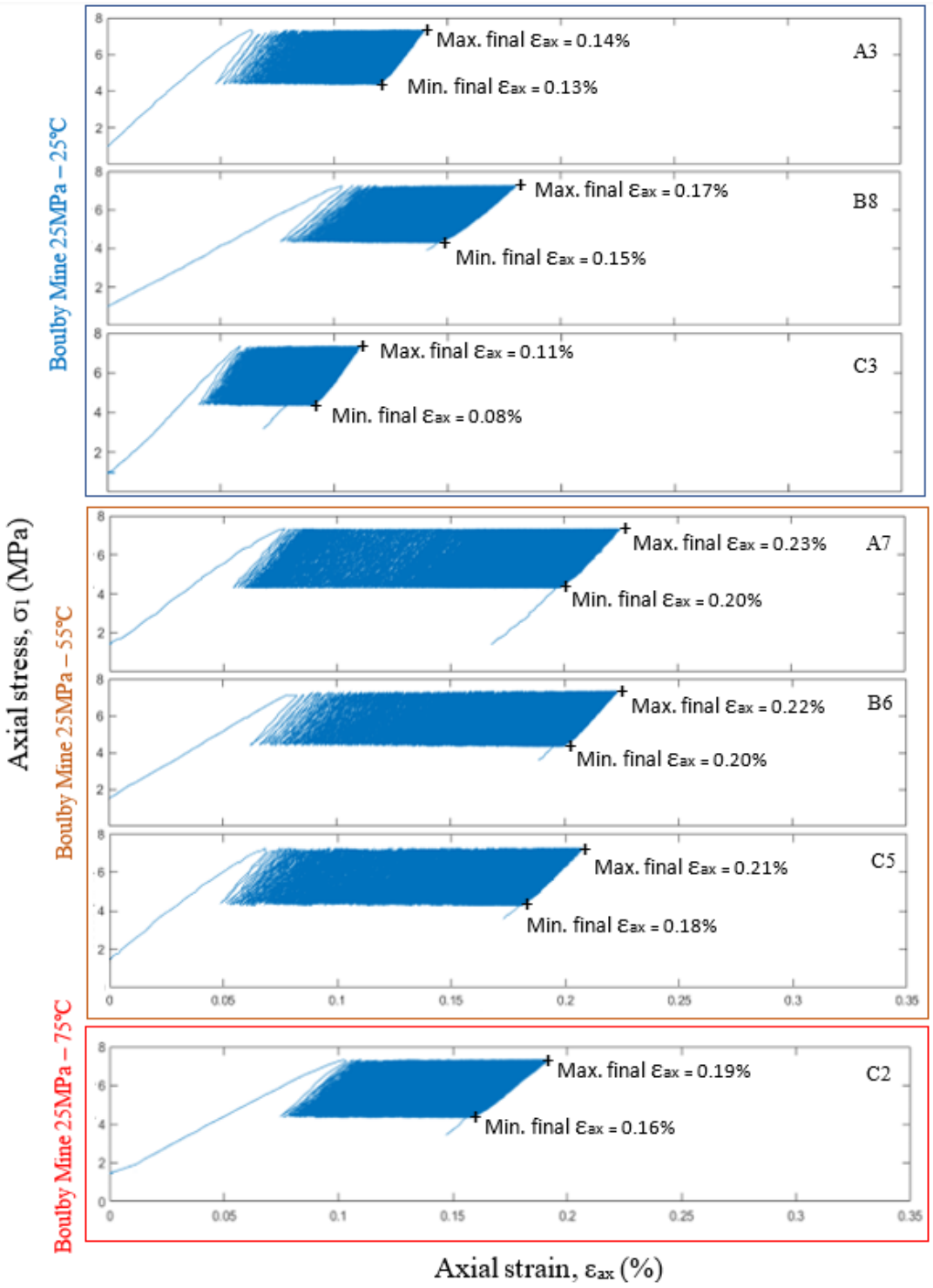

Figure 4.16: *Stress-strain data for Boulby Mine samples tested at 25 MPa and temperatures ranging from ambient to 55° C and 75° C. Series B, with a higher content in anhydrite and polyhalite, presents larger axial strain and slightly lower stiffness in comparison to series A and C tested under the same conditions. However, the increase of temperature reduces this difference in axial strain between samples from different series. At higher temperature, all the samples from different series presents similar final axial strain and similar stiffness.*

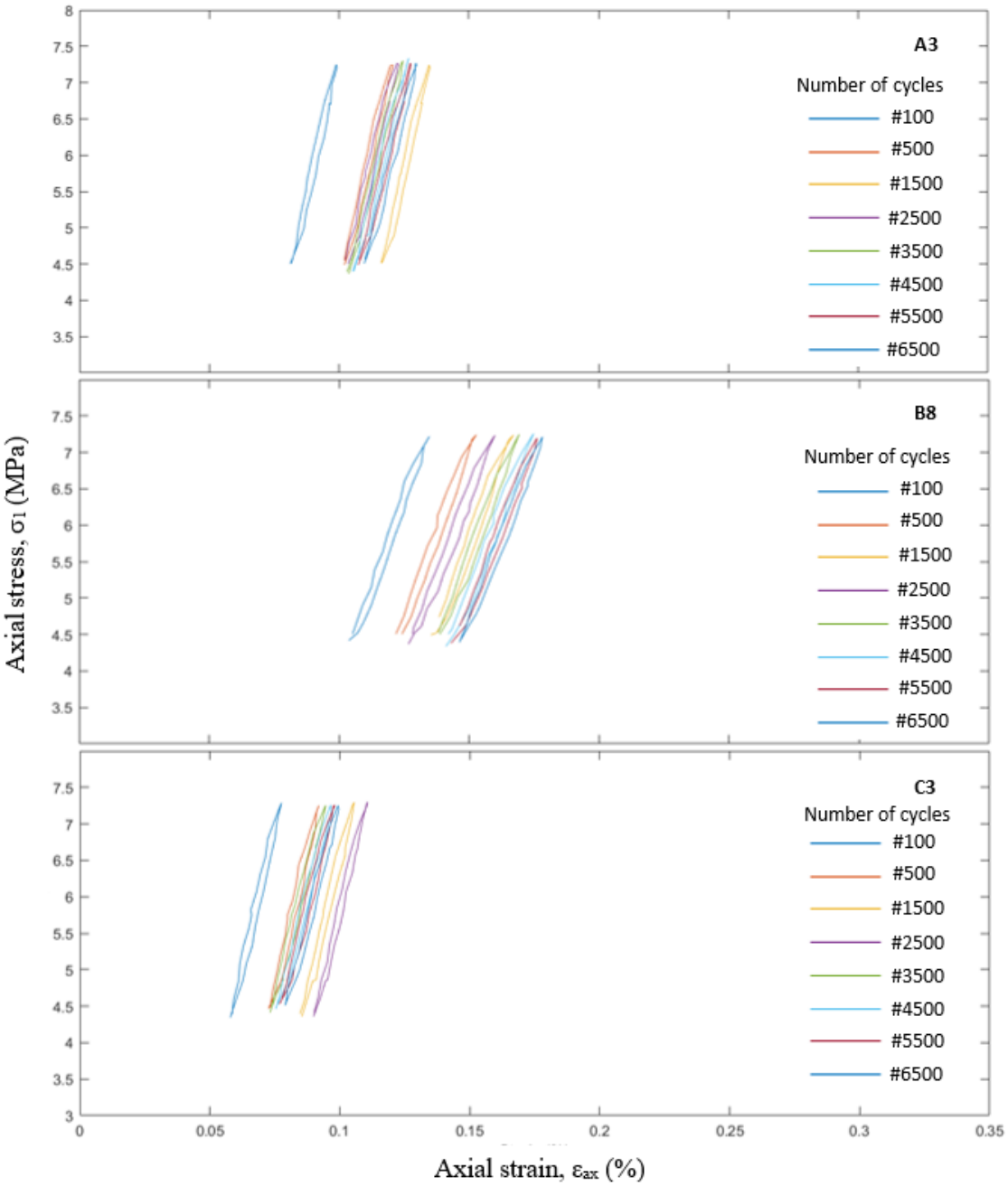

Figure 4.17: *Hysteresis loop analysis from stress-strain data for samples tested at 25MPa and room temperature from Boulby Mine. This figure shows that, as observed in figure 4.8, sample from series B, with a higher content in polyhalite and anhydrite, shows the larger axial strain and slightly bigger hysteresis loop shapes in comparison to series A and C under the same testing conditions.*

At room temperature, both samples A3 and C3 show a constant increase in ε_{ax} until reaching the 1500 cycles, in sample A3, and 2500 cycles, in sample C3. Afterwards, both samples A3 and C3 show a recovery in ε_{ax}, with the hysteresis loops occurring at lower axial strains. The only sample showing a constant increase of ε_{ax} without strain recovery is sample B8. A tendency to

close the hysteresis loop aperture can be observed in all samples from cycle 1500 onward for samples A3 and B8, and cycle 2500 onward for sample C3. This decrease in the loop aperture is related to a decrease in the inelastic (irreversible) deformation of the rock salt along the different cycles. Strain hardening can also be observed from approximately cycles 1500-2500 with the decrease of space between one cycle and another for all samples.

Samples A7, B6 and C5 tested at a higher temperature (55°C) show an important increase in plastic deformation evidenced from a greater distance between hysteresis loops in comparison to samples tested at room temperature. All samples here record the highest plastic deformation during the first 1500 cycles. After the first 1500 cycles, a reduction of distance between consecutive hysteresis loops can be observed. The difference in stiffness from one sample to another seems to be reduced in comparison to samples tested at lower temperatures. B6 and C5 show almost the same pattern along the whole test. The only notable difference is that the hysteresis loop of C5 presents a very narrow aperture during the entire experiment. This could be interpreted as a lower inelastic deformation (and more elastic deformation) within a loading-unloading cycle. Strain hardening is observed around cycle 3500 for A7 and cycles 1500-2500 for B6 and C5.

Sample C2, tested at 75°C, presents a similar stiffness as the samples tested at 55°C. However, it shows a lower plastic deformation as the hysteresis loops seem to have less distance between one to another. Contrary to sample C5, sample C2 shows again well opened hysteresis loops evidencing both elastic and inelastic deformation taking place within one cycle. Strain hardening is observed from cycle 2500.

The lateral strain for the different tested rock salt samples along the cycles is presented in Figure 4.20. Note that due to a technical issue on the circum-

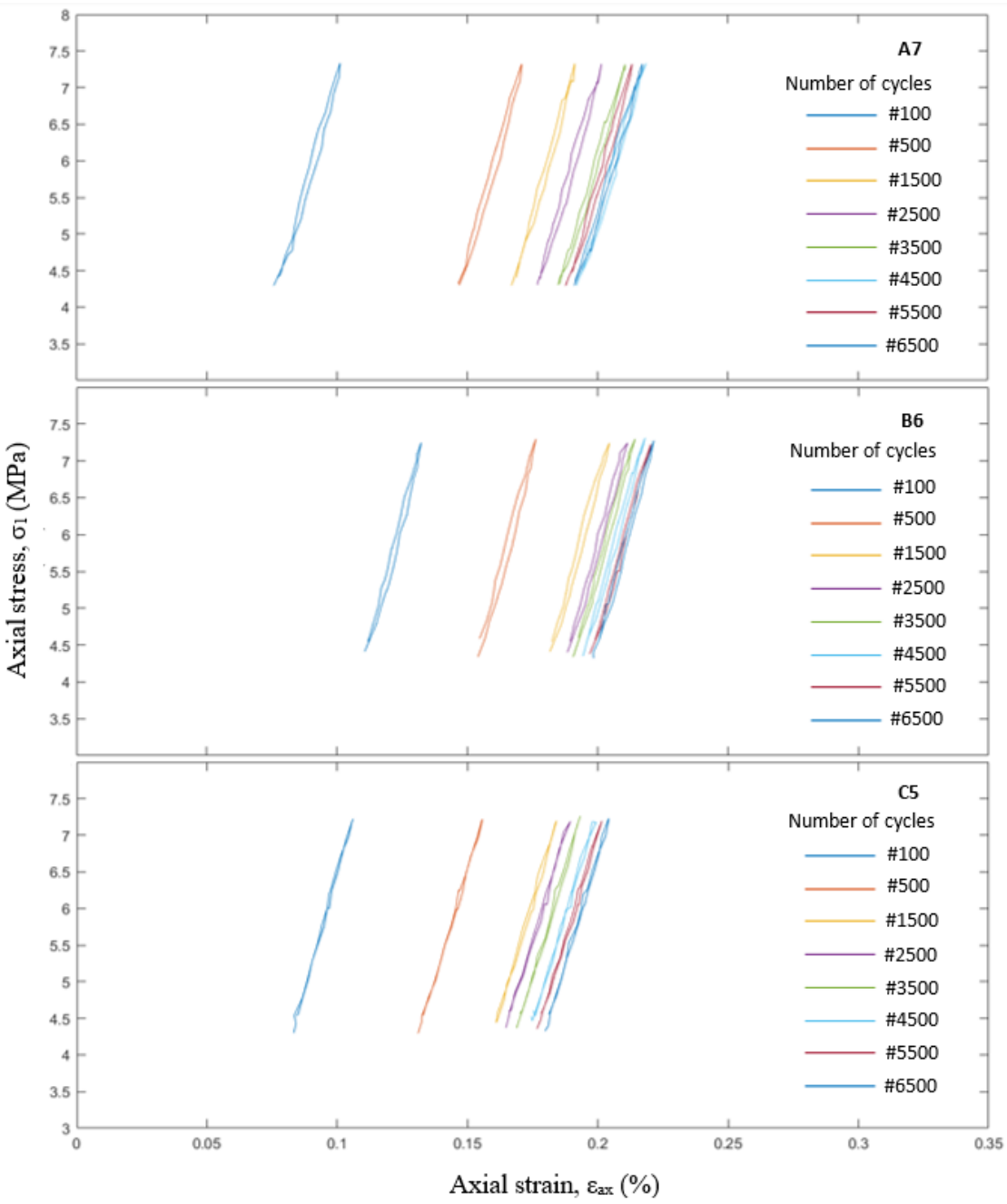

Figure 4.18: *Stress-strain analysis per cycle for samples tested at 25 MPa and room temperature from Boulby Mine. This figure shows how the increase in testing temperature reduces the differences between samples from different series regarding the final axial strain. Although samples B6 and C5 show a slightly lower axial strain recorded withing the first 100 cycles (in comparison to A7), all samples show similar axial strain by the end of the test with similar hysteresis loop shapes.*

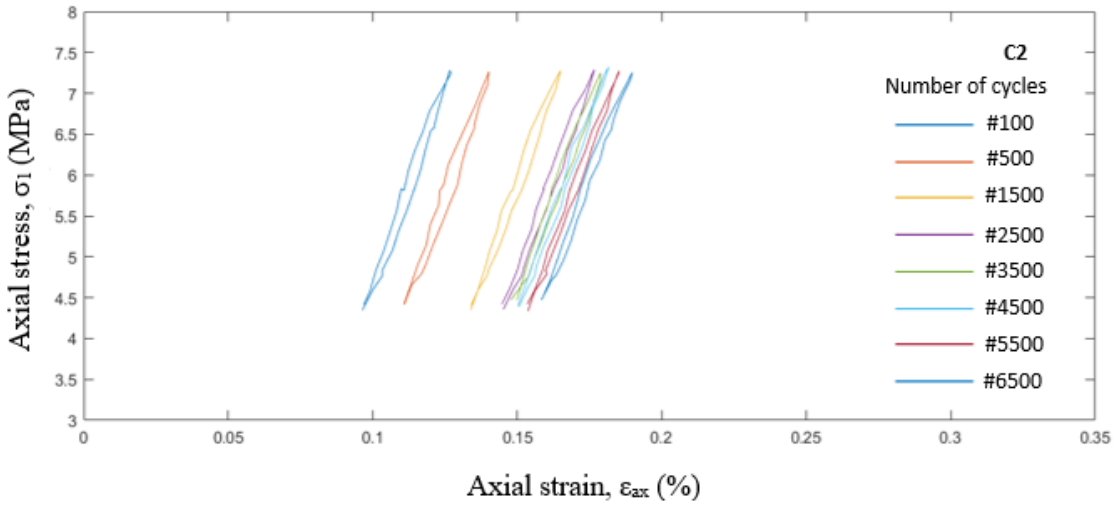

Figure 4.19: *Stress-strain analysis per cycle only for sample C2 tested at 25MPa and 75° C. This figure shows an slightly increase of the hysteresis loop shape with the increase of testing temperature in sample C2.*

ferential strain gauge, unfortunately no ε_{circ} data were recorded for samples A3 and C5. Overall, almost all samples show a smooth negative logarithmic trend. Sample B8 and B6 recorded the largest (maximum $\varepsilon_{circ} = -0.12\%$ and $\varepsilon_{circ} = -0.062\%$ respectively). Between 1000 and 2500 cycle, all ε_{circ} values but A7 ones decrease more slowly; beyond 3000 cycles, the curves reach a near plateau value.

A small initial lateral compression (represented by positive values of ε_{circ}) can be observed during the first 50-100 cycles for samples A7, C2 and B2-1 where samples A7 (55°C) showed the greatest lateral compression with a positive $\varepsilon_{circ} = +0.013\%$ followed by C2 with an initial $\varepsilon_{circ} = +0.009\%$ and B2-1 with a $\varepsilon_{circ} = +0.003\%$. B6 is the sample recording the greatest expansion of ε_{circ}.

Sample A7 is also the only sample with a trend slightly different than a negative logarithm in comparison to the rest of the samples. A7 (represented in yellow in figure 4.20) shows a positive increase of ε_{circ} up to 0.013% for the first 50-100 cycles. Afterwards, a drastic expansion by 0.038% in ε_{circ} is recorded during the following 300-400 cycles (until around 500 cycles).

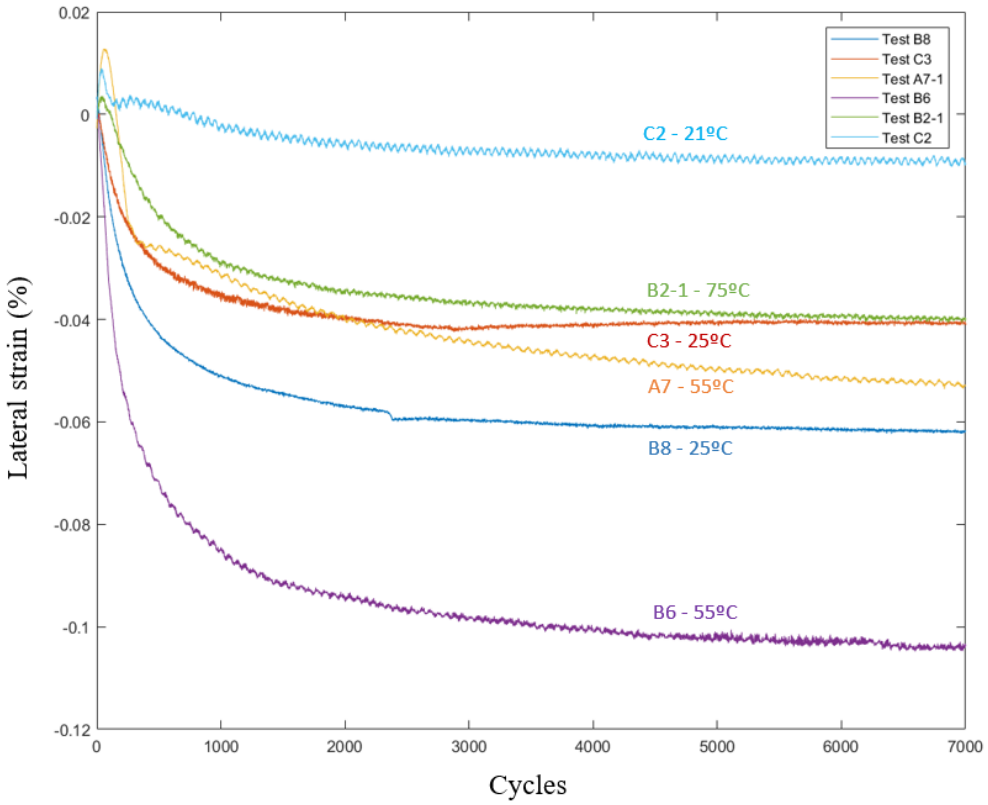

Figure 4.20: *ε_{circ} for samples tested at 25 MPa and room temperature, 55° C and 75° C from Boulby Mine.*

From 500 cycles a slightly plateau value is reached until 800 cycles and from 800 cycles to around 2000 cycles there is a slightly expansion of ε_{circ} from -0.025% to -0.04%. After reaching the 2000 cycles the decrease in ε_{circ} becomes more constant and smoother with a change of $\varepsilon_{circ} = -0.04\%$ to $\varepsilon_{circ} = -0.052\%$.

Samples C2 and B2-1, tested at the highest temperature (75°C), are the samples showing the lowest expansion of ε_{circ}, with C2 being the sample with the lowest change in ε_{circ}. As discussed before, C2 records an initial lateral compression of around $\varepsilon_{circ} = +0.009\%$ during the first 100 cycles (similar to the one observed in A7). After this slightly initial lateral compression (in the first 100 cycles) ε_{circ} tends to almost 0 (within the first 200 cycles). It reaches an slightly positive plateau around this value and after 500 cycles a slow decrease is recorded from 0% to $\varepsilon_{circ} = -0.008\%$ until about 2000 cycles. From 2000 cycles onwards, C2 shows an extremely low rate increase (almost

steady) from $\varepsilon_{circ} = -0.008\%$ to $\varepsilon_{circ} = -0.01\%$. Sample C3 shows an almost perfect negative logarithmic trend with a greater expansion ($\varepsilon_{circ} = -0.035\%$) within the first 1000 cycles. From 1000 to 3000 cycles, C3 ε_{circ} stays quite steady with a very small increase from -0.035% to -0.042%. However, after the first 3000 cycles a slightly recovery in lateral strain is recorded in samples C3 to $\varepsilon_{circ} = -0.04\%$ until the end of the test. C3 is the only sample showing a slight lateral strain recovery.

Figure 4.21 shows the stress-strain data recorded for all rock salt samples with clay and anhydrite content (Winsford Mine) tested at 25MPa and temperatures ranging from room temperature to 55°C and 75°C. Overall, samples from series LB recorded the highest axial strain $\varepsilon_{ax} =$ compared to any sample at any given temperature. Regarding samples tested at room temperature, sample LB4 presents the largest initial axial strain during the first loading, highlighting its strong intrinsic inelastic behavior, with maximum recorded $\varepsilon_{ax} =$0.31% at the last 7.5 MPa loading and $\varepsilon_{ax} =$0.28% at last 4.5 MPa unloading. LB4 recorded twice more axial strain than the other samples from Winsford Mine tested at similar conditions (namely, F3 and WB16). Finally, LB4 stress-strain curve also has a lower slope than the rest of Winsford Mine at room temperature series curves. Sample F3 values range between a maximum $\varepsilon_{ax} =$0.18% at 7.5 MPa and a minimum $\varepsilon_{ax} =$0.16% at 4.5 MPa. Sample WB16 shows similar stiffness to F3 but an slightly higher elastic behavior from the first cycle applied. WB16 shows a maximum recorded $\varepsilon_{ax} =$0.16% at the last 7.5 MPa loading and $\varepsilon_{ax} =$0.13% at last 4.5 MPa unloading.

An important increase in ε_{ax} can be observed for all samples clay and anhydrite content at temperature of 55°C, except for sample LB5. LB5 is the only sample showing a very small decrease in maximum ε_{ax} recorded at a higher temperature (55°C) in comparison to LB4 (room temperature). LB5 shows $\varepsilon_{ax} =$0.26% at the last 7.5 MPa loading and $\varepsilon_{ax} =$0.24% at last 4.5 MPa un-

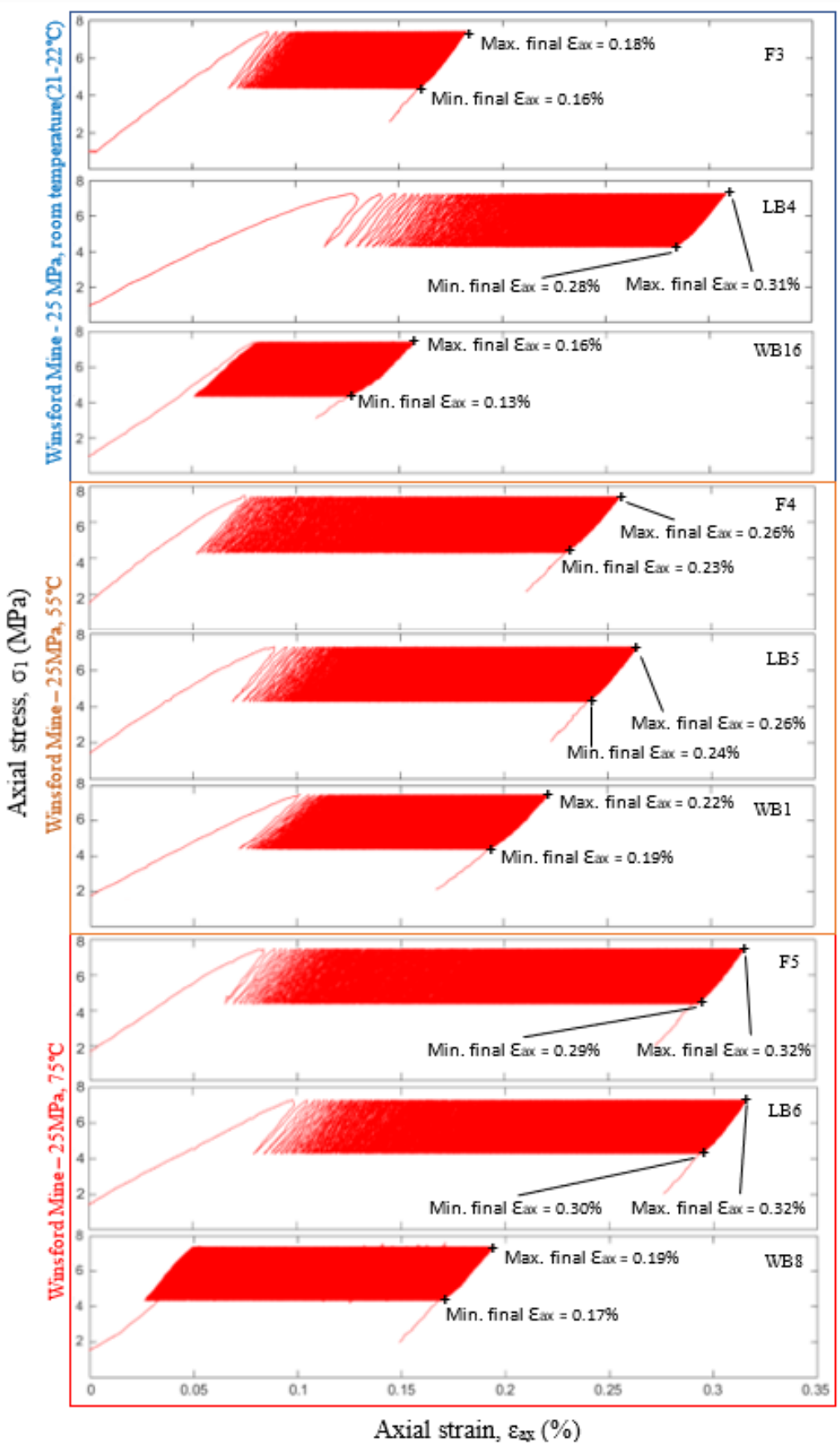

Figure 4.21: *Stress-strain curve for samples tested at 25 MPa and room temperature, 55° C and 75° C from Winsford Mine. Cyclic stress between 4.5-6.5 MPa at a loading rate of 0.5kN/s during 48h.*

loading, which implies a decrease by a 15% approximately in final ε_{ax}. Both F4 and WB1 show an increase in final ε_{ax}, in comparison to sample tested at room temperature, by 30% with a maximum final ε_{ax} =0.26% and minimum final ε_{ax} =0.23%, for sample F4, and maximum final ε_{ax} =0.22% and minimum final ε_{ax} =0.19%, for sample WB1. All samples tested at 55°C show similar stiffness although LB5 shows a slightly higher intrinsic inelastic behaviour in during the very first cycles.

At 75°C, samples F5 and LB6 have very similar rheological behaviour with similar stiffness and final ε_{ax} values. They also both present the greatest amount of final ε_{ax} compared to the other Winsford Mine samples tested, with an increase by 20% of the maximum axial strain in comparison to the same series samples tested at 55°C respectively. Samples F5 ε_{ax} =0.32% at the last 7.5 MPa loading, and ε_{ax} =0.29% at last 4.5 MPa unloading, and sample LB6 has ε_{ax} =0.32% and ε_{ax} =0.30% for maximum and minimum final load respectively. On the contrary, WB8 shows a completely different rheological pattern, both from the one observed in series WB tested at lower temperature and in comparison to all the other samples from Winsford Mine tested at different temperatures. WB8 shows an axial strain recovery in the very first cycles at the beginning of the test. A small increase in stiffness can also be observed in the first load applied with a slight concave stress-strain curve increase during the first 7.5 MPa applied. WB8 shows maximum ε_{ax} =0.19%, at the last 7.5 MPa loading, and ε_{ax} =0.17%, at last 4.5 MPa unloading, implying a decrease by around a 15% in comparison with the ε_{ax} recorded in WB1 (tested at 55°C).

Figures 4.22, 4.23, 4.24 show the stress-strain hysteresis loops per cycle for all samples from Winsford Mine, with clay matrix with anhydrite as second phase content, tested at 25MPa and different temperatures. In general, the hysteresis loop analysis per cycle highlights an increase of plastic deformation between cycles accompanied with a small decrease of inelastic deformation within the

same cycle with temperature increase, as the loop's aperture reduces a bit in samples tested at higher temperatures.

WB16 initially shows a rather elastic trend in the first 500 cycles, as the hysteresis loops from cycle 100 and 500 are quite close. As the number of cycles increase, WB16 exhibits strain hardening (as captured between cycles 1500 and 4500). During the last 2700 cycles, it seems that WB16 experiences a stable state of deformation with hysteresis loops overlapping each other.

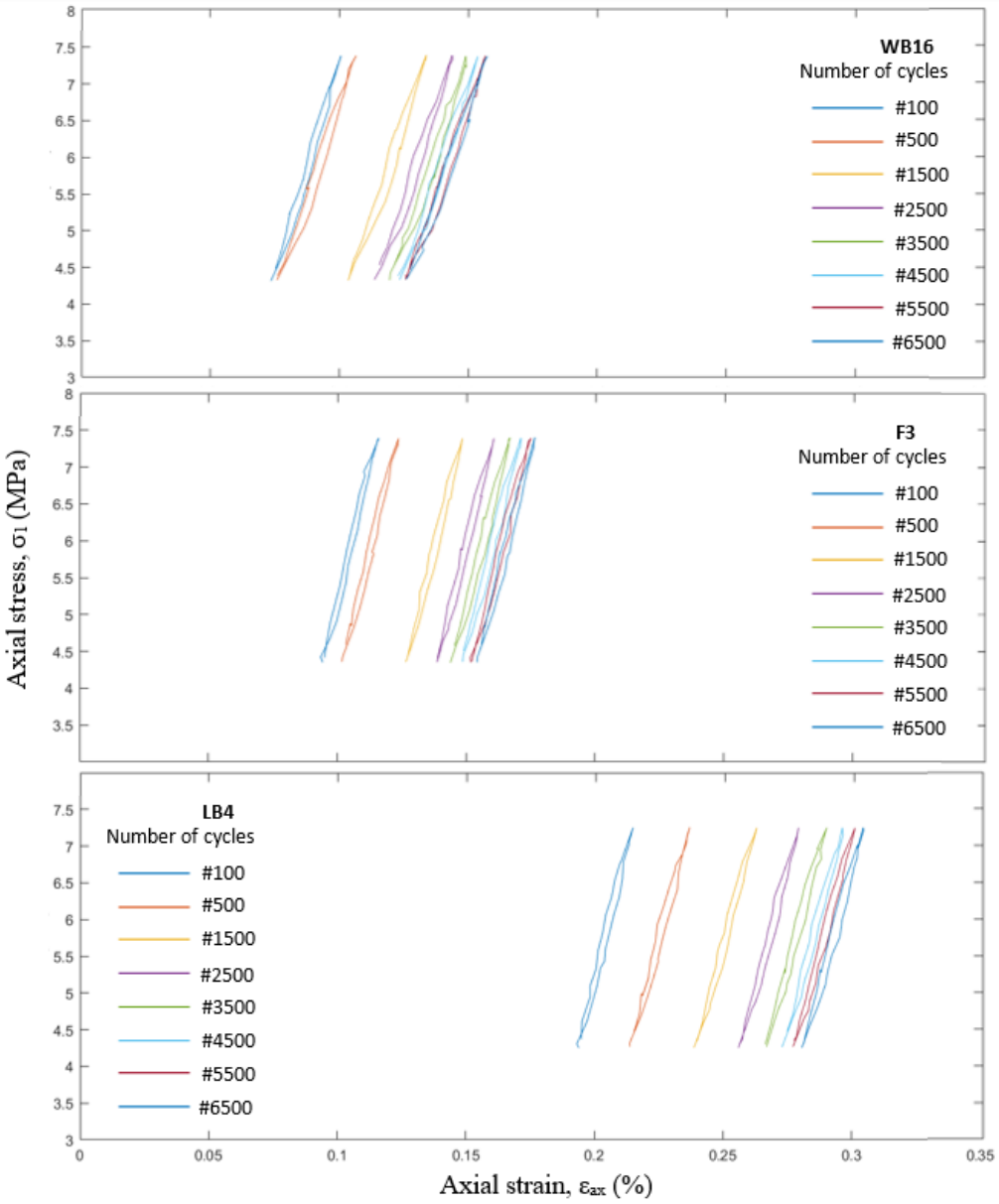

Figure 4.22: *Stress-strain curve for samples tested at 25MPa and room temperture, 55° C and 75° C from Winsford Mine. Cyclic stress between 4.5-6.5 MPa at a loading rate of 0.5kN/s during 48h.*

F3 presents a bit more inelastic deformation in comparison to WB16 then behaves quite similarly. In general, series LB shows the greater inelastic behaviour of all samples from Winsford Mine; here, its strain hardening phase spreads over more cycles, starting later than WB16 and F3, at around 3500-4500 cycles.

An important increase in the inelastic rheological behaviour between cycles (with an increase of hysteresis loops separation distance) can be observed in all samples WB1, F4 and LB5 when compared to the corresponding samples (same series) tested at room temperature (Figure 4.23). The hysteresis loop aperture is also visibly more narrow in comparison, which indicates an increase of the elastic component within each cycle. Samples LB5 and F4 first present very tight hysteresis loops at the beginning of the test (first 1500 cycles) followed by a small widening as the number of cycles goes on, indicating progressive increase of the inelastic component per cycle with the cyclic loading accumulation. A softer, strain hardening can also be observed at around 4500 cycles onward for all samples, although it is more notable in sample WB1.

At 75°C, the same increase of elastic component of deformation within a cycle can be observed in both samples F5 and LB6, with an slight closure of hysteresis loops compared to samples tested at a lower temperature. WB8 is the sample showing a higher inelastic deformation within cycles whereas F5 and LB6 are the samples with a higher inelastic deformation between cycles. Very soft strain hardening can be interpreted from cycles shortening distance after around cycle number 2500.

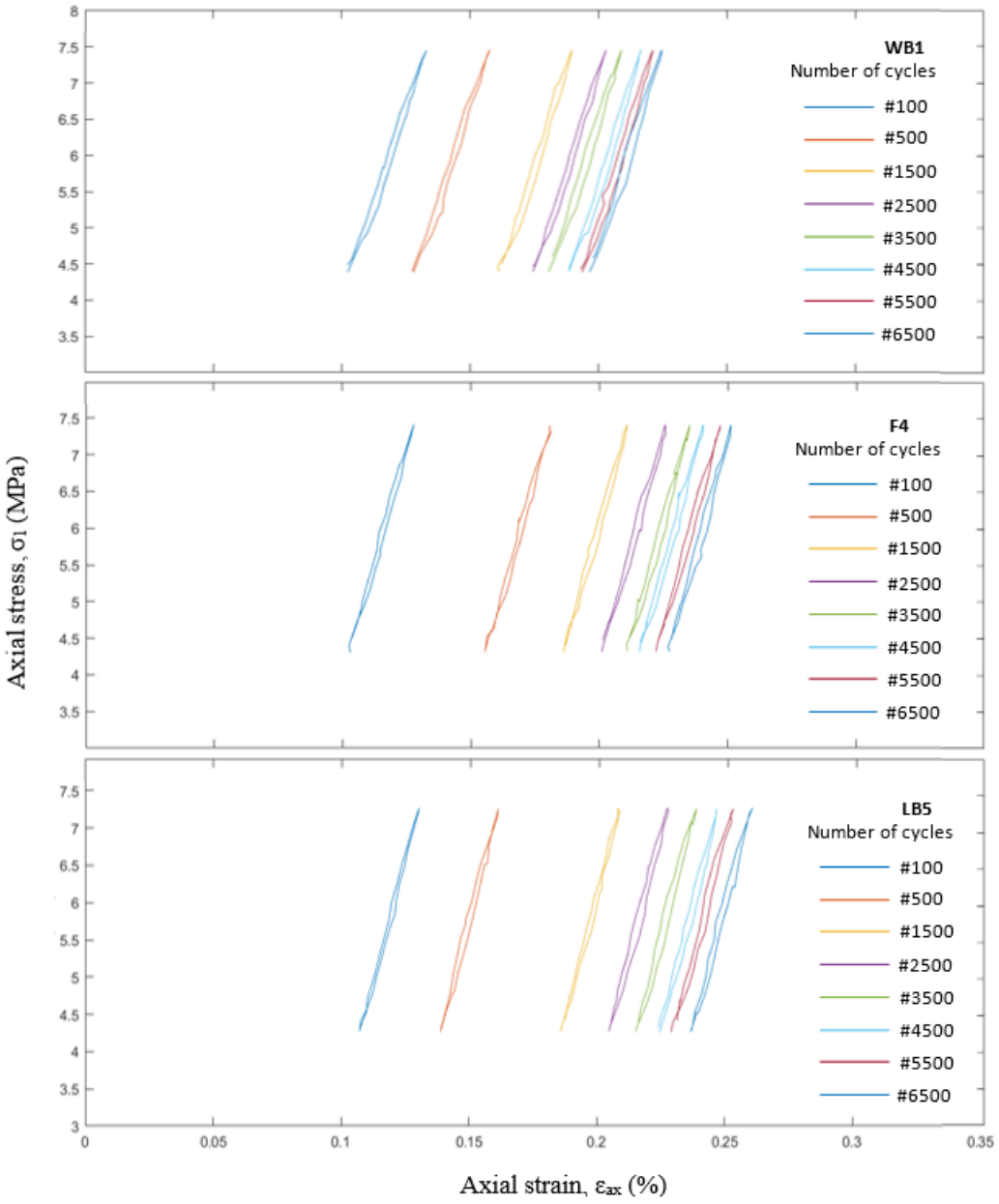

Figure 4.23: *Stress-strain hysteresis loop per cycle for samples tested at 25MPa and 55° C from Winsford Mine. Cyclic stress between 4.5-6.5 MPa at a loading rate of 0.5kN/s during 48h.*

Figure 4.25 shows ε_{circ} for all samples from Winsford Mine tested at 25 MPa of confining pressure and different temperatures (room temperature, 55°C and 75°C). As observed previously with Boulby Mine samples, the lateral strain data presents an overall logarithmic trend for all samples here too. Samples F4 and WB1 (tested at 55°C) show a greater lateral expansion rate within the first 500 cycles whereas sample WB8 (75°C) has the slowest expansion rate. Sample LB4 has recorded the least amount of lateral expansion (maximum

$\varepsilon_{circ} = -0.016\%$).

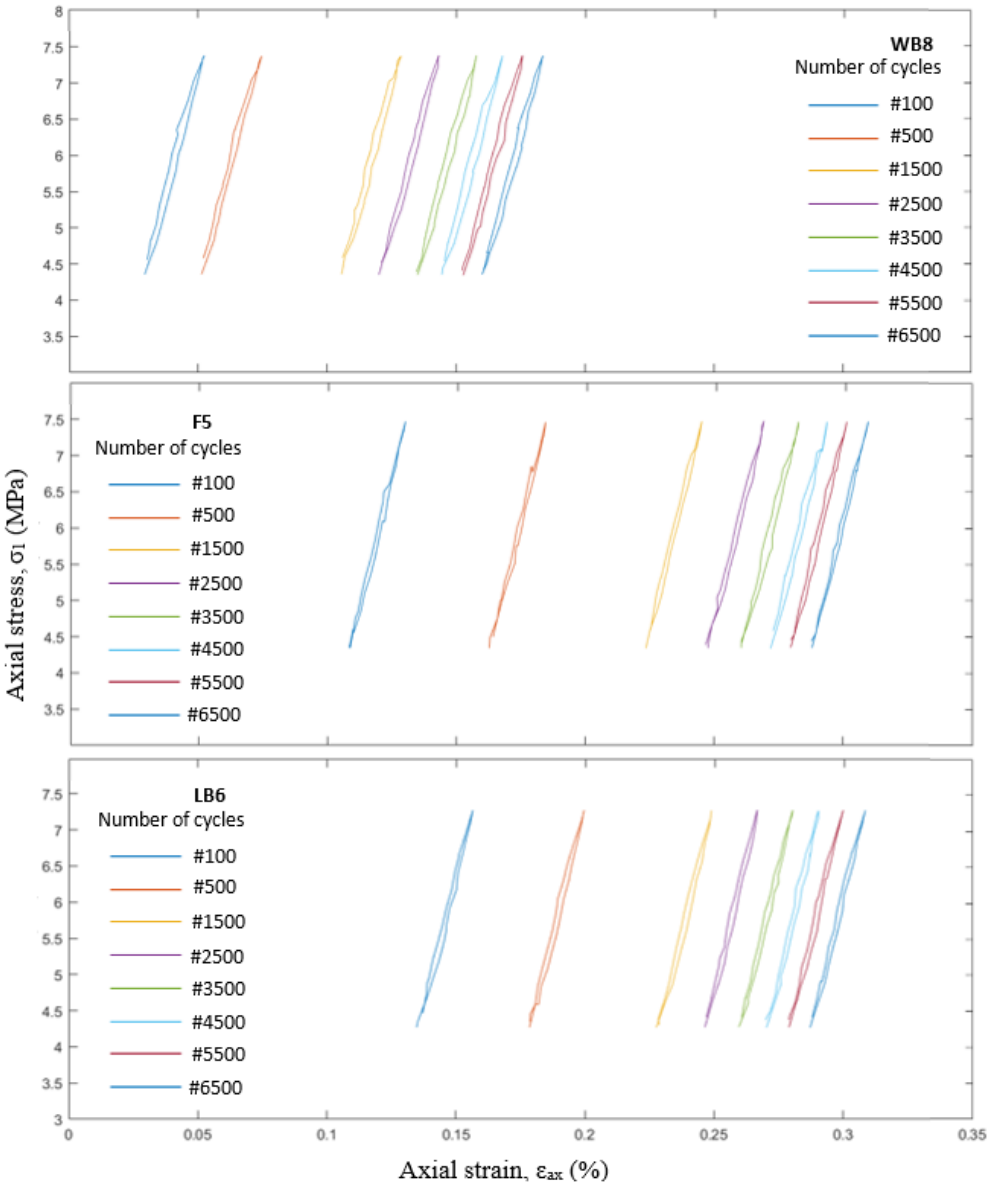

Figure 4.24: *Hysteresis loops per cycle from stress-strain curve for samples tested at 25MPa and 75°C from Winsford Mine. Cyclic stress between 4.5-6.5 MPa at a loading rate of 0.5kN/s during 48h.*

Sample F3 has a distinctive pattern of recurring variations in ε_{circ} on top of the logarithmic trend. Its lateral strain presents a quite fast increase during the first 1000 cycles up to 0.02% followed by a small positive recovery approximately every 200-500 cycles. Indeed, after 1000 cycles several small positive recovery episodes in ε_{circ} can be observed in the form of small jumps of $0.020 - 0.028\%$. Just before reaching 6000 cycles, the curve stabilizes with a

slightly positive recovery to about $\varepsilon_{circ} = 0.025\%$. Regarding the other samples tested at room temperature, sample WB16 has the highest lateral extension with a fast increase of $\varepsilon_{circ} = -0.04\%$ during the first 1000 cycles. After the first 1000 cycles, the lateral extension rate decreases until around 4000 cycles, reaching a $\varepsilon_{circ} = -0.06\%$. At 4000, the curve flattens at around -0.06% until the end of the test.

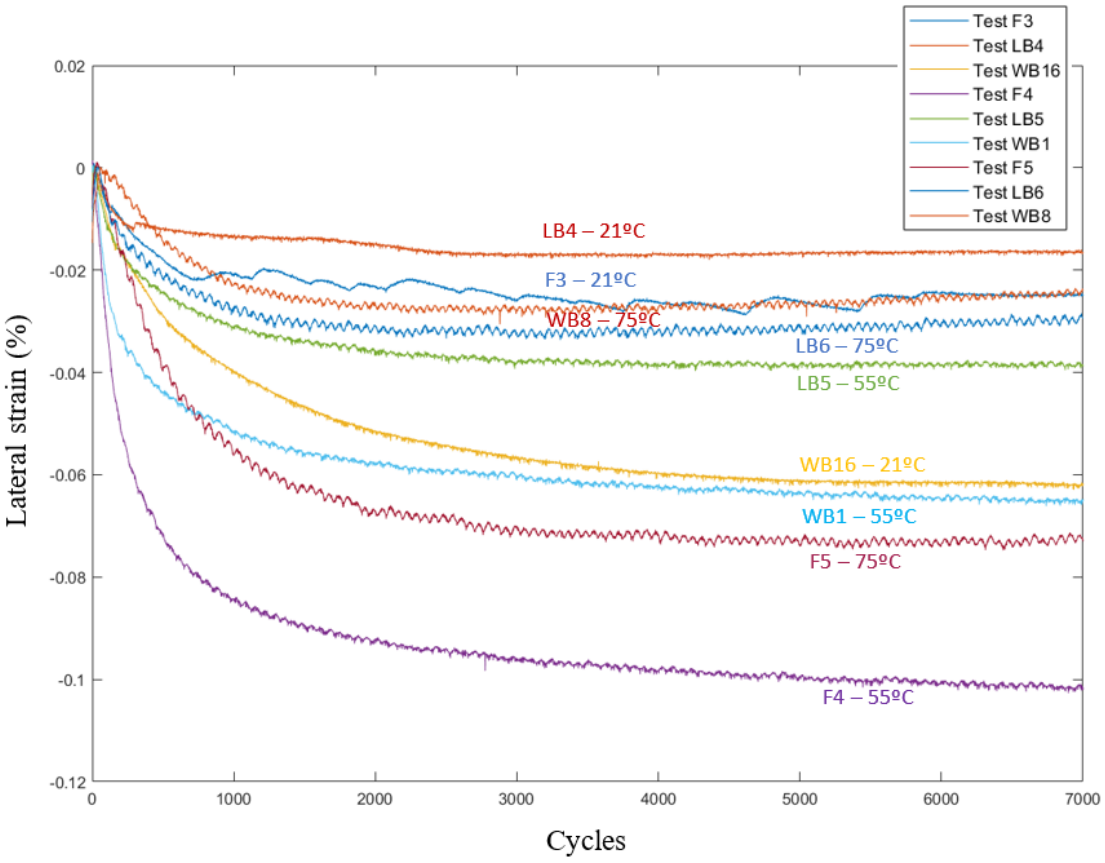

Figure 4.25: *ε_{circ} for samples tested at 25MPa and 21-22° C, 55° C and 75° C from Winsford Mine.*

Samples LB5, WB1 and F4 (tested at 55°C) show almost perfect negative logarithmic trends, with LB5 having the lowest lateral expansion and F4 the highest in this group. All samples tested at 55°C records largest lateral strain expansion within the first 1000 cycles and the curves tends to flatten after the 1000 cycle until around 3000 cycles where the 90% of total lateral deformation has been reached. Samples LB5, WB1 and F4 shows final $\varepsilon_{circ} = -0.04\%$,

$\varepsilon_{circ} = -0.065\%$ and $\varepsilon_{circ} = -0.1\%$ respectively.

Samples tested at 75°C are, in general, the ones showing the lowest initial lateral extension rate, with WB8 the sample with the least initial lateral extension rate from all tested samples at 25MPa and clay/anhydrite content as second phase. An increase of the lateral extension rate (lower than all other samples) can be noticed in WB8 after the first 200 cycles. At around 2000 cycles lateral strain gets steady with a final $\varepsilon_{circ} = -0.025\%$. LB6 shows an parallel trend to WB8 but with a rapid lateral strain accumulation within the first 1000 cycles (as observed in all the other samples tested with clay and anhydrite content). This larger lateral extension rate in the first 200 cycles (in comparison to WB8) seems to be the main reason to show a bit higher final ε_{circ} in comparison to WB8 with a final value of $\varepsilon_{circ} = -0.03\%$. Finally, F5 is the sample within this group (tested at 75°C) showing the larger final lateral strain with a $\varepsilon_{circ} = -0.052\%$. F5 presents a negative logarithmic trend similar to the one observed in the other samples already described.

4.3.1.4 Elastic parameters for samples tested at 25 MPa confining pressure and temperatures of 25, 55 and 75° C

Overall, all rock salt samples tested at 25 MPa and different temperatures show a softening process with a recognizable decrease in Young's modulus. All samples show Young's modulus values between 8.5 and 16 GPa (Figures 4.26 and 4.27).

For all samples tested at room temperature, sample B8 (Boulby Mine), with a higher content in polyhalite and anhydrite, has the lowest Young's modulus with $E \sim 9$ GPa. Sample B8 is also the sample that presents the lowest amplitude oscillation recorded regarding the elastic modulus in comparison to all other samples (Figure 4.28). Samples A3, B8 and C3 record a marked decrease

in Young's modulus value observed consistently between 2000 and 3000 cycles, with sample B8 having the smallest amplitude drop with just about 0.5 GPa of decrease (Figures 4.26). A slightly gradual decrease in the first 900 cycles can be also observed in samples A3 and C3. Samples F3 and LB4 also show a drop in Young's modulus but during the first 500 cycles instead. Sample F3 has a more gradual decrease in Young's modulus along the first 1000 cycles, whereas sample LB4 shows a slightly positive jump in the first 100 cycles and then a more noticeable decrease between the first 100 and 500 cycles from 14 GPa to 13 GPa. F3 also shows a gradual decrease of Young's modulus during the first 900 cycles. WB16 also records an important drop withing the first 400 cycles from 11.5 GPa to 10.2 GPa approximately. After the first 400 cycles, WB16 shows a very small decrease until the end of the test to around 10 GPa.

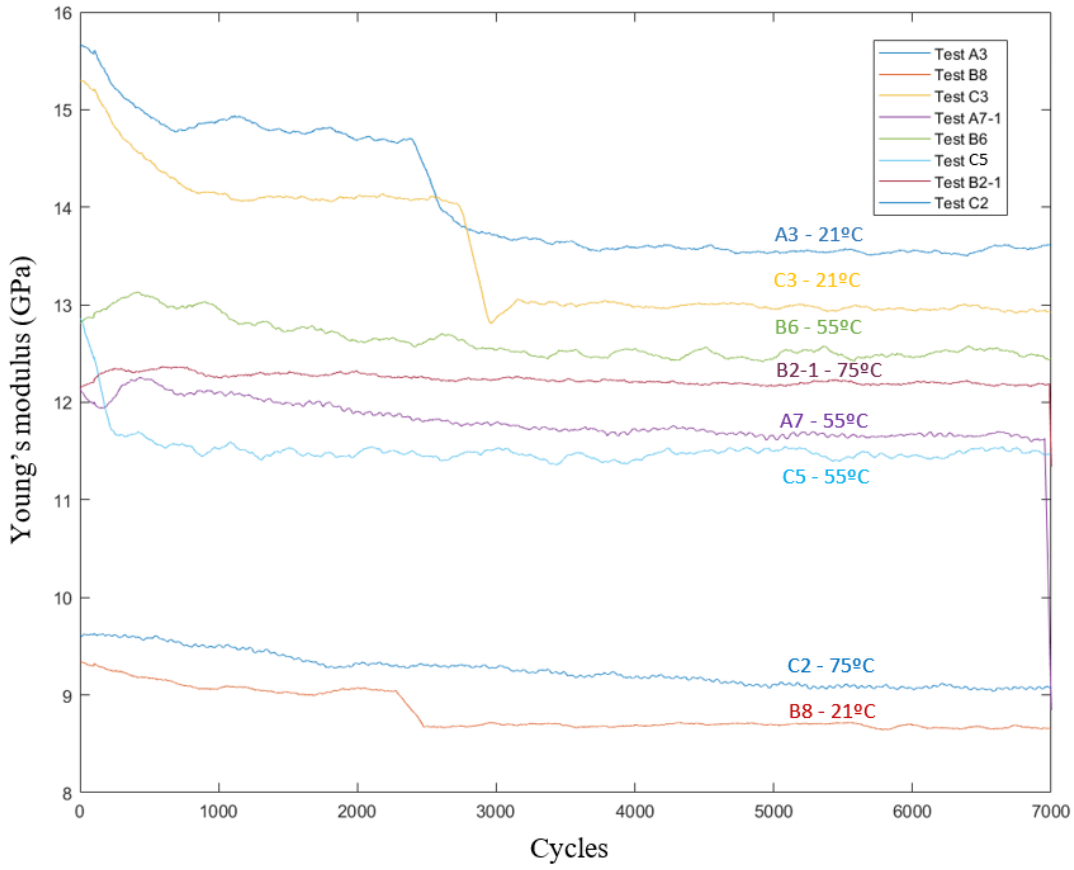

Figure 4.26: *Mean value of E/cycle for samples tested at 25MPa and 21-22° C, 55° C and 75° C from Boulby Mine.*

With the increase of temperature, Young's modulus becomes more stable along the whole test. All samples tested at 55°C show mean E values between 10 and 13 GPa. Sample A7 shows a small increase of Young's modulus around 500 cycles followed by a gradual decrease until 4000 cycles. From 4000 cycles until the end of the test E gets steady around 11.6 GPa. B6 shows also an initial increase in E during the first 500 cycles followed by a gradual decrease with small fluctuations. The decrease of E takes place until around 4000 cycles and after the first 4000 cycles it stays steady with small fluctuations around 12.5GPa.

All samples tested at 75°C show a very smooth and steady trend without important variations along the whole test. The values of E recorded at 75°C were between 9 and 12.5 GPa for rock salt samples with polyhalite and anhydrite content (Figure 4.26) and from 13 to 14.5 GPa for rock salt samples with clay and anhydrite as main second phase content (Figure 4.27). B2-1 shows a very small increase in the first 300 cycles and a very small decrease just after 1000 cycles before it reaches a flat and stable trend around 12.2 GPa. C2 shows a gradually decrease of E from 9.6 to 9.4 GPa approximately during the first 2000 cycles. After the 2000 cycles the gradual decrease of E becomes even slower and stays around 9.1 GPa. Samples LB6 and F5 both show E values around 14 and 14.2 GPa during the whole test without big fluctuations. Only sample LB6 shows a small increase in the first 300 cycles from 13.5 to 14 GPa. Afterwards it stabilises around 14 GPa. WB8 also shows very stable values of E around 12.8 and 13 GPa.

All samples show bulk modulus ranging from 23.3 to 24.8 GPa. Only samples with a higher content of anhydrite and polyhalite and samples tested at 75°C (independently of their second phase content) show bulk modulus values lower than 24 GPa.

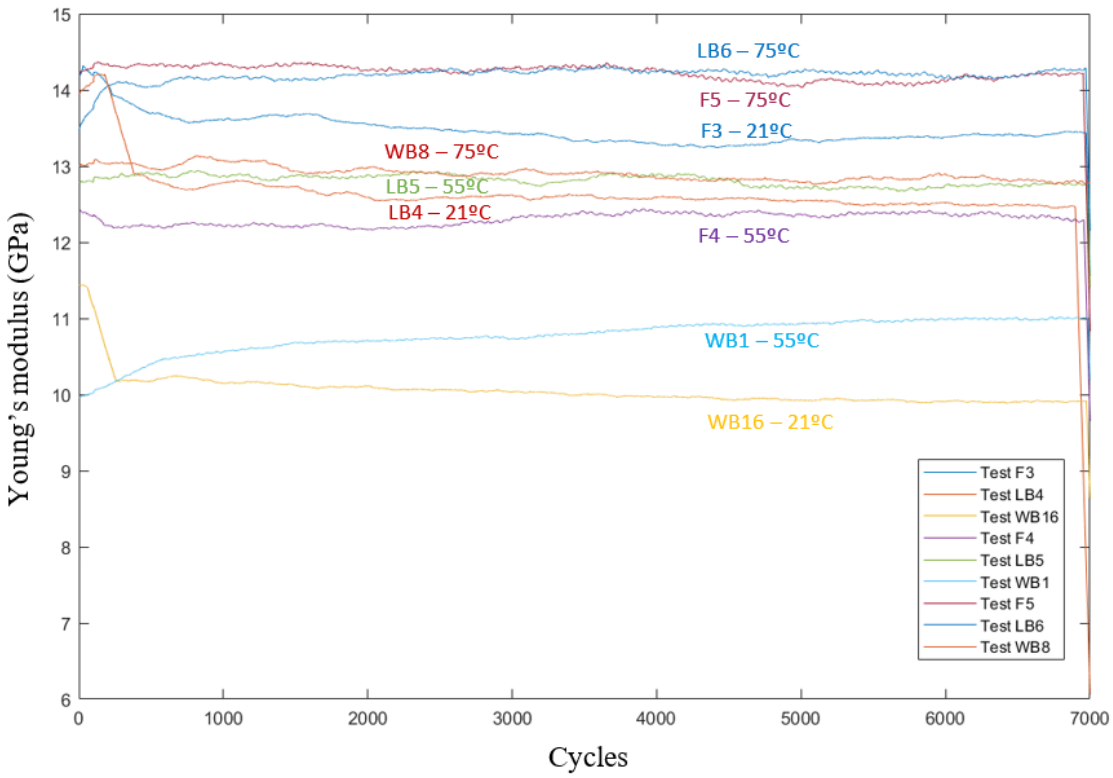

Figure 4.27: *Mean value of E/cycle for samples tested at 25MPa and 21-22° C, 55° C and 75° C from Winsford Mine.*

The Poisson's ratio (ν) does not change during the tests period. Each sample shows a steady ν value ranging between 0.2 and 0.5. Table 4.9 gives the mean value from Poisson's ratio calculated for each cycle. Samples F3 and LB4 show similar Poisson's ratio of 0.23-0.24. No Poisson's ratio was calculated for sample A3 due to the missing circumferential strain data, as previously explained in this section. Samples with a higher Poisson's ratio are the ones with a higher content in anhydrite and tested at room temperature and 55°C, B8 and B6, with values of 0.5 and 0.6. An important decrease in Poisson's ratio is observed with the increase of temperature, becoming more notable in samples tested at 75°C.

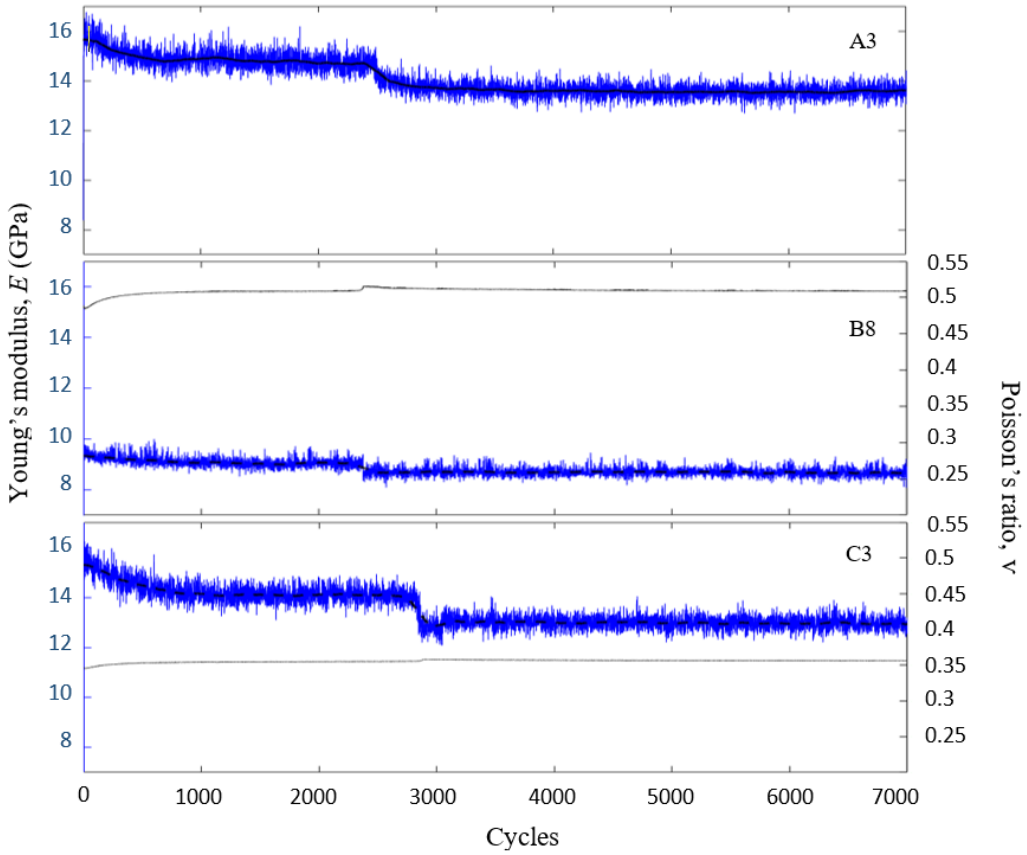

Figure 4.28: *Young's modulus (E) and Poisson's ratio cycle for samples tested at 25MPa and 21-22°C from Winsford Mine. The image shows how B8 was the samples with the lower fluctuation of E/cycle.*

Table 4.7: Minimum and maximum values of the static elastic parameters for tested samples under cyclic loading conditions at 25MPa confining pressure and room temperature (21-22°C), 55°C and 75°C.

Sample origin	Sample ID	Pc MPa	T C°	Young's modulus E (GPa)	Bulk modulus K (GPa)	Poisson's ratio ν
Boulby (Permian)	A3	25	21-22*	13.5-15.6	-*	-*
Boulby (Permian)	B8	25	21-22	8.7-9.3	23.7-24.0	0.50
Boulby (Permian)	C3	25	21-22	12.8-15.3	24.6-24.8	0.35
Boulby (Permian)	A7	25	55	11.6-12.3	24.3-24.4	0.44
Boulby (Permian)	B6	25	55	12.5-13.1	24.0-24.1	0.6
Boulby (Permian)	C5	25	55	11.5-12.86	-*	-*
Boulby (Permian)	B2-1	25	75	12.2	23.3-23.4	0.14
Boulby (Permian)	C2	25	75	9.1-9.6	23.7-23.9	0.1
Winsford (Triassic)	WB16	25	21-22	10.1-11.5	24.3	0.34
Winsford (Triassic)	F3	25	21-22	13.3-14.3	24.2-24.3	0.23
Winsford (Triassic)	LB4	25	21-22	12.5-14.2	24.3-24.4	0.24
Winsford (Triassic)	WB1	25	55	10.0-11.0	24.0	0.017
Winsford (Triassic)	F4	25	55	12.2-12.4	24.0-24.1	0.17
Winsford (Triassic)	LB5	25	55	12.8-12.9	23.8-23.9	0.09
Winsford (Triassic)	WB8	25	75	12.8-13.1	23.6-23.7	0.06
Winsford (Triassic)	F5	25	75	14.0-14.4	23.8-23.9	0.03
Winsford (Triassic)	LB6	25	75	13.6-14.3	23.7	0.015

*Lost data due to a problem with the measuring gauges

4.3.1.5 Tests conducted at 45 MPa confining pressure and temperatures of 55 and 75°C

A total of nine samples with different second phase content (anhydrite, polyhalite and clay) were tested under 45 MPa confining pressure, and temperatures of 55°C and 75°C (Table 4.8). The conditions applied represent the deepest conditions, i.e. a case scenario of 800-1200m depth as discussed in table 4.1. Optimizing the number of sample available allowed to test only 3 series of both at 55°C and 75°C, with only one sample from series A (A5) tested 75°C, and one sample from series B (B12) and series WB (WB9) tested at 55°C.

Table 4.8: Core samples from Boulby and Winsford Mine tested under cyclic axial stress between 4.5 and 7.5 MPa at a loading rate of 0.5 kN/s for a duration of 48h and a maximum number of 7200 cycles at a confining pressure (Pc) of 45 MPa and 55°C and 75°C temperature (T).

Temperature (T)	55°C	75°C
Boulby - Series A	-	A5
Boulby - Series B	B12	-
Boulby - Series C	C6	C1
Winsford - Series F	F6	F7
Winsford - Series LB	LB7	LB2
Winsford - Series WB	WB9	-

Figure 4.29 show stress-strain results for rock salt samples containing polyhalite and anhydrite (from Boulby Mine) tested at 45 MPa confining pressure. It can be noticed that sample B12 (from series B) is not recording the highest final axial strain in comparison to the rest of samples tested under same conditions. At 45 MPa confining pressure and 55°C, sample B12 shows one of the shortest final axial strain with a maximum ε_{ax} =0.12% and minimum ε_{ax} =0.10%. Only sample C1, tested under same confining pressure

but 75°C shows the same values for final maximum ε_{ax} =0.13% and minimum ε_{ax} =0.11%. A small increase in stiffness can be observed in the first load applied on sample B12, by showing a slightly convex trend in the increase from the initial 2MPa to 7.5 MPa. Sample B12 is the sample showing a bit higher stiffness in comparison to the rest of samples tested both at 55°C and 75°C.

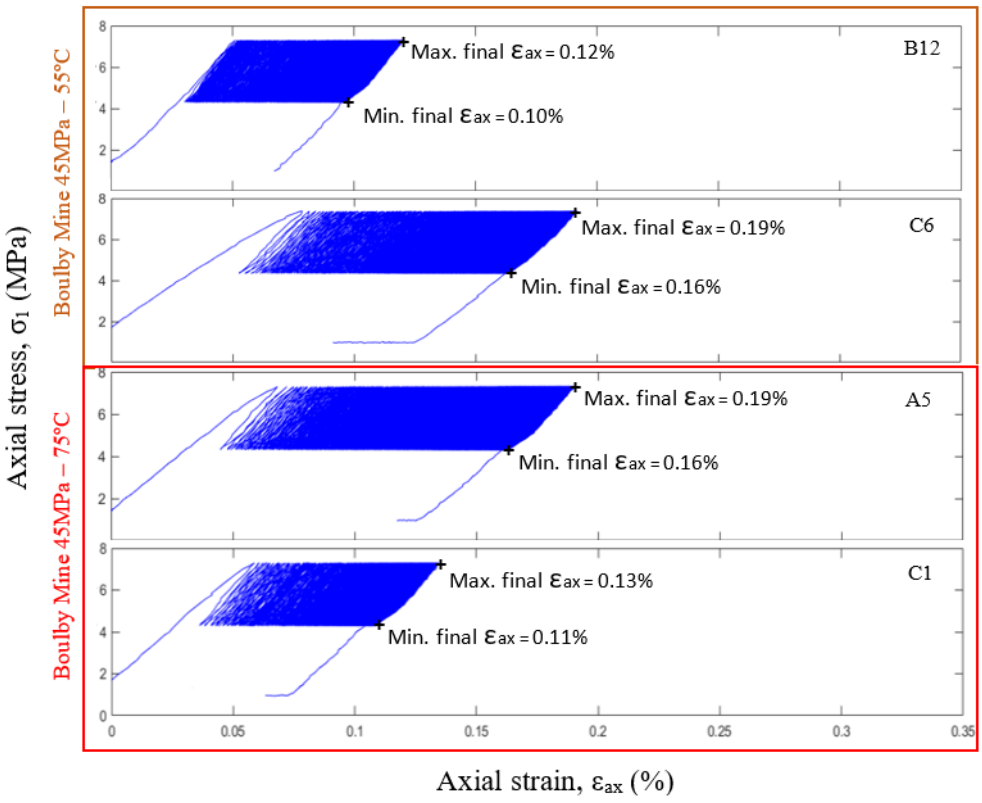

Figure 4.29: *Stress-strain curve for samples tested at 45 MPa confining pressure and 55°C and 75°C from Boulby Mine. Cyclic stress between 4.5-6.5 MPa at a loading rate of 0.5kN/s during 48h.*

Samples C6 and A5 show exactly the same final axial strain despite being tested at different temperatures of 55°C and 75°C respectively. The maximum ε_{ax} and minimum ε_{ax} for both samples were 0.19% and 0.16%, respectively. All samples with a halite content higher than 80% show a lower stiffness in comparison to sample B12 that has a higher content in anhydrite and polyhalite (i.e. less than 80% of halite).

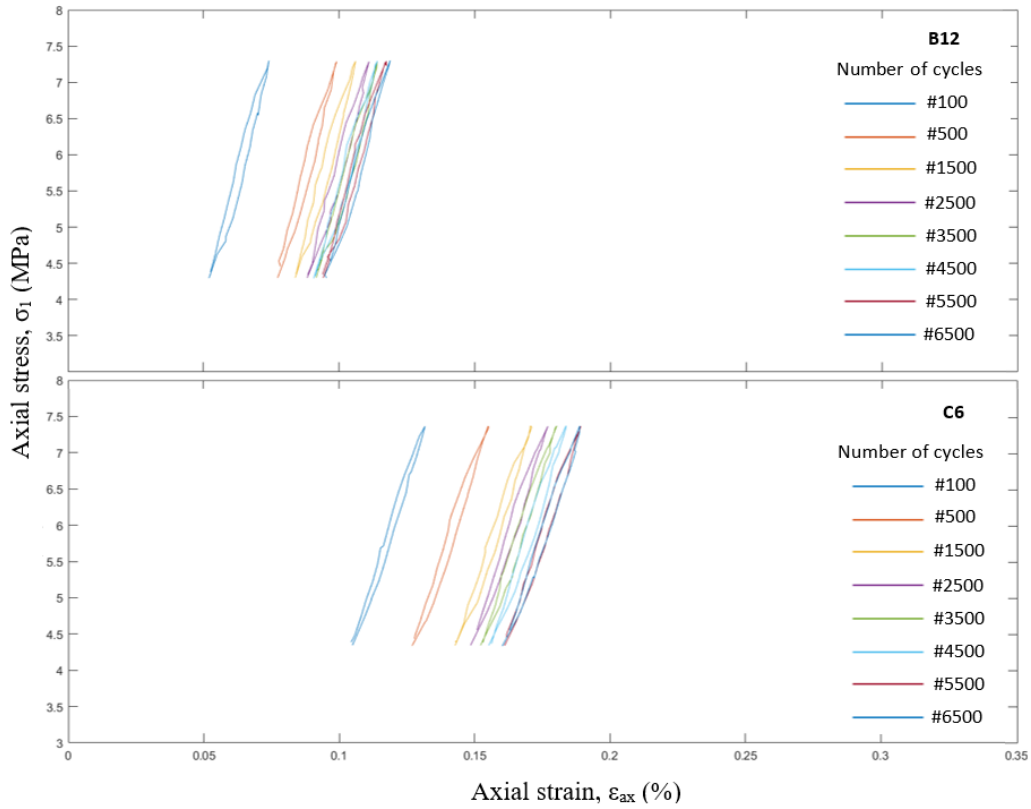

Figure 4.30: *Stress-strain hysteresis loop per cycle for samples tested at 45MPa and 55° C from Boulby Mine. Cyclic stress between 4.5-6.5 MPa at a loading rate of 0.5kN/s during 48h.*

The hysteresis loops from the stress-strain curves for samples B12 and C6 (55°C) evidence the change in rheological behaviour from series B in comparison to the other samples tested at lower temperatures and confining pressures (Figure 4.30). B12 shows greater inelastic deformation the first 500 cycles, and after 500 cycles, one can observe a strain hardening with a decrease of deformation rate. The hysteresis loops get closer from each other after 500 cycles and a slightly decrease in loop shape can be appreciated after 4500 cycles. C6 shows similar behaviour but the strain hardening is observed a bit later in time, after the 1500 cycles.

A significant change in rheological behaviour can be observed from sample C1 (tested at 75°C) if compared to sample C6 (tested at 55°C)(figure 4.31). C1 shows a little decrease in inelastic deformation within a single loop but

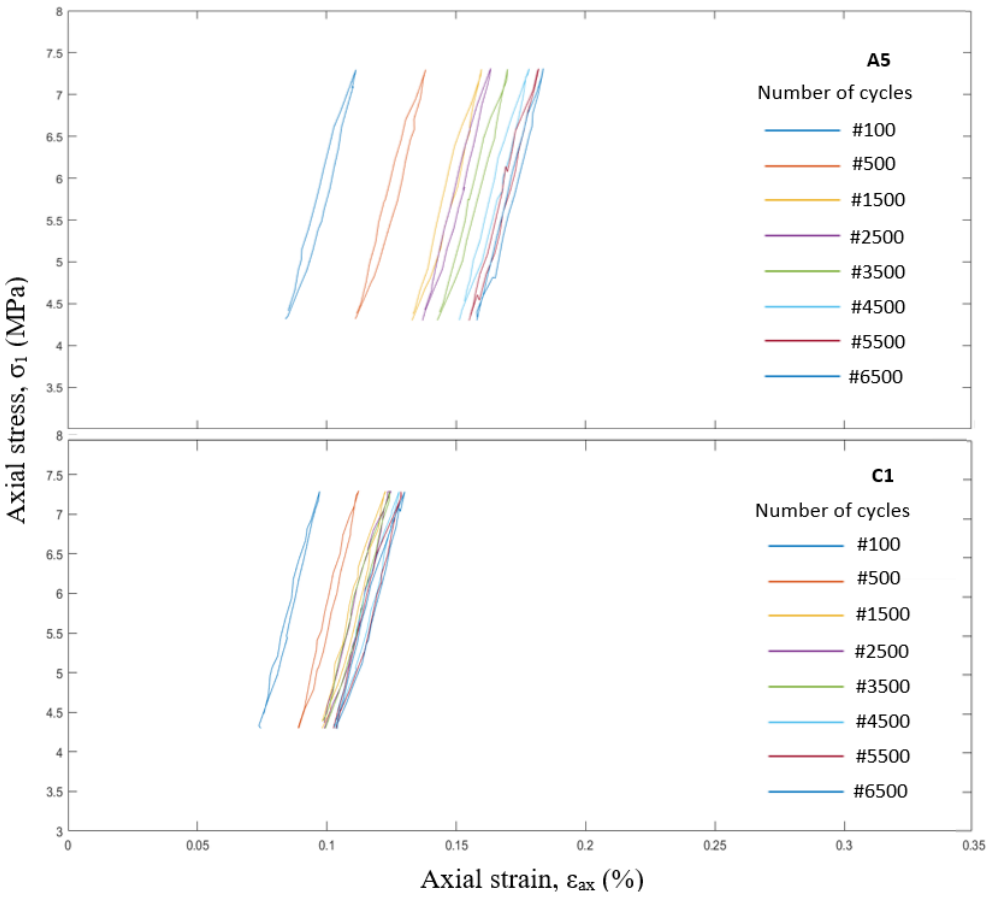

Figure 4.31: *Stress-strain hysteresis loop per cycle for samples tested at 45MPa and 75°C from Boulby Mine. Cyclic stress between 4.5-6.5 MPa at a loading rate of 0.5kN/s during 48h.*

it shows lower inelastic deformation between loading cycles in comparison to C6. A strong strain hardening can be observed after the first 1500 cycles in samples C1. A5 shows a more ductile behaviour although it also shows strain hardening after the first 1500 cycles. Both A5 and C1 seem to show a little recovery of ε_{ax} between 4500 and 5500 cycles.

Figure 4.32 shows ε_{circ} for samples containing polyhalite and anhydrite (Boulby Mine) tested at at 45 MPa. Almost all samples show a positive value of ε_{circ}, implying that the samples compressed laterally too during the cyclic loading mechanical test. Sample A5 (75°C) presents a positive logarithmic trend with an increase of ε_{circ} up to 0.08% by the end of the test: a fast increase in compression is observed during the first 500 cycles, followed by a gradual,

linear positive trend. Sample C1, also tested at 75°C, shows a very small extension ε_{circ}, which stays constant after the first 200-500 cycles. It is followed by an almost steady plateau trend just below 0% until reaching 3000 cycles. From 3000 cycles onwards, C1 ε_{circ} starts to gradually increase from 0.01%, at around 5500 cycles, to 0.03% by the end of the test. Another samples showing a positive recovery of ε_{circ} after experiencing lateral extension during the first 200 cycles is sample C6 (55°C).

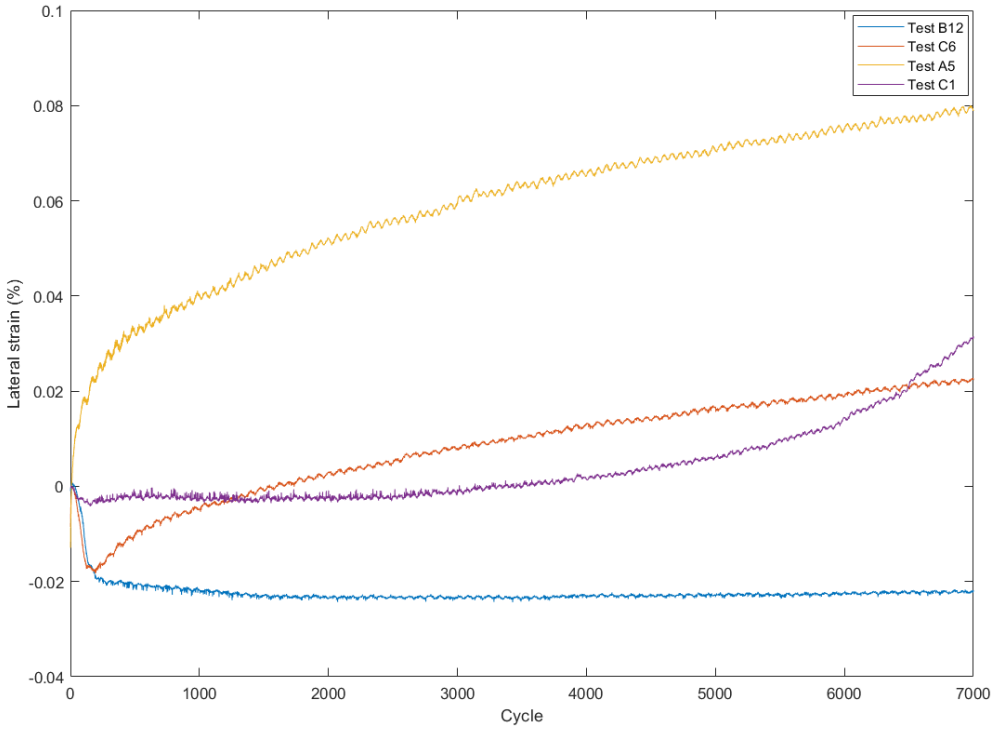

Figure 4.32: *ε_{circ} for samples tested at 45MPa and 55° C and 75° C from Boulby Mine. This figure show the impact of the increase in testing temperature over lateral strain showing lateral strain recovery.*

C6 records a prompt negative increase of ε_{circ} up to -0.019% just during the first 200 cycles. After the 200 cycles ε_{circ} recovers showing a positive logarithmic trend until a final ε_{circ} =+0.022%. The only sample showing a negative ε_{circ}, similar to the deformation behaviours observed in all previous samples tested at lower confining pressures and temperatures, is B12. B12 also shows a fast drop in ε_{circ}, down to -0.02%, during the first 200 cycles. After 200 cycles the negative increase of ε_{circ} stays almost steady reaching an almost plateau

trend with very small increase. B12 shows a final ε_{circ} =-0.022%.

Data of stress-strain for rock salt samples with clay and anhydrite can be seen in figure 4.33. As usual, series LB are the samples recording a higher axial strain in comparison to the rest of the tested series of rocks.

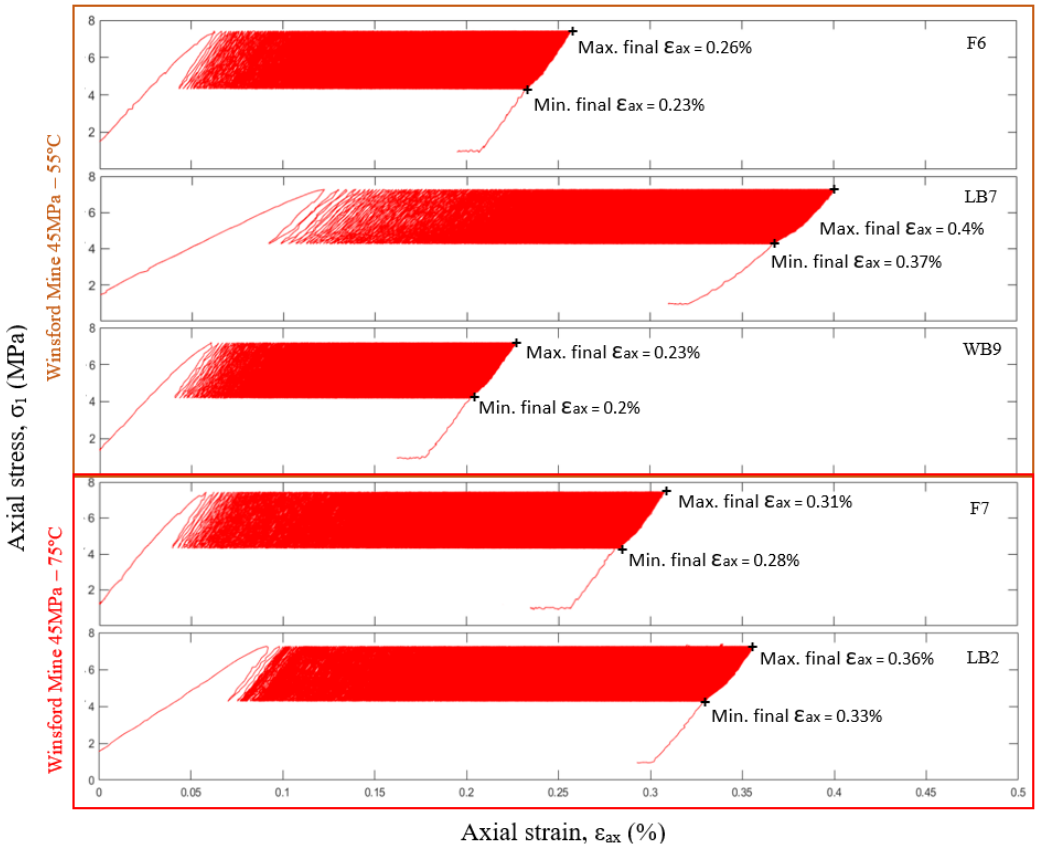

Figure 4.33: *Stress-strain curve for samples tested at 45 MPa confining pressure and 55° C and 75° C from Winsford Mine. Cyclic stress between 4.5-6.5 MPa at a loading rate of 0.5 kN/s during 48h.*

Sample LB7 (55°C) recorded a maximum ε_{ax} =0.4% and a minimum ε_{ax} =0.37% whereas sample LB2 had a maximum ε_{ax} =0.36% and a minimum ε_{ax} =0.33%. Sample LB7 shows the lowest stiffness from all samples tested at 45 MPa. LB2, although it was tested at a higher temperature, shows slightly higher stiffness and lower axial strain in comparison to LB7. The second group of sample with the higher axial strain are samples from series F. Both samples tested at different temperatures show similar stiffness with maximum ε_{ax} =0.26% and minimum ε_{ax} =0.23%, for sample F6 tested at 55°C, and maximum ε_{ax} =0.31%

and minimum ε_{ax} =0.28%, for sample F7 tested at 75°C. Due to a lack of sample availability, specimen WB9 is the only sample from this series that was tested at 45 MPa and 55°C. WB9 shows the same stiffness as F6 and F7 but a lower axial strain with a maximum ε_{ax} =0.23% and minimum ε_{ax} =0.2%.

The analysis of hysteresis loops from samples from Winsford Mine show no ε_{ax} recovery and series LB as the samples with higher inelastic deformation within each loading cycle (Figure 4.34).

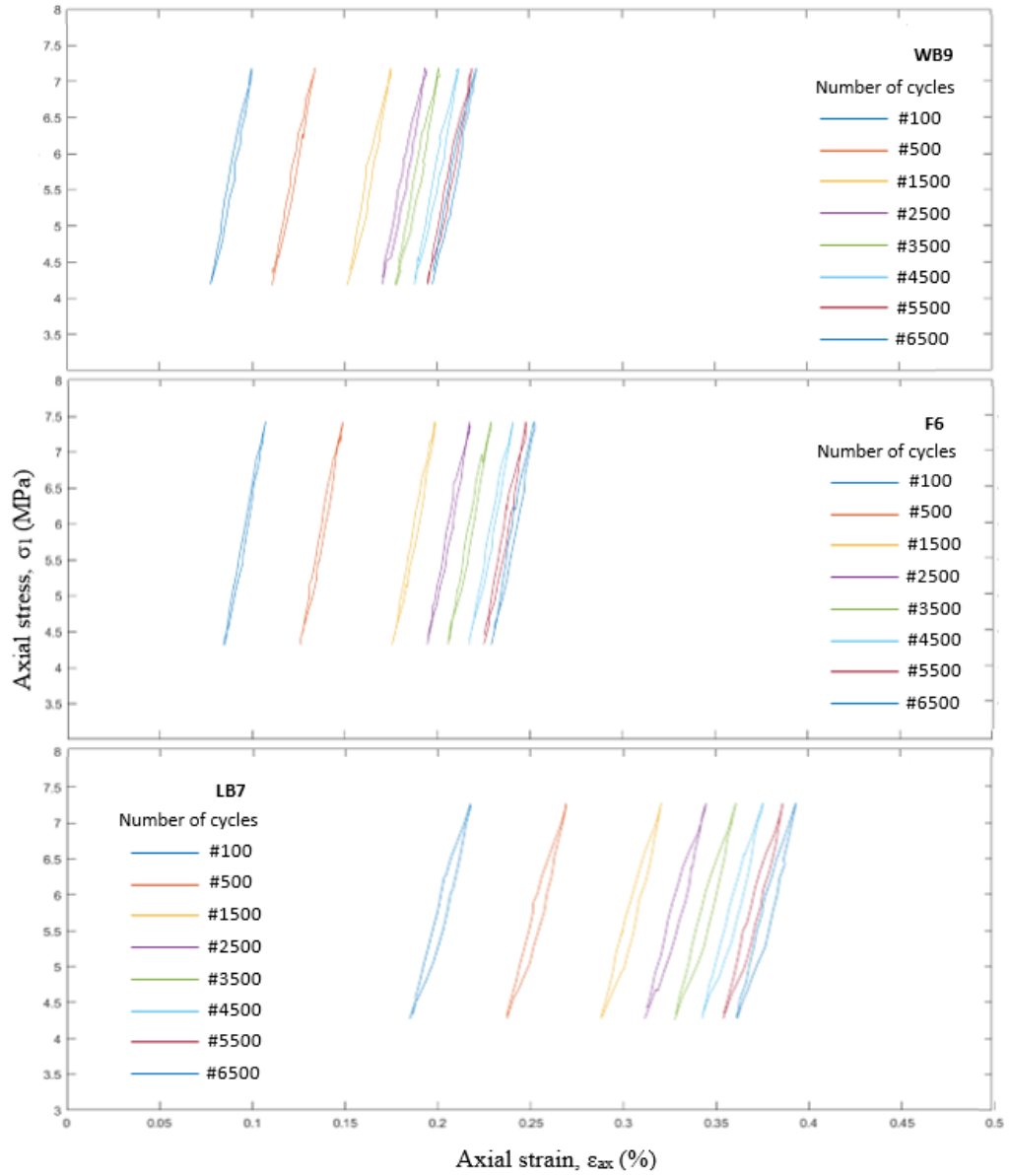

Figure 4.34: *Hysteresis loops per cycle from stress-strain curve for samples tested at 45 MPa and 55° C from Winsford Mine. Cyclic stress between 4.5-6.5 MPa at a loading rate of 0.5kN/s during 48h.*

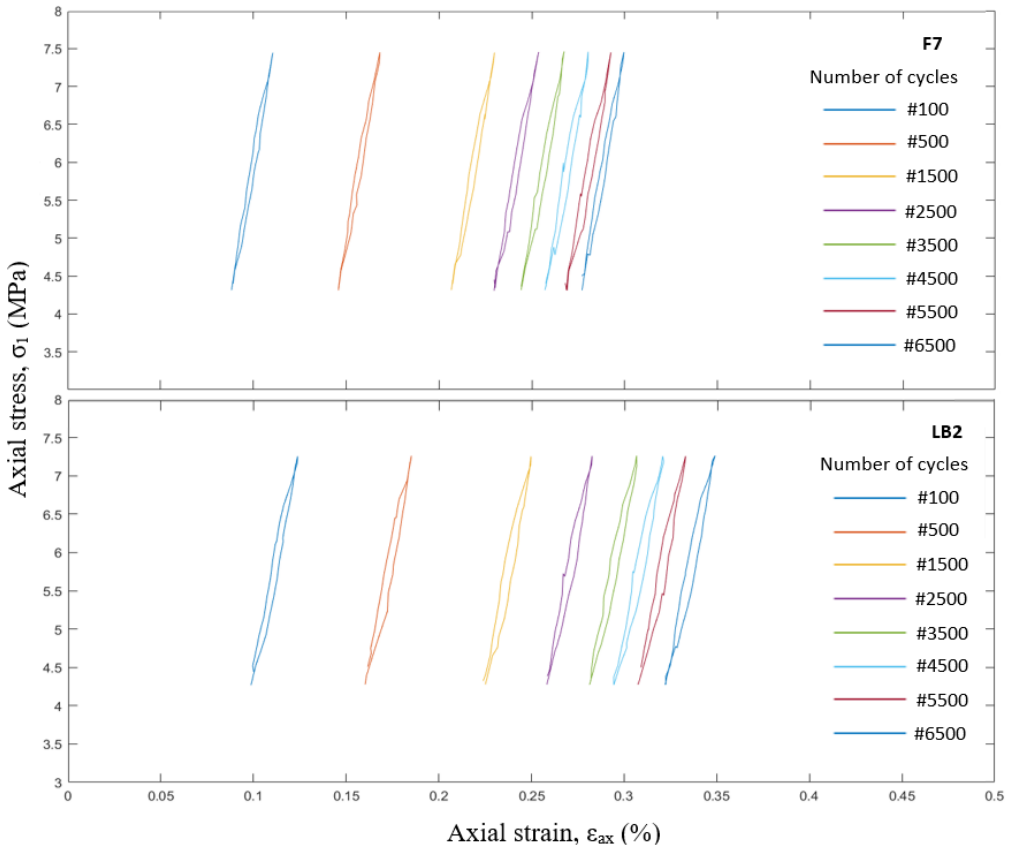

Figure 4.35: *Hysteresis loops per cycle from stress-strain curve for samples tested at 45 MPa and 75°C from Winsford Mine. Cyclic stress between 4.5-6.5 MPa at a loading rate of 0.5kN/s during 48h.*

LB7 (55°C) shows a lower stiffness and higher ductility with a higher inelastic behaviour both between and within a cycle. Samples WB9 and F6 show a very similar behaviour although F6 presents slightly higher plastic deformation between the first 1500 cycles resulting in a higher final ε_{ax} in comparison to WB9. F6 also shows slightly more inelastic deformation from one cycle to another after the 2500 cycles although the difference with WB9 is smaller after this point of the test. Both samples WB9 and F6 seem to have similar elastic behaviour within each mechanical loading cycle and less irreversible deformation in comparison to sample LB7. Samples F7 and LB2 present a great plastic deformation in comparison to the other samples tested at 55°C, being LB2 the sample recording a higher ductility with a higher final ε_{ax} in comparison to F7.

As observed in samples from Boulby Mine (containing polyhalite and anhy-

drite), samples from Winsford Mine (with clay and anhydrite content) F7 and LB2, both tested at 45 MPa confining pressure and 75°C, show either positive values of ε_{circ} or an initial compression previous to a ε_{circ} extension. However, all samples F5, LB6 and WB8 tested at 45 MPa and 55°C, have the usual negative growth trend of lateral strain observed in other samples tested tested at lower temperatures and confining pressures. Sample F6 is, as observed in samples from series F tested at 25 MPa and 55°C and 75°C, the sample with the greatest ε_{circ} extension in comparison to the other samples tested under the same conditions of temperature (55°C) and confining pressure (45 MPa). Sample F6 registers a fast increase in lateral strain during the first 500 cycles recording a ε_{circ}=-0.08%. After the first 500 cycles, lateral strain expansion rate starts to slow down until between 3000 and 4000 cycles reaching a ε_{circ}=-0.12%. After 4000 cycles ε_{circ} keeps decreasing slowly with a small gradual negative trend until reaching ε_{circ}=-0.13% by the end of the test. WB9 shows a similar negative logarithmic trend to sample F6, with a fast increase of ε_{circ} expansion within the first 500 cycles followed by a slow down in expansion rate after 500 cycles until around 2500 cycles, where ε_{circ} reaches -0.05%. After 2500 cycles the negative trend keeps almost steady around -0.05/-0.055%. Sample LB7 shows a faster negative increase in ε_{circ} during the first 200 cycles until getting ε_{circ} around -0.03%. However, after the huge increase in the first 200 cycles, it reaches an almost steady trend for the rest of the test with a final ε_{circ}=-0.035%.

Sample LB2, tested at 75°C, is the only rock salt sample with clay content showing a positive ε_{circ} for the whole test. A previous peak around ε_{circ}=0.02% is recorded just within the first 200 cycles. The peak is followed by a small decrease to ε_{circ}=0.015% approximately and a gradual positive ε_{circ} increase until the end of the test from after the first 200 cycles. LB2 records a final ε_{circ}=0.05%. F7 also presents a peak in ε_{circ} at around 0.01% followed by a drop down to 0%, within the first 200 cycles. From 200 to 1500-2000 cycles,

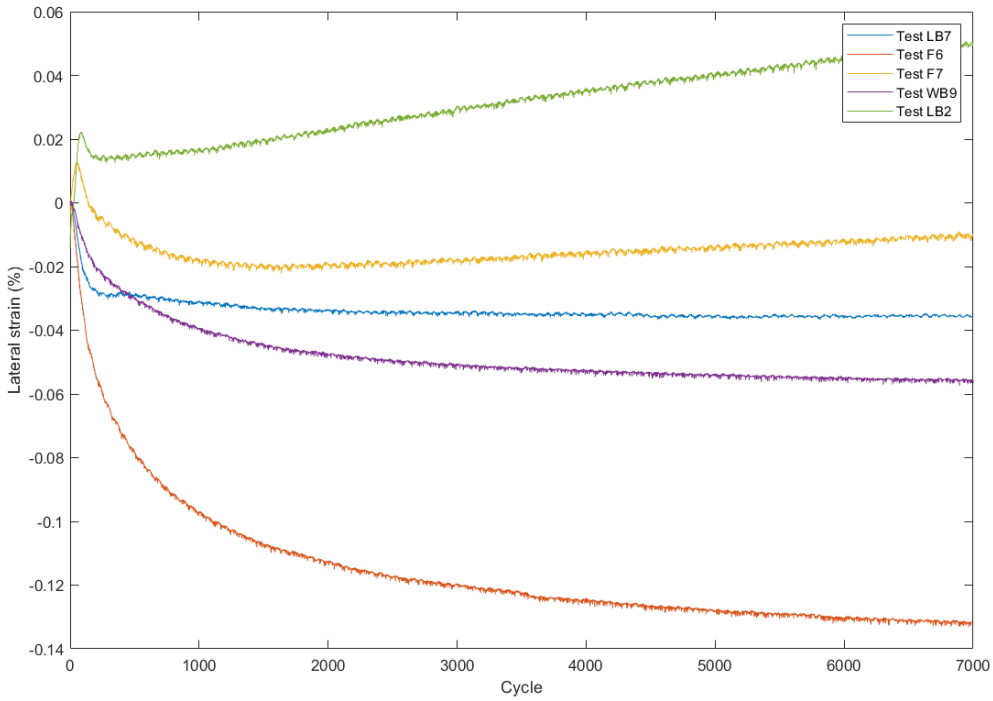

Figure 4.36: *ε_{circ} for samples tested at 45MPa and 55° C and 75° C from Winsford Mine.*

there is a gradual negative increase up to ε_{circ}=0.02%. However, after the 2000 cycles, the negative tendency is reverted and a slightly positive recovery in ε_{circ} can be noticed up to -0.01% by the end of the test.

4.3.1.6 Elastic parameters for samples tested at 45 MPa confining pressure and temperatures of 55 and 75° C

Figure 4.37 shows Young's modulus for all samples tested at 45 MPa confining pressure. All samples show quite smooth curves in comparison to other samples previously discussed. Samples from series F, F6 and F7, show very similar E values with a very similar curve evolution. Both samples record an initial E of 14 GPa and a 13.5 GPa by the end of the test. Sample B12 shows an initial E of 13.8 GPa. After the first 300 cycles there is a small drop followed by a smoother decrease from 500 cycles. By the end of the test B12 records a final E of 13 GPa. Sample WB9 shows a similar trend to B12, although the

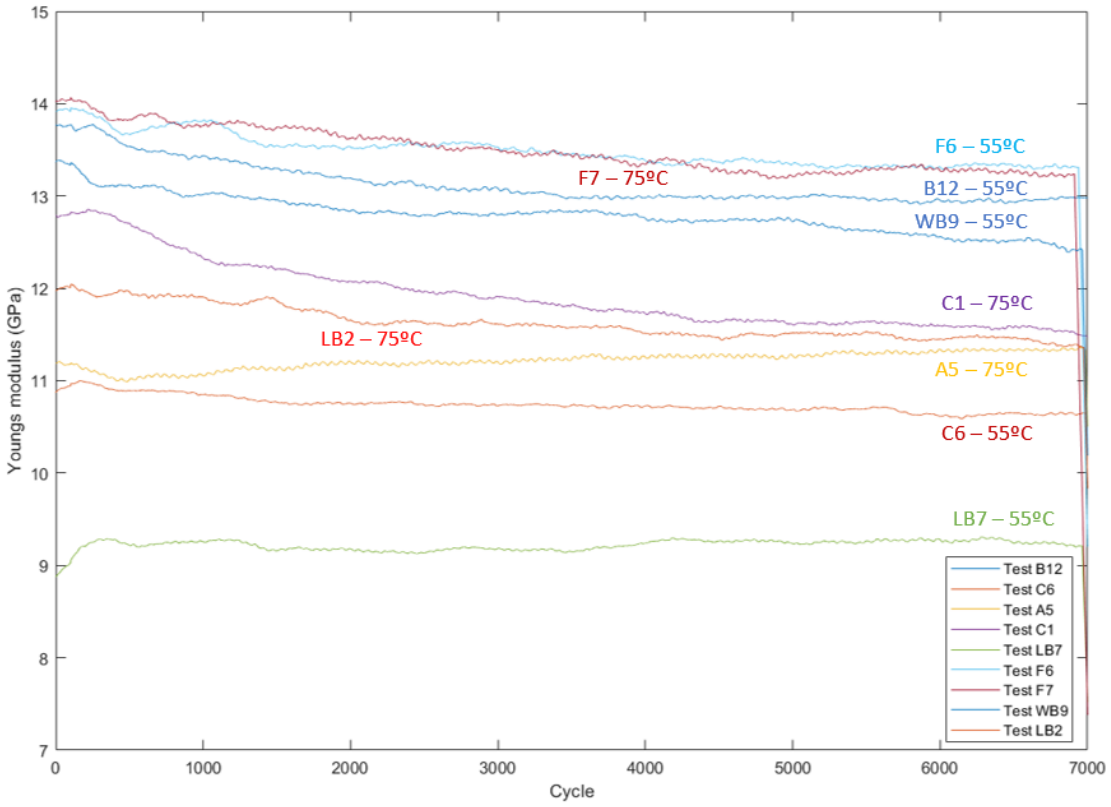

Figure 4.37: *E versus number of cycles for samples tested at 45MPa and temperatures of 55° C and 75° C.*

initial small drop takes place during the first 100-200 cycles. WB9 records a E of approximately 13.5 GPa at the beginning of the test and 12.5 GPa by the end of the test.

All samples tested at 75°C (C1, A5, LB2) show Young's Modulus between 11 and 13 GPa. Sample C1 has an initial Young's Modulus of 12.8 GPa and, from 300 to 1000 cycles, E decreases from 12.8 GPa to 12.2 GPa. After the first 1000 cycles, the decreasing rate slows down reaching a final E of 11.5 GPa. LB2 shows initial E of 12 GPa and a quite slow rate decreasing rate without significant drops after the first 2000 cycles. Prior to the 2000 cycles the E curve nearly plateaus with very small variations around 12 GPa. LB2 records a final E value of 12.5 GPa. Sample A5 is the only sample showing a very small increase of E by the end of the test. A5 starts the tests with an E=11.2 GPa and by the end of the tests A5 shows the same E value of 11.5GPa than

LB2. Finally, both C6 and LB7 show very similar smooth trend almost steady for the whole test, with a very small increase during the first 200 cycles. C6 shows initial E of 11 GPa and final E of 10.6 GPa and LB7 shows initial and final values of E of 9 GPa and 9.2 GPa respectively.

Table 4.9: Minimum and maximum values of the static elastic parameters for tested samples under cyclic loading conditions at 45 MPa confining pressure and temperature of 55°C and 75°C.

Sample origin	Sample ID	Pc MPa	T C°	Young's modulus E (GPa)	Bulk modulus K (GPa)	Poisson's ratio ν
Boulby (Permian)	B12	45	55	13.0-13.8	24.1-24.15	0.50
Boulby (Permian)	C6	45	55	10.6-11.0	24.25-24.3	0.4
Boulby (Permian)	A5	45	75	11.2-11.3	24.0	0.1
Boulby (Permian)	C1	45	75	11.5-12.8	24.15	0.08
Winsford (Triassic)	WB9	45	55	12.4-13.4	23.5	0.3
Winsford (Triassic)	F6	45	55	13.3-14.0	24.2-24.3	0.4
Winsford (Triassic)	LB7	45	55	9.0-9.3	24.2-24.3	0.1
Winsford (Triassic)	F7	45	75	13.3-14.0	24.1-24.2	0.35
Winsford (Triassic)	LB2	45	75	11.4-12.0	23.6	0.06

*Lost data due to a problem with the measuring gauges

4.3.2 Cyclic loading tests between 6 and 20 MPa

A total of 14 samples (from series A, F and WB only) were tested under a higher range of cyclic stress conditions between 6 and 20 MPa, equivalent to in situ hydrogen storage conditions as previously discussed. The tests have the same loading rate (0.5 kN/s) and duration of 48h as previous tests conducted at a lower amplitude of cyclic loading stresses resulting in a total number of 1500 cycles. A structural analysis after deformation was also conducted in some samples; their structural analysis after deformation is discussed in the Chapter 5.

4.3.2.1 Tests conducted at 25 MPa confining pressure and temperatures of 25, 55 and 75°C

A total of three samples from series A (Boulby Mine), series F and series WB (from Winsford Mine) were tested at 25 MPa confining pressure and temperatures of 25, 55 and 75°C under cyclic mechanical conditions between 6 and 20 MPa. Figure 4.38 and 4.39 show the results of the stress-strain curves for samples from Boulby Mine and Winsford Mine, respectively.

From all samples of series A (with anhydrite and polyhalite as main second phase content), sample A1 (55°C) shows a higher final axial strain with a ε_{ax} =3.2%, at the maximum final load, and ε_{ax} =3.1%, at the minimum final load. A1 also shows the highest axial deformation in the first load with an important ductile response. The second sample with the highest final axial strain is sample A9, tested at 75°C, with a maximum and minimum final ε_{ax} of 1.9% and 1.8%. Sample A10 (25°C) is the sample with the lowest axial strain with final ε_{ax} =0.6%, at the maximum final load, and ε_{ax} =0.5%, at the minimum final load.

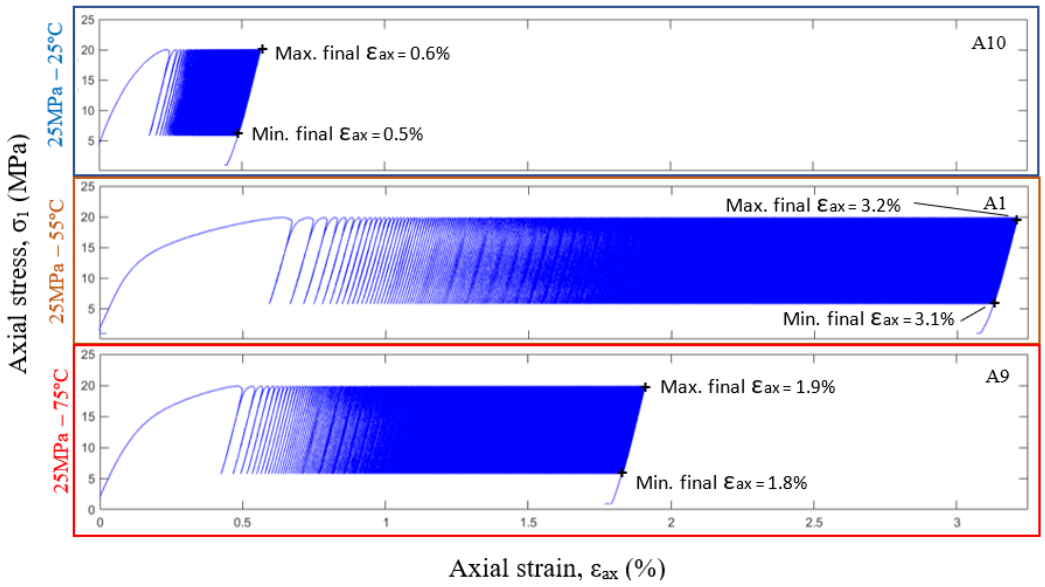

Figure 4.38: *Stress-strain data for samples tested at 25 MPa confining pressure and 25, 55° C and 75° C from Boulby Mine. Cyclic loading stress between 6-20 MPa at a loading rate of 0.5 kN/s during 48h. This figure shows the noticeable increase in final axial strain with the increase of temperature. In this case, the higher final axial strain was recorded in sample A1, tested at 55° C and the second higher axial strain was recorded in sample A9 tested at 75° C.*

All rock salt samples with anhydrite and clay content (Winsford Mine) tested at 25 MPa with a higher range of cyclic mechanical load show a very similar rheological behaviour within the first load independently of the temperature at which were tested. From samples tested at 25°C, WB3 is the sample with the lowest axial strain, with a final maximum load ε_{ax} =1.2% and final minimum load ε_{ax} =1.1%; sample F8 records ε_{ax} =2.1% and ε_{ax} =2%, respectively.

Samples tested at 55°C, F9 and WB4, present the same rheological behaviour both with ε_{ax} =2.1% and ε_{ax} =2% for maximum and minimum final strains.

At 75°C, WB5 also exhibits the same rheological behaviour as WB4, F9 (55°C) and F8 (25°C). Sample F10 is the sample with the greatest amount of axial strain with a maximum final ε_{ax} =3.1% and minimum final ε_{ax} =3.05%. Sample F10 also shows a higher noise resulting in small jumps represented as spikes in the stress-strain curve.

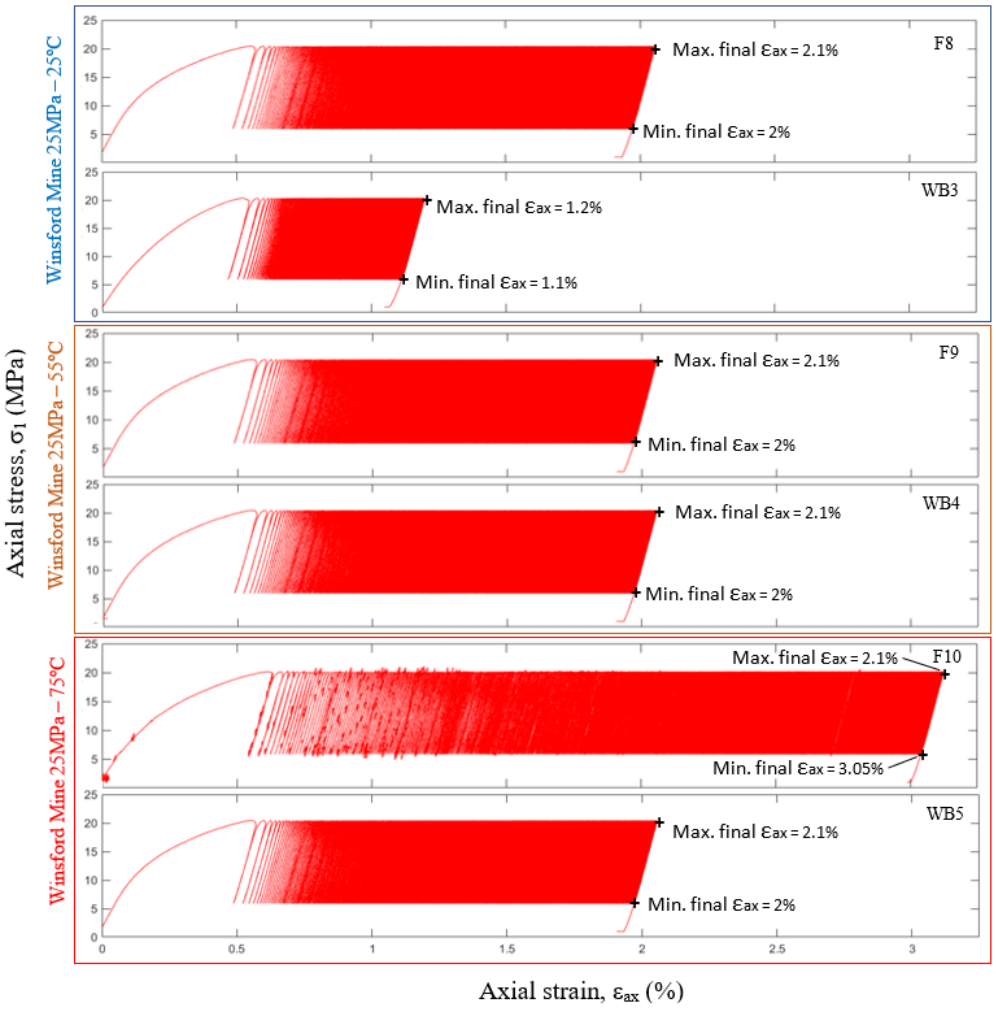

Figure 4.39: *Stress-strain curve for samples tested at 25 MPa confining pressure and 25, 55° C and 75° C from Winsford Mine. Cyclic stress between 6-20 MPa at a loading rate of 0.5 kN/s during 48h. This figure shows the impact of the testing temperature in rock salt deformation. An increase of final axial strain can be observed with an increase of temperature.*

This noise could be related to local fracturing of the sample during the compression cyclic loading test or some instability on the strain gauge signal during the test.

4.3.2.2 Tests conducted at 45 MPa confining pressure and temperatures of 55 and 75°C

A total number of 5 samples were tested at 45 MPa confining pressure and 55 and 75°C under cyclic mechanical loading conditions of 6-20 MPa. Only samples from series A and WB were tested at both 55 and 75°C whereas only one sample from series F was tested at 55°C (Figure 4.40).

In general, samples from Boulby and Winsford Mine have very similar rheological behaviour at the beginning of the test (during the first cyclic load) independently of the testing temperature, although the most similar first stiffness recorded occurs within samples with clay and anhydrite as second phase content. All samples F11, WB6 and WB7 show exactly the same mechanical behaviour with a ε_{ax} =2.1%, at the maximum final load, and ε_{ax} =2%, at the minimum final load. Samples from Winsford Mine also has similar rheological behaviour within the first axial load. Just a very small increase can be observed in axial strain recorded during the first mechanical load in WB6 in comparison to F11.

In general trends, an increase in cyclic loading stress and its amplitude results not only in an increase in the final axial strain, but also a higher ductile behaviour recorded within the first cycle. However, after the first cycle, the cyclic loading pattern from the stress-strain plot is very similar to other samples tested under cyclic loading conditions at a lower amplitude.

4.4 Concluding Remarks

Samples with different second phase content such as anhydrite, polyhalite and clay have been tested under low amplitude cyclic loading conditions between 4.5 and 7.5 MPa and high amplitude cyclic loading conditions of 6 to 20 MPa.

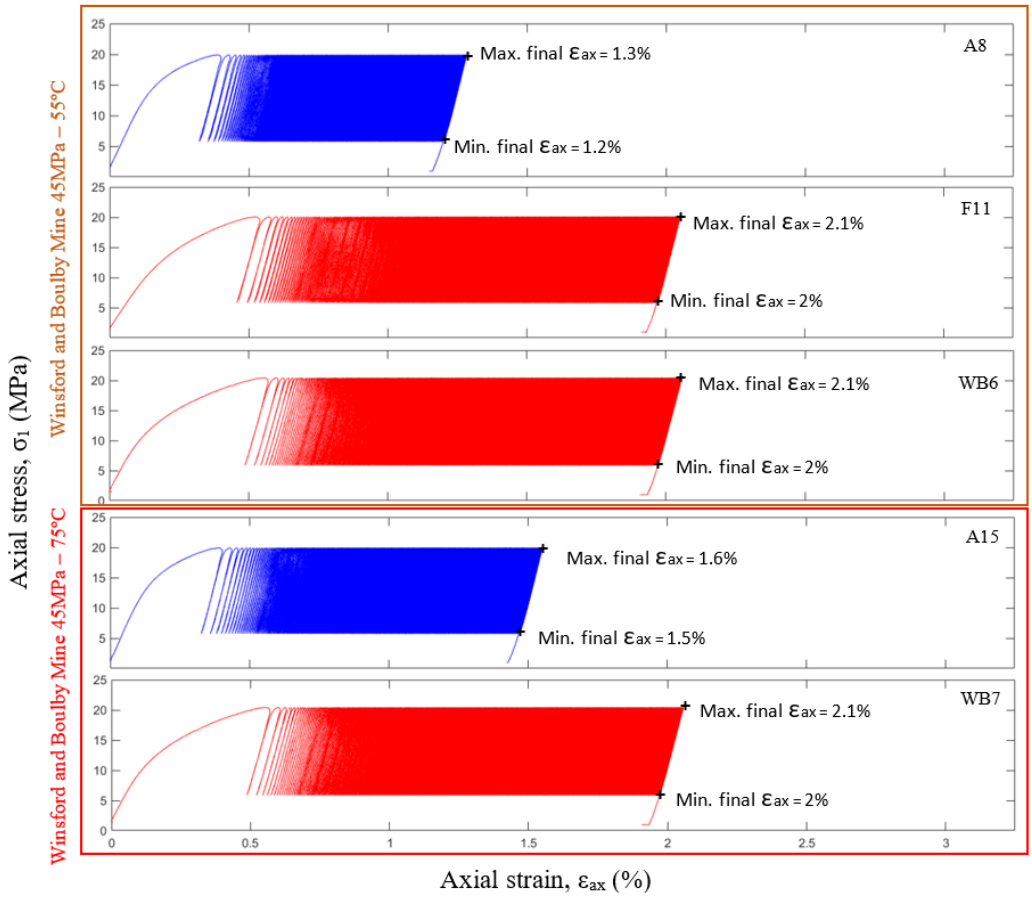

Figure 4.40: *Stress-strain data for samples tested at 45 MPa confining pressure and 55° C and 75° C from Boulby and Winsford Mine. Cyclic stress between 6-20 MPa at a loading rate of 0.5 kN/s during 48h. This figure shows not only the impact of temperature in rheological behaviour of rock salt but also the effect of second phase content. Samples with a higher anhydrite and clay content (in red colour) present larger final axial strains in comparison to samples with anhydrite and polyhalite as main second phase content.*

From samples with anhydrite and polyhalite as main second phase content (Series A, B and C), samples from Series B show higher final ε_{ax} and ε_{circ} when tested at room temperature and 55°C and low confining pressure (12 MPa). Samples from series B also show lower stiffness at room temperature than Series A and C. However, with the increase of temperature, stiffness from Series A and C decreases at similar values as samples from Series B. Although Series B records the larger ε_{circ} at room temperature, with the increase in temperature, it is samples from series C which show a greater lateral expansion in comparison to other samples with anhydrite and polyhalite as main second phase content.

Among all samples with a higher content in clay and anhydrite as second phase content, samples from series LB are the samples showing a higher final axial strain (ε_{ax}) but not the larger lateral expansion (ε_{circ}). Generally, samples from series F are the samples showing the higher lateral strain and second larger final axial strain. Samples tested from Series LB present less stiffness than samples WB and F, and it becomes more noticeable with the increase of temperature. The increase of temperature results in an increase of final ε_{ax} for all samples from series F, LB and WB. Sample F3, tested at room temperature, show relevant fluctuations in lateral strain.

Some samples tested at higher confining pressures and temperatures, independently of the second phase content, show positive ε_{circ} or some positive of ε_{circ} at some point during the cyclic mechanical loading test.

A strain hardening can be observe for all samples with the increase of cycles. In general, the strain hardening can be observed around the 2500-3500 cycles although it is more obvious in samples tested at high confining pressures of 45 MPa and samples tested at room temperature and samples with a second

phase content of anhydrite and polyhalite. In the contrary, samples with a higher content in clay and tested at 25 MPa and high temperature of 75°C showed a less noticeable strain hardening.

Samples tested at low temperature (room temperature), show higher variations of modulus of elasticity (E) in comparison to samples tested at 55-75°C. The range of Young's modulus calculated for all samples is between 9 to 18 GPa with bulk modulus oscillating between 22-25 GPa. Poisson's ratio values can range from around 0.03 to 0.6, depending on the sample.

Chapter 5

Micro-structural analysis after deformation

5.1 Introduction

A post-deformation analysis by using transmitted light and scanning electron microscopy, with thin sections, was performed after the cyclic mechanical loading tests. The aim of this analysis was to identify changes in the sample's micro-structure as result of the cyclic mechanical loading deformation. The micro-structural analysis has been used to better assess the study on the impact of different second phase content and rock texture on the rheological behaviour discussed in the previous chapter.

A total of 33 thin sections of samples from different series of rocks tested have been analysed under transmitted, reflection and Scanning Electron Microscopy. Thin sections were prepared from core samples tested at low and high cyclic mechanical loading. The analysis of blue dye impregnated, one-side polished thin sections after deformation are described and compared to previous to deformation thin sections in order to identify main deformation structures and damage from cyclic loading conditions.

The post-deformation analysis, in combination with the pre-deformation analysis discussed in Chapter 3, offers an insight of the micro-damage linked to the second phase content. At the same time, the post-deformation analysis with thin sections, in combination of the mechanical data, provides a better understanding for the changes in the elastic parameters recorded under the cyclic loading mechanical conditions.

5.2 Methodology

5.2.1 Thin section preparation

After deformation, the tested samples were impregnated similarly to the off-cut samples used for the mineralogical analysis (please refer to Chapter 3 for more details). Then they were sliced in half along the plan parallel to the principal maximum stress applied $\sigma 1$ (Figure 5.1). One half was used to prepare the thin sections (for the structural analysis after deformation) again at the same precision ($\sim 200\mu$m) the off-cuts were prepared. The second half was preserved for XRD analysis to monitor any mineralogical variations in the sample from the initial assessment before the test. Note that the thin sections from the samples done before deformation were performed using the same orientation as the samples after deformation.

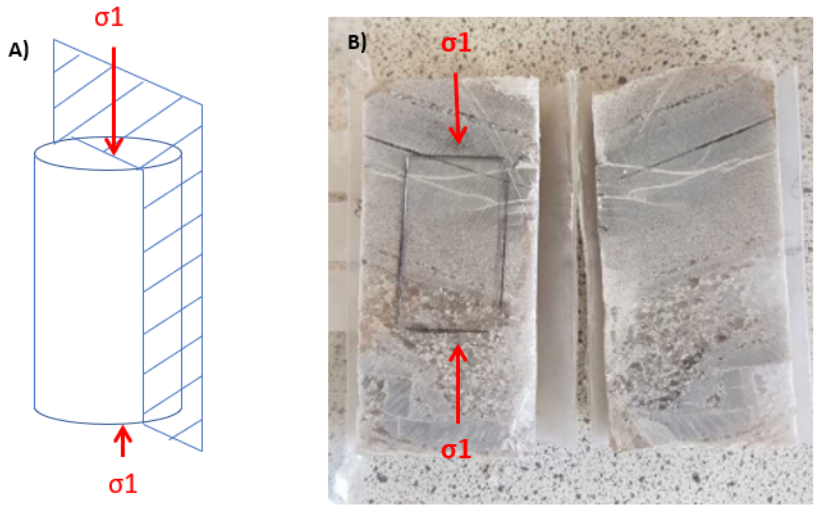

Figure 5.1: *A) Schematic image of core sample preparation for thin sections. B) Image of a core sample already cut with the thin section mark drawn in the surface parallel to the cyclic stress $\sigma 1$ applied during the cyclic mechanical loading test.*

5.2.2 Transmitted and reflected light microscopy

The light transmitted microscopy used to the analysis of thin sections after deformation was the same Zeiss Microscope used for the mineralogical charac-

terisation before deformation (described in Section 3.2.3).

The light in the reflected light microscope, which is originated in the lamp house, goes through the collector lens and the vertical illuminator. The light passing through the vertical illuminator is controlled by the aperture and field diaphragms (Figure 5.2. After passing the vertical illuminator, the light is reflected by a beamsplitter, which consists of an elliptically shaped mirror, before illuminating the sample through the objectives (Zeiss, Zeiss). Finally, the reflected light from the surface of the sample re-enters the objective where it can be observed in the binocular head. Reflected light microscopy is useful to analyse the surface of the sample.

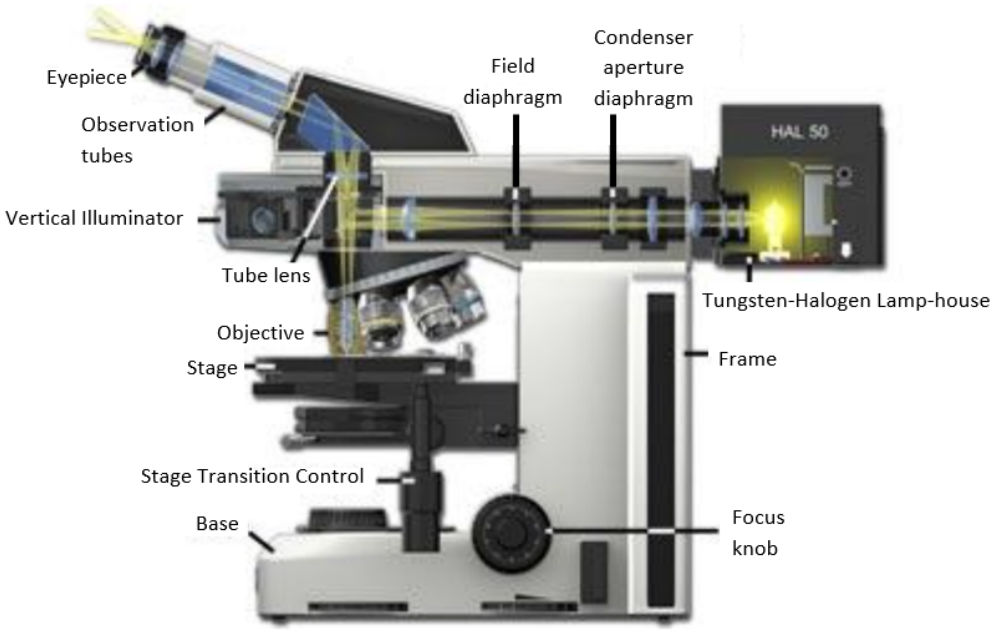

Figure 5.2: *Schematic picture from a Reflected light microscope (Zeiss, Zeiss).*

5.2.3 Scanning Electron Microscope (SEM)

Scanning Electron Microscopy (SEM) allows the characterisation of surfaces and materials at a micrometer (μm) and submicrometer scale by irradiation of the study area with a focused electron beam. Different types of signals

like secondary electrons, back-scattered electrons, characteristic and continuum x-rays, Auger electrons, and photons of various energies, result from the interaction between the electron beam with the specimen surface providing information about the topography of the specimen surface and composition. The signals produced as a result of electron- specimen interactions are secondary electrons, backscattered electrons, Auger electrons, x- ray, and photons of different energies. The SEM technique uses secondary and backscattered electrons and X-ray (Goldstein et al., 2017) to create high resolution images at microscale. Secondary electrons provide information about the topography whereas backscattered electrons are used to characterise samples composed of multiple phases.

X-rays result from the inelastic collisions, or scattering, between the focused electron beam and the electrons of the specimen's atoms. The electron beam is generated at the electron gun and passed through a series of electromagnetic lenses resulting in a focused beam of electrons within the part of the instrumentation called the column. The focused beam of electrons interacts with a specific area of the specimen that is placed on a stage in the chamber. Both the column and the chamber have been previously drawn to vacuum (Goldstein et al., 2017; Choundhary et al., 2017). Figure 5.3 shows a schematic picture of a SEM and the lens the electron beam goes through before arriving to interact with the sample.

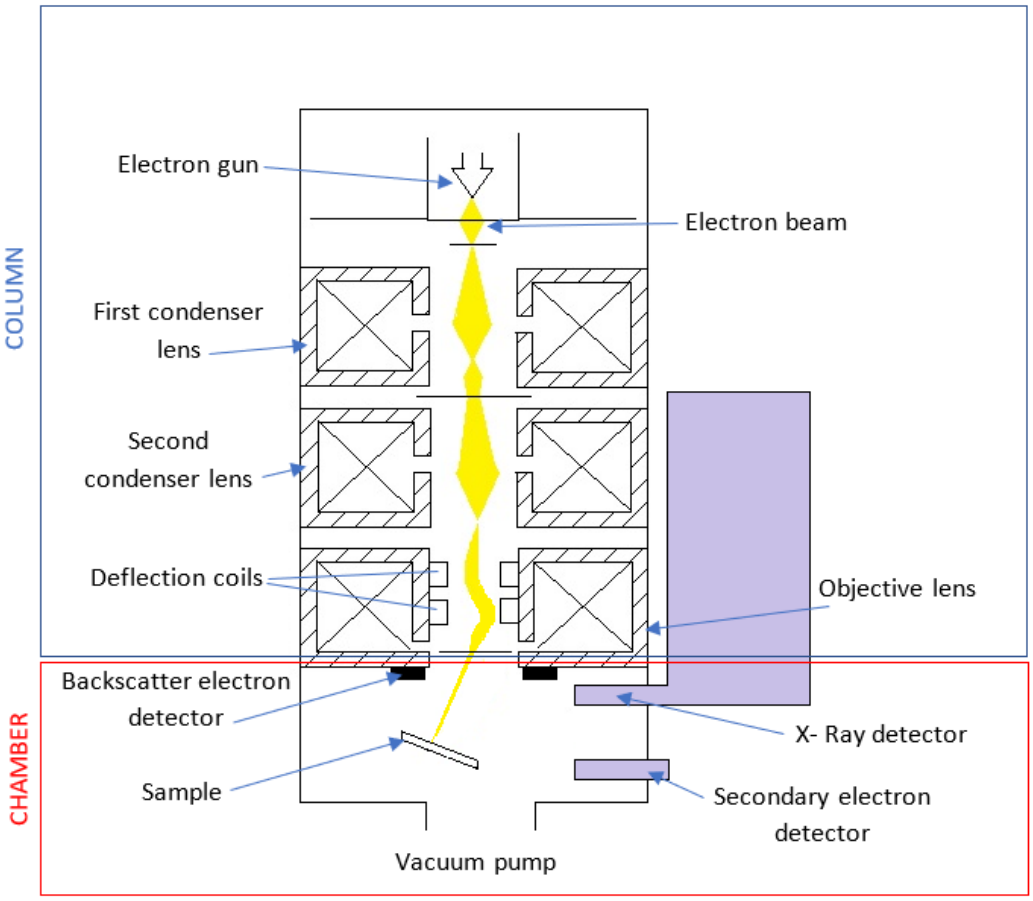

Figure 5.3: *Schematic picture from a Scanning Electron Microscope (SEM) (After Choundhary et al. (2017))*

After the beam passes through the electromagnetic lenses, the deflection coils adjust the incident beam on the sample. The secondary electrons, backscattered electrons and X-ray emitted as a result of interaction between the focused electron beam and the sample is recorded by a secondary electrons detector, backscattered electrons detector and X-ray detector or spectrometer (Goldstein et al., 2017). High resolution images are created through the image formation system by recording the magnitude of the signal from a reduced area of the sample by using a scanning system. The scanning coils deflect the electron beam so the sample surface can be scanned in x- and y- axis direction (Zhou et al., 2006). Figure 5.4 shows a schematic picture for the image formation system in the SEM.

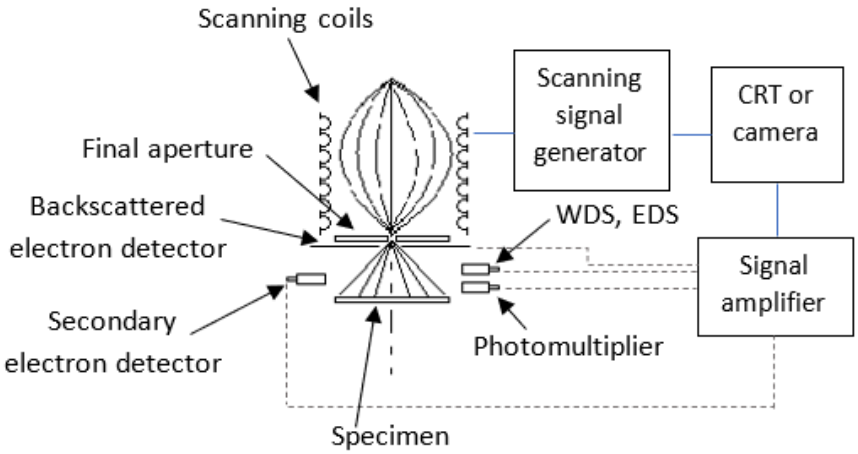

Figure 5.4: *Schematic picture for the Image formation system in the Scanning Electron Microscope (SEM) (After Goldstein et al., 2017).*

5.3 Structural analysis after deformation

A structural analysis after deformation on some samples was performed to analysed the damage and deformation mechanisms induced by the cyclic mechanical loading test.

Table 5.1 show the samples, tested between 4.5 and 7.5 MPa cyclic mechanical conditions, from which thin sections were created after deformation. A total of 24 thin sections were performed after deformation. At 12MPa, thin sections were created only from samples tested at room temperature. At 25MPa, thin sections were performed for all samples tested at different temperatures; room temperature, 55°C and 75°C. Finally, from samples tested at 45MPa, the only thin section created was for sample C1 tested at 75°C.

Table 5.2 show the samples, tested between 6 and 20 MPa cyclic mechanical conditions, from which thin sections were created after deformation. Only samples tested at 25 MPa with room temperature, 55°C and 75°C were use to create thin sections after deformation. A total of 9 thin sections were created.

Table 5.1: Samples from which thin sections were performed for a post-deformation analysis.
*Room temperature oscillated between 21-22°C

Pc	12 MPa		25 MPa			45 MPa	
T	21°C*	55°C	21°C*	55°C	75°C	55°C	75°C
A	A4	-	A3	A7.1	A6	-	-
B	B1.2	-	B8	B6	B2.1	-	-
C	C4	-	C3	C5	C2	-	-
F	F1	-	F3	F4	F5	-	-
LB	LB1	-	LB4	LB5	LB6	-	-
WB	WB18	-	WB16	WB1	WB8	-	-

Table 5.2: Samples from which thin sections were performed for a post-deformation analysis.
*Room temperature oscillated between 21-22°C

Pc	25 MPa			45 MPa	
T	21°C*	55°C	75°C	55°C	75°C
A	A10	A1	A9	-	-
F	F8	F9	F10	-	-
WB	WB3	WB4	WB5	-	-

5.3.1 Deformed micro-structures at 12 MPa confining pressure and room temperature

Figure 5.5 shows the thin sections before (Figure 5.5 A,C,E,G on the left) and after (Figure 5.5 B,D,F,H on the right) deformation for samples A4, B1-2 and C4, all tested at 12 MPa confining pressure and room temperature.

Before deformation, A4 has halite crystals with sizes between 500 μm to 1.5 cm approximately. The second phase content consists mainly of aggregates of anhydrite and elongated crystals of polyhalite with sizes between 50μm and 200μm maximum for both anhydrite and polyhalite grains that is observed randomly arranged along halite grain boundaries without a clear orientation. Some isolated crystals of anhydrite can also be seen interstitially located within halite grains. After deformation, a decrease in halite grain size can be noticed and the second phase content can still be observed mainly along halite grain boundaries without a clear or predominant crystal orientation (Figure

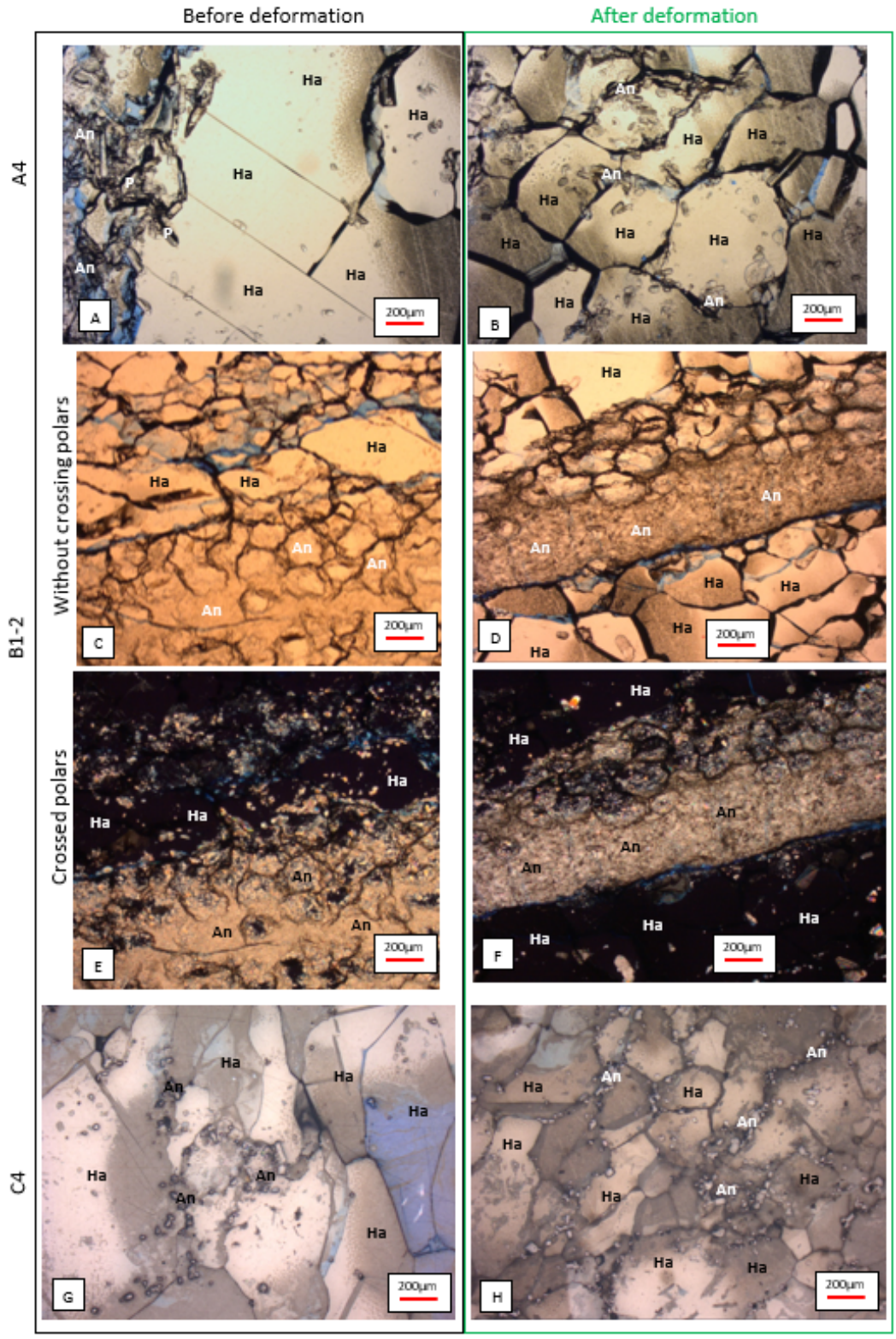

Figure 5.5: *Microphotographs of samples A4, and B2-1 and C4 before (A, B, C) and after (D, E, F) deformation. A decrease in halite (Ha) grain size can be observed with the second phase content mainly located along halite grain boundaries without a clear or predominant crystal orientation in images 5.5 A and B. A slight increase in fractures along anhydrite bands (An) seems to be observed in image 5.5 D and F, however it is difficult to distinguish the real change in the micro-fracture network before (5.5C and E) and after deformation (5.5D and F). An important reduction in halite grain size can also be seen in sample C4 after deformation. A noticeable reduction in halite grain size can also be seen comparing sample C4 from before and after deformation (5.5G and H).*

5.5 B). Sample B1-2 already had fractures along the bands of second phase content before the cyclic mechanical loading tests (Figures 5.5 C, for transmitted light microscope without crossed polars, and E, with crossed polars). A slight increase in fractures along anhydrite bands seems to be observed, however it is difficult to distinguish the real change in the micro-fracture network before and after deformation. An important reduction in halite grain size can also be seen in sample C4 after deformation. C4 has a denser micro-structure with a reduction of grain size from 1 cm (5.5 G) to maximum 1-2 mm (5.5 H).

Micrographs from series F, LB and WB after deformation show strongly deformed halite crystals surrounded by clay and anhydrite as main second phase content. Focusing on the micrographs from 5.6B and 5.6F, microcrystals of clay are filling the halite grain boundaries, and anhydrite is mostly observed surrounding the clay minerals. Figures 5.6C and D show the micrographs from LB1 after deformation. Due to the breccia texture prior to mechanical analysis, it is difficult to distinguish new damage generated after deformation. In samples from series LB, fractures can be observed both along second phase content (clay and anhydrite) and across halite crystals. Blue resin can be observed filling fractures across halite grains in micrographs 5.6C and D. Sample WB18 also shows a grain size decrease after deformation although smaller than samples F1 (figures 5.6A and B and 5.6E and F, respectively). Samples F1 also seems to show higher content of clay surrounding along boundaries of halite grain than the one observed in sample WB18. It seems that a greater amount of second phase content, clay and anhydrite in this case, along the grain boundaries of halite could imply an increase in grain size reduction after deformation.

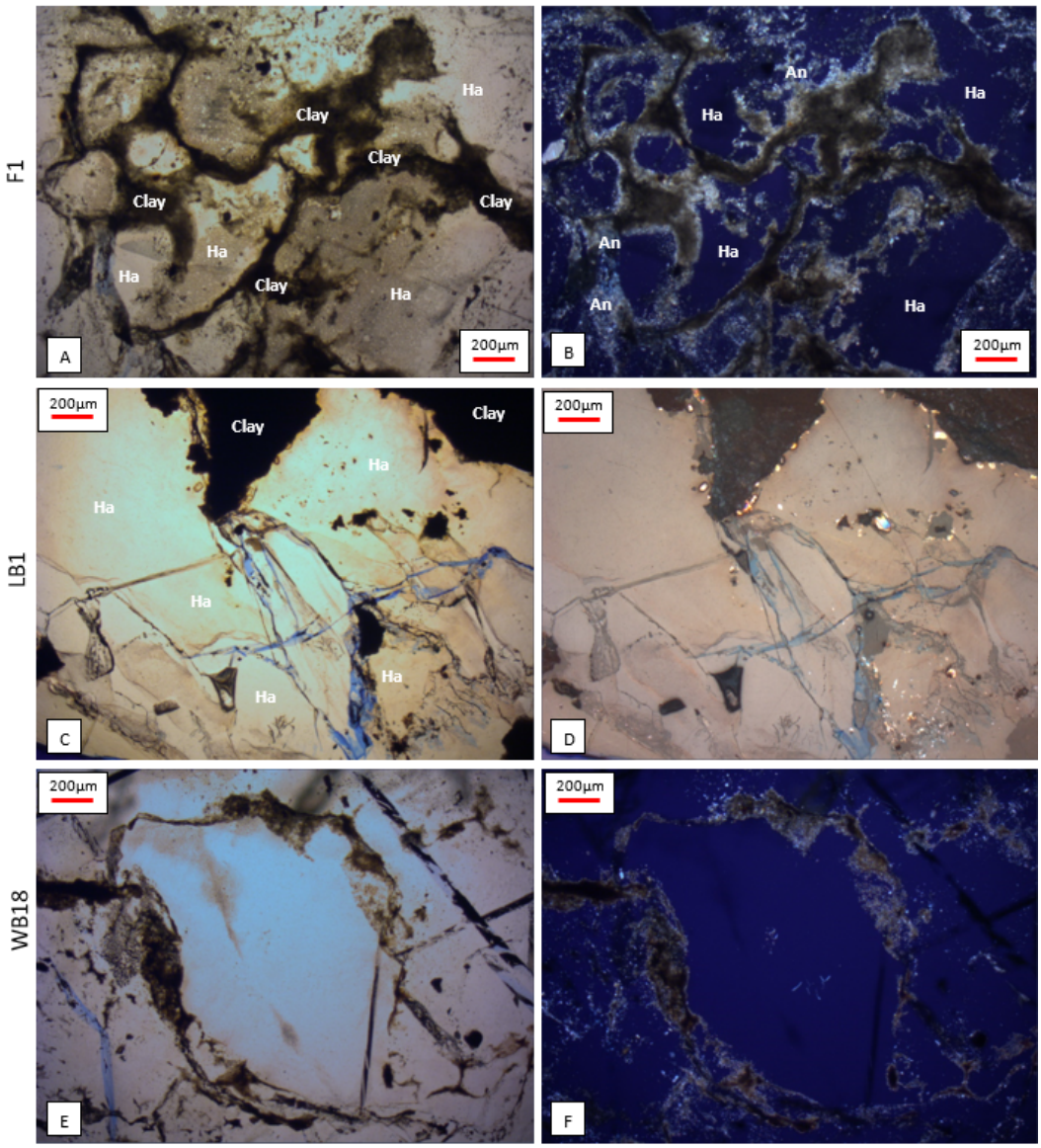

Figure 5.6: *Microphotographs of samples F1, LB1 and WB18 after deformation under transmitted light (A,C,D) and with crossed polars (B,D,F). Strongly deformed halite (Ha) crystals can be observed surrounded by clay and anhydrite (An) as main second phase content. A matrix of clay fills the halite grain boundaries, and anhydrite is mostly observed surrounding the clay minerals as observed in images 5.6B and 5.6F. In images 5.6C and D, from series LB, fractures can be observed both along second phase content (clay and anhydrite) and across halite crystals with blue resin filling the fractures. A more noticeable grain size decrease after deformation can be observed in sample WB18 in images 5.6E and F.*

5.3.2 Deformed micro-structures at 25 MPa confining pressure and room temperature

The microstructural changes of the samples tested at 25 MPa of confining pressure and room temperature are illustrated in Figures 5.7 and 5.8, with images of samples A3, C3 and B8 before deformation on the left (Figure 5.7A-C) and after deformation on the right (Figure 5.7D-F), and images for samples LB4 and F3 before and after deformation in Figure 5.8A-B and 5.8C-D, respectively.

In general, prior to the mechanical stimulation, we observed in all samples annealed structures of subhedral polygonal crystals with straight, strain free grain boundaries presenting 120° intersection. The thin section analysis shows halite crystals of between 500μm and 2mm diameter, lacking major fractures. Cleavage can be observed in the larger halite crystals. Minor microfractures within some second phase minerals can also be identified sporadically, at a very low density and lacking connectivity (Figures 5.7A-C and 5.8A-B).

After deformation, the microfracture network appears drastically denser in areas with higher concentration in second phase minerals. In general, the observed macroscopic axial shortening of the samples results from grain size decrease in the axial direction and subsequent grain size increase of the halite crystals perpendicular to σ_1, in comparison to the pre-deformation subhedral shape of the halite crystals. The grain boundaries perpendicular to the maximum principal stress σ_1 were flattened after deformation.

Halite grains in sample A3 before deformation (Figure 5.7A) are larger than 500μm, whereas after deformation the halite grains are smaller, about 100μm (Figure 5.7D). Sample C3 shows similar grain size modification: a volume decrease from subhedral crystals with straight grain boundaries with high angle intersections of 120° (Figure 5.7B) to more packed anhedral crystals showing

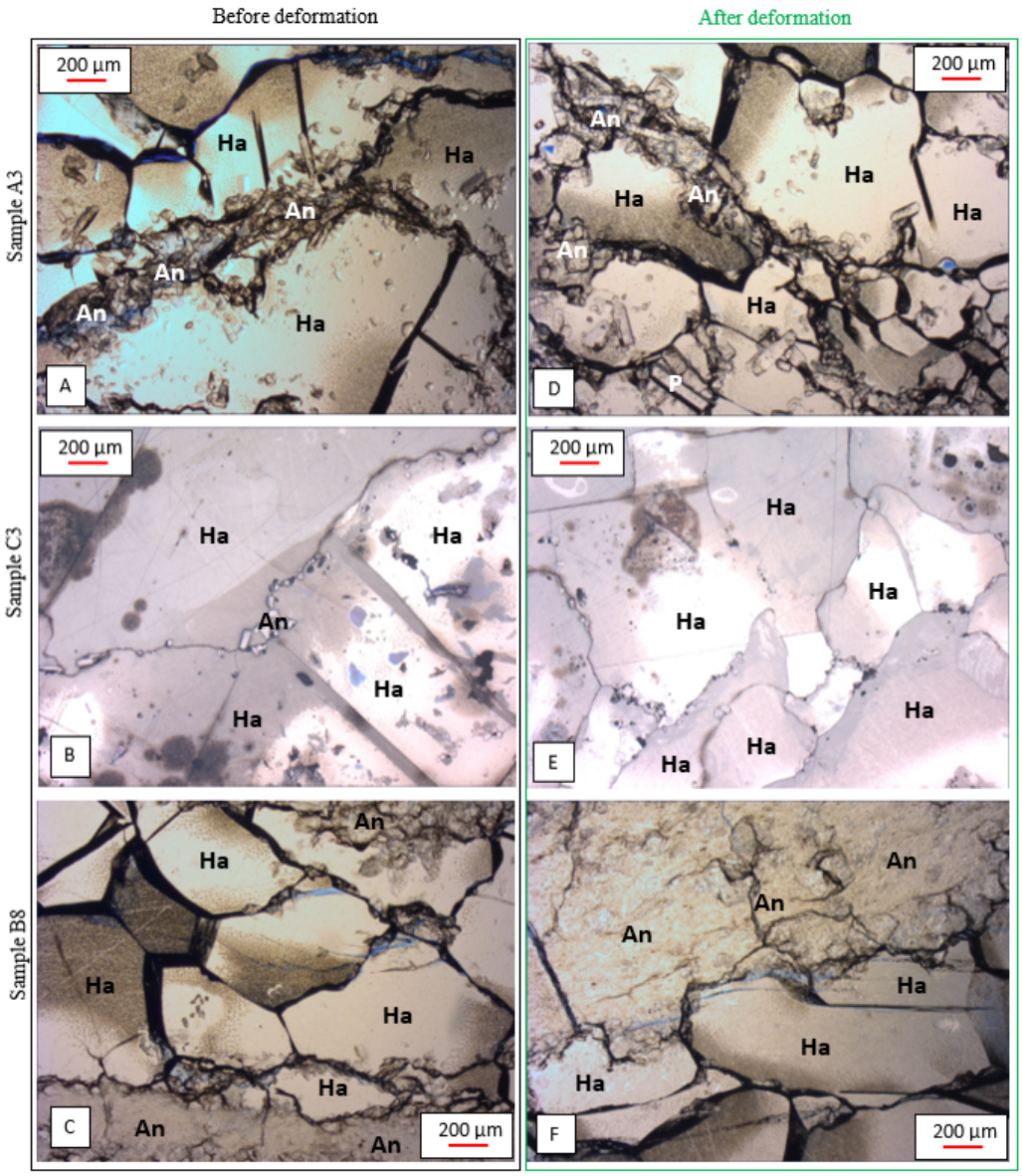

Figure 5.7: *Microphotographs of samples A3, C3 and B8 before (A, B, C) and after (D, E, F) deformation. Annealed structures of subhedral polygonal crystals of halite (Ha) with straight, strain free grain boundaries presenting 120° intersection can be observed in images 5.7A-C before deformation. An increase of microfractures, specially denser in areas with higher concentration in second phase minerals, such as anhydrite (An) and polyhalite (P), can be observed in figure 5.7F. Figures 5.7D and E show a halite grain decrease from subhedral crystals with straight grain boundaries, and high angle intersections of 120°, to more packed anhedral crystals showing curved and lobate grain boundaries.*

curved and lobate grain boundaries (Figure 5.7E). Figure 5.7F gives the microstructure from B8 after deformation with a clear increase in microcracking linked to areas with a higher content in anhydrite and boundary flattened on grain boundary perpendicular to σ_1 resulting in a halite grain elongation. Overall, this sample recorded the highest degree of damage due to microfractures that developed within the anhydrite minerals.

The microstructural analysis of samples F3 and LB4 also shows a slight decrease in grain size compared to the reference intact materials. The deformation mechanism is observed around halite grains and appeared to be related to a higher anhydrite and clay content. Figure 5.8 shows the microstructure of samples from series LB and F before (Figure 5.8A-C) and after (Figure 5.8B-D) the cyclic mechanical loading test. Due to the significant pre-existing microstructural damage in series LB, it is difficult to clearly distinguish the deformation structures before and after the test. Nonetheless, some increase can be seen in the deformed structure similar to dislocation creep following halite cleavage and a decrease of halite grain sizes, related to area with a greater content in anhydrite and clay around grain boundary. However, it is not possible to certify if these structures were produced during the cyclic loading mechanical tests.

5.3.3 Deformed micro-structures at 45 MPa confining pressure and elevated temperatures

Figure 5.9 shows images from A7 (5.9A and B) and B6 (5.9C and D) after deformation. As observed in other samples from series A, sample A7 presents a relevant decrease in axial length of halite grains, parallel to σ_1 applied during cyclic mechanical loading deformation, resulting in an elongation of the halite grains with high angle (120°) grain boundaries intersection. Under crossed po-

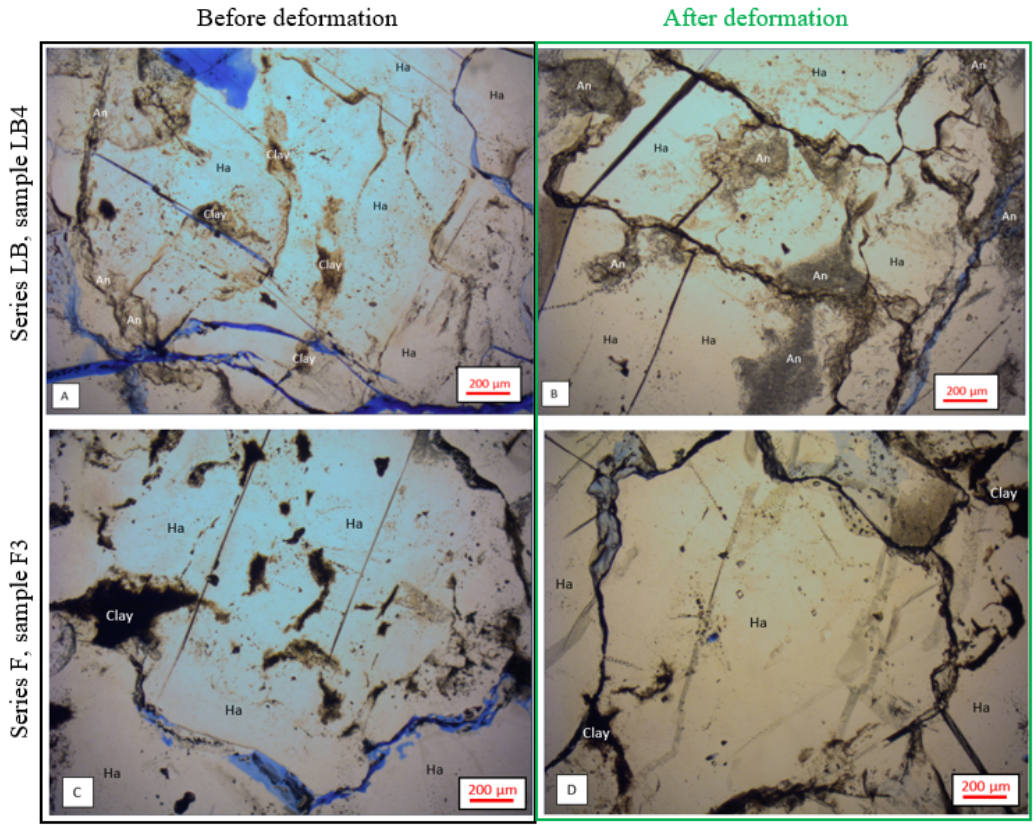

Figure 5.8: *Thin section analysis of samples LB4 and F3 before and after deformation under cyclic loading conditions. A slight decrease in grain size compared to the reference thin section before deformation can be observed. Pre-existing microstructural damage in series LB can be seen in figures 5.8A-B. Other structures observed are dislocation creep following halite (Ha) cleavage and a decrease of halite grain sizes, related to area with a greater content in anhydrite (An) and clay around grain boundary.*

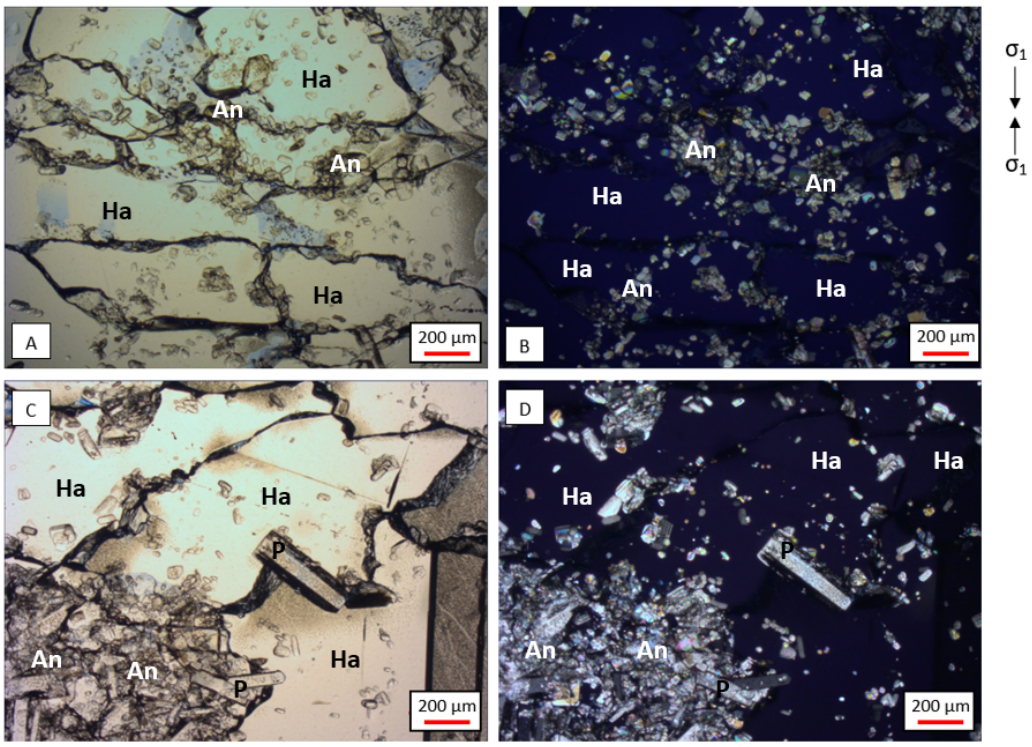

Figure 5.9: *Thin section analysis of samples A7 and B6 after deformation under cyclic loading conditions. A general decrease in axial length of halite grains, parallel to σ_1 applied during cyclic mechanical loading deformation and represented by two black arrows on the top right side of the figure, resulting in an elongation of the halite grains can be observed without a clear orientation of second phase content crystals.*

lars (5.9B), the second phase content can be observed along grain boundaries of halite but also within the halite grains. Although a clear elongation of halite grains can be observed, perpendicular to σ_1, there is not a clear orientation of second phase content crystals. Elongated microcrystals of anhydrite and polyhalite presents sizes of maximum 50 μm.

In sample A7, large intragranular fractures can be observed related to the presence of second phase content. Figure 5.10 shows a big crystal of polyhalite, of about 1.5 mm long with inclusions of anhydrite giving a poikilitic texture as result. The crystal of polyhalite present several micro-cracks showing a main orientation of 45° from the horizontal axis. Although there are several interconnected micro-cracks within the polyhalite grain, most of the micro-fractures do not show continuity through the surrounding halite grains.

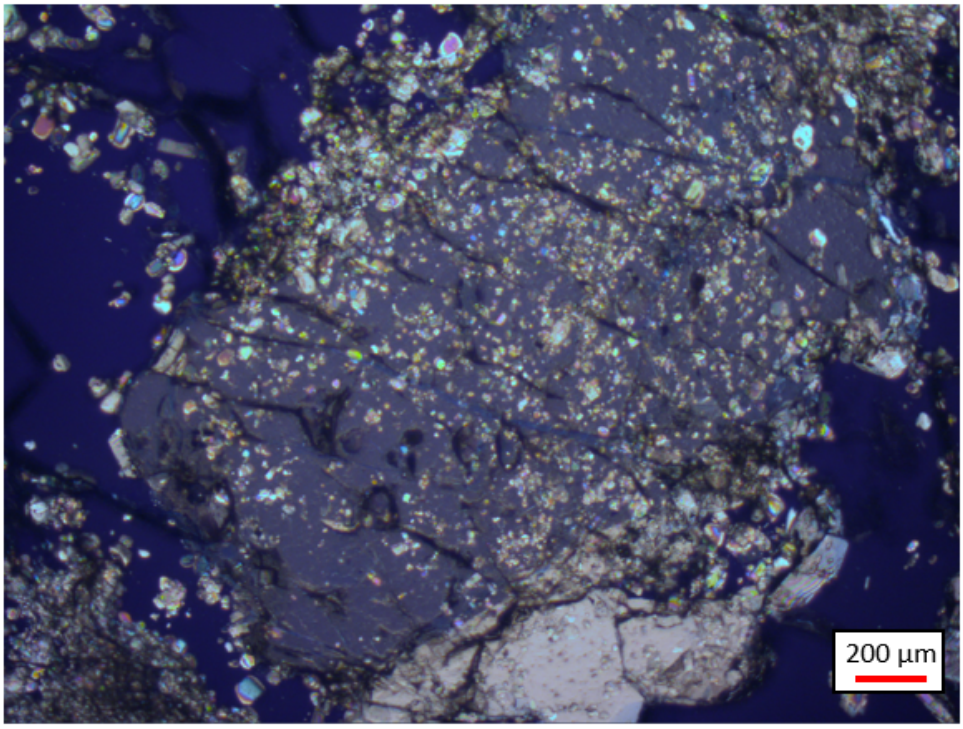

Figure 5.10: *Thin section analysis of samples A7 under crossed polars. The figure shows a rectangular-shaped crystal of polyhalite with inclusions of anhydrite and several fractures.*

Sample B6 (5.9C and D) also shows strongly deformed and elongated halite grains with curved grain boundaries. As in series A, microcrystals of anhydrite and polyhalite do not seem to show a preferred orientation. Highly deformed grain boundaries of halite, containing second phase content, can show very meandering shapes. Figure 5.9C shows a boundary between two grains of halite containing a prismatic crystal of polyhalite which, after axial deformation of the grain boundary of halite, end up presenting an orientation of 45° from the horizontal axis.

Figure 5.11 shows images from samples F4 (5.11A,B), LB5 (5.11C,D) and WB1 (5.11E,D) after deformation. Figure 5.11A seems to presents the growth of a new clear and free of fluid inclusions halite grain (of about 0.5mm) over previous older halite grains presenting cleavage and fluid inclusions. Recrys-

tallisation mechanism of grain boundary migration could explain the contrast between the clear, fluid-inclusion-free halite grain with the other halite grains. Halite grains have sizes from 200 μm up to maximum 1 cm. The potential new crystal also shows some cleavage planes along the horizontal axis, which could have occurred during thin section preparation (Carter and Hansen, 1983; Schléder and Urai, 2005). Figure 5.11B, under crossed polars, shows almost no presence of second phase content which can be favourable for halite grain regrowth processes. However, it is not possible to verify that the structure described took place during the deformation test.

Both samples LB5 (5.11C,D) and WB1 (5.11E,F) show an important amount of fractures not only along second phase content but also across halite grains. Halite grains in LB5 have sizes between 200 μm and 1 cm with several cleavage planes. Fractures can be easily recognised thanks to the impregnation with blue resin from thin section preparation. Red clay and anhydrite can be observed as the main second phase along grain boundaries of halite in sample LB5 under crossed polars (5.11D) and in lower content but also in samples F4 and WB1. No clear halite grain elongation can be appreciated in the analysed samples from F4, LB5 or WB1.

Figure 5.12 shows the images from thin sections of F5 (A,B), LB6 (C,D) and WB8 (E,F) tested at 25MPa confining pressure and 75°C. Note that F5, LB6 and WB8 have a higher content in red clay and anhydrite in comparison to other samples from the same series respectively. A slight reduction in halite grain size may be seen in samples F5 and LB6. Samples F5 presents halite grains with sizes between 200 μm and 1mm surrounded by microcrystaline matrix of red clay and anhydrite. Halite grains have anhedral habit with highly deformed grain boundaries with high angle intersection.

Sample LB6 shows highly fractured halite grains with sizes from 200 μm to 0.5

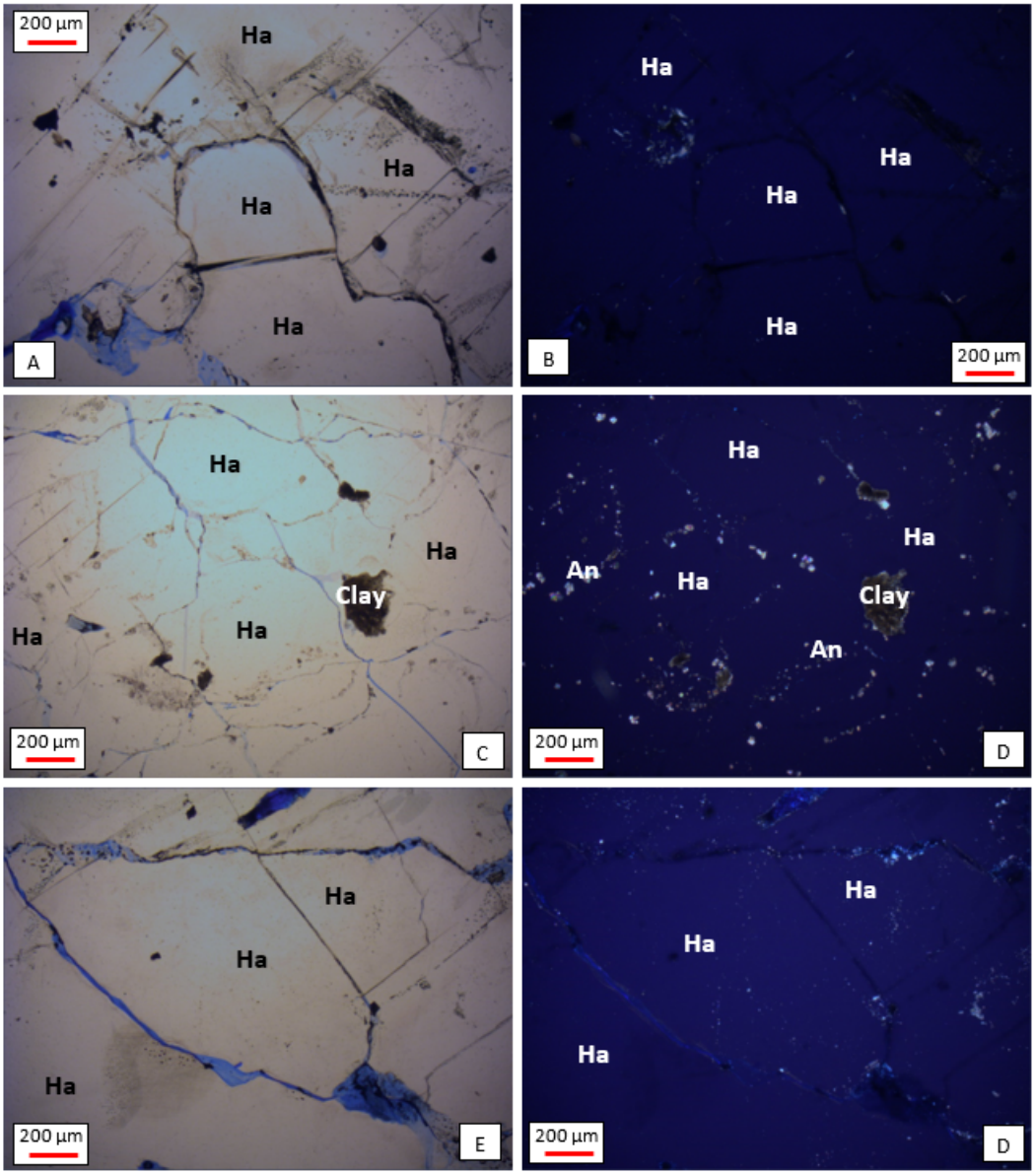

Figure 5.11: *Thin section analysis of samples F4 (5.11A,B) LB5 (5.11C,D) and WB1 (5.11E,D) after deformation under cyclic loading conditions. Figure 5.11A show the growth of a new clear and free of fluid inclusions halite grain (of about 0.5mm) over previous older halite grains presenting cleavage and fluid inclusions. Some fractures can be observed tinted by blue resin.*

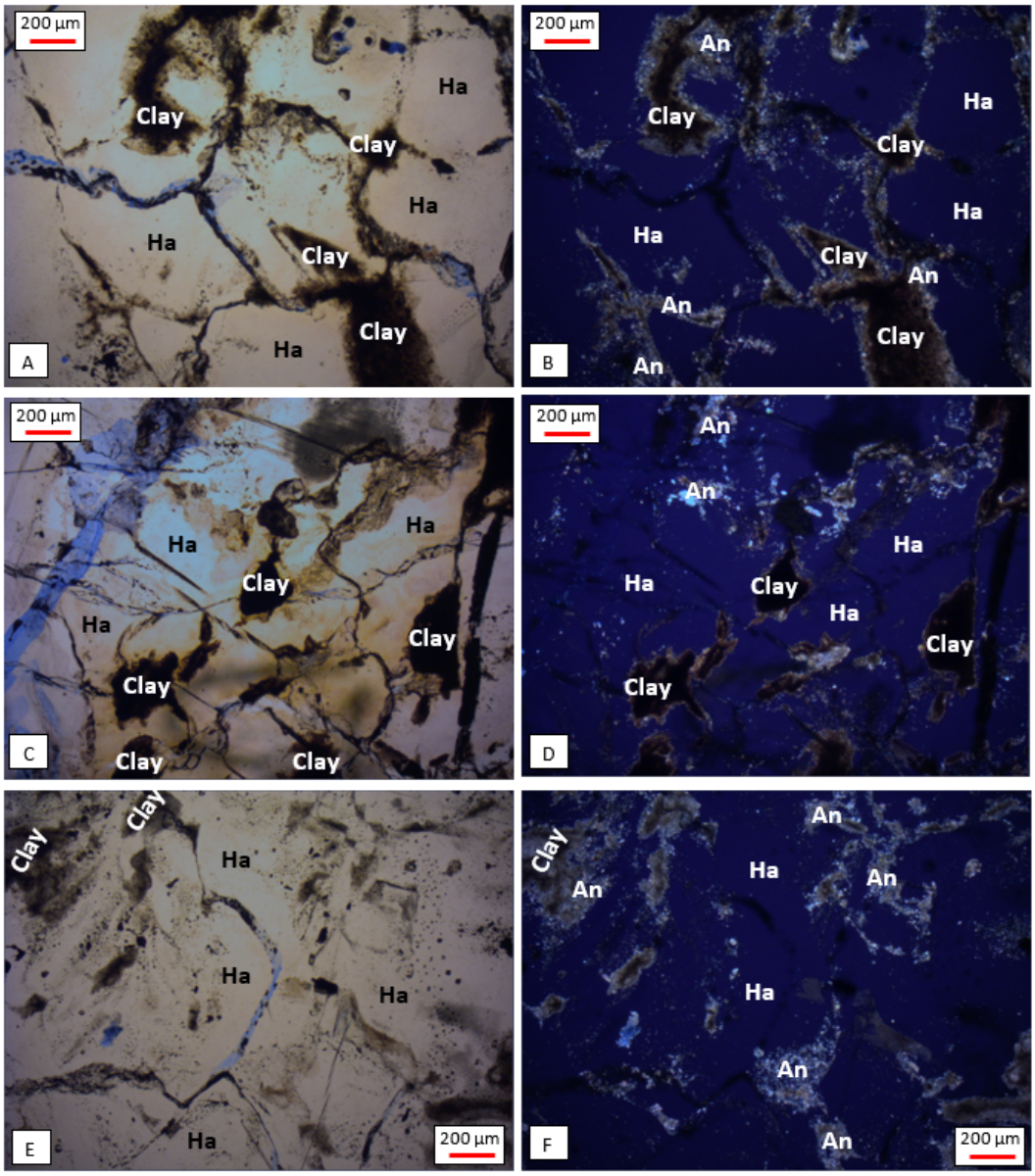

Figure 5.12: *Thin section analysis of samples F5 (A,B), LB6 (C,D) and WB8 (E,F) after deformation under cyclic loading conditions. These samples were tested at 25 MPa confining pressure and 75° C. A slightly decrease in grain size can be observed in both samples F5 (5.12A and B) and WB8 (5.12E and F). Sample LB6 (5.12C and D) shows a higher density of micro-fractures in comparison to the rest of sample due to its breccia texture previous to testing. In general, halite grains with sizes between 200 µm and 1mm can be observed surrounded by microcrystaline matrix of red clay and anhydrite.*

mm also with a high content of red clay matrix characteristic of the breccia texture. Red clay matrix can be found as elongated and curved bands along grain boundary but also as big clusters of red clay where structures of sedimentation can still be observed. Figure 5.13 presents an image from LB6 where a large band of red clay matrix can be seen showing a depositional bedding structures. The clay matrix has a prominent fracture with halite crystallised as a vein. Micro-fractures (marked with red arrows) from the clay matrix extends across halite grains. From all samples tested at 75°C, sample LB6 is the sample showing a more clear elongation of halite grains. However, fractures within the matrix of clay have a wider ramification resulting in a denser micro-fractures network in comparison to fractures in halite grains. LB6 also counts a high amount of cleavage planes which could imply a higher fragility and a higher predisposition to sample damage during thin section preparation.

Sample WB8 also shows highly deformed anhedral halite grains with sizes between 200 μm to 1-2mm. Micro-crystals of anhydrite and clay can be seen along grain boundaries of halite but also located within the halite grains. Structures of grain boundary migration can be observed with slightly clearer grains overgrowing over old and milky fluid-inclusions-rich grains.

5.3.4 Deformed micro-structures at higher amplitude of cyclic mechanical loading, room and elevated temperatures

Nine samples were tested at a higher amplitude of loading axial stress between 6 and 20 MPa for 48h, under 25 MPa of confining pressure, and temperatures ranging from room to 55 and 75°C. Figure 5.14 show the microphotographs of samples from Series A, F and WB before and after deformation.

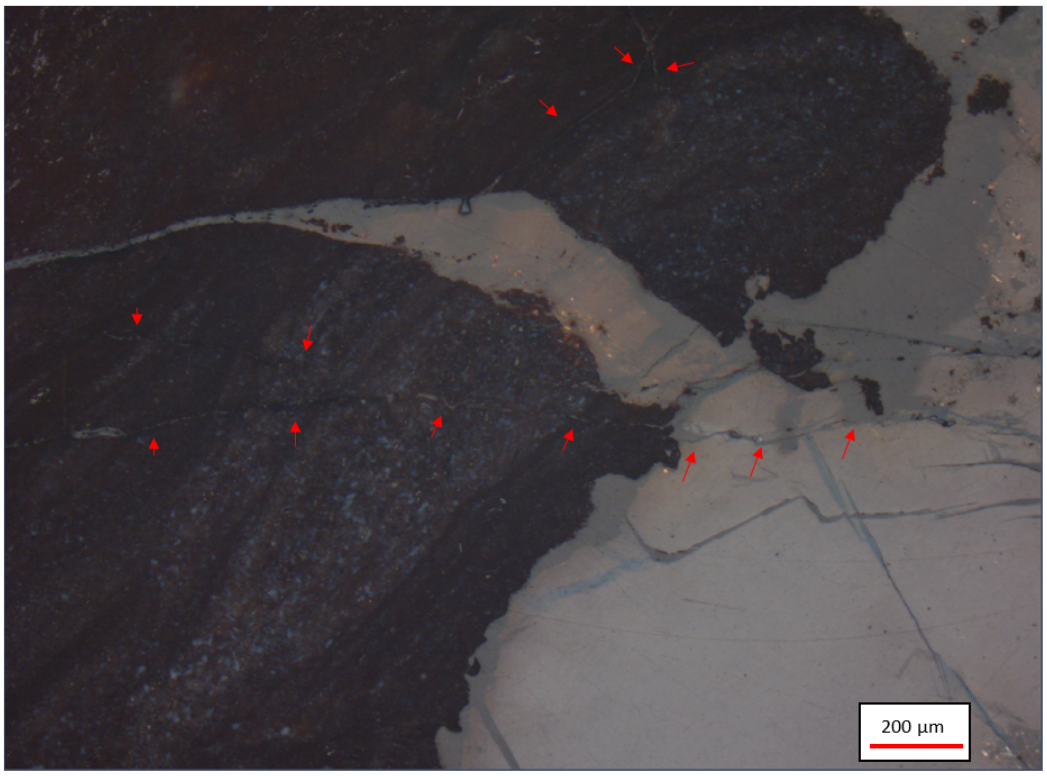

Figure 5.13: *Thin section of sample LB6 after deformation. Red arrows point fractures, from second phase matrix of clay, extending into the halite crystals. This figure shows the clay matrix affected by a prominent fracture filled by halite crystallised as a vein. Micro-fractures (marked with red arrows) from the clay matrix extends across halite grains as transgranular micro-cracks.*

Sample A10, after deformation (5.14B), shows a strong decrease of the axial length (axial flattened), parallel to the σ_1 applied, resulting in a halite grain and elongation. Halite grains present maximum axial length of 0.5mm and about 1mm long in the direction of grain elongation. Second phase content is observed mainly in along halite grain boundary without showing any preferred orientation. Some micro-crystals of anhydrite can be observed interstitially contained within halite grains.

Sample F8 and WB3 both exhibit a large content of intragranular micro-fractures (figure 5.14D and F). An increase of cleavage planes can be observed in this sample too. Some recrystallisation signs can be observed, like grain boundary migration, resulting in irregular and curved halite grain boundaries overgrowing over neighbour halite grains. Surprisingly, grain size does not seem to be extremely reduced in samples F8 and WB3 in comparison to sample A10, which shows a marked halite grain elongation after deformation. Grain sizes in samples F and WB are from 0.5 mm to 1-2 mm with second phase content mainly located along grain boundary of halite. Although the clay matrix is observed mainly along grain boundaries of halite it is possible to observe some crystals of anhydrite and also some clay trapped withing halite grains.

The following figures 5.15 and 5.16 show microphotographs from samples A1, F9 and WB4 deformed at 55°C and samples A9, F10, WB5 deformed at 75°C. Both samples A1 and A9 show the same halite grain elongation discussed previously for sample A10, deformed at room temperature, and high angles in grain boundary intersection (120°). Figures 5.15B and 5.16B show the microphotographs under crossed polars for A1 and A9 respectively. As discussed previously, these samples show anhydrite and polyhalite crystals of maximum 50 μm long mainly distributed along grain boundaies of halite (with some micro-crystals of anhydrite within the halite grains). Grain sizes observed in both A1 and A9 are similar to the ones discussed previously for A10 (with

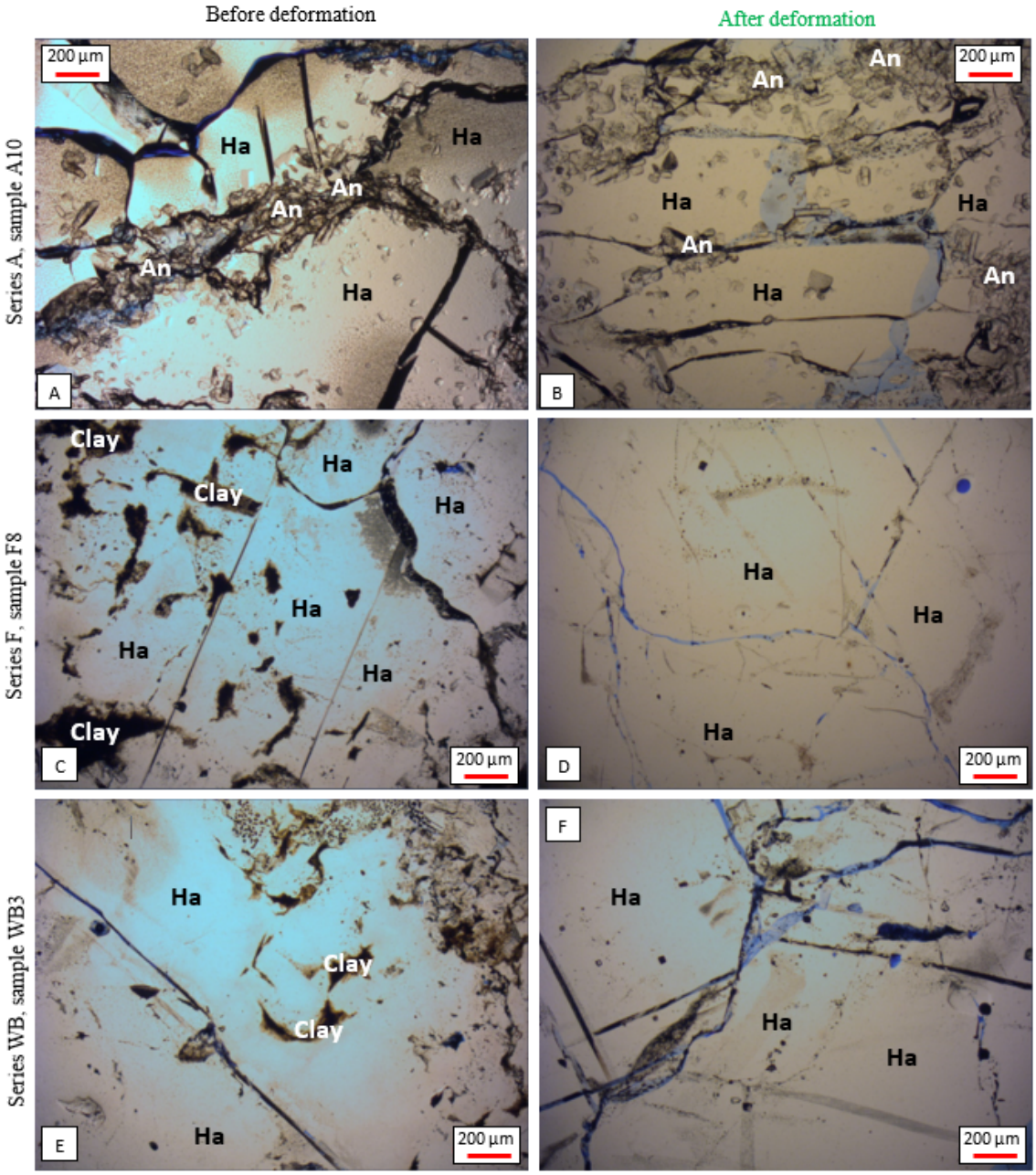

Figure 5.14: *Thin section analysis of samples from Series A, F and WB before deformation (A, C and E respectively) and images from A10 (A), F8 (D) and WB3 (E) after deformation under cyclic loading conditions. Figures 5.14A and B show a strong decrease of the axial length (axial flattened), parallel to the σ_1 applied, resulting in a halite grain and elongation in sample from series A with anhydrite and polyhalite as main second phase content. Second phase content is observed mainly in along halite grain boundary without showing preferred orientation although some micro-crystals of anhydrite can be observed interstitially contained within halite grains. Sample F8 (5.14C and D) and WB3 (5.14E and F) both exhibit a large content of intragranular micro-fractures with an increase of cleavage planes within halite grains.*

maximum axial length of 0.5mm and 1mm long in the direction of grain elongation).

Micrographs from samples F and WB series clearly have more visible blue resin filling along grain boundaries of halite grains, indicating a widening of the halite-halite contact areas. In other words, during high amplitude cyclic loading, damage seems to concentrate along the halite grains boundaries regardless of the content in secondary mineralogy (namely anhydrite, polyhalite or clay). This contrasts from the micro-fractures development along halite grain boundaries with second phase content previously observed in all the others samples. Other features observed are the increase in cleavage planes and also grain boundary migration structures observed in samples both from series WB and F. Grain size observed for halite stays in the range of 200 μm and 1-2 mm.

5.3.5 Fluid inclusions and crystal defects

Both milky fluid inclusions-rich-halite and clear fluid inclusions-poor-halite, as described by Schléder and Urai (2005) can be observed in alternation within a same section in all series of rocks analysed. Figure 5.17 shows milky fluid inclusions chevron of around 0.6-0.7 mm within a halite crystal marked with a red arrow. Some milky bands of fluid inclusions, of maximum 0.5 mm, and small cubic fluid inclusions, of around 10 μm, can be also observed.

Figure 5.18 show micrographs from WB16, WB18, WB1 and WB8 where fluid inclusions (marked with yellow arrows) occur in grain boundaries of halite and are occasionally also observed withing the crystal lattice (observed on the left side in micrograph 5.18D). Fluid inclusions are mostly observed along grain boundaries of halite but they can be also spotted within the crystal lattice.

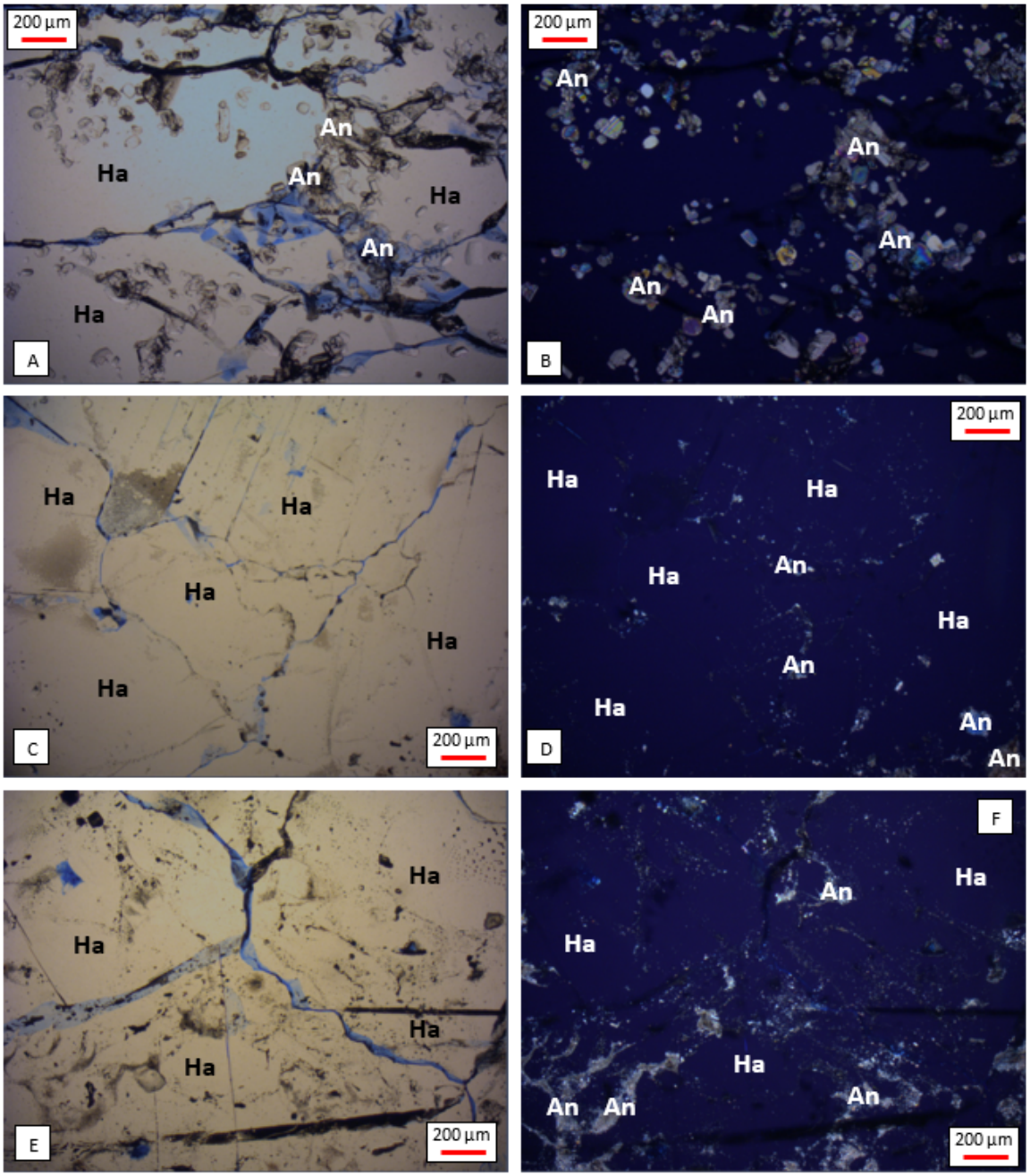

Figure 5.15: *Thin section analysis of samples from A1, F9 and WB4 after deformation under high amplitude cyclic loading conditions with cyclic loading stress between 6 to 20 MPa at a confining pressure of 25 MPa and testing temperature of 55° C. Figures 5.15A and B show samples A1 after deformation. The main structural feature observed is the elongation of halite grains and a higher deformation of halite grain boundaries with lobated shapes. Blue resin can be observed along halite grain boundaries which could imply an increase of damage such as grain boundary openings. Both samples F9 (5.15C and D) and WB4 (5.15E and F) show lower halite grain elongation but also high deformed halite grain boundaries with cleavage planes. Anhydrite crystals have sizes about 50µm with anhedral shapes in sample A1 whereas, in samples F9 and WB4, anhydrite is in a form of a micro-crystalline matrix around halite grains.*

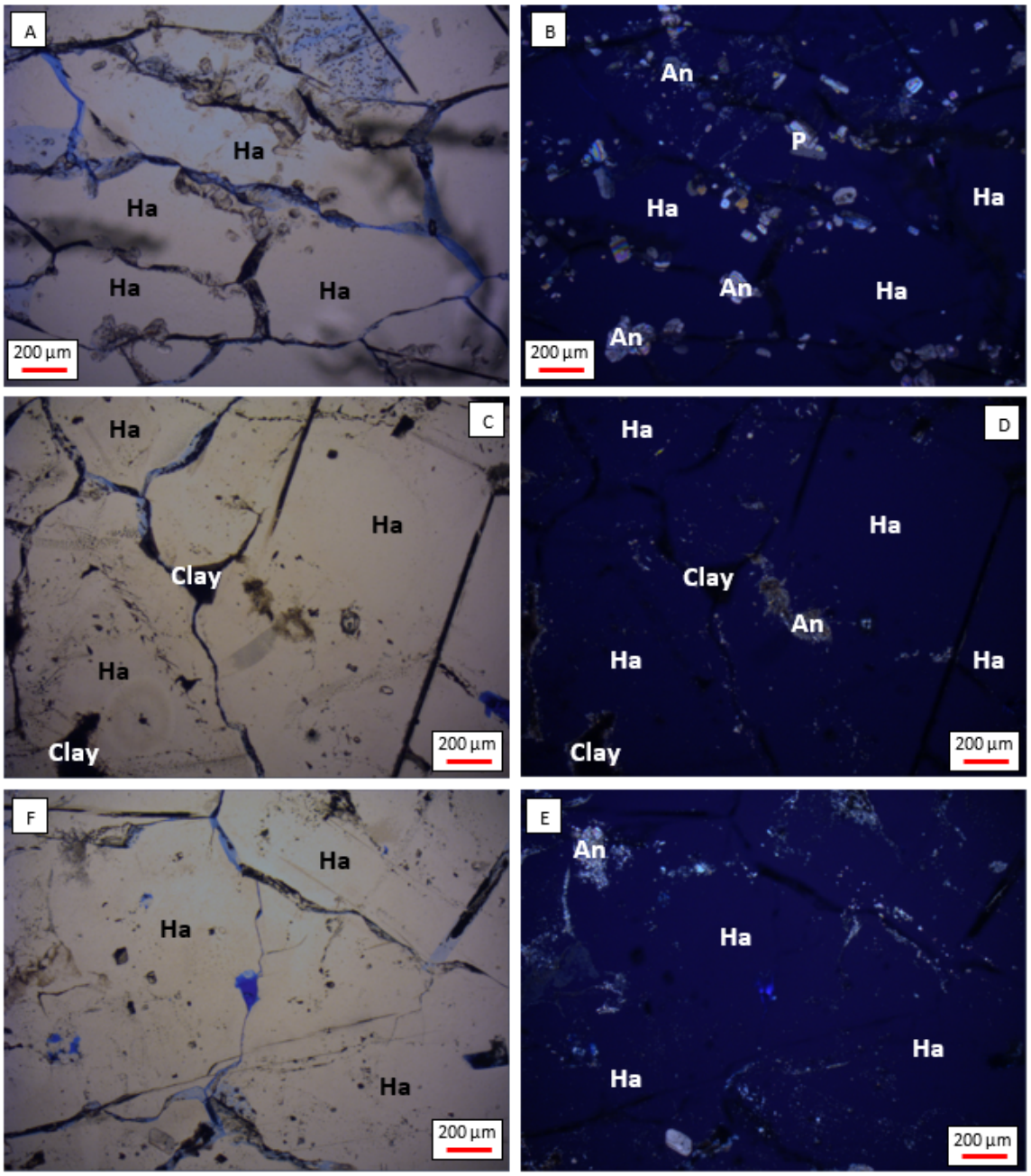

Figure 5.16: *Thin section analysis of samples from A9 (A,B), F10 (C,D) and WB5 (E,F) after deformation after deformation under high amplitude cyclic loading conditions with cyclic loading stress between 6 to 20 MPa at a confining pressure of 25 MPa and testing temperature of 75° C. Same structures discussed in the previous figure 5.15 of elongated and strong deformed halite grains with an increase of cleavage planes and lobated halite grain boundaries can also be observed. Blue resin can be also observed along halite grain boundaries evidencing a damage increase around halite grains due to deformation under cyclic loading conditions.*

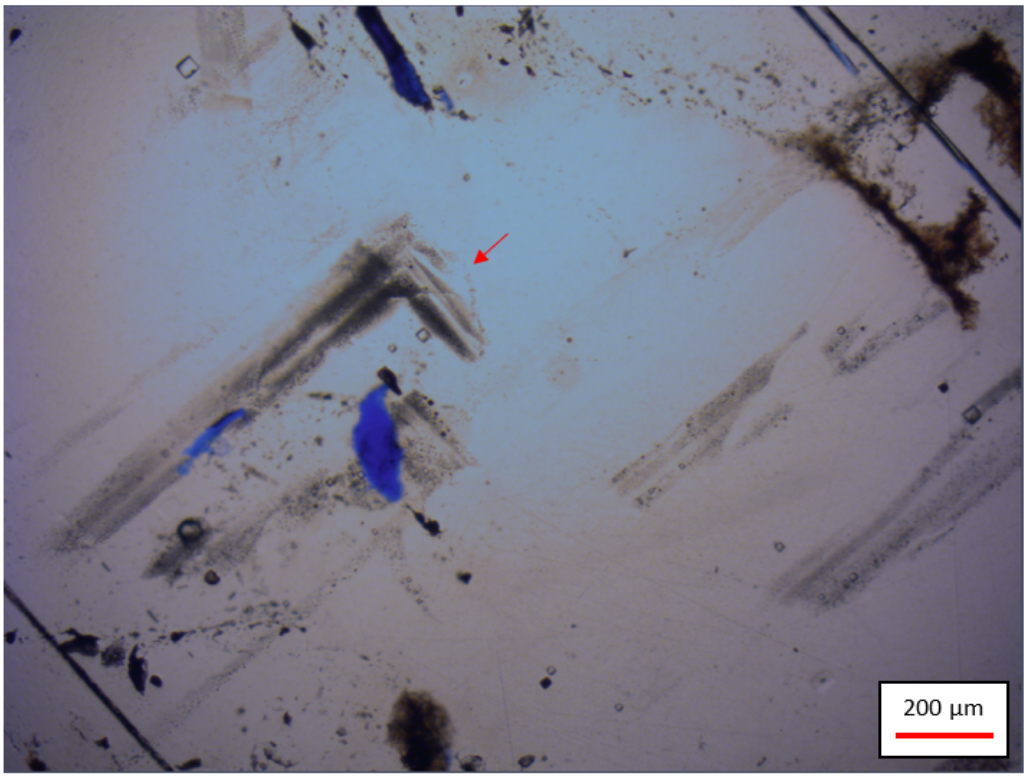

Figure 5.17: *Microphotograph of sample A7 showing (red arrow) a milky fluid inclusions-rich-halite chevron. The image is from a thin section performed after deformation under cyclic mechanical loading conditions.*

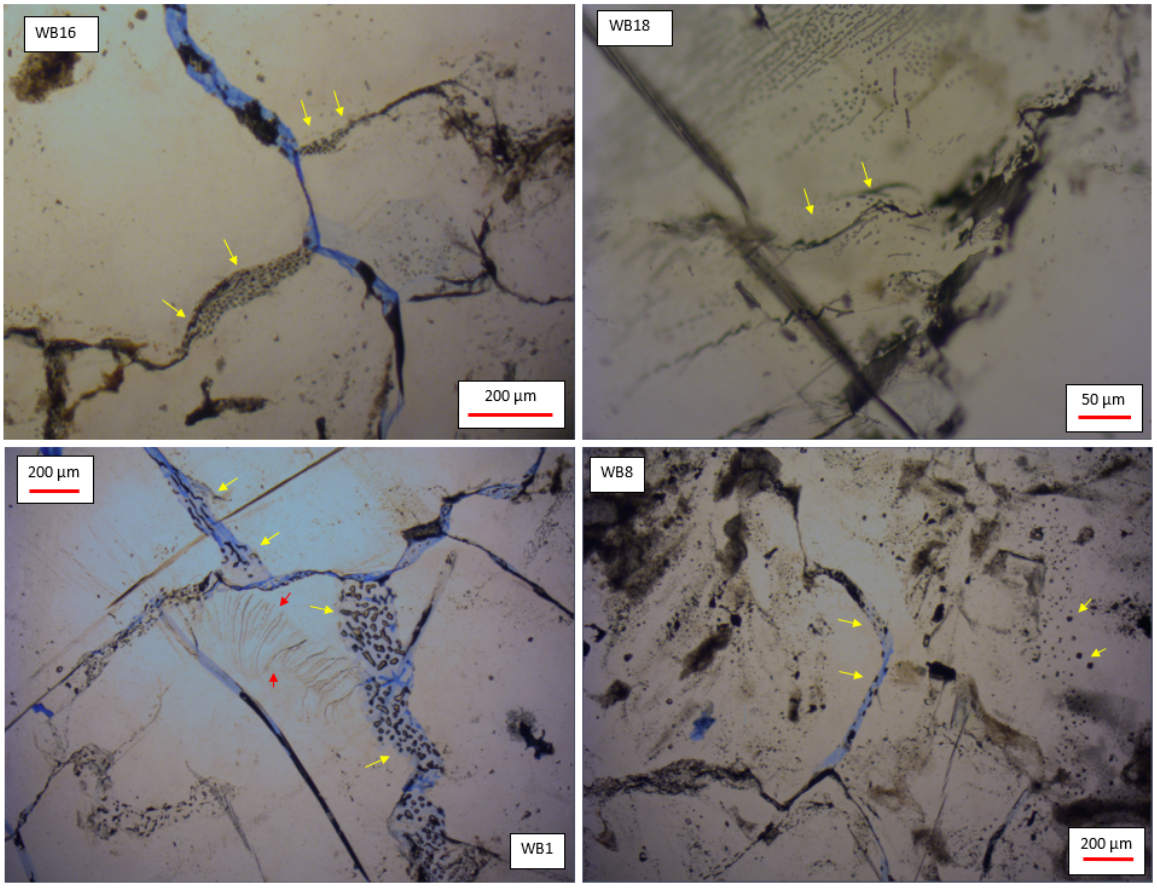

Figure 5.18: *Microphotographs of samples from series WB after deformation under transmitted light. The figure show images from samples WB16, WB18, WB1 and WB8. The different figures show fluid inclusions (marked with yellow arrows) occur in grain boundaries of halite and are occasionally also observed withing the crystal lattice. Fluid inclusions are mostly observed along grain boundaries in the form of milky fluid-inclusions-rich areas limited by curved shapes following grain boundaries with an abrupt transition from fluid-inclusions-rich zone and the area free of fluid inclusions.*

The milky fluid-inclusions-rich areas around grain boundaries are limited by curved shapes following grain boundaries with an abrupt transition from fluid-inclusions-rich zone and the area free of fluid inclusions. In figure 5.18C, close to the grain boundary and marked with red arrows, it is possible to see the track of linear arrangements of the fluid inclusions migration from the centre of the halite grain towards the grain boundary. Fluid inclusions can migrate along a thermal or hydro-mechanical gradient (Carter and Hansen, 1983; Leitner et al., 2011; Shao et al., 2019).

There is also a noticeable increase of crystal defects in the halite crystals with

second phase content along the grain boundary. The crystal defects can be observed both within the crystal lattice using the transmitted light (Figure 5.19) or in the halite grain's surface by using reflected light (Figure 5.20). Figure 5.19 shows two micrographs from sample WB18 after deformation where picture on the top is an image from the transmitted light microscope and the bottom picture is the same caption under crossed polars. Red arrows in the figure point the internal lattice defects whereas arrows in green demarcate the grain boundary where clay is the main mineralogy as second phase content. Figure 5.19B allows to identify both clay and anhydrite surrounding the halite crystal very close to where the crystal defects are. These crystal disturbances are presented as planar defects with an angle of approximately 45° from the horizontal. On the left side, two opposing black arrows show the direction of the principal stress applied during the cyclic loading mechanical test.

5.3.6 Microporosity generation

The analysis by using the Scanning Electron Microscope (SEM) shows new pores being generated around some second phase minerals in sample A3 as a result of mineral rotation (as highlighted by green arrows on Figure 5.21B). The mineral rotation also induced (i) grain boundary opening (Figure 5.21A) and (ii) some micro-fracturing between anhydrite crystals, as indicated by magenta arrows in Figure 5.21C.

Other structures observed in the SEM are the voids created around second phase content in contact with halite grains (Figure 5.22). The differences in rheology seem to generate some sort of local micro-porosity showing island structure where regions between halite and anhydrite crystals do not fit.

The microporosity observed with SEM did not present a connection or net-

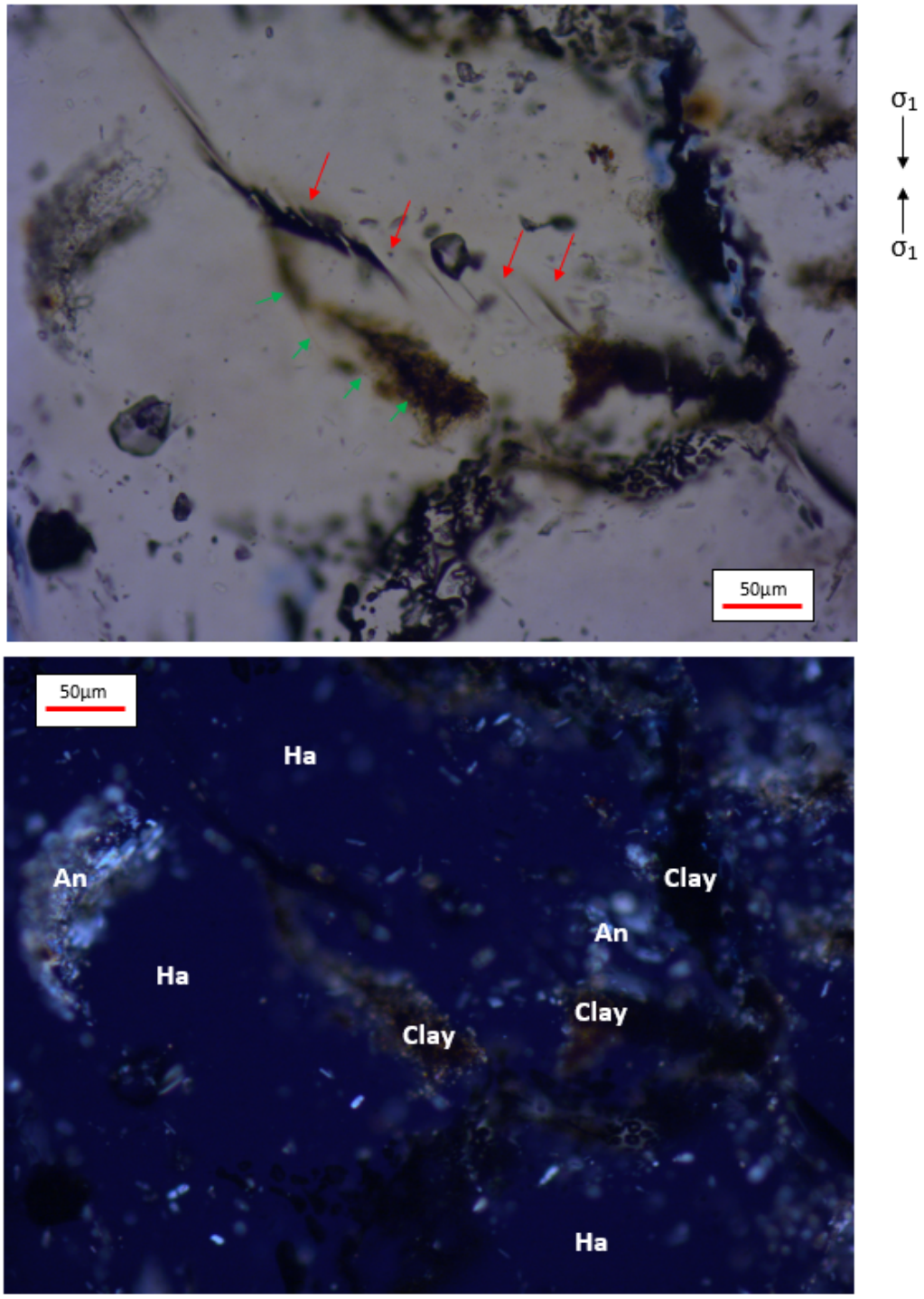

Figure 5.19: *Microphotographs of samples WB18 after deformation under transmitted light (on top) and with crossed polars (bottom). The internal lattice defects are marked with red arrows whereas arrows in green demarcate the grain boundary where clay is the main mineralogy as second phase content. As observed in these captions, clay and anhydrite are located mainly along the halite grain boundary and where the crystal defects are. These crystal defects appears as small defect planes with a 45° from the horizontal which results in a 135° angle from the principal stress applied σ_1 represented with two black arrows on the top right of the figure.*

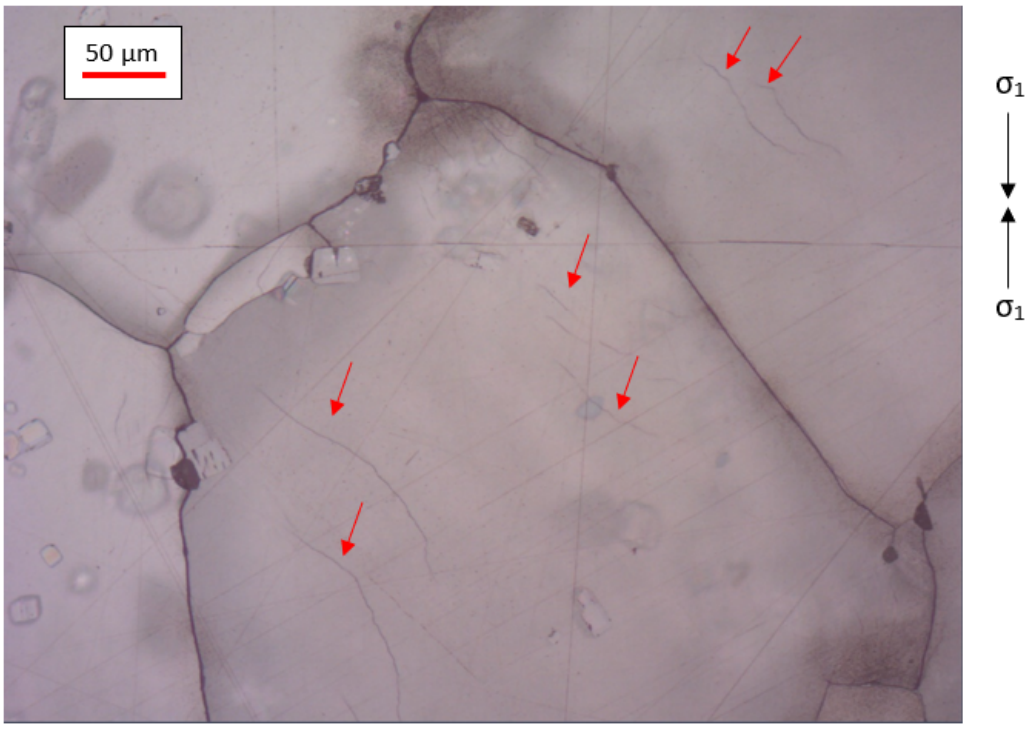

Figure 5.20: *Microphotographs of samples C3 after deformation under reflected light showing plastic deformation on the surface of halite grains. Red arrows mark the crystal defects on halite crystal grains showing a 45° angle from the horizontal also resulting in a 135° angle from the principal stress applied σ_1 represented with two black arrows on the top right of the figure.*

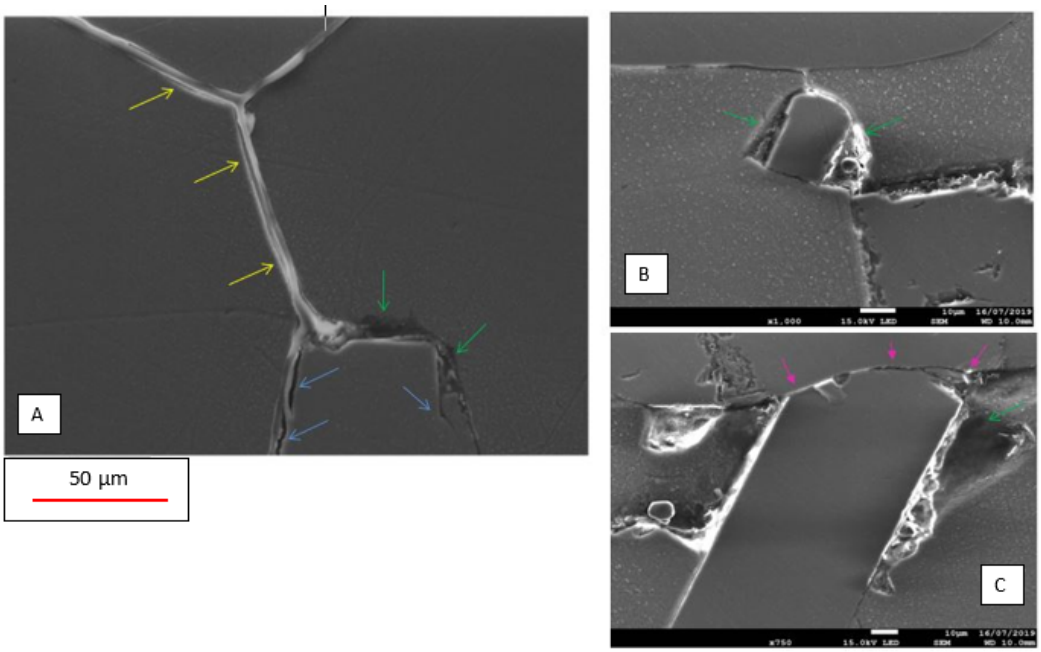

Figure 5.21: *SEM images from sample A3 after deformation. Porosity generation (green arrows) can be observed as a result of second phase mineral rotation under cyclic mechanical loading. Yellow arrows mark the boundary opening at the halite-halite contact and the blue arrows indicate the grain boundary at the halite-anhydrite contact. Purple arrows show plastic deformation between two grains of second phase content as a result of grain rotation during the cyclic mechanical loading test.*

work of fractures as the one observed in samples from Series B which presents alternation of anhydrite and polyhalite-rich layers with halite. This porosity was locally observed only around second phase content.

5.4 Concluding remarks

The main second phase observed in is anhydrite and polyhalite for samples from Boulby Mine (series A, B, and C), and anhydrite and clay for samples from Winsford Mine (series F, WB, and LB).

Samples with a higher second phase content (i.e. anhydrite, polyhalite and clay) presents higher density of fractures and also larger connectivity between micro-cracks.

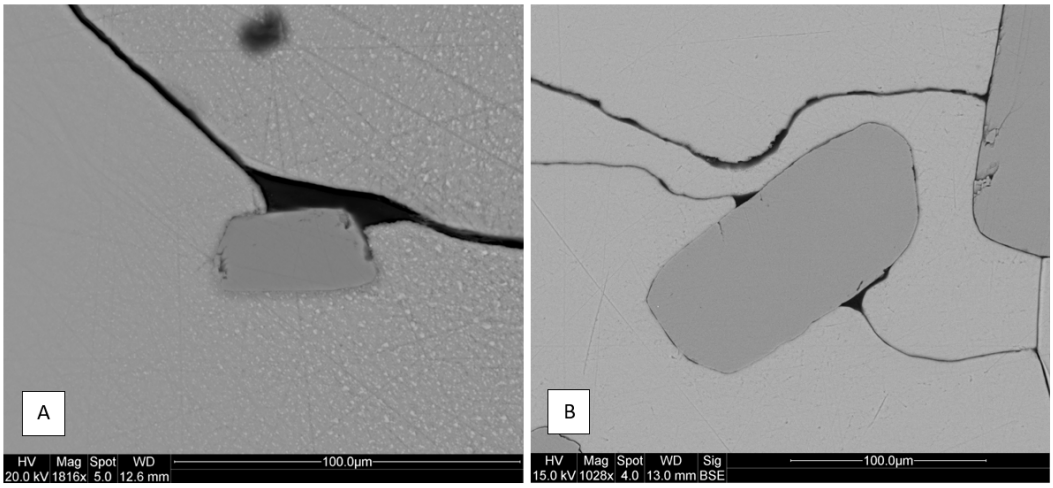

Figure 5.22: *SEM images from sample A4 (A) and A3 (B) after deformation showing island structure.*

Samples from series A have a higher elongation of halite grains in comparison to the other samples. The elongation of halite grains is more notable in samples deformed at higher temperatures and also at a higher amplitude of cyclic mechanical load.

Transgranular fracturing increases in samples tested at higher temperatures and confining pressure and also in samples related to breccia textures like samples from Series LB. Another relevant microstructure observed is grain boundary migration, although it is not possible to verify these structures appeared as a result of the deformation test. Most probably, the structures related to grain boundary migration were already present in the sample before deformation. Fluid inclusions can be observed in all samples although samples from series WB are the ones showing a higher content of fluid inclusions.

Although samples where grouped in different series based on their mineralogical characterisation and second phase content, additional analysis with transmitted light microscopy evidences the limitation of such classification based only on mineral content using XRD analysis.

Analysis of samples tested at a higher amplitude of cyclic loading conditions

(6 to 20 MPa) show large elongation of halite grains in samples from series A and higher impregnation of blue resin from the thin sections preparation, both along transgranular fractures and in halite grain boundaries.

Chapter 6

Discussion and interpretation

6.1 Elastic properties of rock salt under cyclic loading conditions

Most of the samples showed a small decrease in Young's modulus per cycle along the cyclic loading mechanical test. As a result of the damage after every the mechanical loading compression, the Young's modulus per cycle is slightly lower than the initial (undamaged) modulus of elasticity, calculated in the previous cycle, and higher than the Young's modulus after the following compression cycles (Xu et al., 2012). This accumulation of damage cycle after cycle affects the elastic properties of rock salt which can be observed in the elastic recovery of the rock per cycle. The stress-strain plots discussed in Chapter 4 recorded the minimum and maximum ε_{ax} for each minimum and maximum axial stress applied per cycle. Every cycle was loading up to 7.5 MPa and then unloading to 4.5 MPa. Therefore, during every cycle the samples recorded an elastic recovery where the ε_{ax} at maximum axial stress registers a positive recovery when the sample is unloaded. The difference between the maximum ε_{ax} and the minimum ε_{ax} per cycle is interpreted here as the elastic recovery capacity of the sample. Hence, the total deformation of the sample is the sum of the initial deformation by the static load until 4.5 MPa and the creep

and damage deformation induced by the cyclic loading test (Zhenyu and Haihong, 1990). The elastic recovery calculation per cycle for each sample was performed with MATLAB and the information about the calculations can be found in Script 2 in Appendix B (Script 1 is the main script calling for the functions from Script 2 to calculate modulus of elasticity per cycle and elastic recovery).

Figures 6.1, 6.2 6.3, 6.4, 6.5 6.6 show the evolution of the elastic recovery capacity during the cyclic tests for all samples tested at a cyclic loading stress between 4.5 and 7.5 MPa. All graphs present a positive trend, with two distinctive patterns observed. The elastic recovery values for samples from Boulby Mine, with anhydrite and polyhalite as main second phase content, tested at room temperature vary along the cyclic testing, with local increase, decrease or steady periods. Samples from Winsford Mine, with anhydrite and clay as main second phase, also show a significant increase of the elastic recovery during the first 500 cycles before reaching a plateau value of elastic recovery capacity for the rest of the test.

From figures 6.5, and 6.6, all samples show values of axial elastic recovery per cycle between 0.018 and 0.035%. And only some samples from series B, C and LB show slightly higher elastic recovery values in comparison to the rest of tested samples.

From the samples tested at 12 MPa and low temperature (room temperature), sample B1-2 (with a higher content in anhydrite and polyhalite) shows a 10% more elastic recovery per cycle than the rest samples tested under same conditions. The same pattern can be observed in samples tested at 25 MPa and also at room temperature, where sample B8 (room temperature) shows higher elastic recovery in comparison to the rest of samples tested at the same temperature. All samples with a content in anhydrite and polyhalite, tested at

room temperature and 12 MPa confining pressure, show a drastic increase of elastic recovery after 2000 cycles whereas samples with a content in clay shows a small increase within the first 300 cycles, which can be observed as a decrease in Youngs modulus in figures 4.14, 4.15 and 4.26. The prompt increase in the elastic recovery in samples with a higher content in anhydrite and polyhalite could be related to the weakening of rock salt due to second phase content (Liang et al., 2007).

By looking at the data from samples tested at 45 MPa confining pressure and 55-75°C, the majority of the samples show an elastic recovery in axial strain per cycle is between 0.02 and 0.03 %. LB7 is the only sample showing an elastic recovery slightly over 0.03%. All samples from Winsford Mine present constant values with smooth and flat curves whereas samples from Boulby Mine can present some minor variations like sample C1, recording a small increase in elastic recovery per cycle after the first 500 cycles.

The observed increase of elastic recovery per cycle in samples tested at low temperature is inversely proportional to the decrease in Young's modulus per cycle, due to the damage accumulation in each cycle (Zhenyu and Haihong, 1990). Therefore, I propose that the increase in elastic recovery per cycle is related to a micro-fracturing network development due to mechanical loading damage and also observed in the decrease of Young's modulus.

Elastic deformation in rock salt is linked to interatomic forces resisting the distortion produced over the crystal lattice when a stress is applied and then removed, bringing the lattice to the equilibrium position at zero stress. Inelastic deformation is permanent and non-recoverable deformation as a result of line motion from imperfections in the crystal (dislocations), mass diffusion, and, at low pressure, microcracking Senseny et al. (1992). Samples from series B, with the highest second phase content (anhydrite and polyhalite) and lowest

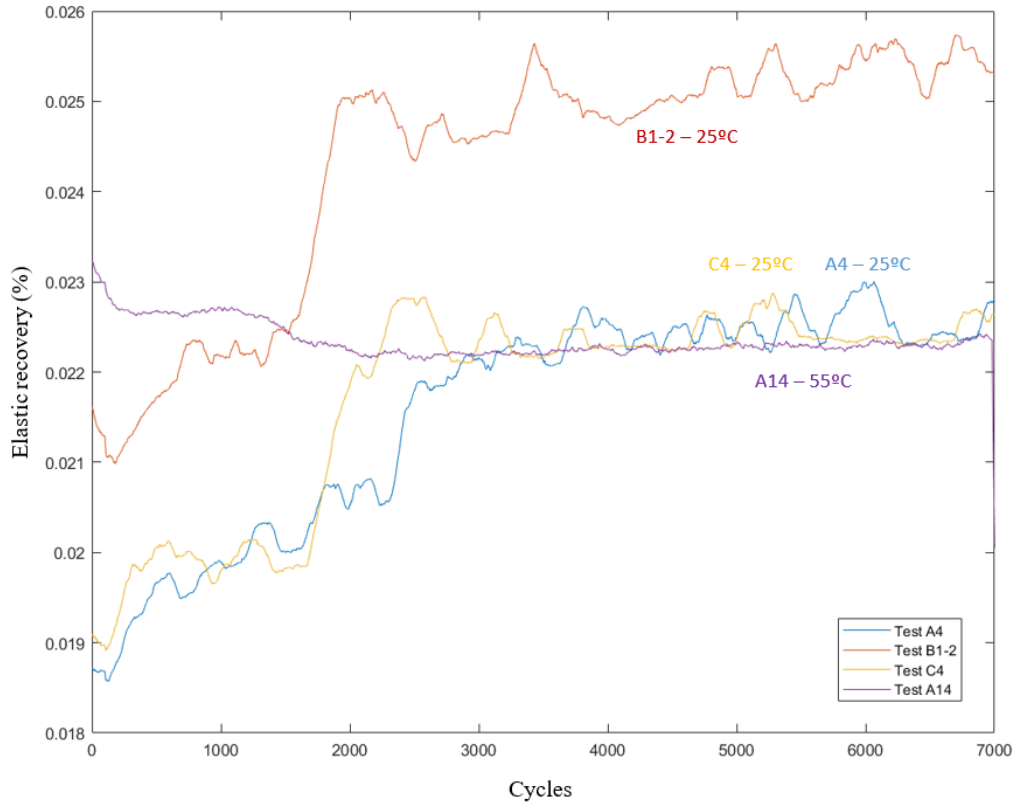

Figure 6.1: *Elastic recovery (%) per cycle versus nymber of cycles for samples tested at 12MPa and room temperature (represented as 25° C), 55 and 75° C from Boulby Mine. In this figure it can be observed how samples with a higher anhydrite and polyhalite content (Sample B1-2) show a higher elastic recovery per cycle. It can also be observed how samples tested at higher temperature (A14) show a lower fluctuation in elastic recovery per cycle.*

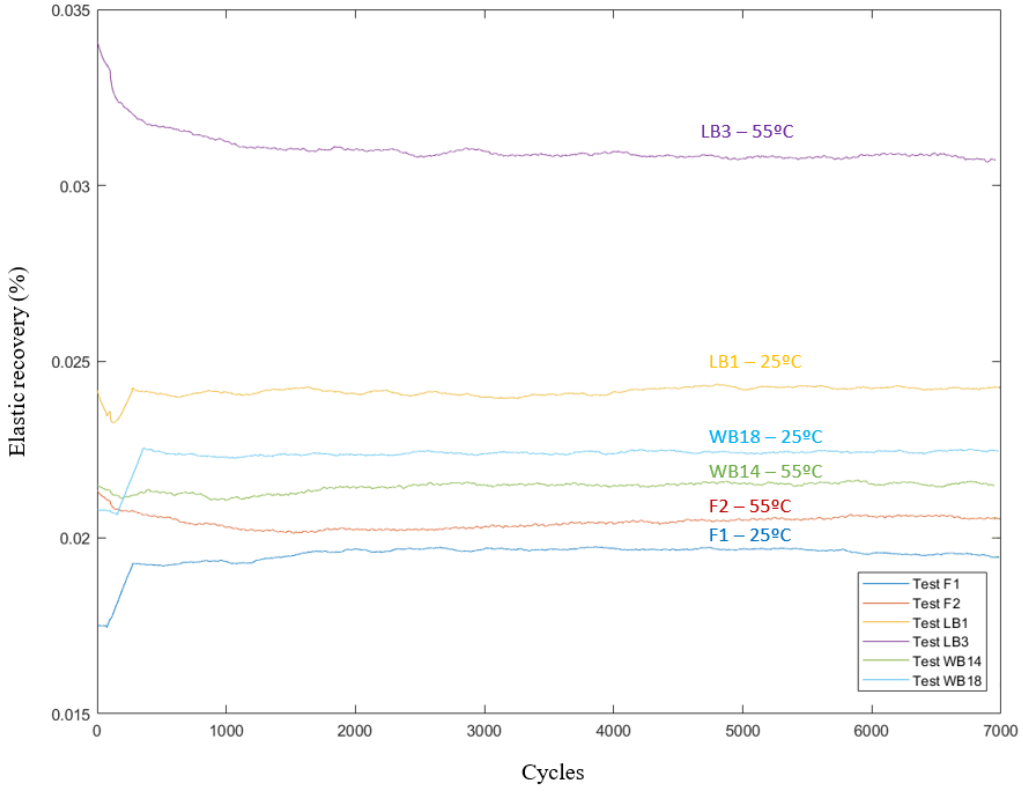

Figure 6.2: *Elastic recovery (%) per cycle versus number of cycles for samples tested at 12MPa and room temperature (represented as 25° C), 55 and 75° C from Winsford Mine.*

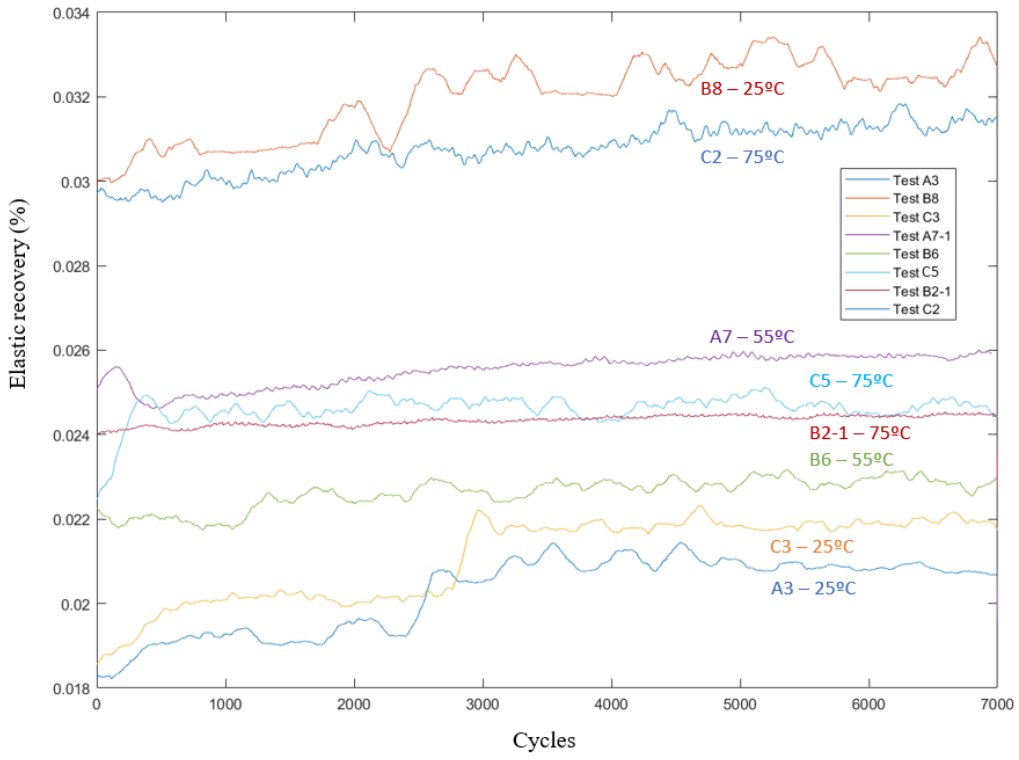

Figure 6.3: *Elastic recovery (%) per cycle versus number of cycles for samples tested at 25MPa and room temperature (represented as 25° C), 55 and 75° C from Boulby Mine.*

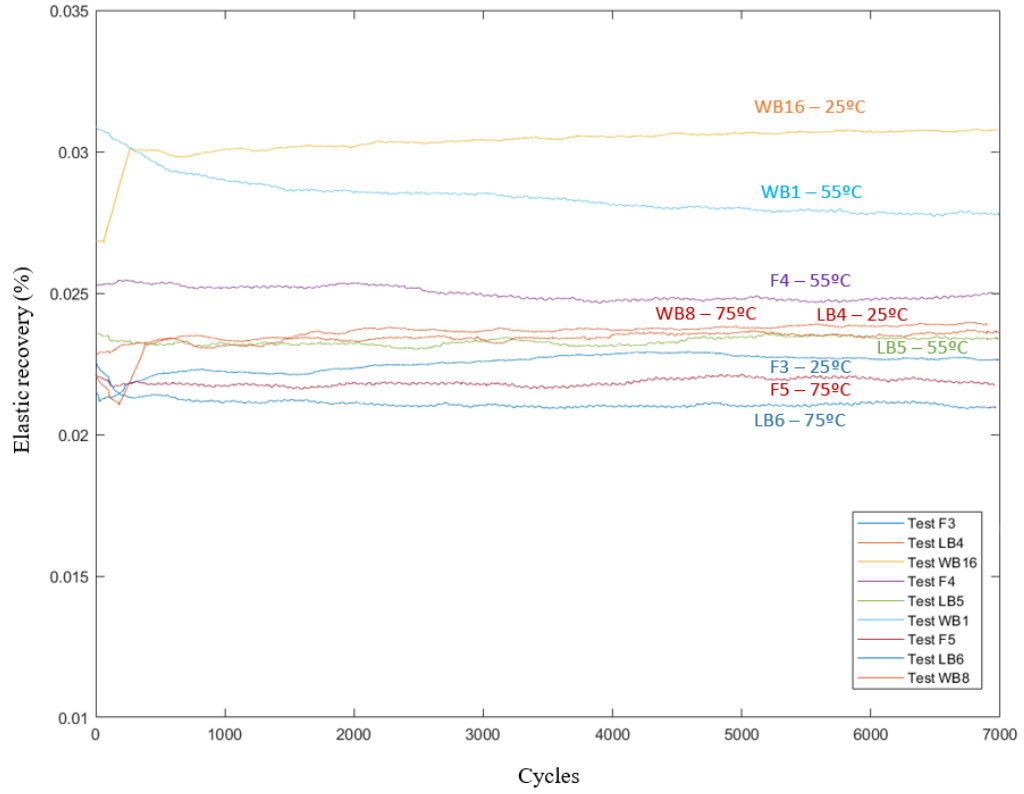

Figure 6.4: *Elastic recovery (%) per cycle versus number of cycles for samples tested at 25MPa and room temperature (represented as 25° C), 55 and 75° C from Winsford Mine.*

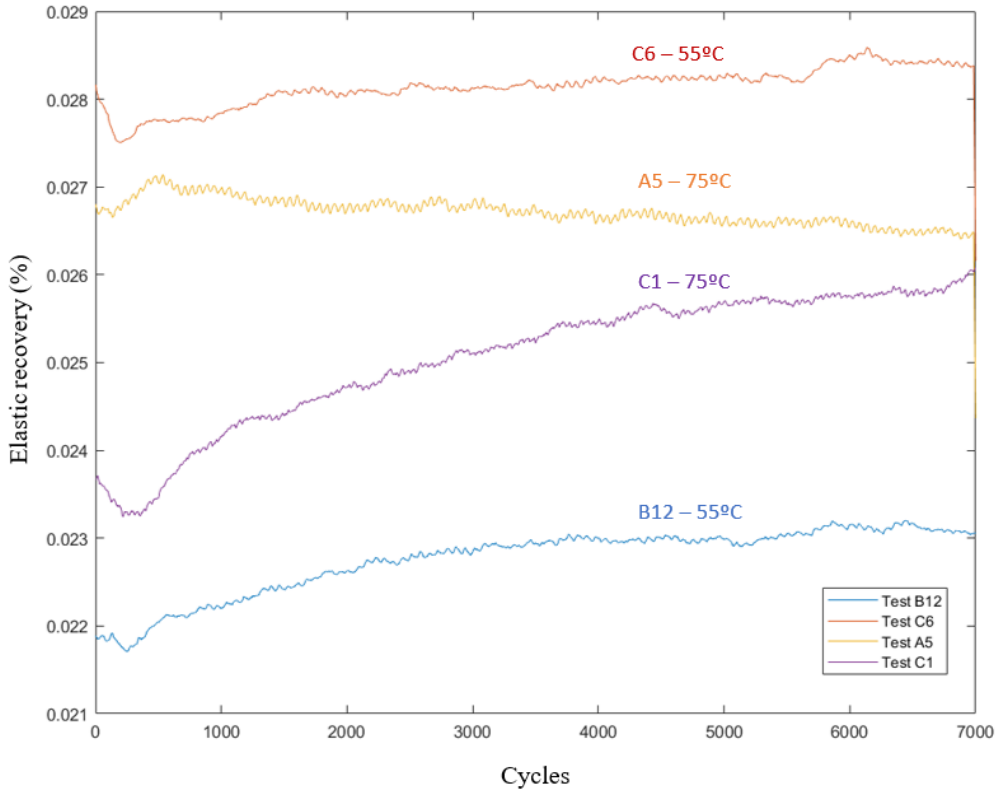

Figure 6.5: *Elastic recovery (%) per cycle versus number of cycles for samples tested at 45MPa and 55-75° C from Boulby Mine.*

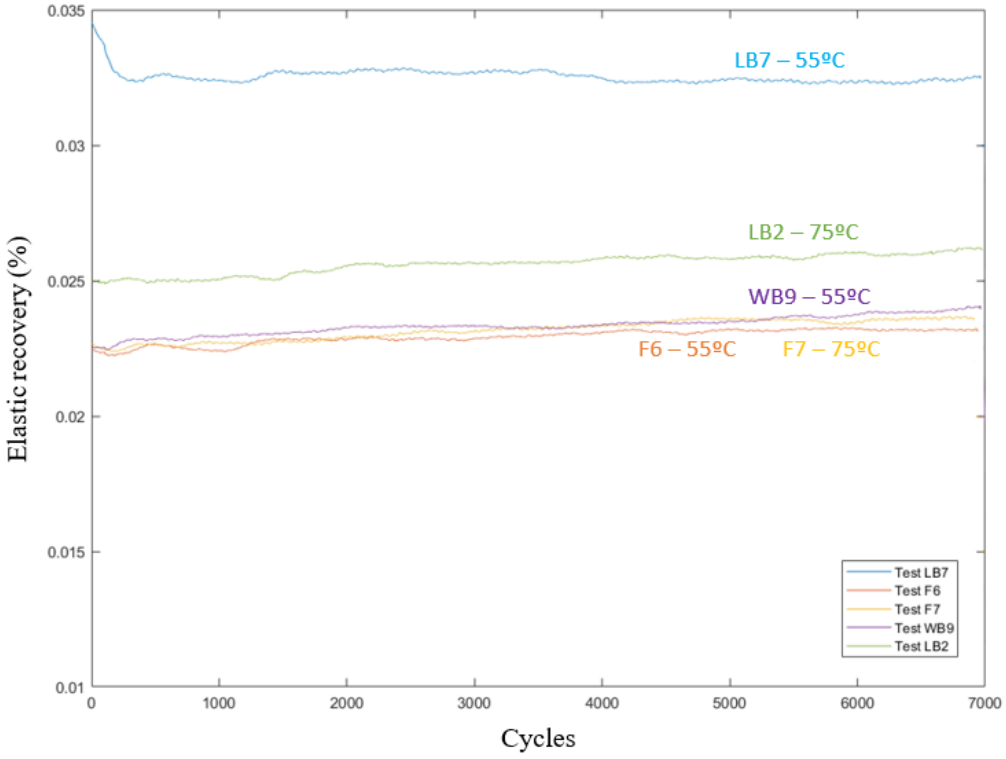

Figure 6.6: *Elastic recovery (%) per cycle versus number of cycles for samples tested at 45MPa and 55-75° C from Winsford Mine.*

halite content (60%), shows a higher elastic recovery capacity per cycle than every other tested samples that have a higher halite content in comparison (more than 80%; tested at room temperature). At 25 MPa and room temperature, the most notable increase in the elastic recovery capacity for samples A3, B8 and C3 is registered between 2000 and 3000 cycles, simultaneously with the drop in Young's modulus and the change in strain versus cycle number. In comparison, samples F3 and LB4 (with clay content) show very stable elastic recovery values of around 0.022-0.024%. Based on post-deformation petrographic analysis, sample B8 shows a major formation of microcracks during the cyclic loading test. These micro-fractures observed were mainly located along the anhydrite layering (almos parallel to the anhydrite layering) with orientations of 20°C, maximum 45°C, from the horizontal. Several authors have investigated the relationship between the effects of differential, effective stress and temperature over permeability of rock salt (Urai et al., 1986; Peach and Spiers, 1996; Peach et al., 2001; Popp et al., 2001). Rock salt permeability can dramatically increase when tested at low effective stress and low temperatures by micro-fracturing and dilatancy. However, the higher concentration of microfractures, in the samples analysed, is linked to the anhydrite and polyhalite bands between halite layers in the sample. For this reason, I propose that the microcracks could act as sliding paths assisting the elastic recovery during axial stress unloading, thus supporting sample B8 higher elastic recovery in comparison to the other samples. The variations observed on the elastic recovery graphs for samples A3, B8 and C3 could be also linked to the polyhalite presence as a second phase minerals.

Elastic recovery curves for samples A3, B8 and C3 show higher variation along the whole test while samples F3 and LB4 show a smoother trend. All samples A3, B8 and C3 have polyhalite as a second content mineralogy which is harder than anhydrite (Pfiefle and Senseny, 1981). The present of polyhalite as second phase content could be an explanation for a higher variability in elastic

recovery along the cyclic mechanical test.

An increase in confining pressure also seems to results in a decrease of elastic recovery fluctuation as observed from samples tested at room temperature and confining pressures of 12 MPa and 25 MPa. Samples from Boulby Mine tested at 12 MPa presents a higher variation and a more significant increase of elastic recovery per cycle than samples tested at 25 MPa. Therefore, not only the increase of temperature but also the increase in confining pressure results in an enhance of plastic behaviour of rock salt. From the hysteresis loops analysis it can be also observed that plastic deformation increases with the number of cyclic loading (Liu et al., 2014). The analysis with hysteresis loops also reveals strain-hardening and an increase of ductile behavior after a certain number of cyclic loading cycles (Ma et al., 2013).

6.2 Effect of temperature over rheological behaviour of rock salt

A general trend of final axial strain increase has been observed in samples tested at higher temperatures in comparison to the equivalent samples (within series of rocks) tested at lower temperatures. This increase in final axial strain is due to an increase in creep rate with temperature (Le Comte, 1965; Taheri et al., 2020). A decrease in Young's modulus can also be observed by comparing samples tested at room temperature (21-22°C) from samples tested at more elevated temperatures. It is also observed that the elastic recovery per cycle tends to stabilise with the increase of temperature. Samples with tested at higher temperature show smoother evolution of elastic recovery in comparison to samples tested at room temperature. Therefore, a decrease in the elastic deformation per cycle can be observed with the increase of temperature which

can be related to an enhance of creep deformation (Le Comte, 1965; Carter and Hansen, 1983).

Creep in rock salt is a thermally activated process meaning that an increase in temperature results in a decrease in the creep rate. For this reason, creep rate can be very sensitive to temperature variations in constant-stress isothermal creep tests (Le Comte, 1965). According to Carter and Hansen (1983), increase in temperature results in a decrease of the ultimate strength with ductile behaviour ruling at low deviatoric stresses and high confining pressures. In general, from the mechanical data analysis, there is an increase of plastic behaviour with the increase of temperature, which can be observed in the hysteresis loop analysis. Samples tested at higher temperature show a slightly larger distance between the final hysteresis loops.

Regarding the lateral strain, all samples showing an initial positive increase in ε_{circ} were samples tested at higher temperatures (55-75°C) and with a minimum content of 80% halite. The only sample tested at 55°C but not showing an initial lateral compression during the first 100 cycles is B6, with a higher content in anhydrite and polyhalite. But also, samples tested at a higher temperature show an increase of small vertical variations linked with the cyclic mechanical loading applied resulting in a curve trend that looks like a saw. This trend is noticeable in samples tested at 55°C and it gets more prominent in samples tested at 75°C which could be related to thermal strain.

According to Hooke's law, variations in temperature can produce thermal stress affecting ε. Equation 6.1 shows how thermal stresses in rock salt will be affected by the coefficient of linear thermal expansion of salt (α) and the increase of temperature (Wang and An, 2017).

$$\varepsilon = \frac{\sigma_T}{E} + \alpha \Delta T \tag{6.1}$$

where E is the Young's modulus, σ_T is thermal stress.

Rock salt, with a thermal expansion coefficient of α=4x10^{-5}/°C, is very sensitive to temperature variations leading additional thermo-elastic strain in low-stress creep tests (Bérest, 2011; Bérest et al., 2019). Therefore, slightly lateral strain recovery observed in samples tested at higher temperature (55-75°C) and confining pressure (45 MPa) could be linked to thermo-elastic strains effect. Small variation in temperature, for samples tested at room temperature, could also result in thermal stresses aftecting the rheological behaviour of the rock sample such as the positive lateral strain recoveries oveserved in samples testsed at higher temperatures (55-75°C).

This suggests that slightly changes in rheological behavior, like the jumps and lateral strain recovery observed in some samples in the lateral strain analysis, could be linked to involuntary small variations in room temperature. Hence, temperature changes during the cyclic mechanical loading experiment were recorded in order to account for any significant variation. Figure 6.7 show the temperature evolution versus lateral strain. All tests show a decrease in temperature from the beginning of the test until the end with variations of temperature from +/-3°C to maximum +/-5°C. Sample F3 shows the greatest temperature variation with a temperature drop of 4.5°C from the beginning (25.5°C) until the end (21°C) of the test. Despite F3 being one of the samples showing the least variation in lateral strain, the significant drop in temperature could be (amongst other factors like second phase content) one of the reasons to explain why F3 shows a repeated recovery in lateral strain around every 500 cycles. Even though thermo-elastic strains can play a significant role over creep rate in long term creep tests in pure halite (Bérest, 2011), the data from samples tested at room temperature do not point to a clear relationship between the room temperature variations and the recorded strains during these short term cyclic mechanical loading tests. The second phase mineral content

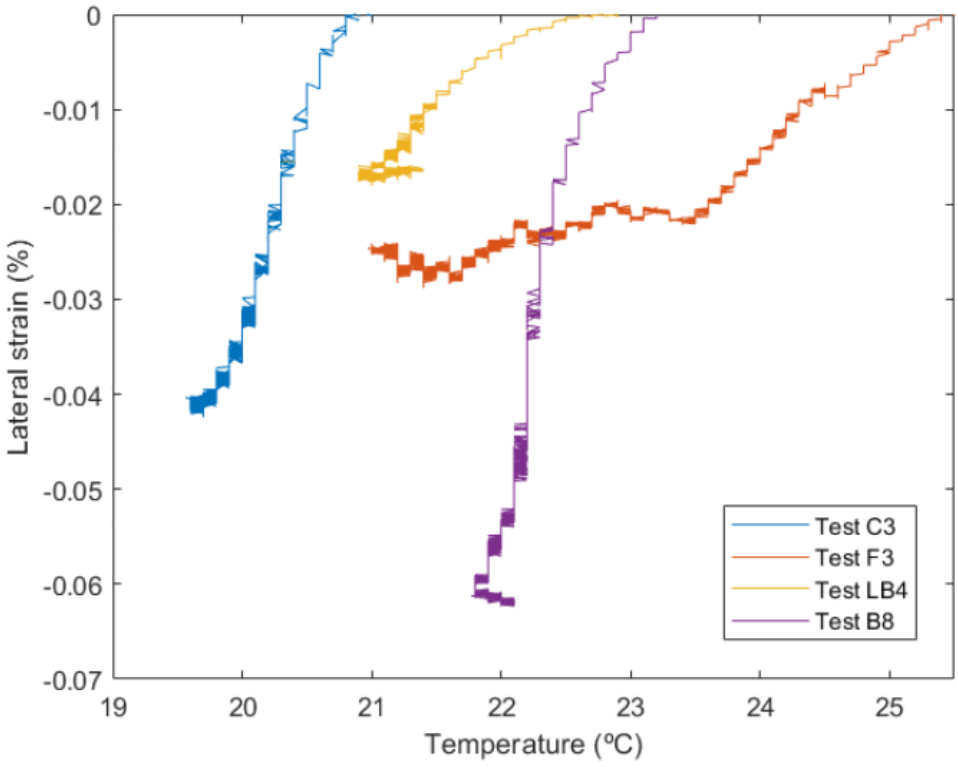

Figure 6.7: *Plot of ε_{circ} (%) against temperature during the cyclic loading mechanical test for samples tested at 25 MPa confining pressure and 25° C.*

may have also have allowed to accommodate this minor temperature effect differently.

6.3 Analysis of deformation micromechanisms

Different type of deformation has been observed with the analysis of thin sections. Both brittle deformation, with micro-fracture network development, and halite re-crystallisation micro-structures can be observed. However, it is necessary to make an exhaustive analysis of temperature and stress conditions necessary for these deformation mechanisms to take place.

6.3.1 Deformation micromechanisms in halite

Rock salt can accommodate deformation via a wide range of micromechanisms. Many micromechanisms, from dislocation creep to pressure-solution and dynamic recrystallisation have been studied for decades. Although an

increase of mechanisms similar to pressure solution can be observed here in the tested samples with a high second phase content, such as anhydrite and polyhalite, a more detailed review of the constitutive laws is needed to fully distinguish between previous internal structures and deformation induced by the cyclic mechanical loading test. Dislocation creep mechanism, which takes place within the halite crystal lattice, dominates deformation on short duration laboratory tests at a high range of temperatures (100-200°C) (Urai and Spiers, 2007; Li et al., 2012). Solution-precipitation creep, which takes place at the grain boundaries, and dynamic recrystallisation play an important role in long-term deformation processes (Li et al., 2012). During dislocation creep, if the halite grains contain significant amounts of water in fluid inclusions or in the grain boundary, fluid assisted grain boundary migration occurs by solution-precipitation transfer across grain boundary water/brine films. This helps to decrease dislocation density and remove the stored energy from dislocations (Urai and Spiers, 2007; Schenk and Urai, 2004; Schenk et al., 2006). Moreover, during pressure-solution, highly stressed boundaries dissolve allowing the diffusion of material through grain boundary fluid which crystallises under low normal stress (Urai and Spiers, 2007; Spiers and Schutjens, 1999). Compaction of porous salt may occur as result of a grain rearrangement by the intergranular sliding and rotation processes accompanying pressure-solution process (Spiers and Schutjens, 1999).

Several factors such as temperature, confining pressure, grain size, second phase content and the presence of brine water in grain boundaries will determine the relative importance of those processes during rock salt deformation (Urai and Spiers, 2007). Although solution-precipitation creep has been described in several laboratory investigations, with temperature ranges of 20-200°C (Urai et al., 1986; Urai and Spiers, 2007; Bérest et al., 2005; Spiers et al., 1990; Spiers and Brzesowsky, 1993; Renard et al., 2002, 2004) due to the strong dependence of grain size and limited duration of laboratory tests, it

is difficult to observe this deformation mechanism in experiments on natural rock salt at laboratory time scale (Urai and Spiers, 2007).

Urai and Spiers (2007) and Li and Urai (2016) conducted a data recompilation from previous analysis on rock salt samples tested at constant-load in the literature. The data has been compiled and plotted with the data analysed in this project for a better understanding of the deformation processes taking place during the cyclic mechanical loading test. Although previous laboratory research on deformation mechanisms in rock salt have been conducted under constant stress deformation, we observed that rock salt samples deformed at a low range of cyclic mechanical loading conditions still presents a similar behavior to the typical creep behavior observed in strain-time plots under a constant stress. For this reason, steady-state strains were calculated from strain versus time plots which can be found in Appendix C.

Figure 6.8 presents the differential stress - strain rate diagram with the data from all samples tested at the maximum axial stress applied during the cyclic mechanical loading test and recompiled data from the literature review (Urai and Spiers, 2007; Li and Urai, 2016; Schléder and Urai, 2005). Data from the different series of samples are represented by different markers, according to the different series, and blue, orange and red colours for room temperature, 55°C and 75°C respectively. Discontinuous line represents extrapolation of the dislocation creep law. Solid lines are the room temperature solution-precipitation creep law in different colours for different grain sizes (after Urai and Spiers (2007); Schléder and Urai (2005)). Creep constitutive laws help to predict and model deformation processes under certain mechanical conditions. The graph shows that, with the strain rates calculated at the steady-state stage of the strain versus time plot for samples at low temperature and low confining pressure, the strain rates are below the domain of pressure-solution for samples with a grain size of 0.1mm. Thus lower strain rates would be

needed for pressure-solution between halite grains to take place in a sample with a grain size from 0.5mm to 1.5/2cm.

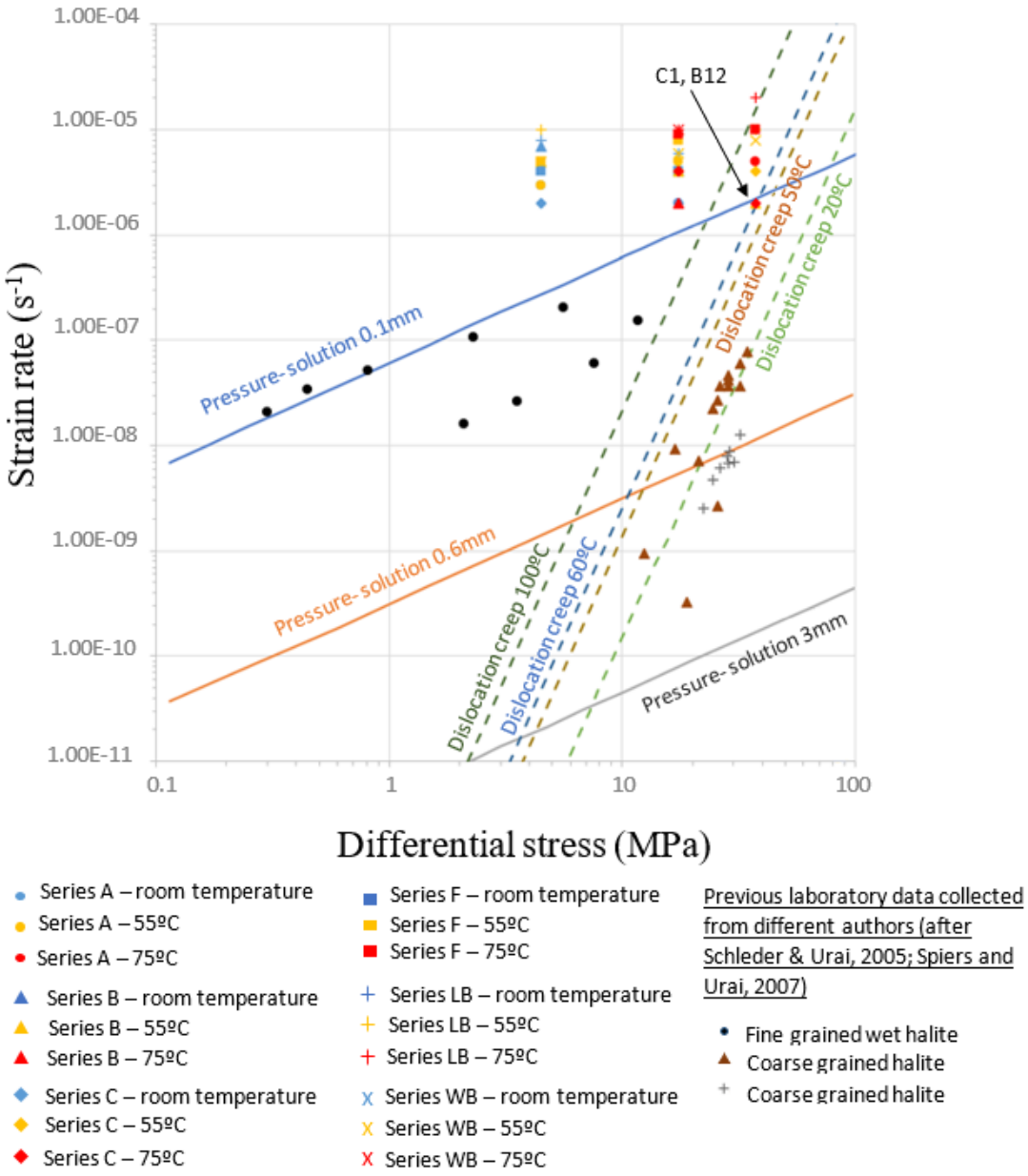

Figure 6.8: *Strain rate (s^{-1}) versus differential stress (MPa) plots for all tested samples and a summary of data from previous tests from the literature review (After Urai and Spiers (2007)).*

Although pressure-solution structures can be observed in rock samples after deformation, it seems unlikely that those structures are a result of the cyclic loading mechanical deformation. However, for samples tested at higher temperatures and confining pressures (i.e. C1 and B12), steady-state strain rates

calculated fit with the theoretical pressure-solution curve for sample with a grain size of 0.1mm. However, to reach real stationary creep rates requires time, from few days to years, depending on temperature and stress (Günther et al., 2015).

Creep in rock salt is driven by dislocations under constant stress. In a typical strain-time plot, we can observe an initial stage of creep, primary creep, where the density of free dislocation inside the sub-grains increases. The increase of dislocation density results in an increase of the resistance against the deformation, also known as strain hardening. During strain hardening, the creep rate is reduced resulting in the transient part of the creep in strain-time plots. During strain hardening, a rearrangement of sub-grain structure takes place resulting in a dislocation recovery (Khaledi et al., 2014). However, although all the samples in this project where tested under cyclic loading conditions, strain versus cycles (equivalent to time) plots from Appendix 3 shows that similar stain trend to the typical creep behavior are observed. Therefore, although the tests were not under constant load, similar deformation micro-mechanisms can be expected to take place such as dislocation creep and pressure solution under cyclic loading conditions.

The thin sections after deformation suggest that most plastic deformation newly observed is driven by a decrease in halite grain size which could be accompanied with grain boundary diffusion in halite crystals. Deformation of rock salt under low-stressed conditions is mainly controlled by pressure-solution creep, involving crystal grain slide with pressure solution and dynamic re-crystallization processes (Urai and Spiers, 2007; Bérest et al., 2005). However, the comparison of our data to other data from the literature suggests that strain rates reached during the cyclic mechanical loading test performed are neither slow enough nor long-lasting in time for pressure-solution creep mechanisms to take place. Small shear deformation traces in halite crystals,

observed in sample C3 after deformation, could be related to defects of crystal misorientation and grain boundary sliding (Figure 6.9).

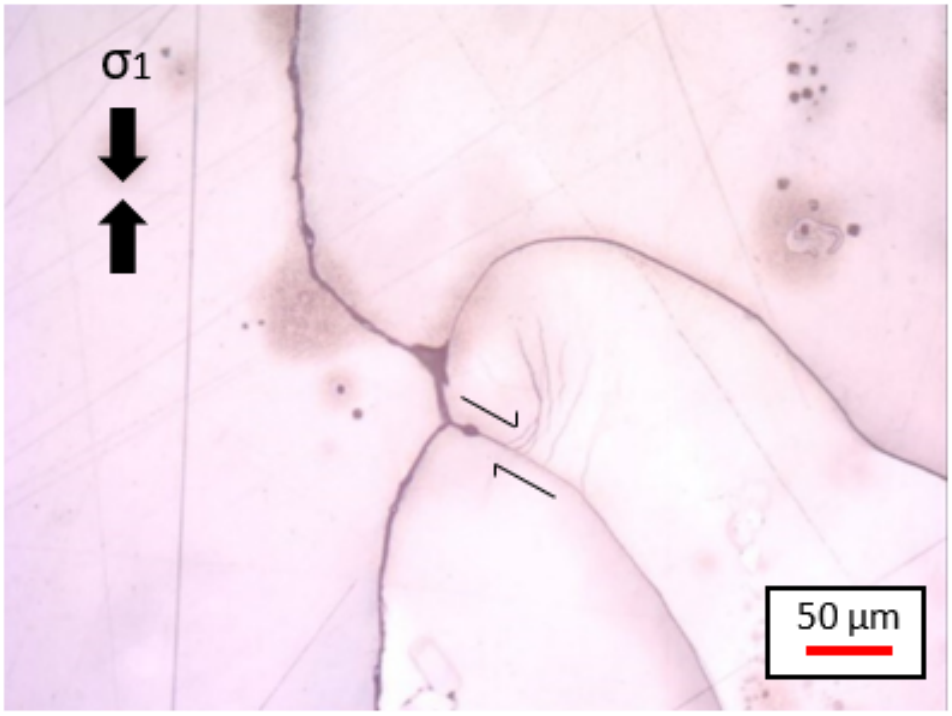

Figure 6.9: *Image in the transmitted light microscope from C3 after deformation. Shear deformation is observed in halite grains. Principal stress σ_1 is represented with black arrows on the top left of the picture.*

Deformation of grain boundaries in Figure 6.9 could have been a result of rotation re-crystallization or boundary rotation (Drury and Urai, 1990) as does the observation of many rocks with 120° triple junction (Urai et al., 1986). As a result of this rotation and the crystal misorientation, plastic deformation appears in the form of plastic micro-fractures with a very low angle from the direction of σ_1 applied (vertical) during the cyclic loading test. Structures of grain boundary migration have also been described in the analysis with thin sections after deformation in Chapter 5, where material from a halite grain enters in the neighbouring grain boundary and recrystallizes on the lattice of that grain (Urai et al., 1986).

6.3.2 Brittle deformation related to second phase content

Samples from series LB tested at higher temperatures and confining pressures (i.e. LB6 and LB7) showed a lower ε_{circ} than the expected from the highest rates of ε_{ax} in comparison to all other samples tested. Series LB presented a micro-structure with a higher content of micro-fractures and second phase content (mainly clay) due to the initial breccia texture. As discussed in chapter 2, according to Hickman and Evans (1995) the presence of montmorillonite clays at the interface between two halite lenses increases the rate of shortening. Moreover, clay minerals can enhance mechano-chemical compaction due to holding a contact at a micron scale and enhance a higher diffusional transport rates (Renard et al., 2001). Therefore, I propose that the micro-fractures and a higher content in clay could have assisted the compaction of the rock sample resulting in a larger axial shortening in comparison to the lateral expansion during deformation.

A clear development of widespread microfracture network can be observed in relation to second phase content presence when comparing deformed and undeformed microstructures from same series samples. This increase in microfractures supports the preliminary assumptions that an increase in second phase content can induce an increase in rock permeability and brittleness. Interestingly, a higher content in anhydrite, polyhalite and clay can also be related to an increase in elastic recovery per cycle. Microfractures seem to act as a sliding pathway assisting the elastic recovery during the unloading. The increase in elastic recovery with the number of cycles would be related to the damage accumulation enhancing the development of new fractures and extension of micro-crack network.

Samples with a higher content in anhydrite and polyhalite (i.e. B6 and B8)

presented a greater rate of initial expansion (within the first 1000 cycles) than the other samples. Rock salt with a high second phase content is therefore more likely to present a higher initial brittle damage than rock salt with a higher content in halite.

A clear relation between micro-crack formation and higher second phase content has been already discussed. The main deformation mechanisms in areas with higher concentration in second phase content is micro-cracking and pressure solution with high grain plasticity (Figure 6.12). This creates new porosity.

Deformation and damage around halite grains can also be observed as transgranular micro-cracking (TMC) in the presence of second phase content. Second phase content acts as a weakening agent in halite crystal deformation (Figure 6.12C). Sample B8 also shows fluid inclusions arranged along linear disposition across some halite grains. According to Urai (1983), during grain boundary migration fluid inclusions encountered are incorporated to the thin fluid layer promoting the migration. When the grain boundary is pinned due to the presence of second phase content, fluid inclusions can be left behind resulting in an array of fluid inclusions. Figure 6.10 show a an image from A4 after deformation where fluid inclusions can be observed close to a grain of anhydrite.

Due to the effect of deviatoric stress, fluid film morphology in grain boundaries of halite can be influenced by the orientation of the boundary with respect to the principal axes of stress (Drury and Urai, 1990). Therefore, according to Drury and Urai (1990) an island structure can be formed in grain boundaries under high normal stress. This phenomenon illustrated in figure 6.11 derives in regions containing fluid bubbles being separated by "thin film" regions which contain the stress-supporting points of contact between the two grains. The

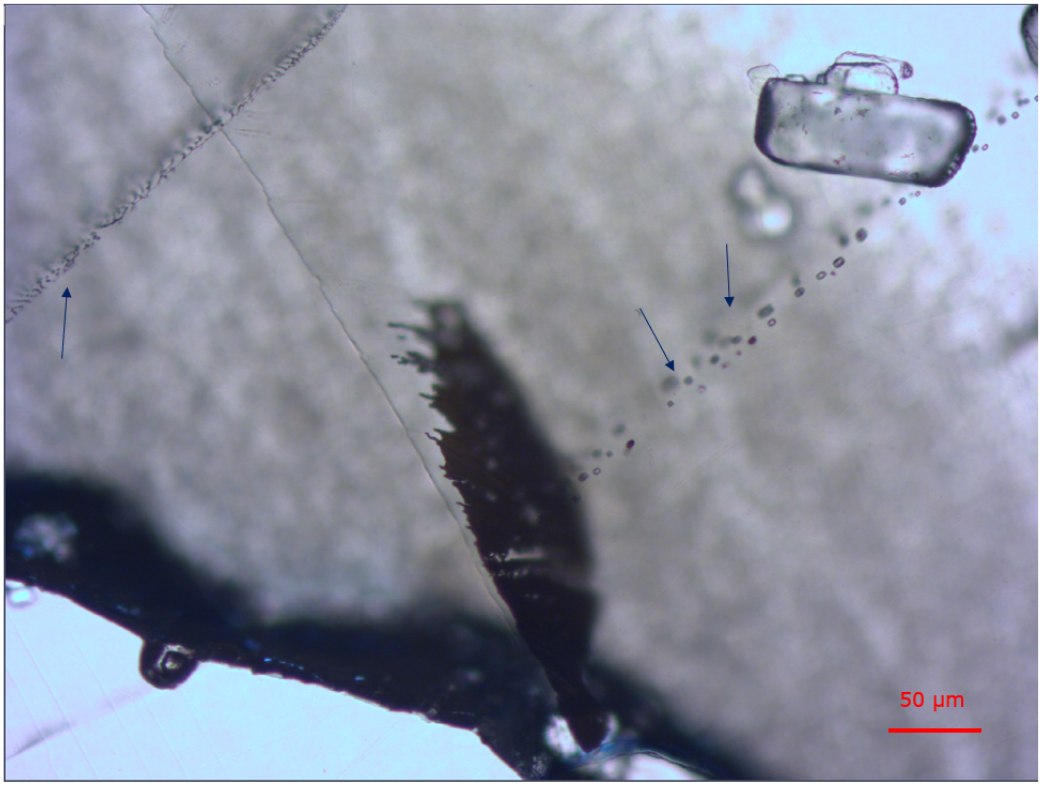

Figure 6.10: *Thin section analysis of samples A4 after deformation showing fluid inclusions marked with blue arrows.*

thick-film boundaries are present in grain boundaries at low angle to σ_1. This phenomenon has been also observed in micrographs from SEM where a island structure was created between halite-second phase contact (Figure 5.22 from Chapter 5).

According to Schulze et al. (2001), both permeability and porosity depend on the state of stresses, the differential stress relative to the dilatancy boundary and on the minimal principle stress. Strain accumulation during mechanical loading and the distribution of hard particles can imply crack patterns and permeability to develop anisotropically, with orientations that depend on load geometry. SEM analyses have shown that other types of damage related to the cyclic mechanical loading can occur by mineral rotation. In spite of an increase of porosity around isolated grains of anhydrite due to crystal rotation under cyclic conditions, there is no evidence here of an increased permeability as the new porosity generated does not show further connectivity with other

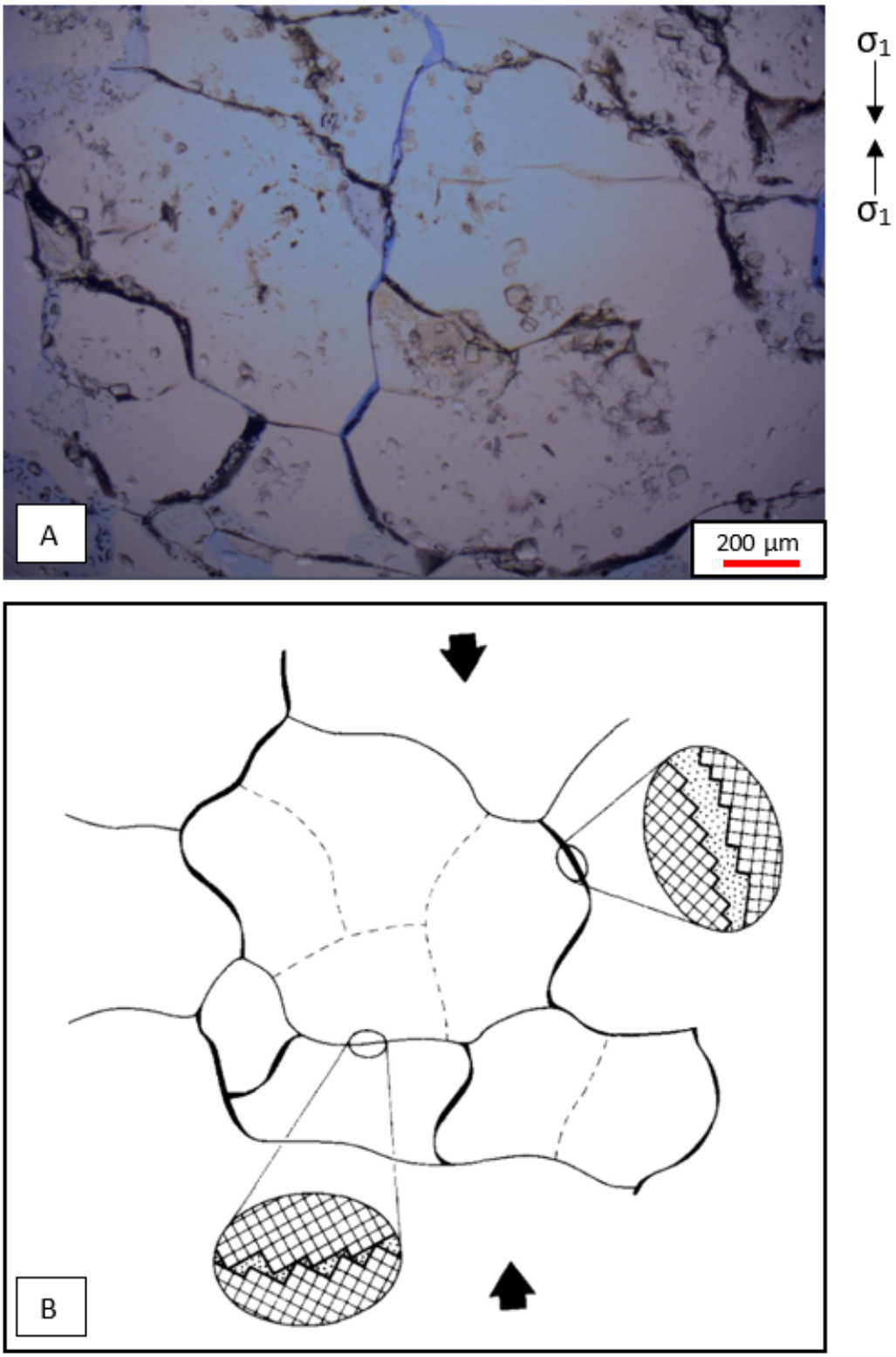

Figure 6.11: *A) Micrograph from sample C1 after deformation where recrystallisation in grain boundary can be observed. B) Schematic picture from Drury and Urai (1990) from grain boundary structure recrystallised under high grain boundary mobility.*

microfractures. However, one can observed an important increase in microfractures connectivity linked to anhydrite layering that could result in a potential increase in rock permeability. A high concentration of such second phase mineral content could thus support the creation of a connected microfractures network capable to impact the transport properties of a rock salt volume.

Boundary diffusion creep is also observed in halite crystals only, where spherical-like crystals are changing shape to more elongated crystals without recording any brittle damage. An example of this micromechanism can been seen in deformed sample B8 (Figure 6.12B), with a micrograph showing a vertical shortening accompanied by an horizontal elongation of halite grains. Second phase content has also a strong influence in solution-precipitation of halite (Hickman and Evans, 1995; Martin et al., 1999; Leitner et al., 2011).

Damage from cyclic loading conditions can be observed by both transmitted light microscopy and SEM. Thin sections showed halite containing blue resin along transgranular fractures but also around grain boundary which would be an indicative of dilatation during the cyclic loading test. Images from SEM, show the rotation of crystals of anhydrite and also grain boundary opening in halite.

Samples tested at a higher amplitude of 6 to 20 MPa of cyclic stress show larger final axial strains in comparison to samples tested between 4.5 and 7.5 MPa. In the analysis after deformation samples from Series A show a more prominent elongation of halite grains and an increase of blue resin impregnation along fractures and halite grain boundaries. As discussed before, the increase of blue resin along grain boundaries of halite would be evidencing dilatation with grain boundary openings under cyclic conditions.

In general, as discussed before, samples with a higher anhydrite and polyhalite

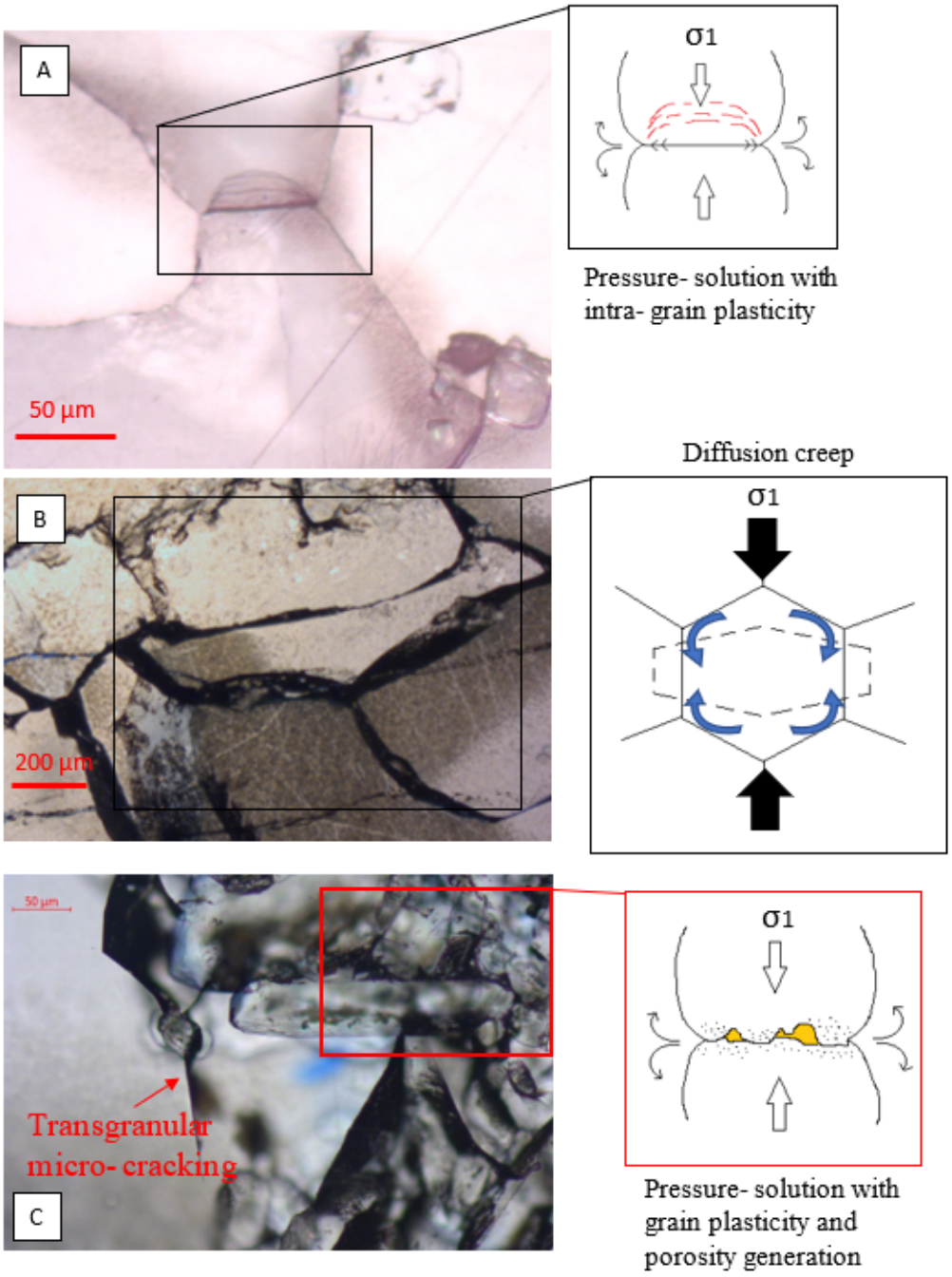

Figure 6.12: *Microphotographs and sketches of main deformation structures observed as a result of pressure solution creep. (A) Sample C3 after deformation. Pressure solution between two grains of halite is observed with intra-grain plasticity. The sketch on the right shows the main axial stress applied and the direction of material transfer. (B) Sample B8 after deformation, showing a decrease and horizontal shortening of halite grains. The schematic diagram on the right displays how crystals undergo axial shortening supported by boundary diffusion creep. (C) Sample A3 showing the main deformation mechanisms implied in a more brittle deformation in relation to the presence of second phase content. The main structures described are transgranular microcracking and pressure solution with grain plasticity. The sketch on the right shows porosity generation (represented in yellow) along the grain boundary as a result of pressure solution between two grains of second phase minerals (after Urai and Spiers (2007)).*

content showed higher axial strain that samples with a higher content in halite. This increase of damage linked to the second phase content is more noticeable for samples tested at lower temperatures. Fingure 6.13 shows the final axial strain versus halite content for samples from Boulby Mine tested at room temperature and 12 MPa confining pressures. It can be observed how sample B2-1, with a 60-70% halite content, recorded the larger axial strain in comparison to samples from different series tested under same conditions. Micrographs 6.13A and B, evidences how the anhydrite layering was the main pathway for micro-fracture development during deformation under cyclic loading conditions. A decrease of second phase content can be observed in micrographs corresponding to samples A4 (6.13C and D) and C4 (6.13E). This decrease in second phase content would explain the decrease in final axial strain for samples A4 and C4 in comparison to sample B1-2.

The same trend can be observed in figure 6.14 showing a plot of the axial strain versus halite content for samples from Boulby mine tested at a confining pressure of 25 MPa. In this case, samples from same series are plotted in different colours according to the testing temperature. The different temperature ranges are represented in blue, for room temperature, orange, for 55°C, and red, for 75°C. It can be observed how, in general, samples from series B with a higher content in anhydrite and polyhalite resulted in a larger final axial strain. Micrographs 6.14A, B, C and D show the already descried characteristic anhydrite layering with an increase of micro-fractures after deformation. Pictures 6.14E and F show images from samples A3 and sample C3 respectively where a decrease in second phase content can be noticed. In general, samples with a higher halite content show the lower final axial strains excepting sample C5. Sample C5 was the only sample showing a very large final axial strain despite the high halite content.

Figure 6.13: *This figure plots the maximum axial strain versus halite content for samples from Boulby Mine tested at 12MPa confining pressure. The micrographs linked to each sample aims to help visualising the second phase content and distribution and main fractures observed after deformation. Sample B1-2, with the lowest halite (Ha) content (and higher anhydrite (An) and polyhalite content) shows the larger final axial strain recorded on samples from Boulby Mine tested at 12 MPa confining pressure and room temperature. Figures 6.13A and B show the characteristic anhydrite (An) layering from samples B which lead to a larger damage compared to other samples with a higher halite content. Figures 6.13C and D and 6.13E and F show a noticeable decrease in second phase content linked to a decrease on damage.*

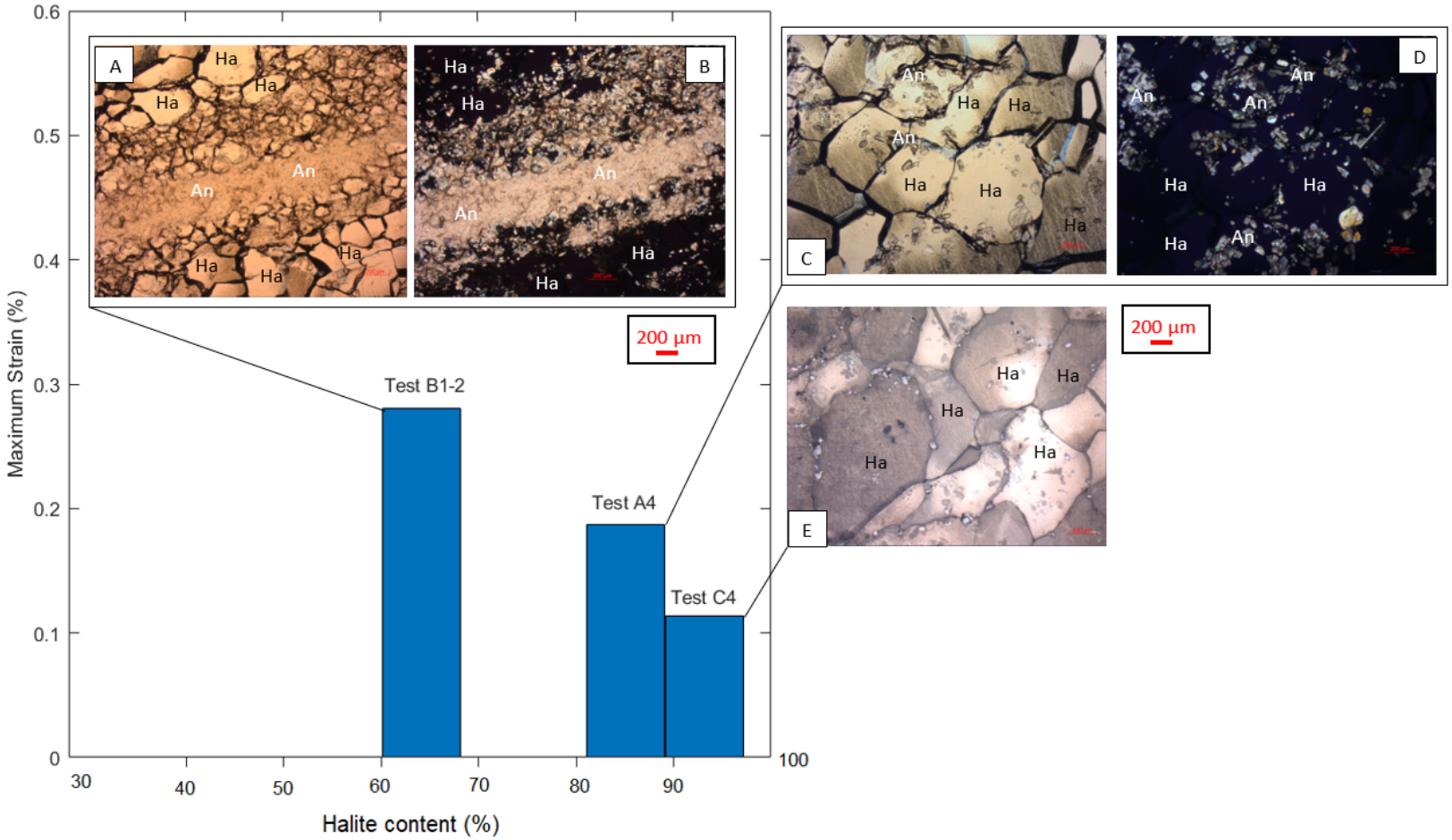

Figure 6.14: *This figure plots the maximum axial strain versus halite content for samples from Boulby Mine tested at 25MPa confining pressure. The micrographs linked to each sample aims to help visualising the second phase content and distribution and main fractures observed after deformation. Samples from series B, and the lowest halite (Ha) content (and higher anhydrite (An) and polyhalite content) shows the larger final axial strain recorded on samples from Boulby Mine tested at same temperature range. The different temperature ranges are represented in blue, for room temperature, orange, for 55° C, and red, for 75° C. Figures 6.14A, B and D show the characteristic anhydrite (An) layering from samples B which lead to a larger microfracture network development compared to other samples with a higher halite content. Figures 6.14C and 6.14E and F show a decrease in second phase content from Series A and C, linked to a decrease in final axial strain. The only sample not following the general trend previously described was sample C5. Although sample C5 had around 90% halite content, it showed very similar final axial train to samples from series B.*

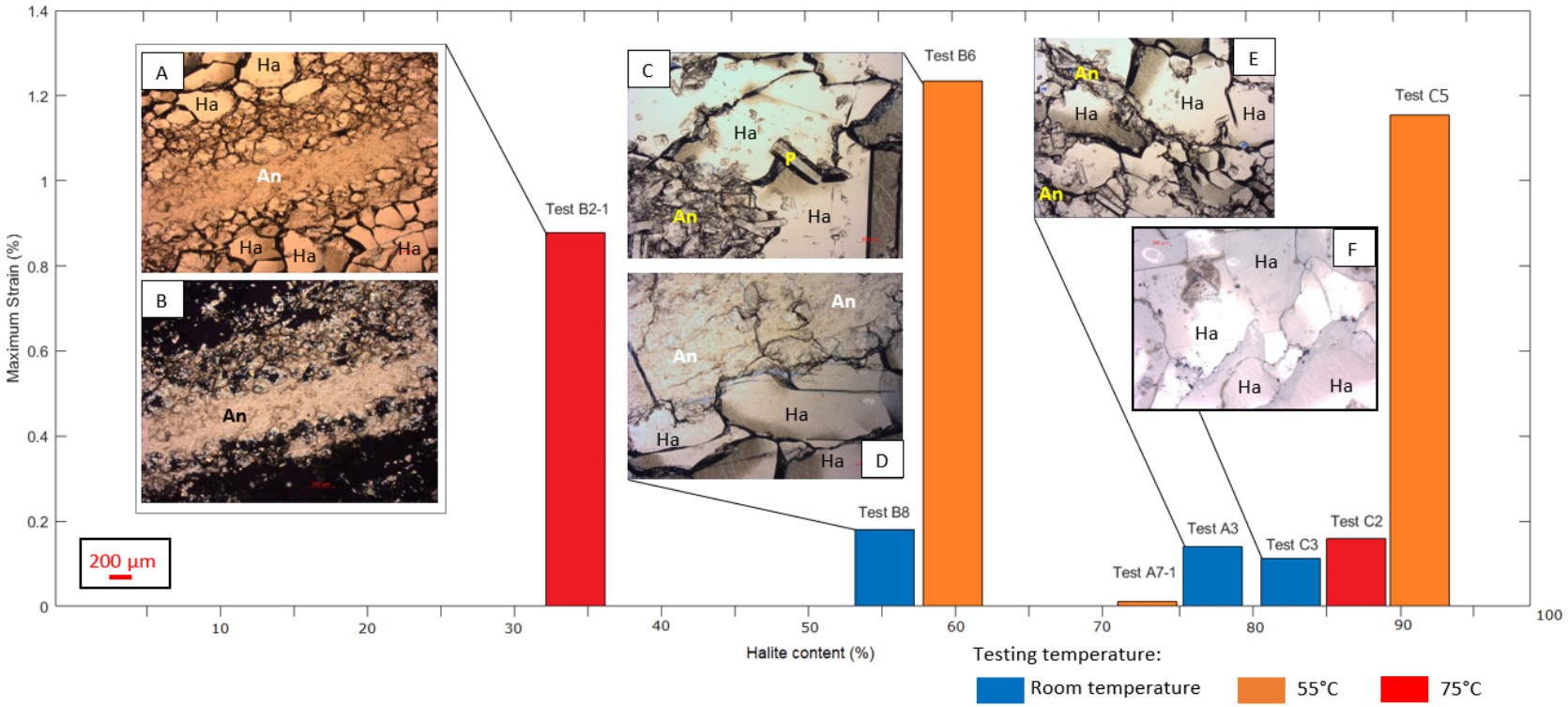

Figure 6.15: *This figure plots the maximum axial strain versus halite content for samples from Winsford Mine tested at 25MPa confining pressure. The micrographs linked to each sample aims to help visualising the second phase content and rock texture observed after deformation. The different temperature ranges are represented in blue, for room temperature, orange, for 55° C, and red, for 75° C. For samples tested at same temperatures, it can be observed that samples from series LB (6.15B), with breccia texture, showed larger final axial strain in comparison to samples from series WB and F (6.15A and C respectively) with a non-clastic and plycrystalline texture.*

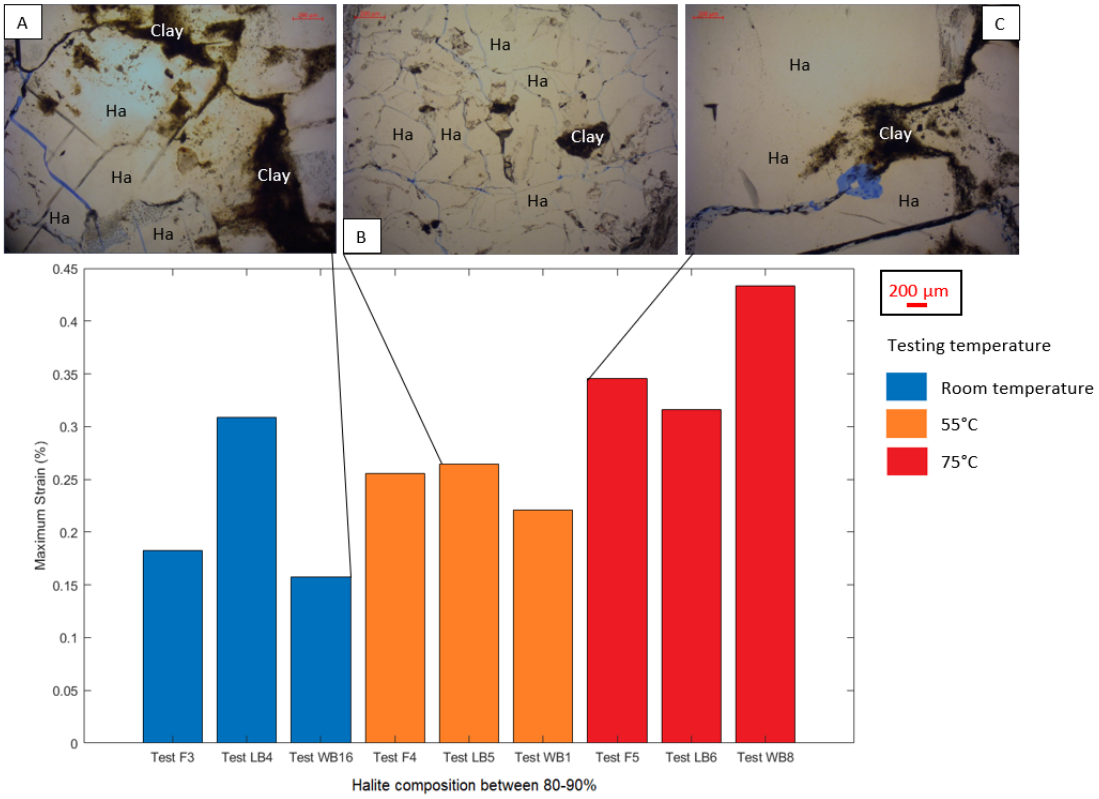

Figure 6.15 shows the final axial strain versus halite content for samples from Winsford Mine tested at temperatures ranging from room temperature to 55°C and 75°C. Almost all samples from Winsford Mine had halite concentration between 80-90%, but presenting with two different rock textures. Series F and WB had a non-clastic polycrystalline texture whereas samples from LB had a breccia texture. Figure 6.15 shows how for samples tested at room temperature and 55°C, samples from series LB show larger final axial strains. At 75°C, sample WB8 is the specimen with the greatest final axial strain. Therefore, at a lower testing temperature, rock texture plays an important role over rheological behaviour with larger axial strain. However, with the increase

of temperature, the impact of a breccia texture over the final deformation seems to decrease.

6.4 Implications for Underground Gas Storage in salt caverns

Second phase content can imply an increase of the brittle deformation. Moreover, the presence of gas could increase local pore pressure and enhance brittle deformation. Different amplitude of cyclic operational pressures will also affect the rock salt deformation differently.

Several authors have investigated the compressibility and strain rate evolution of salt caverns to predict salt cavern closure on both long and short terms based on numerical modelling and in situ monitoring data (Brouard et al., 2013; Moghadam et al., 2015; Wang et al., 2013, 2016). A study from Brouard et al. (2013), analysing in situ elastic parameters and creep closure from the salt cavern at Gellenoncourt (France) states that long term subsidence and possible brine leaks from the cavern should not have an environmental impact. However, none of the previously cited studies consider the impact of secondary minerals in rock salt cavern stability in their models. By testing samples with different second phase content at the same conditions, we have observed how a higher amount of anhydrite content for instance can result in higher strains under differential stress accompanied with an increase in brittle deformation and greater connectivity of the microfracture network.

Rock salt can also creep at high strain rates without showing brittle deformation and tends to self-heal (Wawersik and Preece, 1982). However, microcracks along secondary mineral layers, such as anhydrite, in bedded salt can cause integrity problems resulting in a gas leak through the formation due to a lower

self-healing capacity of anhydrite in comparison to rock salt (Beauheim et al., 1993; Pluymakers and Niemeijer, 2015). Interlayered composite rock salts are more common than pure halite thickened salt formations where secondary mineralogy will act as a weakening agent (Liang et al., 2007). The structural analysis of tested samples with different content in second phase mineralogy after deformation have shown that the layers of anhydrite present the highest concentration of new microfractures after 48 hours of cyclic mechanical deformation. Hence, a clear relationship has been established between an increase in anhydrite content and the creation of new microfractures under cyclic mechanical loading. This implies that even low operation pressure changes inside salt caverns could lead to severe damage propagation throughout the entire cavern structure as well as substantial extension in lateral directions (Han et al., 2006) as a results of the amount of second phase content.

More investigation is needed to fully understand the micromechanisms leading to brittle deformation on the long term and its contribution to potential leaks through the formation. Indeed, it could trigger a self-feed chain reaction whereby pore fluid could migrate in the new space and fluid pressure would likely further enhance rock fracturing (Beauheim et al., 1993). Although the vast majority of microfractures are surrounded by halite crystals likely to self-heal, no work has reported so far what the outcome would be in the previously described conditions here. Such a study would add important information about damage development in long-term operations. The impact of second phase content under mechanical loading conditions linked to gas storage activity is still not well known.

Chapter 7

Conclusions and future works

7.1 Summary and conclusions

The mechanical behaviour of 51 samples of rock salt collected from Boulby and Winsford mines have been studied under cyclic mechanical conditions. The tested samples were differentiated in 6 series (A, B, C, F, LB, and WB) depending on their second phase, mineralogical content. XRD analysis and thin section analysis with transmitted light microscopy revealed that Series A and C had the highest halite content with a halite content of around 75-85% (excluding A8 and A10 whose show high standard deviation from halite) and 87-90%, respectively. Series B presented the highest second phase content with in anhydrite and polyhatite of 10-30% and 15-30%, respectively, up to 10% of kieserite and carnallite, and a content in halite around 30-60%. Series F, WB and LB had a halite content of 75-90%, 5-20% of anhydrite, and up to 10% of clay. Two different textures were considered where i) samples from Series LB were the only samples with a breccia texture and ii) all other series presented a polycrystalline rock salt texture.

The mechanical results show that cyclic mechanical loading induces micro-damage captured in the measured elastic properties variations, especially in samples tested at low temperatures and confining pressures. A slight decrease

in Young's modulus is observed after each cycle as result of the damage accumulation from cyclic mechanical loading conditions. The detailed analysis of elastic recovery per cycle evidences the impact of temperature and confining pressure over rheological behaviour of rock salt. An increase of temperature results in an increase of ductility and decrease of stiffness of the rock. Therefore, samples tested at higher temperatures and confining pressures presented lower elastic recovery capacity per cycle.

Additionally, the elastic recovery capacity of samples is shown to be strongly linked to the second phase content. Mechanical data demonstrate that high second phase content, notably linked to anhydrite layering, acts as a strength weakening agent on both axial and lateral strains accommodating larger brittle deformation in comparison to samples with a lower content in secondary minerals. This rheological behaviour is further exacerbated by cycling the mechanical conditions visible from marked changes in the elastic parameters. Moreover, this elastic response observed per cycle provides a qualitative picture of an existing network of micro-cracks that acts as an sliding pathway and can also imply a potential increase of permeability of rock salt.

Halite grains seems to accommodate most of the induced deformation via brittle deformation with micro-fracturing development directly linked to the presence of second phase content, such as anhydrite and clay. Samples tested at higher temperatures and confining pressures, and with second phase content around halite grain boundaries presented also larger elongation of the halite grains after deformation.

Other deformation micro-mechanisms such as grain boundary migration or pressure solution are observed in thin sections analysed after deformation. However, differential stress - strain rate diagram compiling other data from the literature review and creep constitutive laws curves evidences that lower

creep rates and longer deformation time are required for this deformation mechanisms to have taken place during these cyclic loading tests.

Two types of porosity enhancement have been observed. New porosity was created around isolated crystals of second phase minerals as a result of grain rotation under cyclic mechanical deformation, without further connectivity nor impact on permeability. Porosity is also generated in areas with high concentration of secondary minerals (such as anhydrite, polyhalite, carnallite or kieserite) significantly contributing to the microfracture connectivity, hence likely increasing permeability. Overall, these porosity changes would have implications for the behaviour of the material should the permeability increase by other means.

Overall, second phase content can enhance the connectivity and propagation of micro-fractures forming as such larger networks, and potentially becoming a risk for UGS activities in salt caverns. Connected microfracture networks could support to gas leaks and therefore contamination of surrounding rock formation, for instance. However, more investigation is needed to fully understand the micro-mechanisms leading to brittle deformation on the long term and its contribution to potential leaks through the formation.

7.2 Future works

Further investigation is needed to assess the long-term micro-brittle deformation linked to second phase content under cyclic loading conditions and to integrate the results obtained from laboratory testing into numerical modelling under cyclic loading conditions. Numerical modelling will estimate how rock salt behaves in long-term under the cyclic mechanical conditions, such as the ones addressed in this project. Integrating variations of the elastic properties due to cyclic loading damage of rock salt in numerical modeling would give a

better picture of stability and salt cavern integrity for rock salt with different second phase content.

7.2.1 Synthetic rock salt samples

Synthetic samples were originally planned to be used in this project to control the impurity content and composition of samples to be used for mechanical testing. The objective of using synthetic salt rock was to study the impact of second phase content distribution inside the sample on the rheological behaviour of salt rock under compression conditions. Although there are already some experiments carried out on how to synthesize specimens of salt rock (Price, 1982; Peach, 1991; Franssen, 1994; Peach and Spiers, 1996; Schenk et al., 2006; Ter Heege et al., 2005; Armann, 2008; Marques et al., 2013; Muhammad, 2015), a definitive and agreed procedure to create the synthetic salt samples has not been yet established.

The synthetic samples developed in the laboratory were made using fine-grained sodium chloride powder, with initial grain size of 300-500 µm, and a purity of 99.9%. A first series of synthetic pellets relied on uniaxial cold-pressing the material in a stainless-steel cylinder die of 40 mm diameter and 57 mm long, with a compressive stress of 125 MPa (16 tons) for a duration of about 5 min. Each obtained pellet measured 40 mm diameter and 9-10 mm long. The synthetic samples themselves were then obtained by pressing and bonding the individual synthetic pellets using a manual confining device specially designed for creating the synthetic samples (Figure 7.1), for one week at a temperature of 150°C. However, the produced samples had a very small grain size and higher porosity in comparison to natural salt rock.

In order to obtain larger NaCl crystals, a saturated solution in NaCl was left

in the oven at 50 °C for two weeks. After two weeks, larger NaCl crystals, between 0.5 and 1.5 cm long had grown from the saturated in NaCl solution by evaporation. A second series of samples were then produced using the same method as described in the previous paragraph. If the grain size was improved using this method, the high porosity remained.

A longer compression die was also designed and manufactured to allow for longer synthetic core without having to attach individual pellets. The whole synthetic cores had sizes between 37 mm and 74 mm long. Before taking the sample out from the die used during NaCl compression, the cylindrical steel die was left in a fridge at -12°C for 48h to facilitate the recovery and avoiding the sample to break.

In a last attempt to improve the making of synthetic samples, several pellets and long cores were subjected to annealing experiments. The annealing experiments were done by using pressure vessels at the Hydrothermal Laboratory of the British Geological Survey, with annealing conditions of 100°C and 120 MPa to induce recrystallization in the synthetic salt rock, following the annealing test indications published by Peach and Spiers (1996).

However, despite the iterative improvements, several important limitations where identified when using this method: synthetic specimens have significant structure and grain size differences compared to natural rock salt, resulting in very small grains and lots of porosity. The natural process of salt rock formation includes complex physical and chemical processes involving high temperatures and pressures over long periods of time and those conditions and parameters are difficult to reproduce in a laboratory set-up. The experiments attempted here evidenced the difficulty of reducing inter-granular porosity in samples created at room conditions. Further work focusing on developing a more universal methodology would certainly help to achieve the controlled

details of the microstructure and mineral composition necessary to build a complete catalogue of rock salt rheology as a function of its second phase content.

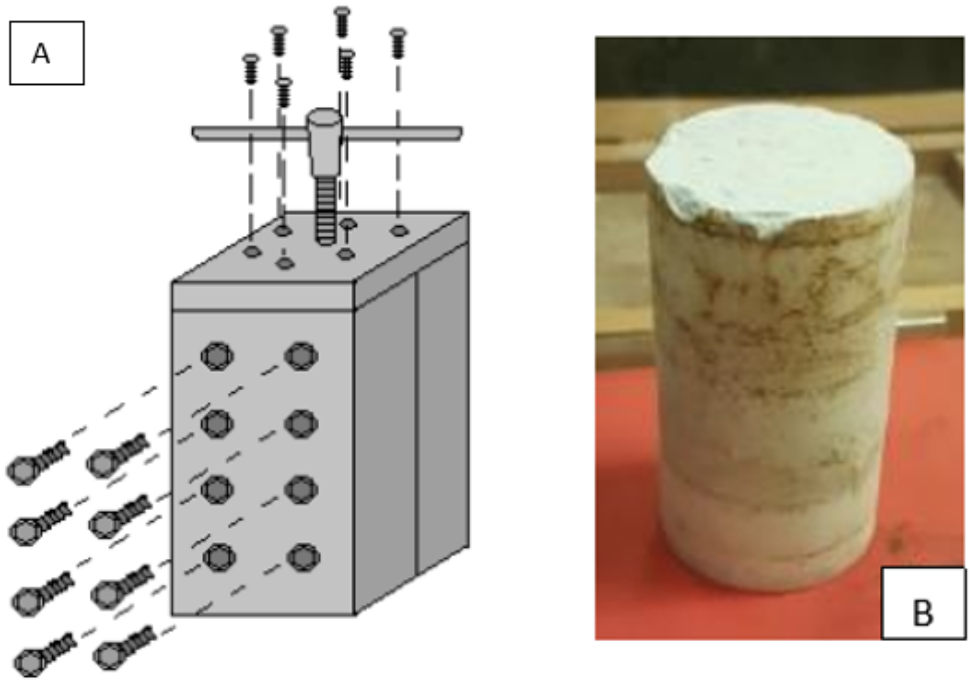

Figure 7.1: *A) Schematic picture from the manually confining devise to hold synthetic samples in the oven at 150°C for one week. B) Image from a synthetic salt rock core sample prepared for mechanical testing.*

7.2.2 Microstructural analysis using the SEM-EBSD

Few initial SEM-Electron Backscatter Diffraction (EBSD) in deformed samples from Boulby Mine were done to study the micro-structural impact of second phase content under cyclic mechanical loading conditions. This technique was thought to further help understanding microstructural implications of different second phase content regarding the Preferred Crystal Orientation of halite under stress.

Electron backscatter diffraction (EBSD) provides information about the crystallography and crystal structure of polycrystalline samples by using a focused-

ion- beam (FIB) system in SEM (Groeber et al., 2006). The analysis of diffracted backscatter electrons allows to analyse crystalline structures, orientation of crystals and microfabrics becoming a very useful microstructural characterisation tool. Diffracted backscattered electrons are generated by the interaction between the primary focused electron beam applied over the sample and the atomic layers of the crystalline material. The diffracted backscattered electrons are recorded by the backscattered electron detector generating visible patterns in form of lines corresponding to lattice planes of the crystal structure from the analysed material. The backscattered electrons form conical trajectories for each lattice plane of the sample, and they are imaged on a phosphor screen as sub- parallel diffraction lines. All diffraction lines create an electron backscatter diffraction pattern (EBSDP). The resolution of EBSDP is related to the accelerating voltage, controlling the penetration depth of the electrons in the sample, known as activation volume. The smaller the activation volume, the higher the resolution (Mariani et al., 2008). EBSD Patterns provide information about crystal type, crystallographic structure and orientation. EBSD maps are created by moving the focused beam of electrons over the analysed sample point by point across a grid of positions. The sample must be placed 70° tilted from the detector in order to increase the quality of the pattern.

Figures 7.2 and 7.3 show a map and data, at a very initial stage, of preferred crystal orientation from sample A4 after deformation by using the SEM-EBSD.

The works started in Autumn 2019 at the nano- and micro-scale Research Centre (nmRC) at the University of Nottingham and would have normally opened a new layer of details in how the second phase content affect the overall rock salt microstructure. However, due to unexpected lockdown early in 2020 and subsequent access restrictions the rest of year, a full analysis for all samples was not achieved. Subsequent work on the rock salt microstructure evolution as a function of its exact mineral composition would certainly benefit from

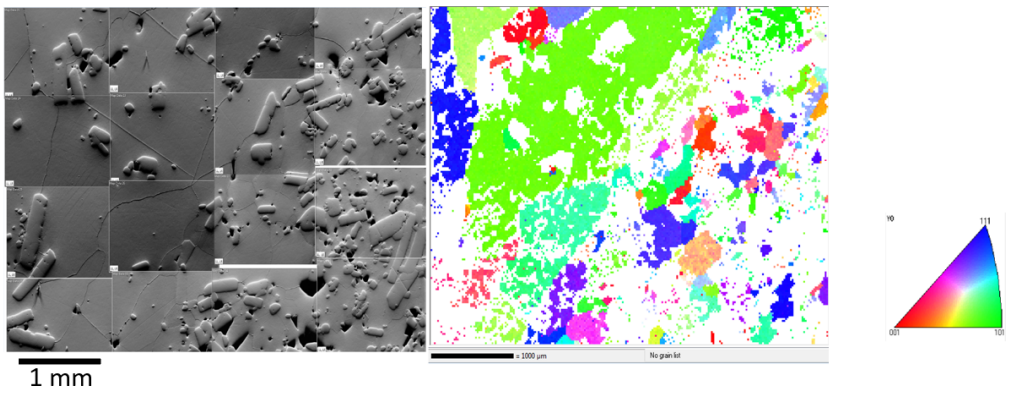

Figure 7.2: *Preferred Crystal Orientation (PCO) analysis performed with the SEM-EBSD on sample A4 after deformation.*

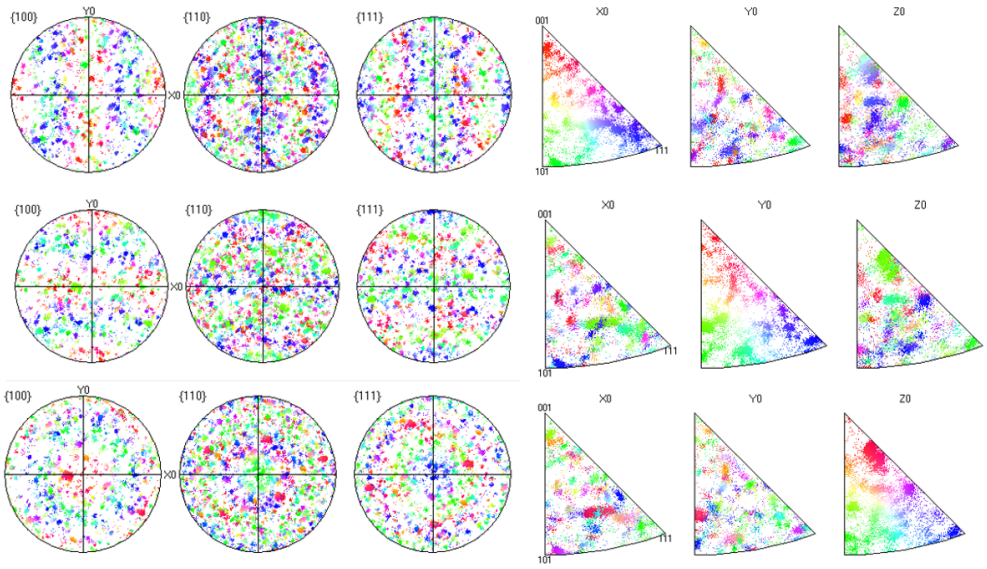

Figure 7.3: *Preferred Crystal Orientation (PCO) analysis performed with the SEM-EBSD on sample A4 after deformation.*

such fine resolution imaging.

7.2.3 Static versus dynamic loading

Integrating some modelling from standard constitutive laws such as Munson-Dawson's to compare our tests results to theoretical data would be the great interest as a future work to study long-term damage evolution. Nonetheless, to compare theoretical data from constitutive law models, a previous investigation on creep deformation under constant stress (static creep tests) would be necessary to know how well the constitutive model meets data for the tested samples.

Creep is generally defined as a time-dependent plastic flow of materials under the conditions of constant load or stress (Kowalewski and Ustrzycka, 2020). Rock salt rheological behaviour has been extensively investigated under constant load deformation conditions in long-term, creep tests. Less known is the fact that dynamic loading conditions, such as the cyclic conditions used here, allow to plot a similar time-strain trend to the typical static creep behaviour. Therefore, it would be of great interest to test samples with same texture, structural and mineralogy features under both static and dynamic creep conditions to quantify any rheological prints as a result of the different mechanical solicitation conditions. In particular, rearrangement of sub-grain structure and dislocation recovery are known to exist in static creep however the short duration (48h) of the tests done in this study may have not suffice to also observe it under dynamic conditions.

7.2.4 Upscaling laboratory data

The UK strategy is to reduce emissions of carbon dioxide by 80% in 2050 by identifying energy storage as one of eight technologies where the UK is set to

become a global leader. Early this year, Department for Business, Energy and Industrial Strategy (BEIS) presented the The Grand Challenge Missions policy paper (BEIS, 2021) where a plan for Clean Growth strategy was released. The Clean Growth strategy will combine carbon capture at scale, fuel switching to hydrogen, integration of renewables, low carbon energy sources, feedstocks changes, together with improved process and energy efficiencies (BEIS, 2021a,b). This strategy proposes industrial clusters where renewable energy, carbon capture, utilisation and storage (CCUS) and hydrogen production will be co-located. Therefore, with the increasing interest in halite cavern storage not only for UGS and CAES, but also for hydrogen and CCUS, it is crucial to perform in-depth analysis of combined Thermo-Chemo-Mechanical processes to scale-up the effects on elastic properties of rock salt observed in the laboratory tests to be applicable to salt cavern modelling in the UK.

The main objective of this project was to assess and quantify how different second phase content affects the rheological behaviour of rock salt under cyclic conditions. Salt caverns numerical modeling tends to use finite element modelling which assume constant boundary conditions for the rock salt formation. However, it has been demonstrated in this work that cyclic conditions can induce brittle deformation resulting in a variations of the elastic property of rock salt, and that the source of this variations is strongly linked to the second phase content. Therefore, long-term numerical modelling works would certainly gain in accuracy by integrating the variations in second phase content of rock salt and its impact on elastic properties.

Bibliography

Abe, F. (2008). 9 - strengthening mechanisms in steel for creep and creep rupture. In F. Abe, T.-U. Kern, and R. Viswanathan (Eds.), *Creep-Resistant Steels*, Woodhead Publishing Series in Metals and Surface Engineering, pp. 279–304. Woodhead Publishing.

Armann, M. (2008). *Microstructural and textural development in synthetic rocksalt deformed in torsion*. Ph. D. thesis, ETH Zurich.

Beauheim, R., W. Wawersik, R. Roberts, et al. (1993). Coupled permeability and hydrofracture tests to assess the waste-containment properties of fractured anhydrite. In *The 34th US Symposium on Rock Mechanics (USRMS)*. American Rock Mechanics Association.

BEIS (2021a). BEIS green boost for regions to cut industry carbon emissions. https://www.gov.uk/government/news/green-boost-for-regions-to-cut-industry-carbon-emissions. Accessed: 2021-04-18.

BEIS (2021b). BEIS policy paper: The grand challenge missions. https://www.gov.uk/government/publications/industrial-strategy-the-grand-challenges/missions. Accessed: 2021-04-18.

Bérest, P. (2011). Thermomechanical aspects of high frequency cycling in salt storage caverns.

Bérest, P. (2013). The mechanical behavior of salt and salt caverns. In *Proceedings of the ISRM International Symposium EUROCK*, pp. 17–30.

Bérest, P., P. Antoine Blum, J. Pierre Charpentier, H. Gharbi, and F. Valès (2005). Very slow creep tests on rock samples. *International Journal of Rock Mechanics and Mining Sciences 42*(4), 569–576.

Bérest, P., B. Brouard, H. Djakeun-Djizanne, and G. Hévin (2014). Thermomechanical effects of a rapid depressurization in a gas cavern. *Acta Geotechnica 9*(1), 181–186.

Bérest, P., B. Brouard, and M. Karimi-Jafari (2005). Deep salt caverns abandonment. In *Post-Mining 2005. November 16-17, Nancy, France*.

Berest, P., B. Brouard, M. Karimi-Jafari, and L. Van Sambeek (2007). Transient behavior of salt caverns—interpretation of mechanical integrity tests. *International Journal of Rock Mechanics and Mining Sciences 44*(5), 767–786.

Bérest, P., H. Gharbi, B. Brouard, D. Brückner, K. DeVries, G. Hévin, G. Hofer, C. Spiers, and J. Urai (2019). Very slow creep tests on salt samples. *Rock Mechanics and Rock Engineering 52*(9), 2917–2934.

Bérest, P., M. Karimi-Jafari, B. Brouard, and B. Bazargan (2006). In situ mechanical tests in salt caverns. In *Solution Mining Institute. Spring 2006 Technical Meeting. Brussels, Belgium, May 1- 3, 2006*.

Beutel, T. and S. Black (2005). Salt deposits and gas cavern storage in the uk with a case study of salt exploration from cheshire. *Oil & Gas European Magazine 1*, 31–35.

Biehl, B., L. Reuning, F. Strozyk, and P. Kukla (2014). Origin and deformation of intra-salt sulphate layers: an example from the dutch zechstein (late permian). *International Journal of Earth Sciences 103*(3), 697–712.

Blumenthal, A. v., E. Mahmoudi, K. Khaledi, D. König, and T. Schanz (2016). Innovative concept for analysing a rock salt cavern under cyclic thermo-mechanical loading. *Energy Procedia 97*, 478–485.

Brouard, B., P. Berest, V. de Greef, J. Béraud, C. Lheur, and E. Hertz (2013). Creep closure rate of a shallow salt cavern at gellenoncourt, france. *International Journal of Rock Mechanics and Mining Sciences 62*, 42–50.

Brouard, B., P. Berest, H. Djizanne, A. Frangi, et al. (2012). Mechanical stability of a salt cavern submitted to high-frequency cycles. In *Mechanical Behavior of Salt VII*, pp. 381–390. Taylor & Francis Group.

Bruker (2020). DIFFRAC.EVA semi-quantitative analysis of mineralogical composition.

Bunaciu, A. A., E. G. UdriŞTioiu, and H. Y. Aboul-Enein (2015). X-ray diffraction: instrumentation and applications. *Critical reviews in analytical chemistry 45*(4), 289–299.

Buschow, K. J., R. W. Cahn, M. C. Flemings, B. Ilschner, E. J. Kramer, and S. Mahajan (2001). Encyclopedia of materials. *Science and technology 1*(11).

Carter, N., S. Horseman, J. Russell, and J. Handin (1993). Rheology of rocksalt. *Journal of Structural Geology 15*(9-10), 1257–1271.

Carter, N. L. and F. D. Hansen (1983). Creep of rocksalt. *Tectonophysics 92*(4), 275–333.

Carter, N. L. and H. C. Heard (1970). Temperature and rate dependent deformation of halite. *American Journal of Science 269*(3), 193–249.

Choundhary, O., P. Kalita, P. Doley, and A. Kalita (2017). 1. scanning electron microscope-advantages and disadvantages in imaging components by op choudhary, pc kalita, pj doley and a. kalita. *LIFE SCIENCES LEAFLETS 85*, 1–to.

Cooper, A. H. (2002). Halite karst geohazards (natural and man-made) in the united kingdom. *Environmental Geology 42*(5), 505–512.

Covey-Crump, S., W. F. Xiao, J. Mecklenburgh, E. Rutter, and S. May (2016). Exploring the influence of loading geometry on the plastic flow properties of geological materials: Results from combined torsion+ axial compression tests on calcite rocks. *Journal of Structural Geology 88*, 20–31.

Cristescu, N. (1993). A general constitutive equation for transient and stationary creep of rock salt. In *International journal of rock mechanics and mining sciences & geomechanics abstracts*, Volume 30, pp. 125–140. Elsevier.

Cristescu, N. D. and U. Hunsche (1998). *Time effects in rock mechanics. Seriea: Materials, Modelling and Computation*. Wiley.

Crotogino, F., K.-U. Mohmeyer, and R. Scharf (2001). Huntorf caes: More than 20 years of successful operation. In *SMRI Spring meeting*, Volume 2001.

Das, R., E. Ali, and S. B. Abd Hamid (2014). Current applications of x-ray powder diffraction-a review. *Reviews on Advanced Materials Science 38*(2).

Djizanne, H. (2014). *Stabilité mécanique d'une cavité saline soumise à des variations rapides de pression: Application au stockage souterrain de gaz naturel, d'air comprimé et d'hydrogène*. Ph. D. thesis, Ecole Doctorale Polytechnique.

Drury, M. R. and J. L. Urai (1990). Deformation-related recrystallization processes. *Tectonophysics 172*(3-4), 235–253.

Evans, D. and S. Holloway (2009). A review of onshore uk salt deposits and their potential for underground gas storage. *Geological Society, London, Special Publications 313*(1), 39–80.

Fan, J., J. Chen, D. Jiang, A. Chemenda, J. Chen, and J. Ambre (2017). Discontinuous cyclic loading tests of salt with acoustic emission monitoring. *International Journal of Fatigue 94*, 140–144.

Fan, J., J. Chen, D. Jiang, S. Ren, and J. Wu (2016). Fatigue properties of rock salt subjected to interval cyclic pressure. *International Journal of Fatigue 90*, 109–115.

Fanchi, J. R. (2002). *Shared Earth Modeling: Methodologies for Integrated Reservoir Simulations*. Gulf Professional Publishing.

Fjar, E., R. M. Holt, A. Raaen, and P. Horsrud (2008). *Petroleum related rock mechanics*. Elsevier.

Frandsen, A. F. (2016). Polarized light microscopy.

Franssen, R. C. (1994). The rheology of synthetic rocksalt in uniaxial compression. *Tectonophysics 233*(1-2), 1–40.

Gevantman, L. and J. Lorenz (1981). *Physical properties data for rock salt*, Volume 167. US Department of Commerce, National Bureau of Standards.

Ging, P. B., D. T. Long, and R. W. Lee (1996). *Selected geochemical characteristics of ground water from the Marshall aquifer in the central Lower Peninsula of Michigan*, Volume 94. Department of the Interior, US Geological Survey.

Goldstein, J. I., D. E. Newbury, J. R. Michael, N. W. Ritchie, J. H. J. Scott, and D. C. Joy (2017). *Scanning electron microscopy and X-ray microanalysis*. Springer.

Griggs, D. (1939). Creep of rocks. *The Journal of Geology 47*(3), 225–251.

Groeber, M. A., B. Haley, M. D. Uchic, D. M. Dimiduk, and S. Ghosh (2006). 3d reconstruction and characterization of polycrystalline microstructures using a fib–sem system. *Materials Characterization 57*(4-5), 259–273.

Guillope, M. and J. Poirier (1979). Dynamic recrystallization during creep of single-crystalline halite: An experimental study. *Journal of Geophysical Research: Solid Earth 84*(B10), 5557–5567.

Günther, R.-M., K. Salzer, T. Popp, and C. Lüdeling (2015). Steady-state creep of rock salt: improved approaches for lab determination and modelling. *Rock mechanics and rock engineering 48*(6), 2603–2613.

Han, G., M. S. Bruno, K. Lao, J. Young, L. Dorfmann, et al. (2006). Gas storage and operations in single-bedded salt caverns: stability analyses. In *SPE Gas Technology Symposium*. Society of Petroleum Engineers.

Harding, R. and M. Huuse (2015). Salt on the move: multi stage evolution of salt diapirs in the netherlands north sea. *Marine and Petroleum Geology 61*, 39–55.

Haupt, M. (1991). A constitutive law for rock salt based on creep and relaxation tests. *Rock Mechanics and Rock Engineering 24*(4), 179–206.

He, W., X. Luo, D. Evans, J. Busby, S. Garvey, D. Parkes, and J. Wang (2017). Exergy storage of compressed air in cavern and cavern volume estimation of the large-scale compressed air energy storage system. *Applied energy 208*, 745–757.

Heald, M. T. (1955). Stylolites in sandstones. *The Journal of Geology 63*(2), 101–114.

Heard, H. C. and F. Ryerson (1986). Effect of cation impurities on steady-state flow of salt. *Mineral and Rock Deformation: Laboratory Studies 36*, 99–115.

Hickman, S. H. and B. Evans (1995). Kinetics of pressure solution at halite-silica interfaces and intergranular clay films. *Journal of Geophysical Research: Solid Earth 100*(B7), 13113–13132.

Howard, A., G. Warrington, K. Ambrose, and J. Rees (2008). A formational framework for the mercia mudstone group (triassic) of england and wales.

Huang, X. and J. Xiong (2011). Numerical simulation of gas leakage in bedded salt rock storage cavern. *Procedia engineering 12*, 254–259.

Hudec, M. R. and M. P. Jackson (2007). Terra infirma: Understanding salt tectonics. *Earth-Science Reviews 82*(1-2), 1–28.

Hunsche, U. (1998). *Time effects in rock mechanics*, Volume 1. John Wiley & Sons.

Hunsche, U. and A. Hampel (1999). Rock salt—the mechanical properties of the host rock material for a radioactive waste repository. *Engineering geology 52*(3-4), 271–291.

Hunsche, U. and O. Schulze (1996). Effect of humidity & confining pressure on creep of rock salt. *SERIES ON ROCK AND SOIL MECHANICS 20*, 237–248.

ICDD, I. C. f. D. D. (2020). PDF4 mineralogical phase identification.

Jackson, M. and B. Vendeville (1994). Regional extension as a geologic trigger for diapirism. *Geological society of America bulletin 106*(1), 57–73.

Jackson, M. P., B. C. Vendeville, and D. D. Schultz-Ela (1994). Structural dynamics of salt systems. *Annual Review of Earth and Planetary Sciences 22*(1), 93–117.

Jaeger, J. C., N. G. Cook, and R. Zimmerman (2007). *Fundamentals of rock mechanics*. John Wiley & Sons.

Jeremic, M. L. (1994). *Rock mechanics in salt mining*. CRC Press.

Jiang, D., J. Fan, J. Chen, L. Li, and Y. Cui (2016). A mechanism of fatigue in salt under discontinuous cycle loading. *International Journal of Rock Mechanics and Mining Sciences 100*(86), 255–260.

Jin, Z., J. Li, and Z. Chen (2020). *Computational modelling of biomechanics and biotribology in the musculoskeletal system: biomaterials and tissues*. Woodhead Publishing.

Kendall, C. G. (2009). A color atlas of rocks and minerals in thin section.

Khaledi, K., E. Mahmoudi, M. Datcheva, and T. Schanz (2014). Finite element modeling of the behavior of salt caverns under cyclic loading. *Geomechanics from Micro to Macro. Informa Limited, UK*, 945–950.

Khaledi, K., E. Mahmoudi, M. Datcheva, and T. Schanz (2016a). Analysis of compressed air storage caverns in rock salt considering thermo-mechanical cyclic loading. *Environmental Earth Sciences 75*(15), 1149.

Khaledi, K., E. Mahmoudi, M. Datcheva, and T. Schanz (2016b). Stability and serviceability of underground energy storage caverns in rock salt subjected to mechanical cyclic loading. *International journal of rock mechanics and mining sciences 86*, 115–131.

Klafki, M., T. Wagler, S. Grosswig, and A. Kneer (2003). Long-term downhole fibre optic temperature measurements and cfd-modeling for investigation of different gas cavern operating modes. In *Technical Conference Paper*, pp. 5–8.

Kossow, D. and C. M. Krawczyk (2002). Structure and quantification of processes controlling the evolution of the inverted ne-german basin. *Marine and Petroleum Geology 19*(5), 601–618.

Kowalewski, Z. L. and A. Ustrzycka (2020). *Creep Deformation*, pp. 499–508. Berlin, Heidelberg: Springer Berlin Heidelberg.

Kruck, O., F. Crotogino, R. Prelicz, and T. Rudolph (2013). Assessment of the potential, the actors and relevant business cases for large scale and seasonal storage of renewable electricity by hydrogen underground storage in europe. *HyUnder Deliverable* (3.1).

Landinger, H., U. Bünger, T. Raksha, J. Simón, and L. Correas (2013). Benchmarking of large scale hydrogen underground storage with competing options.

Le Comte, P. (1965). Creep in rock salt. *The Journal of Geology 73*(3), 469–484.

Leitner, C., F. Neubauer, J. L. Urai, and J. Schoenherr (2011). Structure and evolution of a rocksalt-mudrock-tectonite: The haselgebirge in the northern calcareous alps. *Journal of Structural Geology 33*(5), 970–984.

Li, M., H. Zhang, W. Xing, Z. Hou, and P. Were (2015). Study of the relationship between surface subsidence and internal pressure in salt caverns. *Environmental Earth Sciences 73*(11), 6899–6910.

Li, S., S. Abe, J. Urai, F. Strozyk, P. Kukla, H. Van Gent, P. Berest, M. Ghoreychi, F. Hadj-Hassen, and M. Tijani (2012). A method to evaluate long-term rheology of zechstein salt in the tertiary. *Proc. Mech. Beh. Salt VII*, 215–220.

Li, S.-Y. and J. L. Urai (2016). Rheology of rock salt for salt tectonics modeling. *Petroleum Science 13*(4), 712–724.

Liang, W., C. Zhang, H. Gao, X. Yang, S. Xu, and Y. Zhao (2012). Experiments on mechanical properties of salt rocks under cyclic loading. *Journal of Rock Mechanics and Geotechnical Engineering 4*(1), 54–61.

Liang, W.-g., C.-h. Yang, Y.-s. Zhao, M. Dusseault, and J. Liu (2007). Experimental investigation of mechanical properties of bedded salt rock. *International Journal of Rock Mechanics and Mining Sciences 44*(3), 400–411.

Liu, J., H. Xie, Z. Hou, C. Yang, and L. Chen (2014). Damage evolution of rock salt under cyclic loading in unixial tests. *Acta Geotechnica 9*(1), 153–160.

Liu, L., J. Zhang, and C. Ai (2022). Nickel-based superalloys. In F. G. Caballero (Ed.), *Encyclopedia of Materials: Metals and Allloys*, pp. 294–304. Oxford: Elsevier.

Ma, H., C. Yang, J. Liu, and J. Chen (2013). The influence of cyclic loading on deformation of rock salt. In *3rd ISRM symposium on rock characterisation, modelling and engineering design methods, SINOROCK*, Volume 18, pp. 63–68.

Ma, Y. Z. and S. Holditch (2016). *Unconventional oil and gas resources handbook: Evaluation and development*. Gulf professional publishing.

Mariani, E., D. Prior, D. D. McNamara, M. Pearce, N. Seaton, G. Seward, D. Tatham, and J. Wheeler (2008). Electron backscatter diffraction (ebsd) in the sem: applications to microstructures in minerals and rocks and recent technological advancements. *Seminarios de la Sociedad Espanola de Mineralogıa*.

Marques, F., J.-P. Burg, M. Armann, and E. Martinho (2013). Rheology of synthetic polycrystalline halite in torsion. *Tectonophysics 583*, 124–130.

Martin, B., K. Röller, and B. Stöckhert (1999). Low-stress pressure solution experiments on halite single-crystals. *Tectonophysics 308*(3), 299–310.

Martin-Clave, C., A. Ougier-Simonin, and V. Vandeginste (2021). Impact of second phase content on rock salt rheological behavior under cyclic mechanical conditions. *Rock Mechanics and Rock Engineering*, 1–23.

Mellegard, K. and U. Düsterloh (2012). High frequency cycling of gas storage caverns: phase ii: cyclical loading effects on the damage and creep properties of salt. Technical report, SMRI Research Report RR2012-02. RESPEC, Rapid City.

Melvin, J. L. (1991). *Evaporites, petroleum and mineral resources*. Elsevier.

Moghadam, S. N., K. Nazokkar, R. J. Chalaturnyk, and H. Mirzabozorg (2015). Parametric assessment of salt cavern performance using a creep model describing dilatancy and failure. *International Journal of Rock Mechanics and Mining Sciences 79*, 250–267.

Muhammad, N. (2015). *Deformation and transport processes in salt rocks: an experimental study exploring effects of pressure and stress relaxation*. Ph. D. thesis, UU Dept. of Earth Sciences.

Munson, D. E. (1979). Preliminary deformation-mechanism map for salt (with application to wipp). Technical report, Sandia Labs.

Nikon Instruments, I. (2020). MicroscopyU polarized light microscopy.

Norton, G., A. Bloodworth, D. Cameron, D. Evans, G. Lott, S. Hobbs, N. Spencer, and D. Highley (2005). Mineral resource information in support of national, regional and local planning: Cheshire (comprising cheshire, boroughs of halton and warrington).

Ochsenius, C. (1877). *Die Bildung der Steinsalzlager und ihrer Mutterlaugensalze: unter specieller Berücksichtigung der Flötze von Douglashall in der egeln'schen Mulde*. CEM Pfeffer.

Oldenbourg, R. (1998). Polarized light microscopy of spindles. *Methods in Cell Biology 61*, 175–208.

Ouhadi, V. and R. Yong (2003). Impact of clay microstructure and mass absorption coefficient on the quantitative mineral identification by xrd analysis. *Applied clay science 23*(1-4), 141–148.

Ozarslan, A. (2012). Large-scale hydrogen energy storage in salt caverns. *International Journal of Hydrogen Energy 37*(19), 14265–14277.

Peach, C., C. Spiers, and P. Trimby (2001). Effect of confining pressure on dilatation, recrystallization, and flow of rock salt at 150 c. *Journal of Geophysical Research: Solid Earth 106*(B7), 13315–13328.

Peach, C. J. (1991). *Influence of deformation on the fluid transport properties of salt rocks*. Ph. D. thesis, Faculteit Aardwetenschappen der Rijksuniversiteit te Utrecht.

Peach, C. J. and C. J. Spiers (1996). Influence of crystal plastic deformation on dilatancy and permeability development in synthetic salt rock. *Tectonophysics 256*(1-4), 101–128.

Pelissier, M. A., H. Hoeber, N. van de Coevering, and I. F. Jones (2007). *Classics of elastic wave theory*. Society of Exploration Geophysicists.

Pfeifer, M. (2009). *Materials enabled designs: The materials engineering perspective to product design and manufacturing*. Butterworth-Heinemann.

Pfiefle, T. and P. Senseny (1981). Elastic-plastic deformation of anhydrite and polyhalite as determined from quasi-static triaxial compression tests. Technical report, RE/SPEC.

Plant, J. A., D. G. Jones, and H. Haslam (1999). *The Cheshire Basin: basin evolution, fluid movement and mineral resources in a Permo-Triassic rift setting*. British Geological Survey Keyworth, Nottingham.

Pluymakers, A. M. and A. R. Niemeijer (2015). Healing and sliding stability of simulated anhydrite fault gouge: Effects of water, temperature and co2. *Tectonophysics 656*, 111–130.

Popp, T., H. Kern, and O. Schulze (2001). Evolution of dilatancy and permeability in rock salt during hydrostatic compaction and triaxial deformation. *Journal of Geophysical Research: Solid Earth 106*(B3), 4061–4078.

Price, R. H. (1982). Effects of anhydrite and pressure on the mechanical behavior of synthetic rocksalt. *Geophysical Research Letters 9*(9), 1029–1032.

Renard, F., D. Bernard, X. Thibault, and E. Boller (2004). Synchrotron 3d microtomography of halite aggregates during experimental pressure solution creep and evolution of the permeability. *Geophysical Research Letters 31*(7).

Renard, F., D. Dysthe, J. Feder, K. Bjørlykke, and B. Jamtveit (2001). Enhanced pressure solution creep rates induced by clay particles: Experimental evidence in salt aggregates. *Geophysical Research Letters 28*(7), 1295–1298.

Renard, F., D. Dysthe, J. Feder, and B. Jamtveit (2002). Healing of fluid-filled microcracks. In *Proceedings of the second Biot conference on poromechanics*, pp. 925–31.

Robinson, A., A. Eyres, S. Hudson, H. Hussain, and J. Young (2021). Dynamic systems for ultrahigh temperature energy conversion. In *Ultra-High Temperature Thermal Energy Storage, Transfer and Conversion*, pp. 221–251. Elsevier.

Sato, H. (2013). *Advances in Geophysics*. Academic Press.

Schenk, O., J. Urai, and S. Piazolo (2006). Structure of grain boundaries in wet, synthetic polycrystalline, statically recrystallizing halite–evidence from cryo-sem observations. *Geofluids 6*(1), 93–104.

Schenk, O. and J. L. Urai (2004). Microstructural evolution and grain boundary structure during static recrystallization in synthetic polycrystals of sodium chloride containing saturated brine. *Contributions to Mineralogy and Petrology 146*(6), 671–682.

Schléder, Z. and J. L. Urai (2005). Microstructural evolution of deformation-modified primary halite from the middle triassic röt formation at hengelo, the netherlands. *International Journal of Earth Sciences 94*(5), 941–955.

Schultz-Ela, D. D., M. P. Jackson, and B. Vendeville (1993). Mechanics of active salt diapirism. *Tectonophysics 228*(3-4), 275–312.

Schulze, O., T. Popp, and H. Kern (2001). Development of damage and permeability in deforming rock salt. *Engineering Geology 61*(2-3), 163–180.

Senseny, P., F. Hansen, J. Russell, N. Carter, and J. Handin (1992). Mechanical behaviour of rock salt: phenomenology and micromechanisms. In *International journal of rock mechanics and mining sciences & geomechanics abstracts*, Volume 29, pp. 363–378. Elsevier.

Serbin, K., J. Ślizowski, K. Urbańczyk, and S. Nagy (2015). The influence of thermodynamic effects on gas storage cavern convergence. *International Journal of Rock Mechanics and Mining Sciences 100*(79), 166–171.

Shao, H., Y. Wang, O. Kolditz, T. Nagel, and T. Brüning (2019). Approaches to multi-scale analyses of mechanically and thermally-driven migration of fluid inclusions in salt rocks. *Physics and Chemistry of the Earth, Parts A/B/C 113*, 1–13.

Sonnenfeld, P. (1995). The color of rock salt—a review. *Sedimentary Geology 94*(3-4), 267–276.

Spiers, C. and R. Brzesowsky (1993). Densification behaviour of wet granular salt: Theory versus experiment. In *Seventh Symposium on salt*, Volume 1, pp. 83–92. Elsevier Amsterdam.

Spiers, C. and P. Schutjens (1999). Intergranular pressure solution in nacl: Grain-to-grain contact experiments under the optical microscope. *Oil & Gas Science and Technology 54*(6), 729–750.

Spiers, C., P. Schutjens, R. Brzesowsky, C. Peach, J. Liezenberg, and H. Zwart (1990). Experimental determination of constitutive parameters governing creep of rocksalt by pressure solution. *Geological Society, London, Special Publications 54*(1), 215–227.

Spiers, C. J. and N. L. Carter (1998). Microphysics of rocksalt flow in nature. *Series on rock and soil mechanics*, 115–128.

Spiers, C. J. and P. M. Schutjens (1990). Densification of crystalline aggregates by fluid-phase diffusional creep. In *Deformation processes in minerals, ceramics and rocks*, pp. 334–353. Springer.

Strohmenger, C. and C. Strauss (1996). Sedimentology and palynofacies of the zechstein 2 carbonate (upper permian, northwest germany): implications for sequence stratigraphic subdivision. *Sedimentary Geology 102*(1-2), 55–77.

Swift, G., D. Reddish, P. Lloyd, and R. Dunham (2001). Numerical modelling of time-dependent deformation around an underground mine in rock salt. *Mining Technology 110*(2), 107–113.

Taheri, S. R., A. Pak, S. Shad, B. Mehrgini, and M. Razifar (2020). Investigation of rock salt layer creep and its effects on casing collapse. *International Journal of Mining Science and Technology 30*(3), 357–365.

Talbot, C., C. Tully, and P. Woods (1982). The structural geology of boulby (potash) mine, cleveland, united kingdom. *Tectonophysics 85*(3-4), 167–204.

Tekin, E., B. Varol, and T. Ayyıldız (2010). Sedimentology and paleoenvironmental evolution of messinian evaporites in the iskenderun–hatay basin complex, southern turkey. *Sedimentary Geology 229*(4), 282–298.

Ter Heege, J., J. De Bresser, and C. Spiers (2005). Rheological behaviour of synthetic rocksalt: the interplay between water, dynamic recrystallization and deformation mechanisms. *Journal of Structural Geology 27*(6), 948–963.

Urai, J., W. Means, and G. Lister (1986). Dynamic recrystallization of minerals. In *Mineral and rock deformation: laboratory studies*, Volume 36, pp. 161–199. AGU Washington, DC.

Urai, J., Z. Schléder, C. Spiers, and P. Kukla (2008). Flow and transport properties of salt rocks. *Dynamics of complex intracontinental basins: The central European basin system*, 277–290.

Urai, J. and C. Spiers (2007). The effect of grain boundary water on deformation mechanisms and rheology of rocksalt during long-term deformation. In *The Mechanical Behavior of Salt—Understanding of THMC Processes in Salt: Proceedings of the 6th Conference (SaltMech6), Hannover, Germany, 22–25 May 2007*. CRC Press Boca Raton, Fla.

Urai, J. L. (1983). Water assisted dynamic recrystallization and weakening in polycrystalline bischofite. *Tectonophysics 96*(1-2), 125–157.

Van Sambeek, L. L., J. L. Ratigan, and F. D. Hansen (1993). Dilatancy of rock salt in laboratory tests. In *International journal of rock mechanics and mining sciences & geomechanics abstracts*, Volume 30, pp. 735–738. Elsevier.

Van Wees, J.-D., R. Stephenson, P. Ziegler, U. Bayer, T. McCann, R. Dadlez, R. Gaupp, M. Narkiewicz, F. Bitzer, and M. Scheck (2000). On the origin of the southern permian basin, central europe. *Marine and Petroleum Geology 17*(1), 43–59.

Vendeville, B. C. and M. Jackson (1993). Rates of extension and deposition determine whether growth faults or salt diapirs form. In *Proceedings of the Gulf Coast Section Society of Economic Paleontologists and Mineralogists Foundation 14th Annual Research Conference*, pp. 5–8.

Wang, G., K. Guo, M. Christianson, and H. Konietzky (2011). Deformation characteristics of rock salt with mudstone interbeds surrounding gas and oil storage cavern. *International Journal of Rock Mechanics and Mining Sciences 48*(6), 871–877.

Wang, G. J. and P. Xie (2012). Theoretical analysis of gas and oil storage cavern in bedded salt rock using a love function. In *Applied Mechanics and Materials*, Volume 204, pp. 1499–1502. Trans Tech Publ.

Wang, T., X. Yan, H. Yang, X. Yang, T. Jiang, and S. Zhao (2013). A new shape design method of salt cavern used as underground gas storage. *Applied Energy 104*, 50–61.

Wang, T., C. Yang, H. Ma, Y. Li, X. Shi, J. Li, and J. Daemen (2016). Safety evaluation of salt cavern gas storage close to an old cavern. *International Journal of Rock Mechanics and Mining Sciences 83*, 95–106.

Wang, Z.-T. and Z.-S. An (2017). Theoretical modeling of thermal expansion mechanism of salt-bearing rocks. *Arabian Journal of Geosciences 10*(23), 1–4.

Wawersik, W. and D. Preece (1982). Creep testing of salt: procedures, problems and suggestions. Technical report, Sandia National Labs.

Weck, P. F., E. Kim, C. F. Jové-Colón, and D. C. Sassani (2014). First-principles study of anhydrite, polyhalite and carnallite. *Chemical Physics Letters 594*, 1–5.

Woodman, J. (2020). *Thermo-mechanical loading of intact rock and discontinuities*. Ph. D. thesis, University of Leeds.

Xing, W., J. Zhao, Z. Hou, P. Were, M. Li, and G. Wang (2015). Horizontal natural gas caverns in thin-bedded rock salt formations. *Environmental Earth Sciences 73*(11), 6973–6985.

Xiong, J., X. Huang, and H. Ma (2015). Gas leakage mechanism in bedded salt rock storage cavern considering damaged interface. *Petroleum 1*(4), 366–372.

Xu, H., C. Arson, F. M. Chester, et al. (2012). Stiffness and deformation of salt rock subject to anisotropic damage and temperature-dependent healing. In *46th US Rock Mechanics/Geomechanics Symposium*. American Rock Mechanics Association.

Xu, H., X. Guo, and J. Bai (2017). Thermal behavior of polyhalite: a high-temperature synchrotron xrd study. *Physics and Chemistry of Minerals 44*(2), 125–135.

Závada, P., G. Desbois, J. Urai, K. Schulmann, M. Rahmati, O. Lexa, and U. Wollenberg (2015). Impact of solid second phases on deformation mechanisms of naturally deformed salt rocks (kuh-e-namak, dashti, iran) and rheological stratification of the hormuz salt formation. *Journal of Structural Geology 74*, 117–144.

Zeiss. Microscopy reflected light microscopy.

Zhang, J. J. (2019). *Applied Petroleum Geomechanics*. Gulf Professional Publishing.

Zhang, Q., Z. Song, J. Wang, Y. Zhang, and T. Wang (2021). Creep properties and constitutive model of salt rock. *Advances in Civil Engineering 2021*.

Zhang, Y., M. Krause, and M. Mutti (2013). The formation and structure evolution of zechstein (upper permian) salt in northeast german basin: a review. *Open Journal of Geology 2013*.

Zhenyu, T. and M. Haihong (1990). An experimental study and analysis of the behaviour of rock under cyclic loading. *Intl J of Rock Mech & Mining Sci & Geomechanic Abs 27*(1).

Zhou, W., R. Apkarian, Z. L. Wang, and D. Joy (2006). Fundamentals of scanning electron microscopy (sem). In *Scanning microscopy for nanotechnology*, pp. 1–40. Springer.

Ziegler, P. (1990). *Geological Atlas of Western and Central Europe*. 2nd Edition, Shell Internationale Petroleum Mij. B.V. and Geological Society.

Appendix A

List of Abbreviations

BGS	British Geological Survey
CAES	Compressed Air Energy Storage
CFD	Computational Fluid Dynamics
EBSD	Electron Backscatter Diffraction
EBSDP	Electron Backscatter Diffraction pattern
GBM	Grain boundary migration
GBS	Grain boundary sliding
ISRM	International Society for Rock Mechanics
Mya	Million of years ago
nmRC	nano and microscale Research Centre
Pc	Confining pressure
PCO	Preferred crystal orientation
PXRD	Powder X-Ray Diffraction analysis
SEM	Scanning Electron Microscope
T	temperature
TGF	Transgranular fracturing
UGS	Underground Gas Storage
XRD	X-Ray Diffraction analysis
CO_2	Carbon dioxide
CH_4	Methane/Natural Gas
H_2	Hydrogen
$NaCl$	Sodium Cloride/Halite

α	Thermal expansion coefficient
F	force
x	displacement
σ_1	Principal stress
ε_{ax}	Axial strain
ε_{circ}	circumferential strain
$\dot{\varepsilon}$	strain rate
E	Young's modulus, modulus of elasticity
K	Bulk modulus
ν	Poisson's ratio

Appendix B

Matlab Scripts

B.1 Script 1

```
aa = exist('z','var');

if aa == 0

Carla_cyclic_loading = {};

Carla_cyclic_loading{1,1}='181119_RMPL35_A3';
Carla_cyclic_loading{2,1}='181126_RMPL35_B8';
Carla_cyclic_loading{3,1}='181210_RMPL35_C3';
Carla_cyclic_loading{4,1}='190613_RMPL35_F3';
Carla_cyclic_loading{5,1}='190701_RMPL35_LB4';
Carla_cyclic_loading{6,1}='191023_RMPL35_WB16';
Carla_cyclic_loading{7,1}='190318_RMPL35_A7-1';
Carla_cyclic_loading{8,1}='190130_RMPL35_B6';
Carla_cyclic_loading{9,1}='190206_RMPL35_D3';
Carla_cyclic_loading{10,1}='200302_RMPL35_B2-1';
Carla_cyclic_loading{11,1}='190222_RMPL35_C2';



for iii = 1:15
Carla_cyclic_loading{iii,2}=[];
Carla_cyclic_loading{iii,2}=double(Carla_cyclic_loading{iii,2});
end
% To import data from excel to MATLAB
%Carla_cyclic_loading{1,2} = importfile('Name excel File',...
'Name page of excel file','Columns and rows we want to import');
Carla_cyclic_loading{1,2} = importfile('181119_RMPL35_A3.xlsx',...
'Processed-Data','A26:T195805');
Carla_cyclic_loading{2,2} = importfile('181126_RMPL35_B8.xlsx',...
'Processed-Data','A26:T197420');
Carla_cyclic_loading{3,2} = importfile('181210_RMPL35_C3.xlsx',...
'Processed-Data','A26:T196726');
Carla_cyclic_loading{4,2} = importfile('190613_RMPL35_F3',...
'Processed-Data','A26:T212090');
Carla_cyclic_loading{5,2} = importfile('190701_RMPL35_LB4',...
'Processed-Data','A26:T212000');
Carla_cyclic_loading{6,2} = importfile('191023_RMPL35_WB16',...
```

```
'Processed-Data','A26:T213186');
Carla_cyclic_loading{7,2} = importfile('190318_RMPL35_A7-1',...
'Processed-Data','A26:T215800');
Carla_cyclic_loading{8,2} = importfile('190130_RMPL35_B6.xlsx',...
'Processed-Data','A26:T199276');
Carla_cyclic_loading{9,2} = importfile('190206_RMPL35_D3.xlsx',...
'Processed-Data','A26:T200702');
Carla_cyclic_loading{10,2} = importfile('200302_RMPL35_B2-1',...
'Processed-Data','A26:T212562');
Carla_cyclic_loading{11,2} = importfile('190222_RMPL35_C2.xlsx',...
'Processed-Data','A441:T199566');
end


ff=1; % The number that cycles through the shifts

shft = [0.7803,1.24,2.561,1.6,2.546,1.311,1.387,1.0102,0.9475,0,...
-0.03257]; % List of strain shifts
shft2 = [0.0901,0.1264,0.07186,0.1114,0.196]; %Inital wrong LB4= 2.742
shft3 = [0,-0.6602,-0.9077,-0.3874,-0.6453,0,-0.66,-0.629,-1.092,...
-0.05602,-0.6721];


%1

%Loading tests at 25MPa and 25 C :
plottitle='Test A3';
% figure;
z=Carla_cyclic_loading{1,2};
ss=z(:,5);sn=z(:,6)-shft(ff); % ss = stress, sn = strain.
% plot(z(:,6)-0.7803,z(:,5));
% title('Test A3');
% xlim([0 0.3])
% % legend('unfiltered')
% xlabel('Strain (%)')
% ylabel('Stress (MPa)')
b(ff)=max(sn);
label(ff)=string(plottitle);

[ymod,resstrain,snacc,pstrain,clistr,clisty,clistsn,clistsnacc,...
clistpsn,clistmaxsn,maxstrain,pratio,ConfDisp,AxDisp,lstrainCalc,...
lstrainCalc1,clistpr,bulkm,clistbm,lstrain,clistlsn,clistPc,...
clistLstrainCalc] = ResStrain(z);
maxstrain=maxstrain-shft(ff);
rslist(ff,1:length(resstrain))=resstrain;
SubPlotter(ss,sn,plottitle,ymod,resstrain,clistr,clisty);
PoissonRatio(clistpr,pratio,plottitle);
BulkModulus(clistbm,bulkm,plottitle)
StrainPlotCreepDeformBeh(clistsn,sn,plottitle);
LateralStrain(clistlsn,lstrain,plottitle)
PlotsMinstrain(clistsnacc,snacc);
PlotPlasticStrain(clistpsn,pstrain);
ymlist(ff,1:length(ymod))=ymod;
lstrain=lstrain-shft3(ff);
maxstrain=maxstrain-shft2(ff);
msnlist(ff,1:length(maxstrain))=maxstrain;
prlist(ff,1:length(pratio))=pratio;
bmlist(ff,1:length(bulkm))=bulkm;
snacclist(ff,1:length(snacc))=snacc;
```

```
psnlist(ff,1:length(pstrain))=pstrain;
lsnlist(ff,1:length(lstrain))=lstrain;
%PlotYModAndPratioAll(clisty,ymod,clistpr,pratio);

figure;

plot(clisty,ymod,'b')
xlim([0 7000])
ylim([7 17])
hold on
plot(clisty,movmean(ymod,200),'k',...
    'LineWidth',2);
xlabel('Cycle')
ylabel('Young''s Modulus (GPa)')


ymod=[];resstrain=[];clistr=[];clisty=[];ss=[];sn=[];clistsn=[];clistbm=[];
ff=ff+1;
```

B.2 Script 2

```
function [ymod,resstrain,snacc,pstrain,clistr,clisty,clistsn, ...
clistsnacc,clistpsn,clistmaxsn,maxstrain,pratio,ConfDisp,AxDisp, ...
lstrainCalc,lstrainCalc1,clistpr,bulkm,clistbm,lstrain,clistlsn, ...
clistPc,clistLstrainCalc] = ResStrain(z)

threshold=3; % Gets rid of dodgy data early on
st=find(z(:,5)>threshold,1); % Finds the first value where Y > 3
ss=z(:,5);sn=z(:,6);ad=z(:,4);Pc=z(:,8);lsn=z(:,13);pr=z(:,14); ...
bm=z(:,20); % ss = stress, sn = strain.
cycle=1;

for ik = st:length(ss)-2
    diffb = ss(ik)-ss(ik-1); % Difference before
    diffa = ss(ik+1)-ss(ik); % Difference after
    test = diffa*diffb; % if it's negative, it's a turning point
    diff2b = ss(ik)-ss(ik-2); % Checking 2 points ahead and behind
    diff2a = ss(ik+2)-ss(ik); % Gets rid of random fluctuations in the data
    test2 = diff2a*diff2b; %

    if test2 < 0 && test < 0
        if ss(ik) > 6
            maxstress(cycle,1)=ss(ik);
            maxstrain(cycle,1)=sn(ik);
            pratio(cycle,1) = pr(ik);
            bulkm(cycle,1) = bm(ik);
            lstrain(cycle,1) = lsn(ik);


            cycle=cycle+1;
        elseif ss(ik) < 6

            minstress(cycle,1)=ss(ik);
            minstrain(cycle,1)=sn(ik);
        end
    end

end

bad=find(minstrain==0); % Finds the points that failed to give a value
for ij=bad
    maxstress(ij)=[];maxstrain(ij)=[];minstress(ij)=[]; ...
    minstrain(ij)=[]; % Removes bad data
end



% % Young's Modulus Calculation
ymod(1,1) = ((maxstress(1)*0.001) - (ss(st)*0.001)) / ...
((maxstrain(1)/100) - (sn(st)/100));% Initial Calculation
for il = 2:length(minstrain)-1
    ymod(il,1) = ((maxstress(il)*0.001) - (minstress(il)*0.001)) / ...
    ((maxstrain(il)/100) - (minstrain(il)/100));
end

% % Elastic Recovery Calculation
```

```
resstrain=zeros(length(minstress)-1,1);
for il=1:length(minstress)-2
    resstrain(il,1)=(maxstrain(il+1)-minstrain(il));
end
resstrain(end)=[];

clistr=1:length(resstrain);
clisty=1:length(ymod);
clistsn=1:length(sn);
clistpr=1:length(pratio);
clistbm=1:length(bulkm);
clistmaxsn=1:length(maxstrain);
clistlsn=1:length(lstrain);
```

Appendix C

Strain vs cycles plots

C.1 Series A

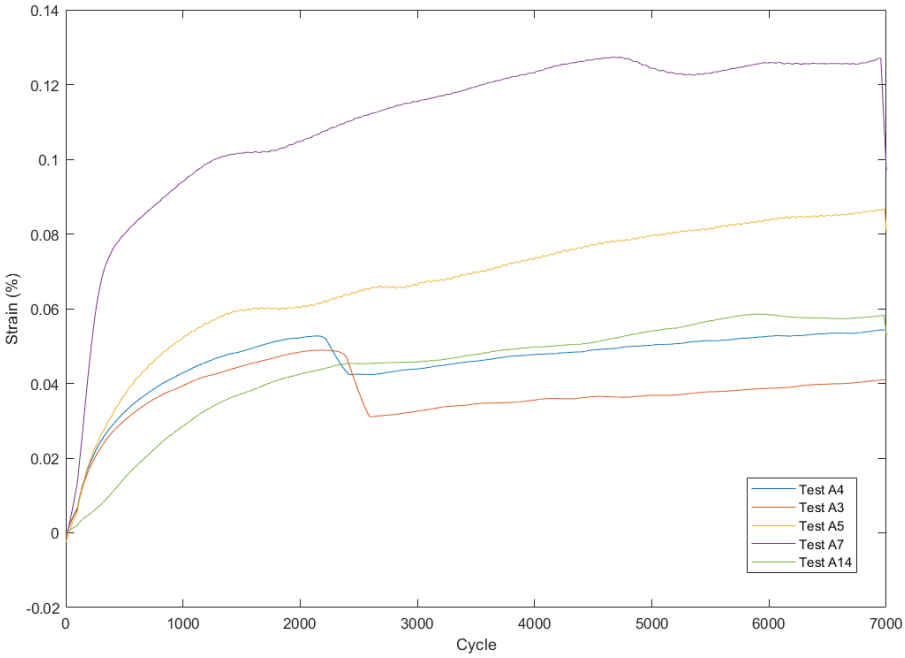

C.2 Series B

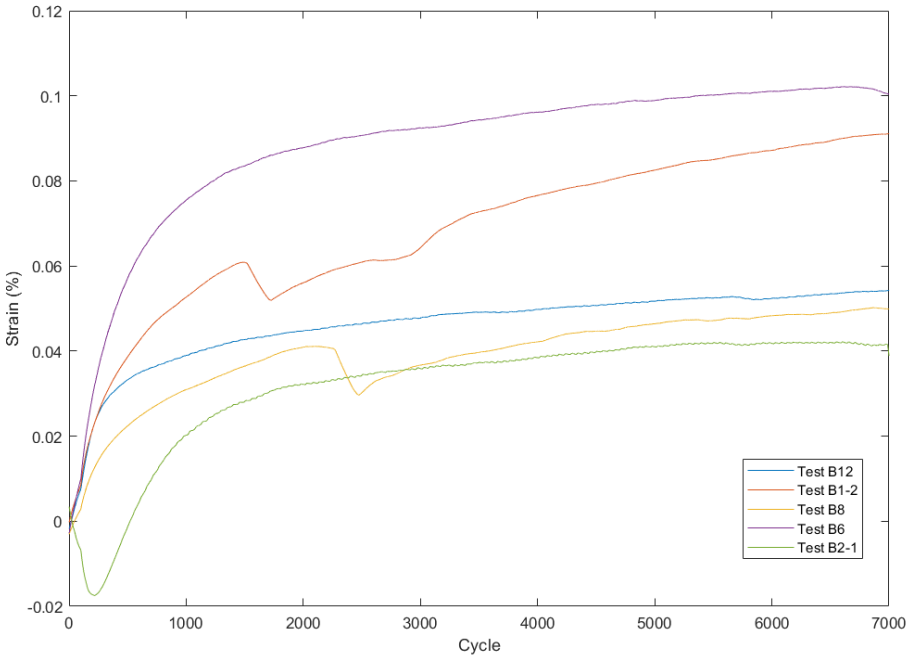

C.3 Series C

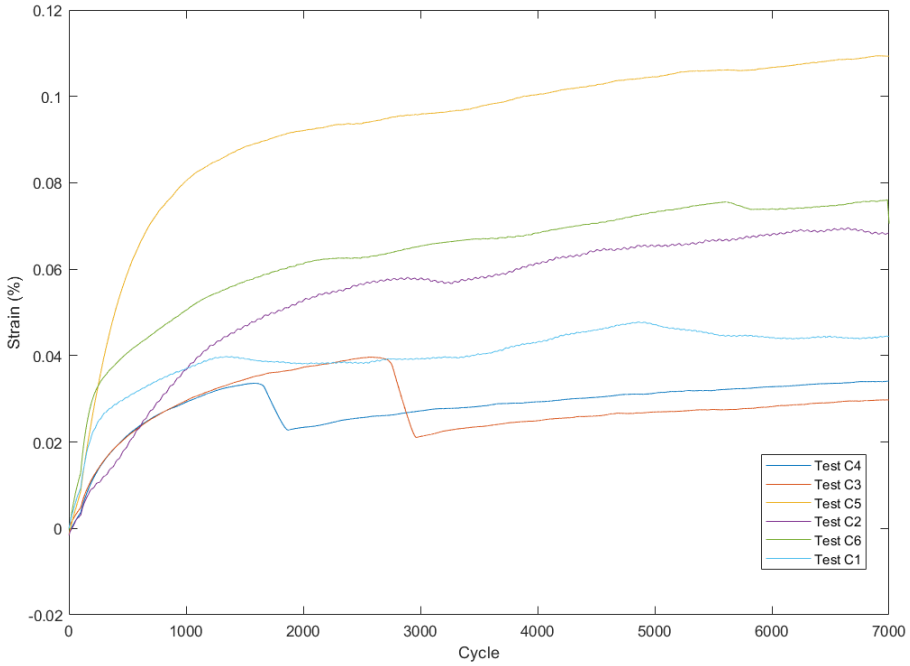

C.4 Series F

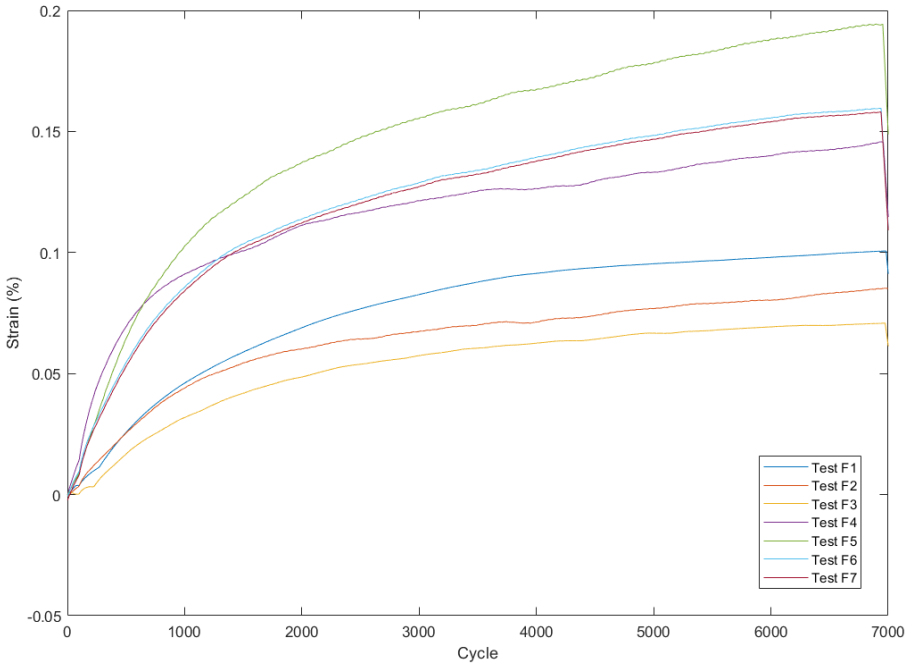

C.5 Series WB

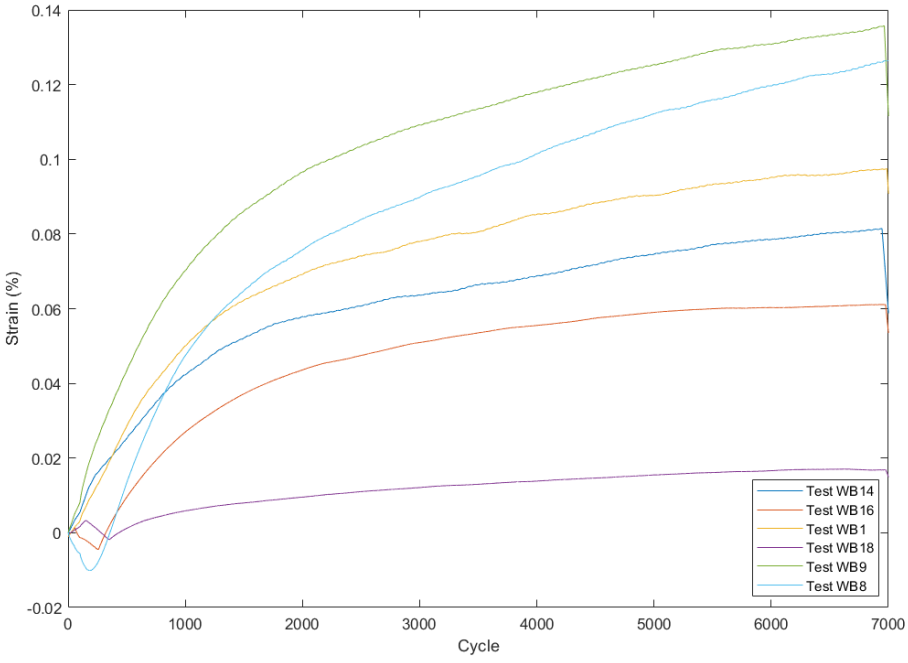

C.6 Series LB

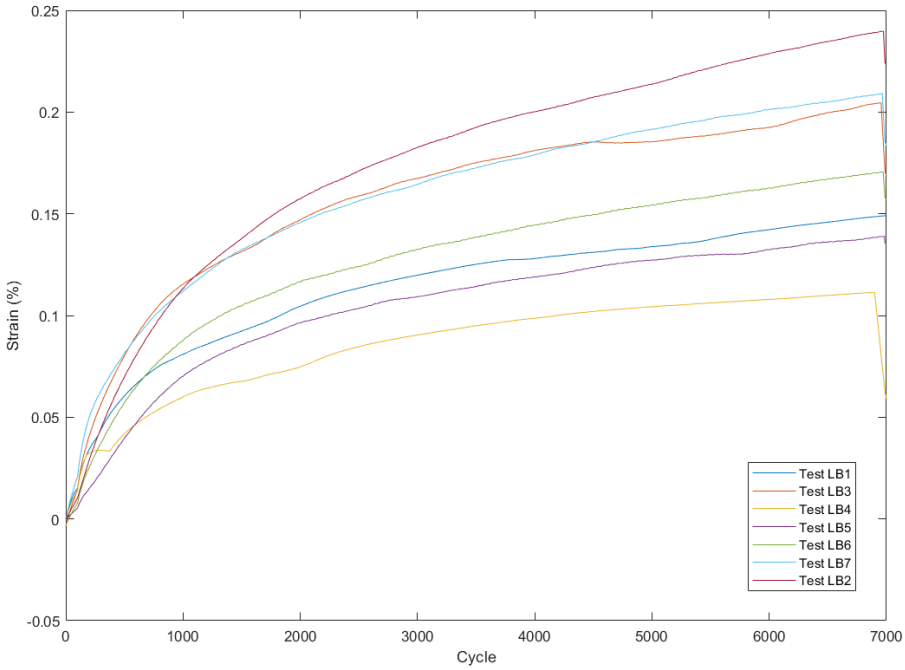
0.25
0.2
0.15
0.1
0.05
0
-0.05
Strain (%)
0
1000
2000
3000
4000
5000
6000
7000
Cycle
Test LB1
Test LB3
Test LB4
Test LB5
Test LB6
Test LB7
Test LB2